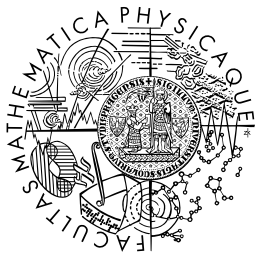

FACULTY
OF MATHEMATICS
AND PHYSICS
Charles University

DOCTORAL THESIS

Mgr. Alžběta Opištilová

Stars at a glance: using high-resolution spectroscopy and long-baseline interferometry

Astronomical Institute of Charles University

Supervisor of the doctoral thesis: doc. Mgr. Miroslav Brož, Ph.D.

Study programme: Theoretical Physics, Astronomy and Astrophysics

Study branch: P4F1

Prague 2025

I declare that I carried out this doctoral thesis independently, and only with the cited sources, literature and other professional sources. It has not been used to obtain another or the same degree.

I understand that my work relates to the rights and obligations under the Act No. 121/2000 Sb., the Copyright Act, as amended, in particular the fact that the Charles University has the right to conclude a license agreement on the use of this work as a school work pursuant to Section 60 subsection 1 of the Copyright Act.

In Prague, July 12, 2025 .....

Alžběta Oplištilová

First and foremost, my sincere appreciation goes to my supervisor, doc. Mgr. Miroslav Brož, Ph.D., for his insightful guidance, generous time, helpful comments, patience, careful proofreading of papers and thesis, and constant willingness to engage in discussions. It has been a pleasure to collaborate with him. I am also grateful to my advisor, prof. RNDr. Petr Harmanec, DrSc., for his valuable advice throughout my studies.

I spent the second year of my studies in the MEYS training programme at the European Southern Observatory in Garching, which was an inspiring, enriching, and truly unique experience. I would like to thank my advisors, Drs. Christian A. Hummel, Antoine Mérand, and Henri M. J. Boffin, for their guidance and for sharing their expertise. I was delighted to meet Dr Dietrich Baade there. I truly valued our inspiring discussions, as well as his thoughtful advice and generous support.

I am thankful to Dr Hrvoje Božić for guiding me in photometric measurements at Hvar Observatory. The Hvar photometric archive proved useful in all my modelling efforts. Many thanks to Dr Denis Mourard and his team for hosting me for several weeks in 2022 and for showing me how observations with CHARA/SPICA are conducted at the Calern Observatory. It was an unforgettable experience.

Last but not least, I express my deepest gratitude to my family, who supported me throughout my studies. Their support allowed me to pursue my academic interests.

Acknowledgement I acknowledge the support of the Grant Agency of Charles University, grant no. 113224 (PI A.O.), and the Grant Agency of the Czech Republic, grant no. 19-01995S (PI prof. RNDr. Petr Harmanec, DrSc.).

Title: **Stars at a glance: using high-resolution spectroscopy and long-baseline interferometry**

Author: Mgr. Alžběta Opištilová

Institute: Astronomical Institute of Charles University

Supervisor: doc. Mgr. Miroslav Brož, Ph.D., Astronomical Institute of Charles University

Advisor: prof. RNDr. Petr Harmanec, DrSc., Astronomical Institute of Charles University

Abstract: Massive stars are cosmic engines—by exploding as supernovæ, they power galaxies, shape the interstellar medium, and enrich it with heavy elements. Yet, their inner workings remain among the most challenging frontiers in stellar astrophysics. The life of massive stars is critically influenced by multiplicity. Most of them have one or more companions, although a few of them remain single. This raises the question: Could these single stars be the end state of multiple systems? Interferometry is one of the best methods for detecting and characterising multiplicity. The Orion complex is our nearest star-forming region, and thus the most suitable for detailed studies. It hosts a number of massive stars, particularly in the Orion Belt. In this work, we aim to interpret interferometric data in synergy with astrometry, photometry, high-resolution spectroscopy, and spectral-energy distribution of stars in the Orion Belt. On the basis of our successful ESO proposal (ID: 112.25JX, PI A. Opištilová) for interferometric observations of $\delta, \varepsilon, \zeta, \sigma$ Ori with the world-class interferometer, the VLTI (the GRAVITY and PIONIER instruments), one can construct well-constrained, complex models of stars in the Orion Belt. After introducing the basics of long-baseline interferometry and presenting an overview of the Orion complex, we present our models of δ Ori, published in Opištilová et al. (2023), and ε Ori (Opištilová et al., 2025, submitted). We found that δ Ori (total mass of $35.0\,\mathrm{M}_\odot$) is currently in the pre-mass-transfer evolutionary stage, and ε Ori (mass of $28.5\,\mathrm{M}_\odot$) is a significantly oblate supergiant due to its fast rotation. Our modelling led to improvements and further development of our n-body modelling tools. We utilised several general methods: i) two-step spectral disentangling, used to detect a spectrum of a faint component in residuals, after disentangling bright components; ii) distance estimation according to faint components of the multiple systems and a verification by diffuse interstellar bands; iii) extensive mapping of χ^2 in 2D and 3D, to find a compromise model when using multi-data modelling.

Keywords: spectroscopy – interferometry – massive stars – Orion Belt – Orion complex

Contents

Introduction

Spectroscopy and interferometry are powerful and complementary techniques for advancing our understanding of the Universe. Using high-resolution spectroscopy we can resolve fine details in velocity fields, achieving $0.1\,\mathrm{m\,s^{-1}}$ (Pepe et al., 2021). Long-baseline interferometry, on the other hand, enables us to study sources on the angular scale of the order of 1.0 mas or less (Eisenhauer et al., 2011). This is achieved using optical to near-infrared wavelengths, 500 nm to $\sim$1.6 μm. It is particularly useful for observing hot stars, binaries, and circumstellar medium. Such studies are carried out with well-known interferometers such as VLTI (Schöller, 2007), CHARA (ten Brummelaar et al., 2005), or NPOI (Armstrong et al., 1998). For comparison, sub-mm and radio interferometry, operating at wavelengths between 0.1 mm and 100 m, reaches angular resolution between 10 mas and 100 mas and aims at cold protostars, disks, dust, and molecular clouds, with arrays such as ALMA (Wootten & Thompson, 2009), SMA (Ho et al., 2004), or NOEMA (Krips et al., 2022).

In this work, we focus on hot, massive stars ($M > 8\,\mathrm{M_\odot}$). In a broader context, massive stars occur in star-forming regions, omnipresent in the Universe. Prominent examples include the Galactic Centre, which hosts the most massive and dense star-forming region in the Milky Way (Ciurlo & Morris, 2025). These young stars drive powerful winds and inject enormous energy into the interstellar medium, influencing further star formation and contributing to the turbulent environment near the central supermassive black hole, Sgr A* (Balick & Brown, 1974). Another example of a star-forming region is the spectacular pair of interacting galaxies, the Antennæ (NGC 4038/4039; Whitmore et al., 2010). The overlapping regions of these galaxies host numerous super star clusters—probable precursors to globular clusters—rich in massive stars. One of the most massive stars are known to be located in the Tarantula Nebula (30 Dor) in the Large Magellanic Cloud, for example R136a1, BAT99-98 with $\approx 200\,\mathrm{M_\odot}$ (Schneider et al., 2018; Kalari et al., 2022). However, due to angular resolution limitations, it is only possible to study in detail massive stars that are relatively nearby; the LMC is 50 kpc away. An ideal region to study massive stars should be somewhere close, within ≈ 0.4 kpc.

In the first section, we thus discuss the basics of **optical interferometry**, a very powerful observing method for resolving multiple systems and studying multiplicity, the key characteristic of massive stars. The second section outlines our nearest star-forming region, which is full of nearby, massive stars, **the Orion complex**. In this context, we focused on the Orion Belt stars and constructed comprehensive models for ***δ* Ori** and ***ε* Ori**, presented in sections three and four, respectively. Each section includes its own conclusions.

Figure 1: Antennæ Galaxies, taken from Whitmore et al. (2010).

1. Optical interferometry

To expand the understanding of the Universe, astronomers need to unlock the fine details of celestial objects and phenomena that are often hidden at scales too small to be resolved by conventional telescopes. Achieving this goal requires improving the resolution of instruments, which is ultimately given by the diffraction limit, further influenced by the atmosphere, and complicated by other imperfections in optical setups. The aberrations are discussed elsewhere, e.g. Gu (2000); Hecht (2002); Smith (2008); Conrady (2013); Kitchin (2020). Hereinafter, we focus on diffraction and seeing, as they significantly influence interferometric observations.

Diffraction The diffraction limit is the classical limit of angular resolution that a telescope or microscope can achieve. In other words, it is the smallest angular separation between two point sources (such as distant stars) that a telescope could theoretically distinguish if it were perfect and free of other distortions. Such a fundamental theoretical constraint is due to the wave nature of light. However, there are some techniques that allow going below these limits (Mugnier et al., 2004; Huang et al., 2009).

An observed star produces a diffraction pattern in the focal plane of a telescope, which closely resembles the diffraction pattern of a point source; this pattern arises from the finite size and shape of the telescope's aperture. Such a diffraction pattern is called the Airy pattern (Fig. 1.1). It consists of a central spot, the Airy disk, surrounded by concentric rings with decreasing intensities. The Airy disk itself does not provide any information about the size or shape of an observed object. Instead, it is inversely proportional to the diameter of a telescope. The larger the diameter, the smaller the central spot, as well as other rings in the Airy pattern. Also, since the signal is higher, the signal to noise ratio is higher, and the number of easily recognisable rings is higher.

The Airy pattern corresponds to the point-spread function (PSF) of a telescope under ideal, diffraction-limited conditions. Diffraction, nevertheless, blurs the ideal image, preventing it from being infinitely sharp, even if lenses are without any aberrations. Eventually, observations are convolutions of an ideal image and the respective PSF.

To set the theoretical resolution limit for a telescope, we need to know when we can resolve two stars (point-like sources). The light from the second star will produce the same diffraction pattern in the focal plane, shifted by the corresponding angular separation. The sum of intensity patterns is shown in Fig. 1.1. As the separation increases, it becomes possible to distinguish the two stars (Fig. 1.1c), and such separation corresponds to the angular resolution of a telescope. Although it depends on more factors, like relative brightness, the theoretical criterion for the separation defining when the stars are just being resolved is the Rayleigh criterion

$$\Delta\theta = 1.22\,\frac{\lambda}{d}, \tag{1.1}$$

where λ denotes the wavelength; and d, the diameter of the telescopes' aperture. The separation $\Delta\theta$ is in radians.

According to Rayleigh's criterion, two stars are considered resolved when the central maximum of the diffraction pattern of one star coincides with the first minimum of

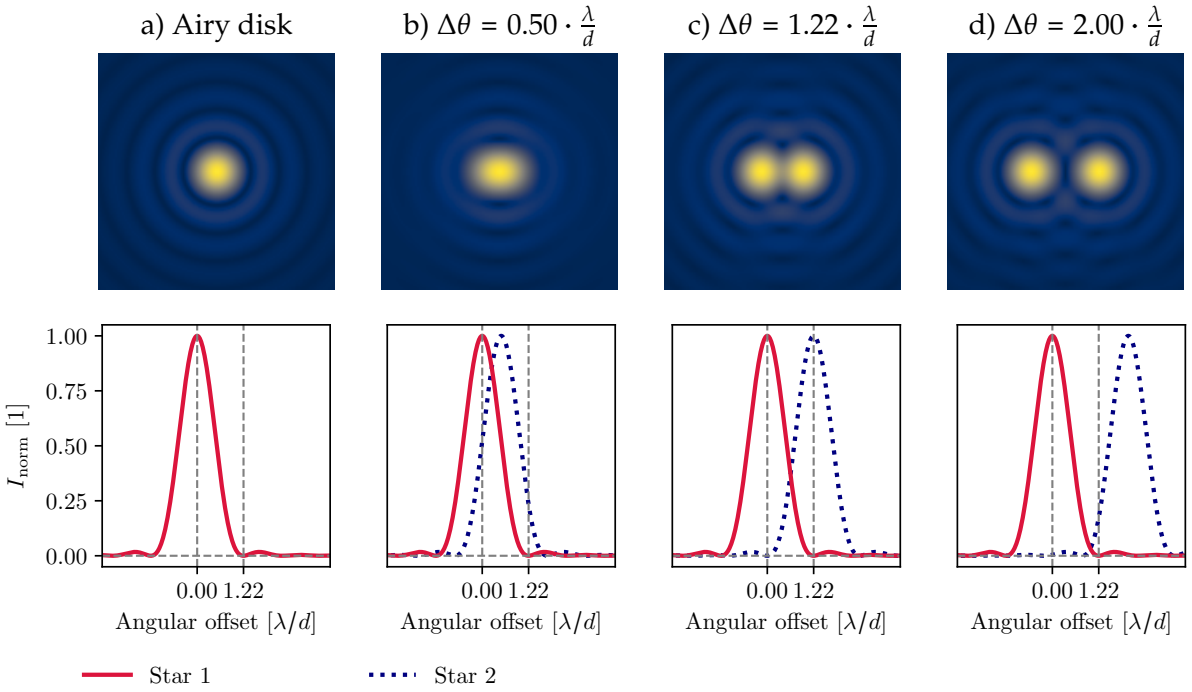

Figure 1.1: Top row: Airy disk for a point-like object (the central spot has a diameter of $2.44\,\lambda/d$) and Airy disks of two such sources with different angular offsets. Bottom row: Corresponding intensity profiles of the Airy disks above as a function of the angular separation. The second column represents the situation when two point-like objects are still unresolved according to the definition (the Airy criterion), although we see that the PSF is not perfectly spherical and can assume a two point-like objects; the third is just resolved (the Airy criterion is met); and the fourth is well resolved. The data for the diffraction patterns are from Buscher (2015).

the diffraction pattern of the other (Fig. 1.1c). The intensity of the Airy disk is dampened by the Bessel function $J_1(kr\sin\theta)$, see Eq. (1.6.1), where $k = \frac{2\pi}{\lambda}$ is the wavenumber; r, the radius; and θ, the angular separation. It holds that $J_1(x) = 0$ for $x \approx 3.8317$. Using the small-angle approximation for θ, we see that the factor of 1.22 is the first minimum of the Bessel function $J_1(x)$ divided by π

$$\theta \approx \frac{3.84}{\pi}\frac{\lambda}{d}. \tag{1.2}$$

Therefore, the resolution can be improved by decreasing the wavelength or increasing the size of the mirror. However, telescopes with diameters exceeding a few meters are expensive and challenging to build; the heavy mirrors would deform and sag due to the effects of gravity. To prevent mirrors with $D > 4\,\mathrm{m}$ from sagging, the active optics must be used to compensate for the bending. It enables the building of, for instance, 8.2-m UTs telescopes of the Very Large Telescope Interferometer (VLTI). Another solution is segmented mirrors. Such a kind is used for the Extremely Large Telescope (ELT) with the primary mirror of 39 m, which achieve a diffraction limit of 3.2 mas in visible (V-band $0.5\,\mu$m), 7.7 mas in near-infrared (J-band $1.2\,\mu$m), or 22.3 mas in mid-infrared (L-band $3.45\,\mu$m). Nevertheless, even this, currently the largest mirror, is small to distinguish fine details ($< 2\,$mas) on a stellar surfaces, even for the closest stars.

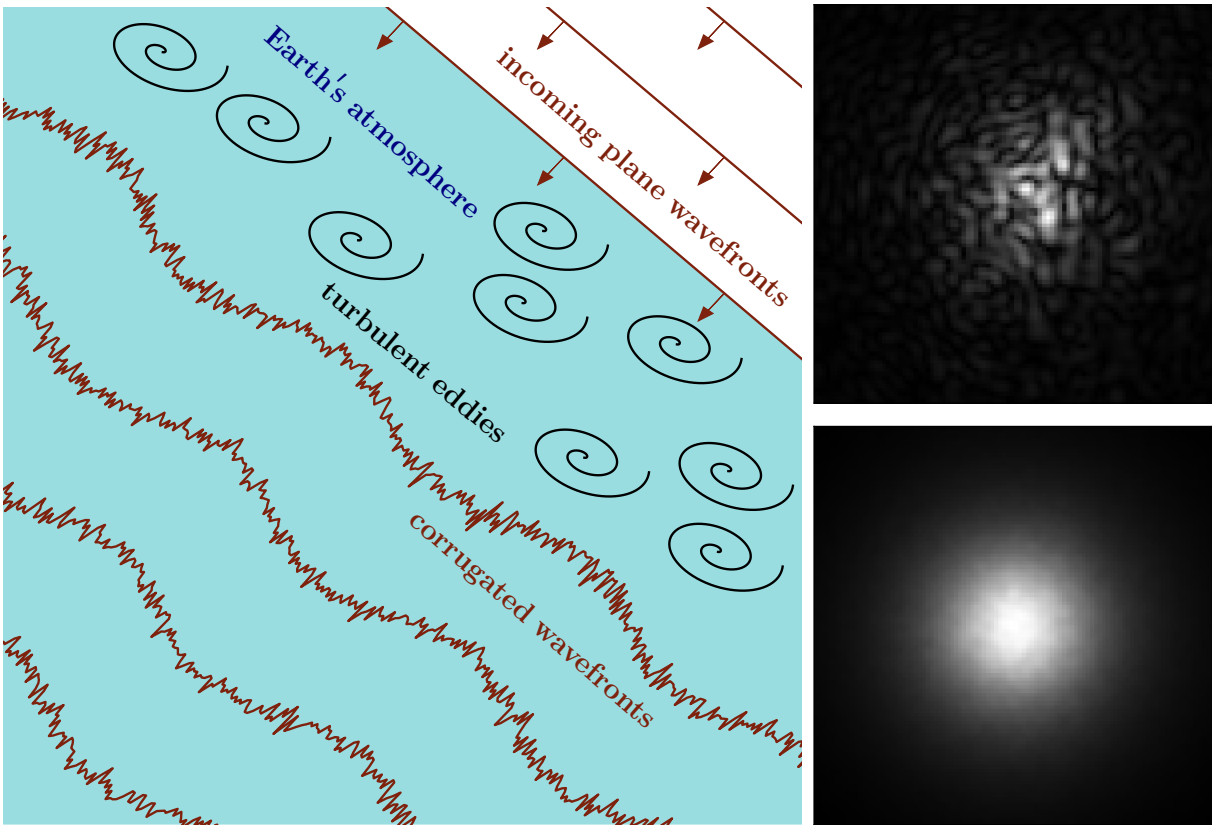

Figure 1.2: Effects of the Earth's atmosphere on incoming planar wavefronts and their images. Left panel: Incoming planar wavefronts are deformed as they pass through the Earth's atmosphere due to atmospheric turbulence. Right panels: A point source is then seen as a speckle pattern due to the impact of the atmosphere, when we observe it for a few milliseconds (upper figure). If we observe a point source with a longer exposure time (a few seconds), the speckles are averaged over time, and we observe a seeing disk (lower figure). The data for the diffraction patterns are from Buscher (2015).

Seeing The second complication during observation is the effect of the atmosphere, particularly atmospheric turbulence, known as seeing, which is addressed by the adaptive optics (see Sect. 1.4). Planar wavefronts arriving from distant sources or stars turn into corrugated wavefronts after going through Earth's atmosphere, which is filled with turbulent eddies; see Fig. 1.2. We use two parameters, Fried's coherence length or the atmospheric coherence time, for measuring the quality of optical transmission through the atmosphere that is affected by random inhomogeneities in the atmosphere's refractive index. Such inhomogeneities blur the image, primarily due to small variations in density, and consequently, in the refractive index $n(\rho)$. The refractivity, $n-1$, is proportional to ρ that is proportional to $\frac{p}{T}$, according to the gas law

$$n-1 \propto \rho \propto \frac{p}{T}. \tag{1.3}$$

Assuming the standard temperature and pressure (15 °C and 1013.25 hPa) and the green light, $\lambda = 0.5\,\mu$m, the refractive index of air is $n \approx 1.000277$ (Edlén, 1966). The relative change of the refractivity corresponds to a negative relative change in temperature

$$\frac{\Delta(n-1)}{n-1} \approx -\frac{\Delta T}{T}. \tag{1.4}$$

If the temperature is 15 °C, i.e. 288 K, and the change is $\Delta T = 0.01\,\mathrm{K}$, then

$$\Delta n \approx -\frac{0.01}{288} \cdot 2.77 \cdot 10^{-4} = -9.6 \cdot 10^{-9}. \tag{1.5}$$

Therefore, the change of 0.01 K in temperature leads to the change of 10^{-8} in the refractive index. Now consider the corresponding change in phase given by

$$\Delta\Phi = \frac{2\pi}{\lambda}\Delta\mathrm{OPL} = \frac{2\pi}{\lambda} L\,\Delta n, \tag{1.6}$$

where OPL is the optical path length; and L, the physical path length, i.e. the thickness of the turbulent layer, which matters, of the order of 100 m (the near-surface layer). This expression shows that shorter wavelengths are more affected than the longer ones, like infrared. For the given example, the change in phase is

$$\Delta\Phi = \frac{2\pi}{500 \cdot 10^{-9}} \cdot 100 \cdot 10^{-8} = 12.6\,\mathrm{rad}, \tag{1.7}$$

which is a substantial phase distortion. The corresponding optical path difference is

$$\Delta\mathrm{OPL} = \frac{\lambda}{2\pi}\Delta\Phi = \frac{500 \cdot 10^{-9}}{2\pi} \cdot 12.6 \approx 10 \cdot 10^{-1}\,\mathrm{m} = 1\,\mu\mathrm{m}. \tag{1.8}$$

Therefore, even such small changes in T leads to optical phase differences significantly degrading image quality. Nevertheless, one can be 'lucky' and the ΔOPL can be smaller, which is the principle of lucky imaging.

Fried's parameter Fried's parameter (or coherence length), denoted by r_0, describes the extent of turbulence, and therefore, the seeing conditions for astronomical observations. It is defined as the diameter of a circular patch of the incoming wavefront with a phase variance of $1\,\mathrm{rad}^2$. It indicates the maximum area of the telescope's mirror over which the atmosphere does not significantly distort the incoming light, allowing for sharp imaging. The Fried's parameter has units of length and is usually given in centimetres. The larger the parameter, the larger the characteristic size of turbulence is, which is better; one can achieve a better resolution. If the turbulent eddies are small, the observations are difficult. A few centimetres indicate poor seeing, more than twenty centimetres means excellent seeing. If telescope's aperture is smaller than r_0, then the image is primarily limited by the diffraction limit, and the impact of the atmosphere is negligible. If a telescope is larger than r_0, then the image becomes limited by atmospheric turbulence and appears blurry. The formula expressing r_0 is (Buscher, 2015)

$$r_0 = \left(0.423\,k^2\,(\cos\zeta)^{-1} \int C_n^2\,(h)\,\mathrm{d}h\right)^{-\frac{3}{5}}, \tag{1.9}$$

where $k = \frac{2\pi}{\lambda}$ is the wavenumber; ζ, the zenith angle; and $C_n^2\,(h)$, the atmospheric turbulence strength, which is a function of temperature fluctuations and turbulence along the starlight path at height h. Note that $r_0 \propto \lambda^{\frac{6}{5}}$ implies that turbulence becomes less significant at longer wavelengths. That is one of the reasons why infrared interferometry is easier than interferometry in the visible spectral range, where the turbulence scale is smaller, making corrections more challenging.

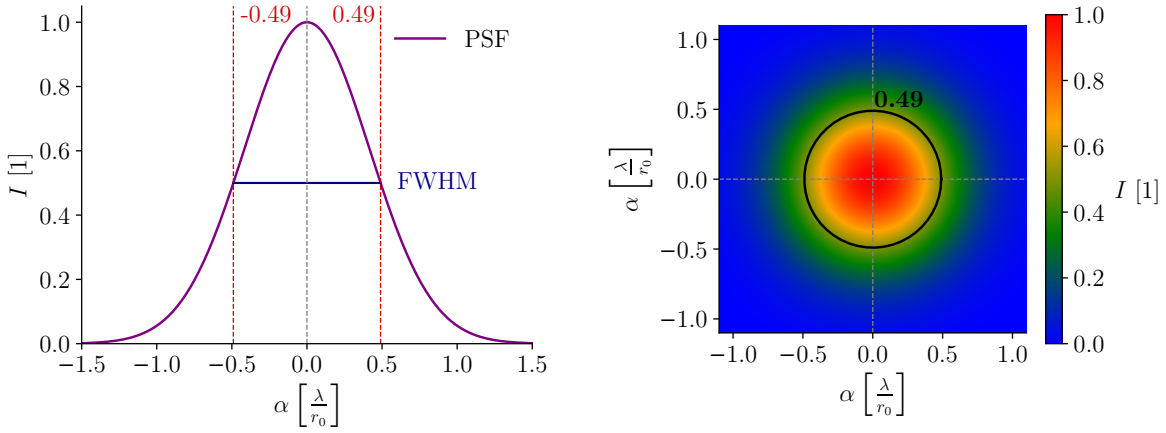

Figure 1.3: Gauss function in 1D and 2D. The Gauss function represents a suitable approximation of the PSF, the intensity profile seen for a seeing disk in a telescope. The seeing value 0.49 of normalised intensity is marked. This value corresponds to the full width at half maximum of the PSF of a point-source, as seen through a telescope. The spatial frequency α is in the units of wavelength λ per Fried's parameter r_0.

Coherence time The atmospheric coherence time τ_0 characterises how fast the atmosphere changes from the point of view of a telescope. It is the time when the turbulence in the atmosphere stays roughly the same (coherent). It is defined as the time difference when the root mean square phase fluctuations at a single point have a value of 1 rad. If τ_0 is large (about 10–20 ms), the atmosphere changes slowly, which is suitable for long exposures or adaptive optics. If τ_0 is small (about 1–5 ms), the atmosphere changes quickly, and the distortion blurs the image faster. The formula for the atmospheric coherence time is (Buscher, 2015)

$$\tau_0 = 0.314\,\frac{r_0}{\overline{v}} = \left(2.91\,k^2 \int C_n^2\,(h)\,v^{\frac{5}{3}}\,\mathrm{d}h\right)^{-\frac{3}{5}}, \tag{1.10}$$

where v is the effective transverse wind speed that transports the turbulence. Note that atmospheric coherence time is related to the Fried parameter r_0.

Due to atmospheric effects, we usually do not see the Airy disk. If we observe with a telescope larger than r_0 and use a short exposure of the order of milliseconds, we see a smeared-out image called a speckle pattern (upper right panel of Fig. 1.2). The speckle pattern consists of many spots ('speckles'), and their number roughly corresponds to the number of coherence patches of size r_0 across the telescope's aperture. For longer exposures (a few seconds), we observe a seeing disk (bottom right panel of Fig. 1.2) resulting from the time-averaged superposition of many speckles. The intensity profile of a seeing disk, PSF, can be approximated by the Gauss function, see Fig. 1.3.

The full width at half maximum of the PSF, as observed in a telescope, serves as an indicator of atmospheric blurring, commonly referred to as 'seeing' and measured in arcseconds. Seeing is given as the FWHM of the PSF

$$\theta_{\text{seeing}} = \text{FWHM}_{\text{seeing}} = 0.98\,\frac{\lambda}{r_0}. \tag{1.11}$$

It is related to the Fried parameter r_0 and tells us how much a point source (e.g. a star) is broadened due to turbulence. Fig. 1.3 illustrates the region where the seeing is measured.

Observers at VLTI use Eq. (1.11) to quantify observational quality by seeing, whereas at CHARA, they use the Fried parameter r_0 directly. For instance, if we observe with a wavelength of 550 nm and the Fried parameter is 10 cm (mediocre observing conditions), we obtain a seeing in arcseconds

$$\mathrm{FWHM}_{\mathrm{seeing}} = 0.98 \cdot \frac{5.5 \cdot 10^{-7}}{0.1}\,\mathrm{rad} = 1.11\,\mathrm{arcsec}.$$

A larger r_0 indicates better seeing, corresponding to a smaller FWHM of the PSF.

There are four fundamental methods to reach the diffraction limit and suppress the impact of the atmosphere:

1. *Aperture masking*, will be mentioned in Sect. 1.1.

2. *Lucky imaging* records many short-exposure images, with timescales comparable to or shorter than the coherence time τ_0. Occasionally, some images are sharper due to brief instants of reduced atmospheric turbulence[1]. Alternatively, one can use a large set of short-exposure speckle patterns, compute their power spectrum via Fourier analysis, and combine the information to reconstruct a high-resolution image.

3. *Adaptive optics* is used the most broadly nowadays. Further details on this technique will be discussed in Sect. 1.4.

4. *Deconvolution* (Vernazza et al., 2021) is a mathematical process used to reverse the effects of convolution in recorded data. In imaging, the observed image O can be modelled as
$$O = I * \mathrm{PSF} + N, \tag{1.12}$$
where I is the ideal image; PSF, the PSF; and N, the noise. Using deconvolution enables a (partial) recovery of the ideal image I.

The technique that enables astronomers to overcome the diffraction limit is called *interferometry*. The very word 'interferometry' is derived from interfero (meaning 'interference') and metron (meaning 'measurement'). In astronomy, it refers to measuring stellar properties via the interference of light (i.e. mutual influence of two waves) received from stars or other objects. This technique enables microarcsecond resolution (e.g. Schöller, 2007; Khodadi et al., 2024), allowing astronomers to measure orbits of close binaries, stellar and circumstellar disk diameters, surface features, and complex circumstellar structures.

A recent milestone in angular resolution (in sub-mm interferometry) was the imaging of the black hole's shadow and surrounding emission in M87* (Akiyama et al., 2019) and later Sgr A* (Akiyama et al., 2022). The measurements were made by the Event Horizon Telescope (EHT), using the technique of Very Long Baseline Interferometry (VLBI), which links together radio telescopes around the globe, forming an Earth-sized virtual telescope. This approach enabled an unprecedented resolution of $\theta \approx 10\,\mu$as at a wavelength of $\lambda = 1.3\,$mm.

[1] Actually, a conceptual precursor was used by Galileo Galilei, who in 1613 relied on the human eye's natural 'short exposures' to mentally integrate clearer views of sunspots (Galilei, 1613)

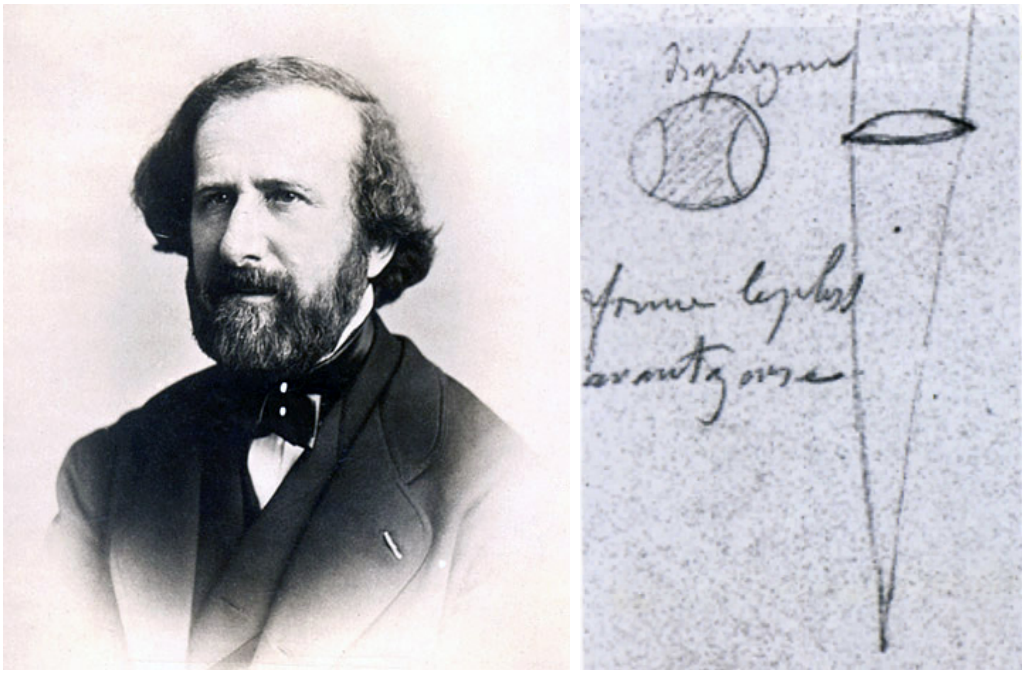

Figure 1.4: Hippolyte Fizeau (1819–1896) and his original drawing of a lens with aperture mask allowing performing interferometric measurement. Taken from Trégon (2020–2025).

1.1 Brief history

In 1868, Hippolyte Fizeau, a French physicist famous for measuring the speed of light, introduced the concept of stellar interferometry as a double-slit experiment (Fizeau, 1868). He proposed observing stars through two apertures (see Fig. 1.4) to get inferences that would provide him with a spatial distribution of the intensity.

Six years later, the director of the Marseille Observatory, Édouard Jean-Marie Stephan, first tested this method and derived upper limits for stellar diameters. For this purpose, he converted the 80-cm telescope at the Marseille Observatory into an interferometer (Stephan, 1874). This reflector was the largest in the world at that time. He masked the aperture to get two identical smaller apertures with the largest possible separation on the edges. With such an equipment, he observed fringes ('franges' in French original) for several stars and estimated an upper limit of their diameters. With this technique, known as aperture masking, É. Stephan achieved the use of a single telescope as an interferometer for the first time.

Albert A. Michelson proved that this method is efficient when he measured Jupiter's satellites. Their diameters were already determined by other methods, and he obtained excellent agreement. He predicted the results not only for uniform disks and but also for limb-darkened disks, according to a model developed to describe the Sun's intensity profile. One of his major contributions was the Michelson stellar interferometer. He used the instrument to measure the diameter of α Ori, Betelgeuse, to be 47 mas (Michelson & Pease, 1921). The larger the observed object, the more it blurs the interferometric fringes, allowing its angular size to be estimated from the extent of this blurring. They used a pair of mirrors to form the two apertures of the interferometer and observed fringes for different separations of these mirrors. The separation at which the fringes disappeared,

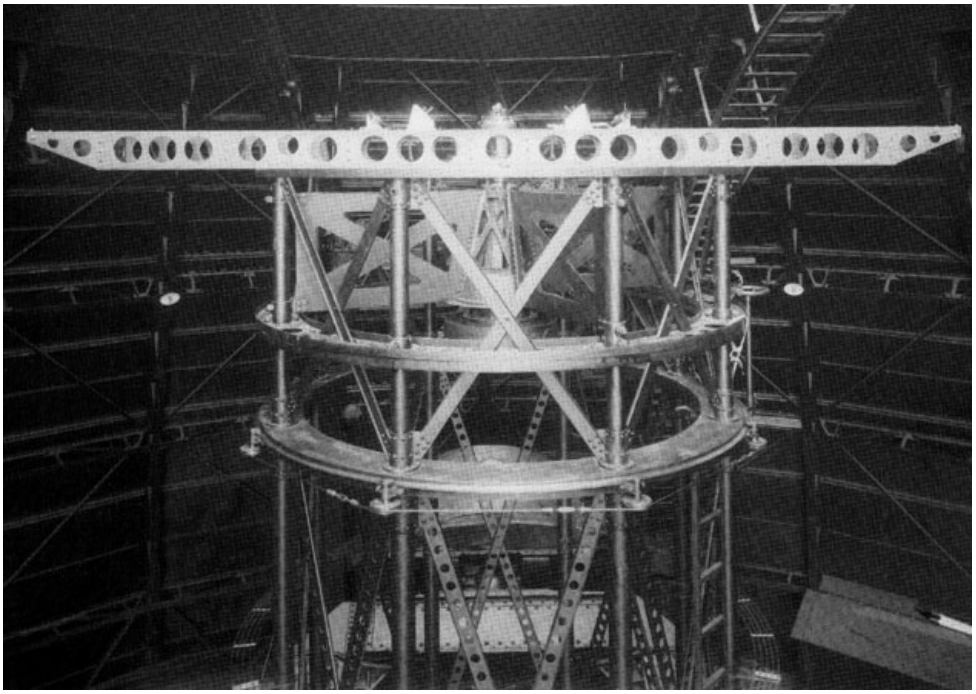

Figure 1.5: Michelson interferometer with a baseline of 20 ft on the 2.5m Hooker Telescope, Mount Wilson Observatory. Taken from Surdej (2019).

B_{null}, provides the angular diameter according to

$$\theta = \frac{1.22\,\lambda}{B_{\text{null}}}, \tag{1.13}$$

which is discussed further in Sect. 1.6.4. They used visible light with the wavelength of 500 nm; thus, the fringes should disappear at a separation of

$$B_{\text{null}} = \frac{1.22\,\lambda}{\theta} = \frac{1.22 \cdot 500 \cdot 10^{-9}}{47\,\text{mas}} = 2.7\,\text{m}. \tag{1.14}$$

They subsequently measured diameters of six additional stars with a baseline of 20 ft (see Fig. 1.5) and one star using a baseline of 50 ft (Pease, 1931).

Hanbury Brown (1956) came up with the next milestone, the intensity interferometer, which relies on intensity correlations rather than wavefront phase, which makes this method largely immune to atmospheric fluctuations. It was possible to measure diameters of several bright stars with this instrument (Hanbury Brown et al., 1974).

Labeyrie (1975) demonstrated the interference between two telescopes separated by 13.8 m as the basis for modern optical interferometry. They compensated the optical path difference by mechanical alignment. Since then, many research groups and observatories have worked toward building interferometers with increasingly large baselines to achieve higher angular resolution, leading to instruments such as SUSI (the Sydney University Stellar Interferometer; Davis, 1994), the Mark III (Shao et al., 1988), followed by the Navy Prototype Optical Interferometer (NPOI; Armstrong et al., 1998), the Palomar Testbed Interferometer (PTI; Colavita et al., 1999), and Grand Interféromètre à 2 Télescopes (GI2T; Tallon-Bosc et al., 1994) interferometer on Plateau de Calern (Mourard et al., 1994). The delay line carriage used for GI2T was later used for CHARA, and the experience gained led to the development of the Very Large Telescope Interferometer (VLTI; Schöller, 2007).

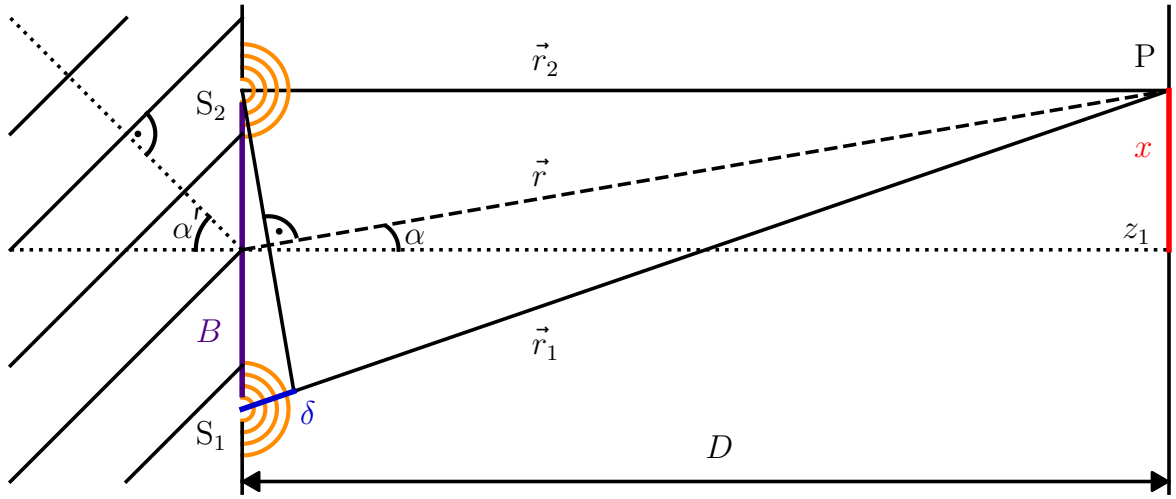

Figure 1.6: Diagram of Young's double-slit experiment. A monochromatic wave arrives at the angle α' on two slits S_1 and S_2 separated by distance B. Each slit then becomes a source of spherical waves that propagates on the screen into the distance of D. Their path difference is δ. In the point P under the angle α, they interfere with each other. On a screen placed beyond the slits, the interference produces a pattern of alternating bright and dark fringes. Inspired by Millour (2008).

1.2 Young's double-slit experiment

The fundamental mathematical description of interferometry can be illustrated by Thomas Young's double-slit experiment, first performed in 1801 (Young, 1804). This experiment demonstrated the wave nature of light through the appearance of an interference pattern.

A schema of the experiment is shown in Fig. 1.6. Monochromatic light from a distant point source offset from the axis by the angle α' on two narrow, closely spaced slits at points S_1 and S_2, separated by the distance of B (purple). According to Huygens' principle (Huygens, 1690), each slit acts as a coherent source of spherical wavefronts, which interfere on the screen, located at the distance of D. We will derive the intensity at point P, offset from the axis z_1 by the angle of α and located at a lateral displacement x (red). The vectors $\vec{r}_1$ and $\vec{r}_2$ show the paths from points S_1 and S_2 to point P, whereas their path difference is $\delta = ||S_2P| - |S_1P|| \approx \sin\alpha$ and $\sin\alpha = \frac{\delta}{B}$ (blue). The vector $\vec{r}$ is connecting the center between the slits and point P and determines the angle α under which we observe the interference pattern at point P. The waves interfere on the screen in two ways:

1. constructively—show bright fringes on the screen, they are in phase (both reach maximum or minimum at the same time), their path difference δ is an integer multiple of their wavelength, i.e. λk, where $k = 0, \pm1, \pm2, \pm3, \ldots$; or

2. destructively—show dark fringes on the screen, they are in anti-phase (the darkest fringe is when one has maximum while the other has minimum), their path difference δ is an odd multiple of half the wavelength, i.e. $\delta = \frac{1}{2}(2k+1)\lambda$, where again $k = 0, \pm1, \pm2, \pm3, \ldots$.

The positions of bright fringes with respect to x are determined using similar triangles. If the angle α is small, it applies also at point S_2; thus, $\delta = B\sin\alpha = k\lambda$, taking into account the condition for constructive interference. From the triangle with sides rxz_1, using the small angle approximation, $\sin\alpha \approx \tan\alpha \approx \frac{x}{D}$. By substituting the relations, we obtain the positions of the bright fringes as

$$x = \frac{k\lambda D}{B}. \tag{1.15}$$

To derive the intensity on the screen at point P, let us represent a flat monochromatic electromagnetic wave by a dimensionless disturbance $\vec{D}$, meaning either $\vec{E}$ or $\vec{B}$. The disturbance in the complex notation is (Brož & Wolf, 2017)

$$D(\vec{r},t) = D_0\,\mathrm{e}^{-\mathrm{i}(\omega t - \vec{k}\cdot\vec{r})} = D(\vec{r})\,\mathrm{e}^{-\mathrm{i}\omega t}, \tag{1.16}$$

where the angular frequency is $\omega = \frac{2\pi c}{\lambda}$ and the wave vector is $\vec{k} = \frac{2\pi}{\lambda}\hat{k}$. According to the Huygens principle, the sum of two spherical wavefronts (complex amplitudes) on the screen at the distance of z_1 is

$$\begin{aligned} D(\vec{r}) = D(\vec{r}_1) + D(\vec{r}_2) = \frac{D_0}{r_1}\mathrm{e}^{-\mathrm{i}k\cdot r_1} + \frac{D_0}{r_2}\mathrm{e}^{-\mathrm{i}k\cdot r_2} \approx \frac{D_0}{z_1}\left(\mathrm{e}^{\mathrm{i}kr_1} + \mathrm{e}^{\mathrm{i}kr_2}\right) = \\ = \frac{D_0}{z_1}\mathrm{e}^{\mathrm{i}kr_1}\left(1 + \mathrm{e}^{\mathrm{i}k(r_2-r_1)}\right). \end{aligned} \tag{1.17}$$

On the screen, we observe the flux given by the Poynting vector $\vec{S} = \vec{E}\times\vec{H}$, where $\vec{E}$ is the electric field vector and $\vec{H}$ is the magnetic field's auxiliary field vector. After averaging and computing the square ('intensity'), we get

$$\begin{aligned} I(\vec{r}) \equiv \langle DD^*\rangle &= \left[\frac{D_0}{z_1}\,\mathrm{e}^{\mathrm{i}kr_1}\left(1 + \mathrm{e}^{\mathrm{i}k(r_2-r_1)}\right)\right]\left[\frac{D_0^*}{z_1}\,\mathrm{e}^{-\mathrm{i}kr_1}\left(1 + \mathrm{e}^{-\mathrm{i}k(r_2-r_1)}\right)\right] = \\ &= \frac{D_0^2}{z_1^2}\left[(1 + \mathrm{e}^{-\mathrm{i}k(r_2-r_1)} + \mathrm{e}^{\mathrm{i}k(r_2-r_1)} + 1\right] = \\ &= \frac{D_0^2}{z_1^2}\left\{2 + \cos\left[k(r_1-r_2)\right] + \mathrm{i}\sin\left[k(r_1-r_2)\right] + \cos\left[k(r_2-r_1)\right] + \mathrm{i}\sin\left[k(r_2-r_1)\right]\right\} = \\ &= \frac{D_0^2}{z_1^2}\left\{2 + 2\cos\left[k(r_1-r_2)\right]\right\} = 2\cdot\frac{D_0^2}{z_1^2}\{1 + \cos\left[k(r_1-r_2)\right]\}. \end{aligned} \tag{1.18}$$

The asterisk * denotes the complex conjugation. By denoting the factor before parenthesis I_0 and rewriting the argument of the cosine function as the path difference in α, we get

$$I(\alpha) = I_0\left[1 + \cos(k\alpha B)\right]. \tag{1.19}$$

It is the simplest case, stating the intensity at the location offset from the axis of the slits. If the monochromatic wave impinges at the angle of α', then

$$I(\alpha,\alpha') = I_0\{1 + \cos\left[k(\alpha+\alpha')B\right]\}. \tag{1.20}$$

Based on Eq. (1.20), Fig. 1.7 displays the four basic intensity patterns we can see in Young's double-slit experiment.

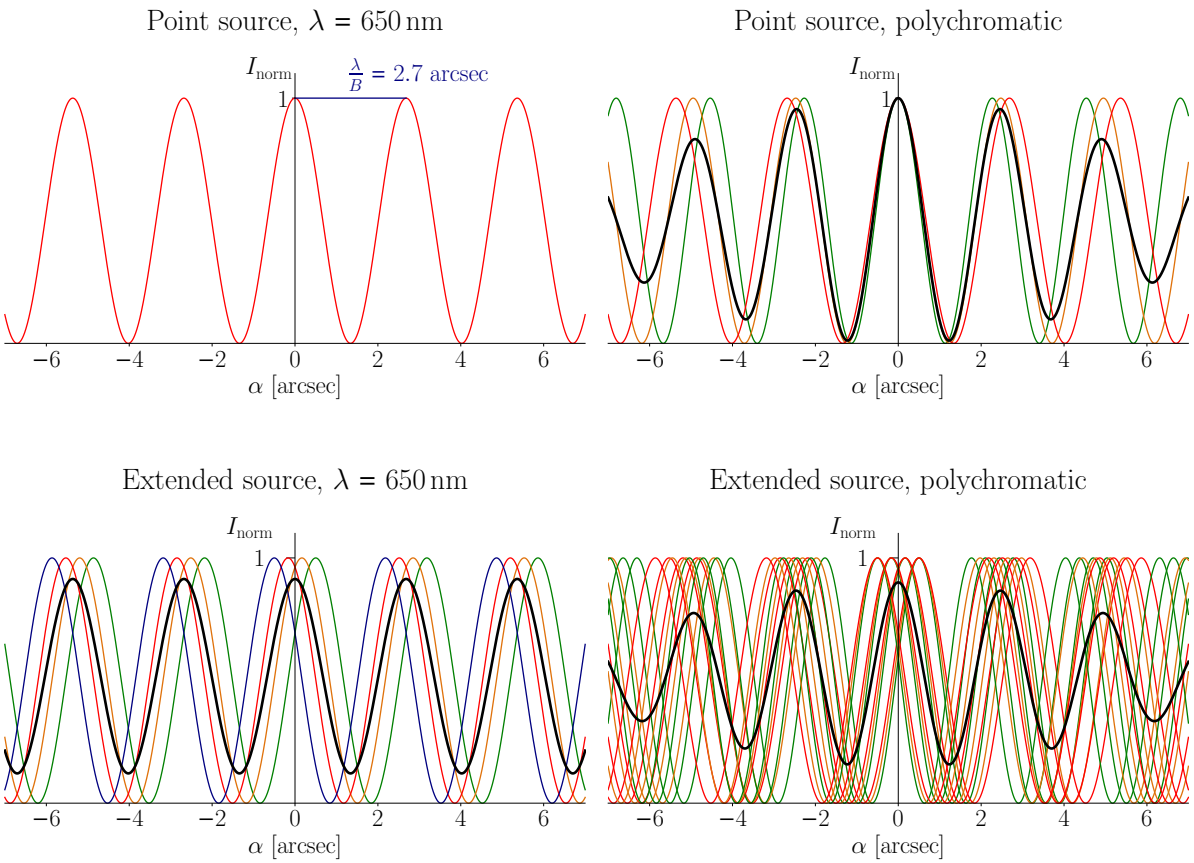

Figure 1.7: Normalised intensities of basic sources in Young's double-slit experiment based on Eq. (1.20). The pinhole separation (the baseline) is 5 cm for all cases. From upper left: I) Point source and monochromatic light ($\lambda = 650\,\text{nm}$); II) Point source and polychromatic light ($\lambda \in [550, 600, 650]\,\text{nm}$); III) Extended source of 1 arcsec and monochromatic light ($\lambda = 650\,\text{nm}$); IV) Extended source of 1 arcsec and polychromatic light ($\lambda \in [550, 600, 650]\,\text{nm}$). The contrast of the fringes is therefore reduced due to temporal coherence in the case of larger band-width and due to spatial coherence when the source is extended. Inspired by Glindemann (2013).

1. A point source (located at $\alpha' = 0$) emitting a monochromatic light results in a cosine function on the screen, see top left panel. The distance between the maxima of this function is given by $\frac{\lambda}{B}$.

2. A point source emitting a polychromatic light results in a cosine function with decreasing amplitude with the distance from the central (white) fringe, see top right panel. Increasing wavelength range λ makes the monochromatic fringes more and more distant and less coherent.

3. An extended source (non-zero intensities at various angles α') emitting a monochromatic light under different angles results in a cosine function with reduced amplitude. Light waves coming from different directions shift the cosine function, but with the same shift, independent of the distance from the central (white) fringe.

4. An extended source emitting a polychromatic light is a combination of the previous cases. It results in a cosine function with reduced amplitude at the centre and moreover decreasing amplitude with distance.

1.3 Complex visibility vs source intensity

To describe the contrast of fringes, we use the quantity called visibility, which quantifies the contrast between the maximum and minimum intensity of fringes as

$$V = \frac{I_{\max} - I_{\min}}{I_{\max} + I_{\min}}. \tag{1.21}$$

The visibility is the most important quantity in interferometry. To clarify the nomenclature, there is also the complex visibility μ, which extends the concept of fringe visibility to include information about the phase of fringes, alongside with their contrast. The absolute value of complex visibility $|\mu|$ is the real visibility V

$$V = |\mu|. \tag{1.22}$$

To get the intensity on the screen, we have to integrate the intensity of an extended source, given by Eq. (1.20), over the angle α'

$$\begin{aligned} I(\alpha) &= \int I(\alpha, \alpha')\,\mathrm{d}\alpha' = \int I(\alpha')\,\mathrm{d}\alpha' + \int I(\alpha')\cos[k(\alpha+\alpha')B]\,\mathrm{d}\alpha' = \\ &= I_0 + \Re\left[e^{\mathrm{i}k\alpha B}\int I(\alpha')\,\mathrm{e}^{\mathrm{i}k\alpha' B}\,\mathrm{d}\alpha'\right]. \end{aligned} \tag{1.23}$$

This brings us to the van Cittert-Zernike theorem (van Cittert, 1934; Zernike, 1938).

The complex visibility is the Fourier transform of the angular intensity distribution of an extended, monochromatic, spatially incoherent source

$$\mu(B) \equiv \frac{\int I(\alpha')\,\mathrm{e}^{-\mathrm{i}k\alpha' B}\mathrm{d}\alpha'}{I_0}. \tag{1.24}$$

The assumption of 'spatially incoherent source' means that waves arriving from individual locations within a source are random, they were not emitted in phase or in anti-phase.

By identifying Eq. (1.24) in Eq. (1.23), the respective intensity on the screen is a cosinusoidal, fringe pattern given by

$$I(\alpha) = I_0 \left\{ 1 + \Re \left[\mu(B)\, \mathrm{e}^{\mathrm{i}k\alpha B} \right] \right\}. \tag{1.25}$$

Alternatively, the complex visibility can be calculated as the normalised coherent flux[2]

$$\mu = \frac{F(B)}{F(0)}, \tag{1.26}$$

where the coherent flux is defined as

$$F(B) \equiv \int_{-\infty}^{\infty} I(\alpha')\, \mathrm{e}^{-\mathrm{i}k\alpha' B}\, \mathrm{d}\alpha'. \tag{1.27}$$

The coherent flux and the complex visibility contain essentially the same information but have different advantages. The coherent flux, being a linear function of the brightness distribution, is more useful mathematically. For example, it is additive: the coherent flux of a system composed of two sources is simply the sum of their individual coherent fluxes. On the other hand, normalised complex visibility is obtained by dividing the complex visibility by the total flux. The key advantage of this normalisation is that it removes sensitivity to the source's total intensity. As a result, objects with the same spatial structure but different total fluxes have the same normalised visibility.

Vector notation For 2D sources, Eqs. (1.24) and (1.25) can be written in vector notation as

$$\mu(\vec{B}) = \frac{\int I(\vec{\alpha}')\, \mathrm{e}^{-\mathrm{i}k\vec{\alpha}'\cdot\vec{B}} \mathrm{d}\vec{\alpha}'}{I_0}, \tag{1.28}$$

$$I(\vec{\alpha}) = I_0 \left\{ 1 + \Re \left[\mu(\vec{B})\, \mathrm{e}^{\mathrm{i}k\vec{\alpha}\cdot\vec{B}} \right] \right\}. \tag{1.29}$$

(u, v) **notation** Another option is to define

$$(u, v) \equiv \frac{\vec{B}}{\lambda}, \tag{1.30}$$

$$\mu(u, v) = \frac{\iint I(x, y)\, \mathrm{e}^{-2\pi\mathrm{i}(ux+vy)}\, \mathrm{d}x\, \mathrm{d}y}{I_0}, \tag{1.31}$$

and interpret u, v as spatial frequencies, in 'cycles per baseline' units.

1.4 Interferometers

Let us now compare the angular resolution of a single telescope with an interferometer. The single telescope has a diffraction limit in radians (Kitchin, 2020)

$$\Delta\theta_{\mathrm{T}} = 1.22\, \frac{\lambda}{D}. \tag{1.32}$$

[2] sometimes called correlated flux, mutual intensity, or mutual coherence

Larger telescopes, with larger aperture stop (diameter) D, provide smaller diffraction limits. For instance, let us consider the Extremely Large Telescope (ELT) on Cerro Armazones in Chile. It is currently under construction and, as of July 2025, it is the largest ground-based, optical telescope. Its inherent (neglecting atmosphere) angular resolution in median performance wavelength (0.4-14 μm) is

$$\Delta\theta_{\mathrm{T}} = 1.22 \cdot \frac{0.8 \cdot 10^{-6}}{39.3}\,\mathrm{rad} \approx 6.2\,\mathrm{mas}.$$

For comparison, the diffraction limit of an interferometer, which combines light coming from two or more telescopes, is

$$\Delta\,\theta_{\mathrm{I}} = \frac{\lambda}{B}, \tag{1.33}$$

where B stands for the baseline, the separation of two telescopes in the interferometer. For instance, the Very Large Telescope Interferometer on Cerro Paranal in Chile can achieve $B = 130\,\mathrm{m}$ among the Unit Telescopes (UTs) and $B = 200\,\mathrm{m}$ among the Auxiliary Telescopes (ATs). Then, the angular resolution from the previous example would be significantly improved

$$\Delta\theta_{\mathrm{I}} = \frac{0.8 \cdot 10^{-6}}{200}\,\mathrm{rad} \approx 0.8\,\mathrm{mas}.$$

Therefore, long-baseline interferometry provides the only way to achieve higher resolution without the need to build enormous telescopes that are technically (and financially) unfeasible.

Interferometers collect light from a single, small region of the sky at two or more locations (apertures, telescopes) and bring the light beams collected at each telescope to a beam combiner, where the light beams interfere and form an interference pattern (fringes). A basic interferometer is shown in Fig. 1.8. It consists of one or more pairs of light collectors (siderostats, telescopes, etc.) that form a baseline $\vec{B} = \vec{P}_2 - \vec{P}_1$, where the collectors are situated at positions $\vec{P}_1$ and $\vec{P}_2$. The distance $|\vec{B}|$ between them is typically hundreds of meters, much larger than the diameter of a collector. The wavefronts collected by the siderostats or telescopes are distorted by the atmospheric turbulence and are thus sent to an adaptive-optics system (Fig. 1.8, upper right). The correcting elements are placed close to the siderostats because the largest aberrations must be corrected before the light come toward the beam combiner.

In the adaptive-optics system, the incoming wavefront from a source is split between a wavefront sensor and a scientific camera. The wavefront sensor, e.g. Hartman-Shack (Pretheesh Kumar & Ganesan, 2022), measures distortions caused by atmospheric turbulence. To characterise how the system responds to different types of wavefront distortions, a calibration process must be performed. During this process, a known set of wavefront perturbations is applied to the deformable mirror. For each applied mode, the wavefront sensor records the resulting 'echo'. These data are used to construct the system's interaction matrix, which maps deformable mirror actuator inputs to wavefront sensor outputs.

To correct for an arbitrarily distorted wavefront in real time, the interaction matrix is inverted, yielding the reconstruction matrix. This matrix allows computing the required deformable mirror actuators from the current wavefront sensor measurements. During

operation, the wavefront sensor continuously monitors the distortions in the reference source's wavefront. These measurements are multiplied by the reconstruction matrix to actuate the appropriate adaptive element. The deformable mirror adjusts its surface in real time to compensate for the current atmospheric distortions.

Corrected, less distorted wavefronts continue toward the interferometer. They are brought to the beam combiner and detector using a series of mirrors and delay lines, which serve to control the relative delays between the light beams coming from different collectors (e.g. Earth rotation, vibrations of the system or due to the environment), in order to produce coherent fringes. However, the perfect control of all vibrations is impossible; thus, the fringe trackers are used (e.g. Menu et al., 2012).

Adaptive optics systems differ for different instruments. The above description is only one of the concepts. The most common variation is having only a tip-tilt mirror instead of a deformable mirror. While the deformable mirror corrects higher-order aberrations, complex distortions across the wavefront caused by atmospheric turbulence, the tip-tilt corrects only the lowest-order aberration, overall angular motion of the wavefront such as image motion, including jitter. All long-baseline interferometers have adaptive optics, at least at the level of a tip-tilt correction.

This technique solves the challenges caused by the atmosphere, however, other factors may ruin the appearance of fringes. When light from one collector is blocked or when the beams fail to interfere, the fringes disappear, and we see only a uniformly illuminated Airy disk, like the one with $|V| = 0$ in Fig. 1.8.

The condition for the interference is the temporal coherence for the combination of beams. The beams must maintain constant phase delay over time; specifically, the phase shift between the beams must be smaller than the wavelength of incoming light. Movable delay lines serve this purpose. They optimise the optical path difference (OPD) to compensate for the geometrical delay from the position of the telescopes $|B_0| \cos \varphi$ and to achieve an appropriate phase shift. For optical interferometers, the precision of the optical path needs to be on the order of tens of nanometers; otherwise, the beams will not produce interference fringes. The precision of the setting can be more relaxed for interferometers using longer wavelengths. To conclude, producing interference fringes with an interferometer is certainly challenging.

1.5 Fringe analysis

By analysing interferometric fringes, we can recover information about the size, shape, or structure of a source. The aim is either to model or to reconstruct the intensity distribution of a source. The reconstruction of the intensity distribution is stated in the inverse version of the van Cittert-Zernike theorem:

For an extended, monochromatic, spatially incoherent source, the angular intensity distribution of the source is the inverse Fourier transform of the complex visibility

$$I(x, y) = \iint \mu(u, v)\, \mathrm{e}^{2\pi \mathrm{i}(ux + vy)}\, \mathrm{d}u\, \mathrm{d}v. \tag{1.34}$$

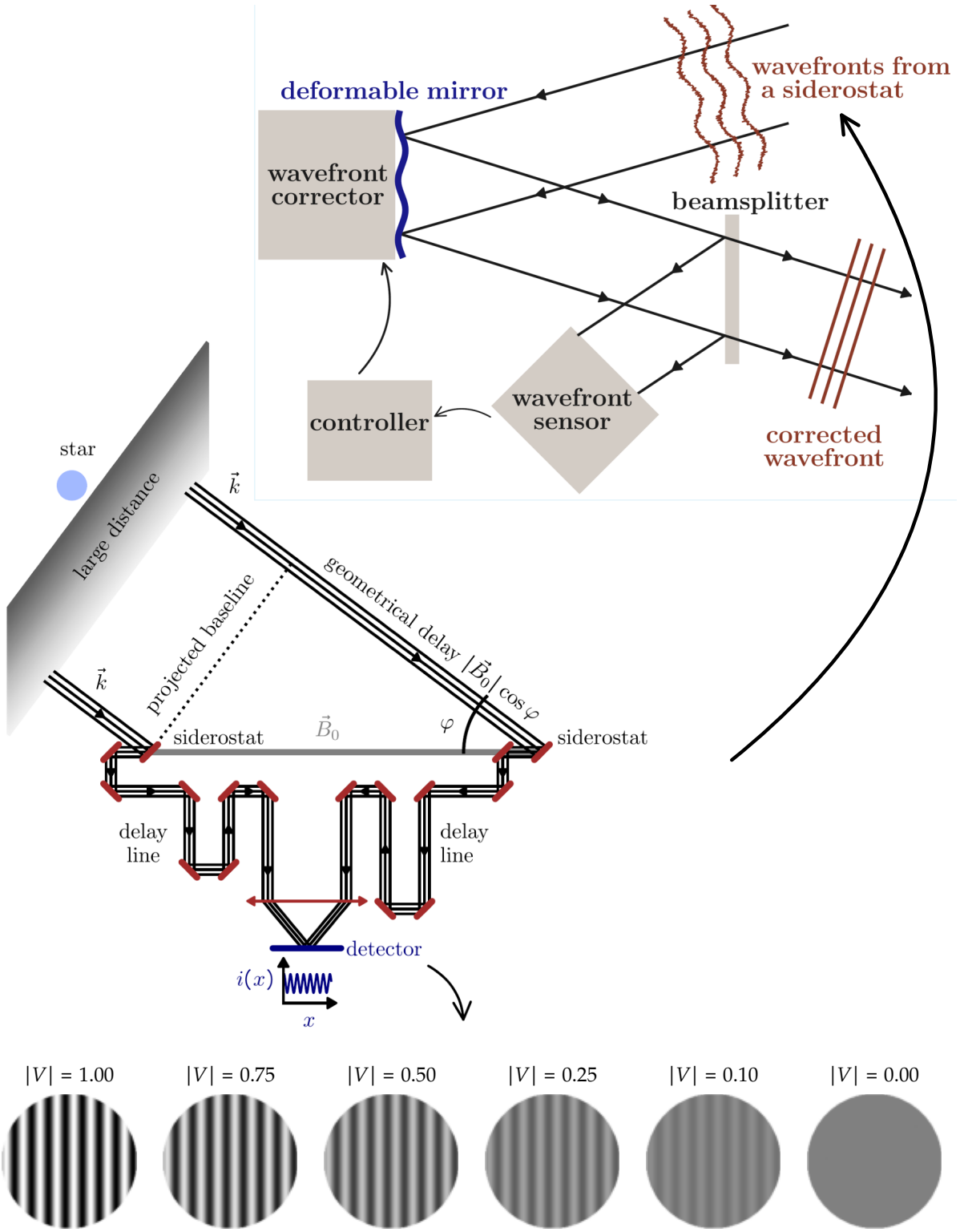

Figure 1.8: Basic optical interferometer setup. Two siderostat mirrors collect starlight. Interferometers aiming for fainter targets, have larger telescopes instead of siderostats. Wavefronts distorted by atmosphere pass through adaptive optics systems, which correct them before recombination. The light beams are combined after delay lines carefully adjust optical path difference (OPD) so that they interfere. This creates a pattern of bright and dark fringes on the detector, aligned perpendicular to the baseline between the telescopes. The contrast is expressed by the visibility; several example values of the visibility $|V|$ are shown. Inspired by Buscher (2015).

The exponentials $e^{2\pi i(ux+vy)}$ represent cosinusoidal (and sinusoidal) waves, Fourier modes. Each Fourier component has a spatial frequency (how fast it oscillates), amplitude (how strong it is), and a phase (where it starts). The complex visibility μ is what interferometers measure. Its amplitude, the real visibility $V = |\mu|$, defined by Eq. (1.21), tells us how much of a particular cosinusoidal wave is present in the source. In other words, it is obvious that the intensity distribution is mathematically treated as an infinite superposition of cosine and sine waves, scaled by the complex visibility.

There are two main quantities we need to extract from the fringes: the visibility (the contrast) and the phase (the shift). On the other hand, the spacing of the fringes is not related to the size, shape, or structure of the source. Instead, it is related to the way we combine the beams. We can extract this information by modelling the complex visibility, or using Fourier imaging, i.e. Eq. (1.34) directly. The approach depends on the obtained number of measurements and on the coverage of the so-called uv-plane.

A uv-plane is a plane in the Fourier space[3]. All interferometers measure the Fourier transform of the source intensity distribution, i.e. in the Fourier space. They map the brightness distribution on the sky, described by the vector $\vec{\alpha}' = (x, y, z)$, from the tangent plane into the projected baseline vectors $\vec{B} = \lambda(u, v, w)$ in the uv-plane. For small fields of view, we can omit the third dimension, hence $\vec{B} \cdot \vec{\alpha}' = \lambda\,(ux + vy)$.

We can understand the (u, v) coordinates in two ways. The first one is geometrical, the uv-plane represents the projection of telescopes' baselines to the tangent plane

$$(u, v) = \frac{1}{\lambda}\,(B_x, B_y)\,. \tag{1.35}$$

The second way of understanding (u, v) is to realise that $\vec{B}/\lambda$ is the spatial frequency in the Fourier transform, sampled by baselines $\vec{B}$. Spatial frequencies describe how many cycles occur per baselines. Longer baselines sample higher frequencies (finer spatial scales). If a spatial frequency is higher, one can detect finer details. Since each (u, v) point corresponds to only one Fourier component with given spatial frequencies, it is necessary to measure many different baselines.

Given an array composed of n telescopes, we obtain $\frac{n(n-1)}{2}$ baselines and $n(n-1)$ points in the uv-plane. For instance, for six telescopes, we have 15 baselines. We also obtain symmetric points at opposite u and v, which are the complex conjugates of the corresponding positive points. This arises from the Hermitian symmetry property inherent to all visibility. It holds that

$$\mu(\vec{B}) = \mu^*(-\vec{B}), \tag{1.36}$$

where * denotes the complex conjugate. Another point of view is that it arises from the fact that the same pair of telescopes (1 and 2, 2 and 1) can be equally well used to give a baseline vector in the opposite direction and $\vec{B_{12}} = -\vec{B_{21}}$. The only difference when interchanging the telescope order is the direction of fringe displacement: a positive phase change becomes negative. For six telescopes, we therefore obtain 30 points in total in the uv-plane. The required uv-coverage depends on the scientific goals of the observation.

[3]also called an aperture plane

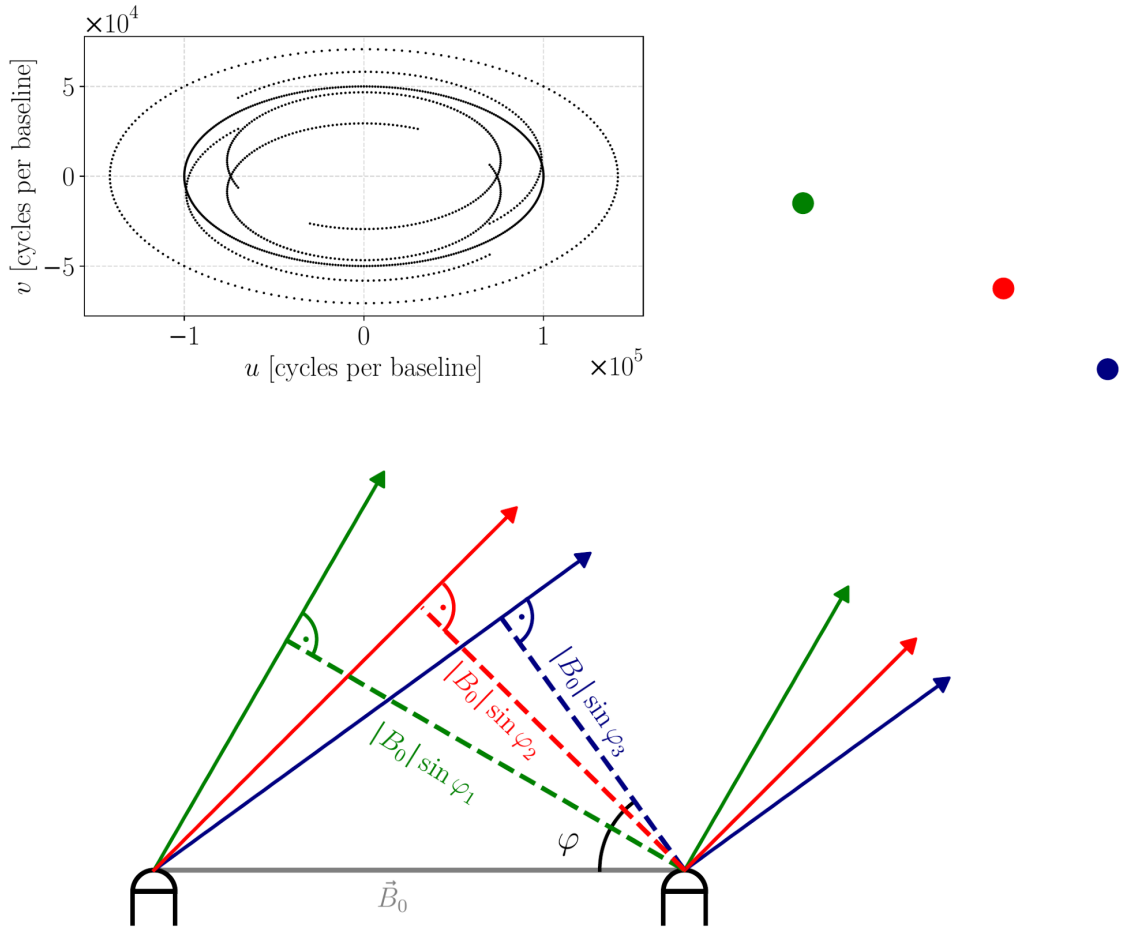

Figure 1.9: Different projected baselines resulting from the Earth's rotation and an example of a uv-plane coverage obtained using this technique. Lower panel: As a star moves, the projected baselines are different and correspond to different (u, v) points. One measurement with a particular projected baseline $|\vec{B}_0| \sin \varphi$ adds one point to the uv-plane. Top panel: An example of the uv-plane coverage obtained by 'Earth rotation synthesis'.

Supersynthesis The van Cittern-Zernike theorem implies that if we measure the complex visibility for all baselines $\vec{B} = \lambda(u, v)$, we can reconstruct the intensity distribution of the source using the inverse Fourier transform. The most common and powerful method to cover the uv-plane, especially for imaging, is to use Earth rotation synthesis (or 'supersynthesis'). We subsequently obtain measurements with different projected baselines (see Fig. 1.8), because a projected baseline changes when the star moves across the sky, see Fig. 1.9. The uv-plane coverage also increases with more and more telescopes (baselines). The combination of the two is known as aperture synthesis. Further improvement is done by using more spectral channels as the unit of u, v is cycles per baseline, by a reconfiguration of telescopes, or by both.

Imaging vs modelling For a reconstruction of an image, we need to have a dense coverage of the uv plane. Only this allows us to apply the inverse Fourier transform on the complex visibility (though some gaps in the uv plane and assumptions remain

unavoidable) and obtain a reconstructed image of the observed source. This method is called *Fourier imaging*.

An alternative approach that does not require so dense coverage of the uv-plane is modelling of the visibility $V(\vec{B})$. We need fewer measurements, values of the real visibility, with respect to projected baselines. Having them, we can determine the angular size of a source by fitting the visibility $V(\vec{B})$, as a function of a baseline. The difficulty is that this function varies for different types of sources, see Sect. 1.6. So, we need to correctly assume the nature of the observed source.

1.6 Visibility functions of various sources

As discussed in Sect. 1.5, the complex or real visibility differ with the nature of observed sources. This section shows the visibility dependences of various sources.

1.6.1 Bessel function

The visibility often includes special functions like the Bessel function. Bessel functions naturally arise when describing diffraction or interference patterns when integrating over circularly symmetric apertures. They are a family of solutions to Bessel's differential equation, which appears with circular or cylindrical symmetry

$$z^2\frac{\mathrm{d}^2 y}{\mathrm{d}\, z^2} + x\frac{\mathrm{d}\, y}{\mathrm{d}\, z} + (z^2 - n^2)y = 0. \tag{1.37}$$

The general Bessel function of order n is defined as

$$J_n(z) = \frac{1}{\pi}\int_0^\pi \cos(z\sin\theta - n\theta)\,\mathrm{d}\theta. \tag{1.38}$$

Specifically, the Bessel function of order zero J_0 is even

$$J_0(z) = \frac{1}{\pi}\int_0^\pi \cos(z\sin\theta)\,\mathrm{d}\theta = \frac{1}{\pi}\cos(z\cos\theta)\,\mathrm{d}\theta, \tag{1.39}$$

while the Bessel function of order one J_1 is odd

$$J_1(z) = \frac{1}{\pi}\int_0^\pi \cos\theta\sin(z\cos\theta)\,\mathrm{d}\theta = \frac{1}{\pi}\int_0^\pi \cos(\theta - z\sin\theta)\,\mathrm{d}\theta = \frac{1}{\pi}\int_0^\pi \cos(z\sin\theta - \theta)\,\mathrm{d}\theta; \tag{1.40}$$

see Fig. 1.10. It also holds that

$$\lim_{z\to 0}\frac{J_1(z)}{z} = \frac{1}{2}. \tag{1.41}$$

1.6.2 Point source

The simplest object that can be observed is a single, point-like source (i.e. unresolved source), e.g. a star with the angular diameter much smaller than the interferometer's resolution. The intensity of such a source is represented by the Dirac δ-function, Eq. (1.81),

$$I(\vec{\alpha}') = I_0\,\delta(\vec{\alpha}' - \vec{\alpha}'_0), \tag{1.42}$$

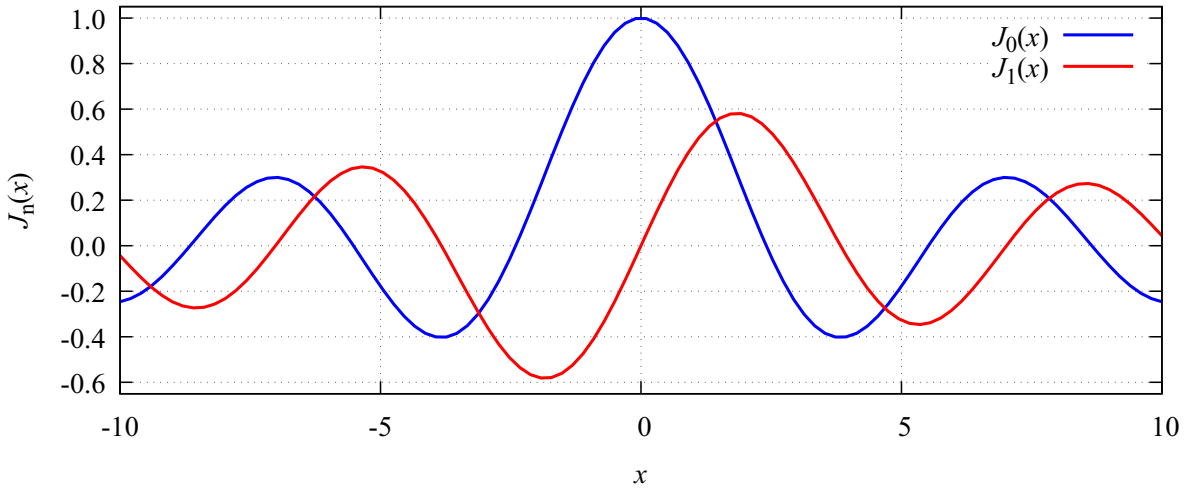

Figure 1.10: Bessel function of order zero $J_0(x)$ and one $J_1(x)$.

where $\vec{\alpha}'_0$ is the angular position of the source. Its Fourier transform is the complex exponential function Eq. (1.82); thus, the coherent flux is

$$F(\vec{B}) = I_0 \, \mathrm{e}^{\mathrm{i}k\vec{\alpha}'_0 \cdot \vec{B}} \tag{1.43}$$

and after normalisation, we have

$$\mu(\vec{B}) = \mathrm{e}^{\mathrm{i}k\vec{\alpha}'_0 \cdot \vec{B}}. \tag{1.44}$$

Therefore, $|V(\vec{B})| = \mu = 1 + 0\mathrm{i} = 1$, which implies that the fringe contrast is unity and independent of the baseline length or orientation.

1.6.3 Binary

For a binary star system, the linearity of the Fourier transform Eq. (1.76) is used. Owing to this property, the coherent flux observed for two stars is the sum of the coherent fluxes for each star observed separately. If both stars are unresolved ($\theta \ll \frac{\lambda}{B_{\max}}$), i.e. point-like sources, and if the first one lies at the phase centre, while the second is offset by $\vec{\alpha}_0$, their ratio of intensities is $I_{\mathrm{rel}} = \frac{I_1}{I_0}$, then, their brightness distribution is given by

$$I = I_0[\delta(\vec{\alpha}') + I_{\mathrm{rel}} \, \delta(\vec{\alpha}' - \vec{\alpha}'_0)], \tag{1.45}$$

the total coherent flux is given by the Fourier transform, Eq. (1.43),

$$F(\vec{B}) = F_0 + F_1 \mathrm{e}^{\mathrm{i}k\vec{\alpha}'_0 \cdot \vec{B}}, \tag{1.46}$$

and the complex visibility μ according to Eq. (1.24) is the modulus of the normalised coherent flux

$$V = \left| \frac{1 + I_{\mathrm{rel}} \, \mathrm{e}^{-\mathrm{i}k\vec{\alpha}'_0 \cdot \vec{B}}}{1 + I_{\mathrm{rel}}} \right| = \frac{\sqrt{(1 + I_{\mathrm{rel}} \, \mathrm{e}^{-\mathrm{i}k\vec{\alpha}'_0 \cdot \vec{B}})(1 + I_{\mathrm{rel}} \, \mathrm{e}^{\mathrm{i}k\vec{\alpha}'_0 \cdot \vec{B}})}}{1 + I_{\mathrm{rel}}}. \tag{1.47}$$

We used the fact that the denominator is always larger than zero and the complex modulus identity $|z| = \sqrt{zz^*}$. After applying the trigonometric identity for the cosine function

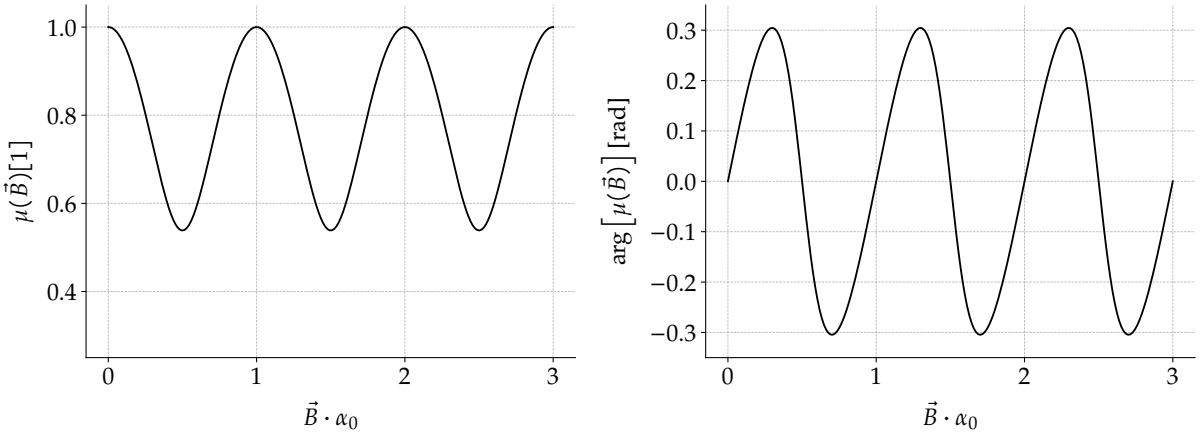

Figure 1.11: Behaviour of interferometric quantities for a binary system. Left: Complex visibility modulus $|\mu(\vec{B})|$. Right: complex visibility phase $\arg[\mu(\vec{B})]$. The flux of the secondary is 30% of the flux from the primary.

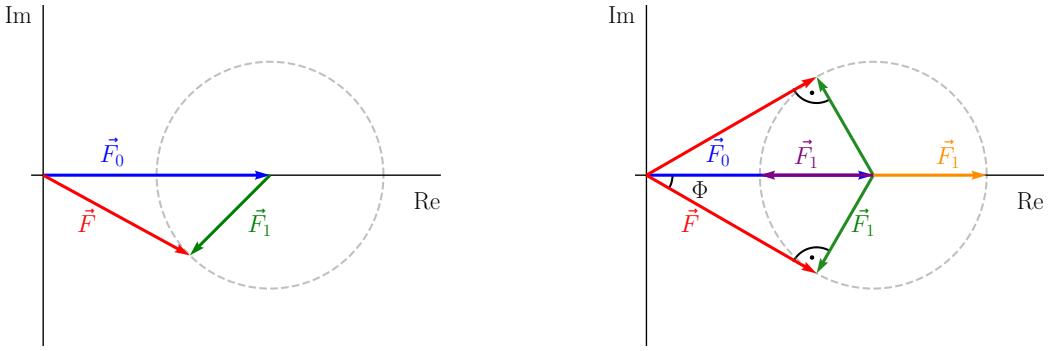

Figure 1.12: Argand diagram with coherent flux $\vec{F}$ of a binary in a vectorial representation, in the complex plane. Left: General example. Right: Positions of vector $\vec{F}_1$ that determine the maxima of visibility modulus and phase. Inspired by Buscher (2015).

$\cos x = \Re\left[e^{\mathrm{i}x}\right] = \frac{e^{ix}+e^{-ix}}{2}$, we obtain the real visibility for a binary

$$V = \frac{\sqrt{1 + I_{\mathrm{rel}}^2 + 2I_{\mathrm{rel}} \cos(k\vec{\alpha}_0' \cdot \vec{B})}}{1 + I_{\mathrm{rel}}}. \tag{1.48}$$

An example is shown in Fig. 1.11.

We can represent coherent fluxes in the Argand diagram, see Fig. 1.12. The coherent flux of the primary star without any offset is a vector $\vec{F}_0$ and lies along the direction of the real axis. Its imaginary part is zero, since it has no angular offset. The vector of the secondary star with a non-zero offset $\vec{F}_1$ rotates in the complex plane with changing (u, v) coordinates. The vector $\vec{F}$ representing the flux of the binary is the vectorial sum of vectors $\vec{F}_0$ and $\vec{F}_1$. Its length ranges from the minimal value of $F_0 - F_1$ to the maximal value of $F_0 + F_1$ (assuming $F_0 > F_1$). Therefore, the visibility modulus oscillates between $\frac{F_0-F_1}{F_0+F_1}$ and 1. The phase oscillations reaches its maximum when the vector $\vec{F}$ is tangent to the circular locus traced by the rotating vector $\vec{F}_1$. The maximum phase is thus $\arcsin\left(\frac{F_1}{F_0}\right)$.

1.6.4 Uniform disk

The brightness distribution of stars is sometimes approximated as a uniform disk. The intensity of a uniform disk with the angular diameter θ is $I = \frac{4}{\pi\theta^2}$ for the angle $\alpha' < \frac{\theta}{2}$, otherwise $I = 0$. Let us compute a Fourier transform from (x, y) angular coordinates to the spatial frequencies (u, v)

$$\begin{aligned}\mu(u,v) = \mathcal{F}\left\{f(x,y)\right\} &= \int_{-\infty}^{\infty}\int_{-\infty}^{\infty} f(x,y)\,\mathrm{e}^{2\pi\mathrm{i}ux}\,\mathrm{e}^{2\pi\mathrm{i}vy}\,\mathrm{d}x\,\mathrm{d}y = \\ &= \int_{-\infty}^{\infty}\int_{-\infty}^{\infty} f(x,y)\,\mathrm{e}^{2\pi\mathrm{i}(ux+vy)}\,\mathrm{d}x\,\mathrm{d}y.\end{aligned} \tag{1.49}$$

For the calculation of the scalar product $\vec{B}\cdot\vec{\alpha}' = (ux + vy)$, we use polar coordinates, i.e. $x = r\cos\varphi$, $y = r\sin\varphi$ and $u = \rho\cos\Phi$, $v = \rho\sin\Phi$

$$ux + vy = \rho r(\cos\Phi\cos\varphi + \sin\Phi\sin\varphi) = \rho r\cos(\Phi - \varphi). \tag{1.50}$$

With the spatial element $r\,\mathrm{d}r\,\mathrm{d}\varphi$, we can rewrite Eq. (1.49) as

$$\mu(\rho,\Phi) = \mathcal{F}\left\{f(r,\varphi)\right\} = \int_0^{2\pi}\int_0^{\frac{\theta}{2}} I_0\,\mathrm{e}^{2\pi\mathrm{i}\rho r\cos(\Phi-\varphi)}\,r\,\mathrm{d}r\,\mathrm{d}\varphi, \tag{1.51}$$

where $f(r, \varphi)$ is a circularly symmetric function that is separable

$$f(r,\varphi) = f_r(r)f_\varphi(\varphi). \tag{1.52}$$

Using this property, we recognise the Bessel function of order zero with the argument $a = 2\pi\rho r$

$$J_0(a) = \frac{1}{2\pi}\int_0^{2\pi}\mathrm{e}^{\mathrm{i}a\cos(\Phi-\varphi)}\,\mathrm{d}\varphi, \tag{1.53}$$

therefore,

$$\mu(\rho,\Phi) = 2\pi\,\frac{4}{\pi\theta^2}\int_0^{\frac{\theta}{2}} r\,J_0(2\pi\rho r)\,\mathrm{d}r = \begin{bmatrix} r' = 2\pi\rho r \\ \mathrm{d}r' = 2\pi\rho\,\mathrm{d}r\end{bmatrix} = \frac{2}{\pi^2\theta^2\rho^2}\int_0^{\pi\rho\theta} r' J_0(r')\,\mathrm{d}r'. \tag{1.54}$$

The integral of the Bessel function J_0 is

$$\int_0^{\alpha} xJ_0(x)\,\mathrm{d}x = \alpha J_1(\alpha), \tag{1.55}$$

therefore,

$$\mu(\rho,\Phi) = \frac{2}{\pi^2\theta^2\rho^2}\pi\rho\,\theta J_1(\pi\rho\,\theta) = \frac{2}{\pi\rho\,\theta}J_1(\pi\rho\,\theta). \tag{1.56}$$

Using the (u, v) coordinates back again, we get the visibility of a uniform disk

$$\mu(u,v) = \frac{2J_1(\pi\theta\sqrt{u^2+v^2})}{\pi\theta\sqrt{u^2+v^2}}, \tag{1.57}$$

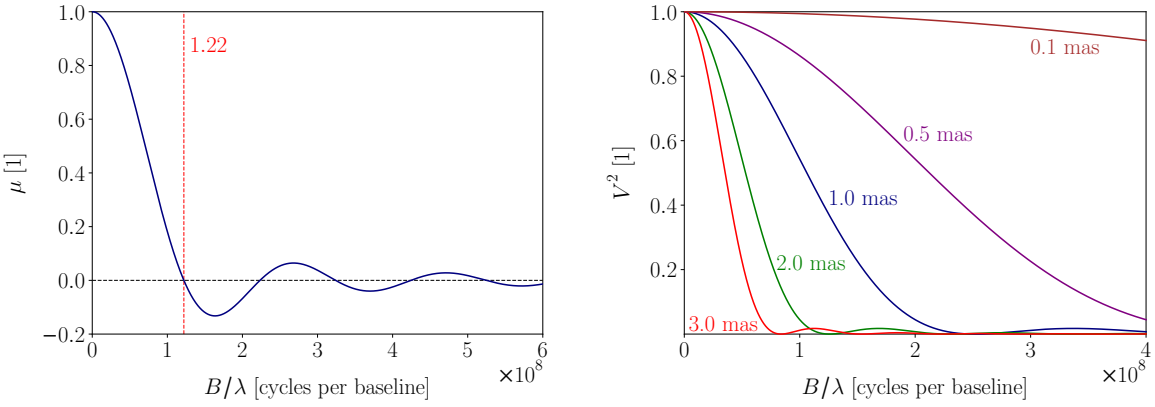

Figure 1.13: Uniform disk visibility. The visibility is real everywhere and circularly symmetric in the (u, v) plane. Left: Visibility modulus of a uniform disk. The visibility modulus decreases with increasing projected baseline and intersects a zero value for $|\vec{B}| = \frac{1.22}{\theta}$, which means that the projected baseline has a length of $\frac{1.22\lambda}{\theta}$. Right: Squared visibilities of uniform disks with different angular diameters. The larger the diameter, the faster the visibility drops.

where the angular diameter θ is in rad; u, v, in cycles per baseline. The visibility can also be written as the jinc function $\mathrm{jinc}(x) \equiv \frac{J_1(x)}{x}$

$$\mu(u, v) = 2\,\mathrm{jinc}(\pi\theta\sqrt{u^2 + v^2}). \tag{1.58}$$

Such a model is commonly used for calibrators in interferometric pipelines such as the ESO's EsoReflex (Freudling et al., 2013) and is illustrated in Fig. 1.13. The 'null' in visibility means that the contrast of fringes goes to zero, the fringes disappear, and the fringe pattern becomes a uniformly illuminated field. Michelson & Pease (1921) used the position of this null in the visibility for measuring the diameter of Betelgeuse (see Sect. 1.1).

A brightness distribution, which is symmetric about the phase centre, has a purely real visibility. This implies that the phase is either 0 ° or 180 ° for all baseline vectors $\vec{B}$. This behaviour is a general property of the Fourier transform of real, point-symmetric functions $f(x)$ that satisfy $f(x) = f(-x)$ everywhere.

1.6.5 Gaussian disk

A Gaussian disk may represent highly-evolved stars, which exhibit extended atmospheres with circumstellar matter, and the edges of their disks are diffuse. They can also be described by various limb-darkening models, but a Gaussian disk is a simple model with strong limb-darkening, extending smoothly to zero. Specifically the intensity of such a source is

$$I(\vec{\alpha}') = I_0\,\mathrm{e}^{-|\vec{\alpha}'|^2/(2\sigma^2)} \tag{1.59}$$

The visibility is, in accord with Eq. (1.103)

$$\mu(\vec{B}) = \mathrm{e}^{-2\pi^2(u^2+v^2)\sigma^2}, \tag{1.60}$$

where $\sigma = \frac{\mathrm{FWHM}}{2\sqrt{2\ln 2}}$ is related to the FWHM.

1.6.6 Offsets

The visibility as a function of a baseline becomes a bit more complicated when the source is offset from the phase centre. Then, the convolution theorem given by Eq. (1.79) is invoked. Convolving any function with the Dirac δ-function offset from the origin by an amount of $\vec{x}_0$ has an effect of shifting a function by $\vec{x}_0$, i.e.

$$f(\vec{x}) * \delta(\vec{x} - \vec{x}_0) = f(\vec{x} - \vec{x}_0). \tag{1.61}$$

For instance, to compute the complex visibility of a star modelled as a uniform disk that is offset from the phase centre by the angle $\vec{\alpha}'_0$, the brightness distribution of the star is

$$I(\vec{\alpha}') = \frac{4}{\pi\vec{\alpha}'^2} * \delta(\vec{\alpha}' - \vec{\alpha}'_0). \tag{1.62}$$

According to the convolution theorem, the total visibility is the product of the visibilities of the centred disk and of exponential that is Fourier transform of the δ-function

$$\mu(\vec{B}) = \frac{2J_1(\pi\theta|\vec{B}|)}{\pi\theta|\vec{B}|}\, \mathrm{e}^{\mathrm{i}k\vec{\alpha}_0\cdot\vec{B}}. \tag{1.63}$$

The expression shows that the phase component of the visibility reflects the star's displacement from the phase centre, whereas the modulus conveys details about the source's angular size or structure.

1.7 Measuring complex visibilities

While the real visibility (modulus) can be more or less preserved after applying atmospheric compensation techniques, the information about the phase of waves is usually lost. Due to atmospheric turbulence, the disturbance D from Eq. (1.16) for each telescope is changed (Haniff et al., 2006)

$$\widetilde{D} = GD = |G|\mathrm{e}^{\mathrm{i}\Phi}D, \tag{1.64}$$

where $|G|$ is the gain of a telescope including its throughput, Φ, the distorted phase, influenced by seeing, thermal expansion, etc. The visibility satisfies $\mu \propto D_1 D_2^*$; thus, the actual observed complex visibility, without any correction, is changed

$$\widetilde{\mu} = G_1 G_2^* \mu = |G_1||G_2|\mathrm{e}^{\mathrm{i}(\Phi_1 - \Phi_2)}\mu. \tag{1.65}$$

The amplitude becomes lower and the phase shifted, no longer reflecting the true source structure. Yet, the phase is a crucial component of the complex visibility. Most importantly, the phase encodes asymmetries in the source's intensity distribution. For a point-symmetric source, the phase is typically zero or constant. A non-zero phase suggests offsets, binary companions, structure, or asymmetric emission (e.g. spots, jets). Several techniques exist to recover the phase information, such as the closure phase or the differential phase.

1.7.1 Closure phase

To recover reliable phase information, the concept of the closure phase was introduced (Jennison, 1958). The closure phase is formed by combining measurements around

a closed triangle of baselines. They are robust observables that are immune to atmospheric turbulence, which makes them powerful for detecting asymmetries and structures in observed sources. Using n telescopes will provide $\frac{1}{2}n(n-1)$ independent closure phase measurements.

Let us consider telescopes 1, 2, and 3, which create three baselines. The closure phase Φ_{123} is given by the sum of phases around the triangle of the baselines, but each phase between two telescopes also includes atmospheric perturbation associated with the respective telescope (Brož & Wolf, 2017)

$$\begin{aligned}\Phi_{123} = \Phi_{12} + \Phi_{23} + \Phi_{31} = \phi_{12} + \Phi_1 - \Phi_2 + \phi_{23} + \Phi_2 - \Phi_3 + \phi_{31} + \Phi_3 - \Phi_1 = \\ = \phi_{12} + \phi_{23} + \phi_{31},\end{aligned} \tag{1.66}$$

where ϕ denotes the intrinsic, unperturbed phases. All the atmospheric phase error terms Φ are cancelled, leaving observables that depend only on the original phases.

If we further define the triple product[4] as

$$T_3 = \mu_{12}\mu_{23}\mu_{31} \tag{1.67}$$

and substitute according to Eq. (1.65), we obtain

$$\begin{aligned}\widetilde{T_3} = \widetilde{\mu_{12}}\widetilde{\mu_{23}}\widetilde{\mu_{31}} = |G_1||G_2|\mathrm{e}^{\mathrm{i}(\Phi_1-\Phi_2)}\mu_{12}|G_2||G_3|\mathrm{e}^{\mathrm{i}(\Phi_2-\Phi_3)}\mu_{23}|G_3||G_1|\mathrm{e}^{\mathrm{i}(\Phi_3-\Phi_1)}\mu_{31} = \\ = |G_1||G_2||G_3|\mu_{12}\mu_{23}\mu_{31},\end{aligned} \tag{1.68}$$

where the amplitude is again lower, but the phase is not shifted. The triple product is a complex quantity whose argument $\arg T_3 = \phi_{12} + \phi_{23} + \phi_{31}$ is the closure phase.

Alternately, the triple product can be defined using the coherent fluxes

$$T_3 = F_{12}F_{23}F_{31}. \tag{1.69}$$

Specifically

$$T_3 = F(\vec{B}_{12})F(\vec{B}_{23})F(\vec{B}_{31}), \tag{1.70}$$

where the baselines creating a triangle satisfy $\vec{B}_{12} + \vec{B}_{23} + \vec{B}_{31} = 0$. Thus, it can be expressed as a function of two baselines

$$T_3(\vec{B}_{12}, \vec{B}_{23}) = F(\vec{B}_{12})F(\vec{B}_{23})F(-\vec{B}_{12} - \vec{B}_{23}). \tag{1.71}$$

1.7.2 Differential phase

Another observable independent of the atmosphere is called the differential phase. It uses a combination of phases measured on the same baseline but at different wavelengths. The commonly used wavelength for this method is the Brackett-gamma (Brγ) line. We can normalise the phase in continuum to zero and other phases measured in the line will be relative to this continuum.

The measured fringe phase in the spectral channel i is given by

$$\Phi(\nu_i) = \phi(\nu_i) + \epsilon_0 + \epsilon_1\nu_i, \tag{1.72}$$

[4] or the bispectrum

where $\phi(\nu_i)$ is the object visibility phase at frequency ν_i; ϵ_0, a wavelength-independent atmospheric phase error; and ϵ_1, the chromatic atmospheric error. The fringes are measured simultaneously at three or more wavelengths. Let us assume three different wavelengths that are equally spaced in frequency, i.e. $\nu_i = [\nu_0 - \Delta\nu, \nu_0, \nu_0 + \Delta\nu]$, where ν_0 is the central frequency and $\Delta\nu$ is a frequency spacing. The procedure is to subtract the average fringe phase at the outer wavelengths from that at the central wavelength

$$\begin{aligned}\Phi_{\mathbf{diff}}(\nu_0) &\equiv \Phi(\nu_0) - \frac{1}{2}\left[\Phi(\nu_0 - \Delta\nu) + \Phi(\nu_0 + \Delta\nu)\right] \\ &= \phi(\nu_0) + \epsilon_0 + \epsilon_1\nu_0 - \frac{1}{2}\left[\phi(\nu_0 - \Delta\nu) + \epsilon_0 + \epsilon_1\nu_0 - \epsilon_1\Delta\nu\right] - \\ &- \frac{1}{2}\left[\phi(\nu_0 + \Delta\nu) + \epsilon_0 + \epsilon_1\nu_0 + \epsilon_1\Delta\nu\right] = \phi_{\text{diff}}(\nu_0).\end{aligned} \tag{1.73}$$

After substituting according to Eq. (1.72), the atmospheric error terms were cancelled.

The differential phases reveal how the structure differs accross the emission line, which is very useful information, especially if circumstellar medium is present.

1.8 Interferometric instruments

Interferometers are useful for studying many types of objects, from cold gas clouds to exoplanets, surfaces of stars, or relativistic environments around black holes. The largest interferometers are described below. Detailed information about the interferometers and the instruments (some of them decommissioned) is in Table 1.1. The of spatial resolution of each instrument means the value when the visibility reaches the first zero. However, to estimate the size of a source (if we know what we observe), this is not necessary. It is possible to use a partial resolution of the interferometer to estimate the size of the target with a model that fits the measured visibilities, even if they are close to 1.

CHARA The optical interferometric array with the largest baseline in the world (in 2025), $B_{\max} = 331\,\text{m}$, is the Georgia State University's (GSU) Centre for High Angular Resolution Astronomy (CHARA). The CHARA is located at Mt. Wilson in California. It uses six 1-m telescopes in a fixed, Y-shaped configuration, see Fig. 1.14. Each of the six light beam paths is equipped with two adaptive optics systems, one at the telescope and the other in the optical laboratory, just before entering the beam-combining instrument (Che et al., 2013). CHARA can resolve objects as small as 0.2 mas at visible wavelengths and 0.5 mas in the near-infrared. The CHARA routinely achieves stellar diameter measurements with precision better than 1%. A recently new instrument of CHARA is a visible beam combiner, SPICA, which is being developed by Mourard et al. (2017) and is able to combine all six telescopes at the CHARA Array. The SPICA project's goal is to measure the angular diameters of 1 000 stars and provide a large set of stellar parameters across the Hertzsprung–Russell diagram (Pannetier et al., 2020). Another new instrument SILMARIL is in commissioning (Anugu et al., 2024). It will be a next-generation optical interferometric instrument.

VLTI The European Southern Observatory (ESO) has the Very Large Telescope Interferometer (VLTI) with larger telescopes but shorter baselines than CHARA. The VLTI can use four 8.2-m Unit Telescopes (UTs) with a maximum baseline of 130 m or four 1.8-m Auxiliary Telescopes (ATs) with the maximum baseline of 200 m (extended configuration), see Fig. 1.14. The UTs are fixed while ATs can be positioned to more than 10 different

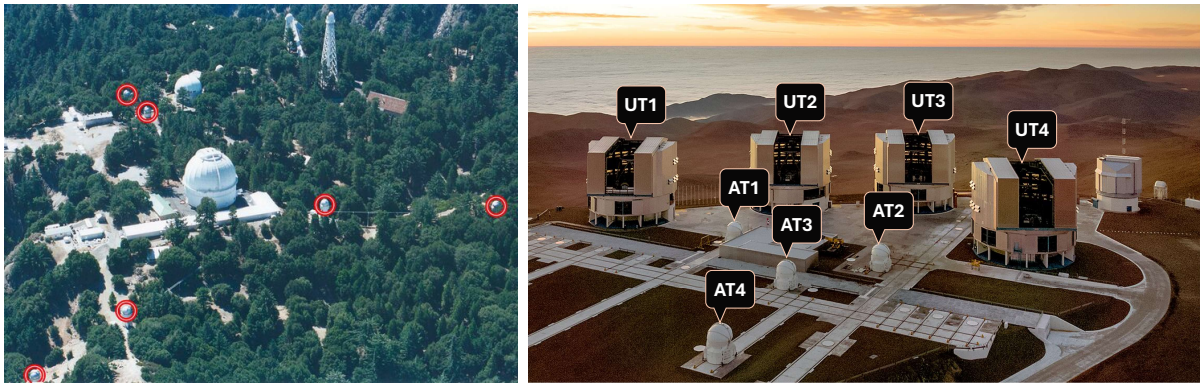

Figure 1.14: Left: CHARA Array, From (Surdej, 2019). Right: VLTI interferometer, credit of backgroud: ESO/G. Hüdepohl.

stations. The interferometer is equipped with the NAOMI adaptive optics in the coherent combination. The VLTI instruments, GRAVITY (Eisenhauer et al., 2011), PIONIER (Le Bouquin et al., 2011), and MATISSE (Lopez et al., 2022), combine the light from four telescopes simultaneously.

NPOI The Navy Precision Optical Interferometer (NPOI) offers the best *uv* coverage in visible light over the 570–750 nm range. Operating with six telescopes simultaneously, it enables high-precision, high-fidelity imaging at milliarcsecond angular resolution. Its imaging instrument, VISION, is uniquely capable of combining light from six telescopes in the visible band, with photometric calibration on each beam—a capability unmatched by any other optical interferometer. NPOI's visible-light performance allows it to probe stellar surface features, spots, or rotational distortion, particularly in hot stars and binaries, where other interferometers may have limited sensitivity. The dense *uv*-plane coverage provided during a single night supports snapshot imaging, making the NPOI an essential facility for time-variable or rapidly rotating targets.

The arrays VLTI and CHARA are complementary; they cover different part of sky with an overlap. CHARA can observed north part of sky, while VLTI covers southern sky. NPOI is also located in the northern hemisphere.

A major leap forward in the capabilities of optical long-baseline interferometry will be the GRAVITY+ project. It aims to significantly enhance the capabilities of the VLTI by pushing sensitivity limits, improving astrometric precision, and expanding sky coverage through new adaptive optics and multiple laser guide stars for each AT. It will enable detailed studies of black holes in distant galaxies as well as accretion disks or faint exoplanets. GRAVITY+ thus exemplifies how ground-based interferometry continues to evolve, combining precision and sensitivity.

A potential future project might be a space-based interferometer, which offers the possibility to eliminate atmospheric turbulence entirely and use extended baselines. Such concepts have been explored in the past by Bely et al. (1990). Recent visionary designs of lunar-based arrays, which could benefit from the Moon's stable environment and also a lack of atmosphere, are discussed in van Belle et al. (2024) and Carpenter et al. (2025).

Table 1.1: Long-baseline optical/near-infrared (NIR)/mid-infrared (MIR) interferometers with possible baselines over 100 m.

Facility	Instrument	$\lvert\vec{B}\rvert$ [m]	Telescopes	Resolution	Band	Ref.	Location	Note
VLTI	GRAVITY	8–130	4×UTs	∼1 mas	NIR: K	[1]		most precise astrometry
	PIONIER	11–200	mostly ATs	∼1 mas	NIR: H	[2]		most efficient in H-band
	MATISSE	12–200	4×ATs 4×ATs	∼3.6/5.0/10.3 mas ∼5.6/7.6/15.8 mas	MIR: $L/M/N$ MIR: $L/M/N$	[3]	Paranal	best for dusty environments
	AMBER	8–200	4×UTs/ATs	∼10 mas	NIR: J, H, K	[4]	Chile	decommissioned 2018
	MIDI	8–200	4×UTs/ATs	∼10 mas	MIR: N (8–13) μm	[5]		decommissioned 2015
	PRIMA	8–200	4×UTs/ATs	∼10 mas	MIR	[6]		decommissioned 2015
	VINCI	8–200	4×UTs/ATs	∼10 mas	MIR: K	[7]		decommissioned 2004
CHARA Aray	CLIMB	331	3×1-m	0.2 mas 0.5 mas	visible NIR	[8]		first 3-T beam combiner at CHARA
	VEGA		(3–4)×1-m	∼0.3 mas	visible: (450–850) nm	[9]		decommissioned 2020
	MYSTIC		6×1-m	∼0.7 mas	K	[10]	Mt. Wilson	best 6-T K combiner
	MIRC-X		6×1-m	∼(0.4–0.5) mas	J, H	[11]	California	high-fidelity imaging
	PAVO		(2–3)×1-m	∼0.2 mas	visible: (630–950) nm	[11]	USA	precise visible astrometry
	SPICA		6×1-m	∼0.1–0.2 mas	R (600–800) nm	[13]		survey instrument
	SILMARIL		3×1-m	∼0.5 mas	NIR: H, K	[14]		in commissioning
	MIRC		4×1-m	0.5 mas	H, K	[15]		decommissioned
NPOI	VISION	up to 432	6×50-cm	∼0.3 mas	optical	[16]	Arizona	best uv coverage in visible
	classic	2–437 m	(2–3)×50-cm	∼0.6 mas	optical	[17]	USA	decommissioned

[1] Eisenhauer et al. (2011), [2] Le Bouquin et al. (2011), [3] Lopez et al. (2022), [4] Petrov et al. (2007), [5] Leinert et al. (2000), [6] Sahlmann et al. (2009), [7] Longinotti et al. (2002), [8] ten Brummelaar et al. (2013), [9] Mourard et al. (2009), [10] Monnier et al. (2018), [11] Anugu et al. (2020), [12] Maestro et al. (2012), [13] Mourard et al. (2022), [14] Anugu et al. (2024), [15] Monnier et al. (2006), [16] Garcia et al. (2014) [17] Armstrong et al. (1998)

→ 34 ←

1.9 Appendix: Fourier transform as theoretical basis

Since the Fourier transform is the theoretical basis for interferometry, hereinafter, we summarise the basic relations.

The Fourier transform of a time-domain signal $g(t)$, yielding its frequency-domain representation $G(\omega)$, is defined as

$$G(\omega) = \mathcal{F}[g(t)] = \int_{-\infty}^{+\infty} g(t) e^{-\mathrm{i}\omega t} \mathrm{d}t, \tag{1.74}$$

where $\omega = 2\pi\nu = \frac{2\pi c}{\lambda}$ is the angular frequency and $\vec{k} = \frac{2\pi}{\lambda}\hat{k}$ is the wave vector. The inverse Fourier transform is

$$g(t) = \mathcal{F}^{-1}[G(\omega)] = \frac{1}{2\pi} \int_{-\infty}^{+\infty} G(\omega)\, e^{\mathrm{i}\omega t} \mathrm{d}t. \tag{1.75}$$

A crucial property of the Fourier transform is its linearity, i.e. for any functions $f(t)$ and $g(t)$ and scalars a and b, it satisfies

$$\mathcal{F}[af(t) + bg(t)] = a\,\mathcal{F}[f(t)] + b\,\mathcal{F}[g(t)]. \tag{1.76}$$

This means that the Fourier transform of a linear combination of functions equals the same linear combination of their individual Fourier transforms.

Another important property is a consequence of the convolution theorem. It states that under suitable conditions, the Fourier transform of a convolution of two functions is the product of their Fourier transforms. In other words, convolution in one domain equals multiplication in the other domain. For functions $f(t)$ and $g(t)$ with their Fourier transforms $F(\omega)$ and $G(\omega)$, respectively, the convolution theorem states that

$$\mathcal{F}[f \cdot g] = F * G \tag{1.77}$$

and

$$\mathcal{F}[f * g] = F \cdot G. \tag{1.78}$$

The convolution of two-dimmensional functions $f(\vec{x})$ and $g(\vec{x})$ is defined as

$$(f * g)(\vec{x}) \equiv \iint f(\vec{x}')g(\vec{x} - \vec{x}')\, \mathrm{d}A, \tag{1.79}$$

where $\mathrm{d}A$ is an element of area.

The Fourier transforms of selected fundamental functions are presented in the following paragraphs.

Constant function

$$\mathcal{F}(1) = \int_{-\infty}^{\infty} 1 e^{-\mathrm{i}\omega t} \mathrm{d}t = 2\pi\delta(\omega). \tag{1.80}$$

The Fourier transform of a unit is the Dirac function.

Dirac function

$$\delta(x) = \begin{cases} 0 & \text{if } x \neq 0, \\ \lim_{x\to 0}\delta(x) = \infty & \text{if } x = 0, \end{cases} \tag{1.81}$$

$$\mathcal{F}[\delta(t-t_0)] = \int_{-\infty}^{\infty} \delta(t-t_0)e^{-\mathrm{i}\omega t}\mathrm{d}t = e^{-\mathrm{i}\omega t_0}. \tag{1.82}$$

The Fourier transform of a shifted Dirac δ-function is a complex exponential, with the argument representing the corresponding phase shift.

Complex exponential function

$$\mathcal{F}[e^{\mathrm{i}\omega_0 t}] = \int_{-\infty}^{\infty} e^{\mathrm{i}\omega_0 t}e^{-\mathrm{i}\omega t}\mathrm{d}t = \int_{-\infty}^{\infty} e^{\mathrm{i}t(\omega_0-\omega)}\mathrm{d}t = \delta(\omega_0-\omega) = \delta(\omega-\omega_0). \tag{1.83}$$

The Fourier transform of a complex exponential function corresponds to a Dirac δ-function in the frequency domain.

Cosine function

$$\begin{aligned} \mathcal{F}[\cos(\omega_0 t)] &= \int_{-\infty}^{\infty} \cos(\omega_0 t)e^{-\mathrm{i}\omega t}\mathrm{d}t = \int_{-\infty}^{\infty} \frac{e^{\mathrm{i}t\omega_0}+e^{-\mathrm{i}t\omega_0}}{2}e^{-\mathrm{i}\omega t}\mathrm{d}t = \\ &= \frac{1}{2}\left[\int_{-\infty}^{\infty} \mathrm{e}^{-\mathrm{i}t(\omega-\omega_0)}\mathrm{d}t + \int_{-\infty}^{\infty} \mathrm{e}^{-\mathrm{i}t(\omega+\omega_0)}\mathrm{d}t\right] = \frac{1}{2}\left[\delta(\omega-\omega_0)+\delta(\omega+\omega_0)\right]. \end{aligned} \tag{1.84}$$

The Fourier transform of a cosine function is two Dirac δ-functions in the frequency domain, symmetric at $\pm\omega_0$.

Sine function

$$\begin{aligned} \mathcal{F}[\sin(\omega_0 t)] &= \int_{-\infty}^{\infty} \sin(\omega_0 t)\mathrm{e}^{-\mathrm{i}\omega t}\mathrm{d}t = \int_{-\infty}^{\infty} \frac{\mathrm{e}^{\mathrm{i}t\omega_0}-\mathrm{e}^{-\mathrm{i}t\omega_0}}{2\mathrm{i}}\mathrm{e}^{-\mathrm{i}\omega t}\mathrm{d}t = \\ &= \frac{1}{2\mathrm{i}}\left[\int_{-\infty}^{\infty} \mathrm{e}^{-\mathrm{i}t(\omega-\omega_0)}\mathrm{d}t - \int_{-\infty}^{\infty} \mathrm{e}^{-\mathrm{i}t(\omega+\omega_0)}\mathrm{d}t\right] = \\ &= -\frac{\mathrm{i}}{2}\left[\delta(\omega-\omega_0)-\delta(\omega+\omega_0)\right]. \end{aligned} \tag{1.85}$$

The Fourier transform of a sine function is the same as for the cosine function, but antisymmetric and imaginary.

Rectangle

$$\begin{aligned} \mathcal{F}\left\{\mathrm{rect}(t)\right\} &= \int_{-\infty}^{\infty} \mathrm{rect}(t)\mathrm{e}^{-\mathrm{i}\omega t}\mathrm{d}t = \int_{-\frac{\tau}{2}}^{\frac{\tau}{2}} 1\cdot\mathrm{e}^{-\mathrm{i}\omega t}\mathrm{d}t = \left[\frac{\mathrm{e}^{\mathrm{i}\omega t}}{-\mathrm{i}\omega}\right]_{-\frac{\tau}{2}}^{\frac{\tau}{2}} = -\frac{\mathrm{e}^{-\mathrm{i}\omega\frac{\tau}{2}}}{\mathrm{i}\omega} = \\ &= 2\tau\frac{\mathrm{e}^{\mathrm{i}\omega\frac{\tau}{2}}-\mathrm{e}^{-\mathrm{i}\omega\frac{\tau}{2}}}{2\tau\mathrm{i}\omega} = \frac{\tau}{\omega\frac{\tau}{2}}\sin\left(\omega\frac{\tau}{2}\right) = \tau\,\mathrm{sinc}\left(\omega\frac{\tau}{2}\right). \end{aligned} \tag{1.86}$$

The Fourier transform of a rectangle is a sinc function. One can see the general property of the Fourier transform that the broader the function, the narrower its transform is.

Step function

$$s(t) = \frac{1}{2}\left[1 + \operatorname{sgn}(t)\right] \tag{1.87}$$

$$\begin{aligned}\mathcal{F}\left\{s(t)\right\} &= \int_{-\infty}^{\infty} s(t)\mathrm{e}^{-\mathrm{i}\omega t}\mathrm{d}t = \int_{-\infty}^{\infty} \frac{1}{2}\left[1+\operatorname{sgn}(t)\right]\mathrm{e}^{-\mathrm{i}\omega t}\mathrm{d}t = \\ &= \frac{1}{2}\left[\int_{-\infty}^{\infty}\mathrm{e}^{-\mathrm{i}\omega t}\mathrm{d}t + \int_{-\infty}^{\infty}\operatorname{sgn}(t)\,\mathrm{e}^{-\mathrm{i}\omega t}\mathrm{d}t\right] = \frac{1}{2}\left[2\pi\delta(\omega) + \frac{2}{\mathrm{i}\omega}\right] = \\ &= \pi\delta(\omega) + \frac{1}{\mathrm{i}\omega}.\end{aligned} \tag{1.88}$$

The Fourier transform of a step function is a 'spike' at zero frequency (due to the constant offset), and a phase term $\propto 1/\omega$.

Signum function

$$\operatorname{sgn}(x) = \begin{cases} 1 & \text{if } x > 0, \\ -1 & \text{if } x < 0, \end{cases} \tag{1.89}$$

$$\operatorname{sgn}(t) = \lim_{a\to 0}\mathrm{e}^{-a|t|}\operatorname{sgn}(t) = \lim_{a\to 0}\left[\mathrm{e}^{-at}\operatorname{sgn}(t) - \mathrm{e}^{at}\operatorname{sgn}(-t)\right], \tag{1.90}$$

$$\begin{aligned}\mathcal{F}\left\{\operatorname{sgn}(t)\right\} &= \int_{-\infty}^{\infty}\left\{\lim_{a\to 0}\left[\mathrm{e}^{-at}\operatorname{sgn}(t) - \mathrm{e}^{at}\operatorname{sgn}(-t)\right]\mathrm{e}^{-\mathrm{i}\omega t}\right\}\mathrm{d}t = \\ &= \lim_{a\to 0}\left[\int_{-\infty}^{\infty}\mathrm{e}^{-at}\,\mathrm{e}^{-\mathrm{i}\omega t}\operatorname{sgn}(t)\,\mathrm{d}t - \int_{-\infty}^{\infty}\mathrm{e}^{at}\,\mathrm{e}^{-\mathrm{i}\omega t}\operatorname{sgn}(-t)\,\mathrm{d}t\right] = \\ &= \lim_{a\to 0}\left[\int_{0}^{\infty}\mathrm{e}^{-(a+\mathrm{i}\omega)t}\mathrm{d}t - \int_{-\infty}^{0}\mathrm{e}^{(a-\mathrm{i}\omega)t}\mathrm{d}t\right] = \\ &= \lim_{a\to 0}\left[\int_{0}^{\infty}\mathrm{e}^{-(a+\mathrm{i}\omega)t}\mathrm{d}t - \int_{0}^{-\infty}\mathrm{e}^{-(a-\mathrm{i}\omega)t}\,\mathrm{d}t\right] = \\ &= \lim_{a\to 0}\left\{\left[-\frac{\mathrm{e}^{-(a+\mathrm{i}\omega)t}}{(a+\mathrm{i}\omega}\right]_0^{\infty} - \left[-\frac{\mathrm{e}^{-(a-\mathrm{i}\omega)t}}{a-\mathrm{i}\omega}\right]_0^{\infty}\right\} = \\ &= \lim_{a\to 0}\left[-\frac{\mathrm{e}^{-\infty} - e^0}{a+\mathrm{i}\omega} + \frac{\mathrm{e}^{-\infty-\mathrm{e}^0}}{a-\mathrm{i}\omega}\right] = \\ &= \lim_{a\to 0}\left(\frac{1}{a+\mathrm{i}\omega} - \frac{1}{a-\mathrm{i}\omega}\right) = \frac{1}{\mathrm{i}\omega} + \frac{1}{\mathrm{i}\omega} = \frac{2}{\mathrm{i}\omega}.\end{aligned} \tag{1.91}$$

The Fourier transform of a signum function is purely imaginary and antisymmetric.

Sinc function

$$\operatorname{sinc}(\omega_0 t) \equiv \frac{\sin(\omega_0 t)}{\omega_0 t}, \tag{1.92}$$

$$
\begin{aligned}
\mathcal{F}\left\{\operatorname{sinc}(\omega_0 t)\right\} &= \int\limits_{-\infty}^{\infty} \frac{\sin(\omega_0 t)\mathrm{e}^{-\mathrm{i}\omega t}}{\omega_0 t}\,\mathrm{d}t = \\
&= \int\limits_{-\infty}^{\infty} \frac{\sin(\omega_0 t)\cos(\omega_0 t)}{\omega_0 t}\mathrm{d}t - \int\limits_{-\infty}^{\infty} \frac{i\sin(\omega_0 t)\sin(\omega t)}{\omega_0 t}\,\mathrm{d}t = \\
&= \left| \begin{array}{l} \sin(\omega_0 t)\cos(\omega t) = \dfrac{1}{2}\left\{\sin\left[(\omega+\omega_0)\,t\right] - \sin\left[(\omega-\omega_0)\,t\right]\right\} \\ \sin(\omega_0 t)\sin(\omega t) = \dfrac{1}{2}\left\{\cos\left[(\omega-\omega_0)\,t\right] - \cos\left[(\omega+\omega_0)\,t\right]\right\} \end{array} \right| = \\
&= \left| \frac{1}{\omega_0 t} = \int_0^{\infty} \left(-\frac{\mathrm{e}^{-\omega t_0 s}}{\omega\, t_0}\right) \right| = \\
&= \frac{1}{2}\int\limits_0^{\infty} \left\{ \int\limits_{-\infty}^{\infty} \sin\left[(\omega+\omega_0)\,t\right]\mathrm{e}^{-\omega_0 t x}\mathrm{d}t \right\}\mathrm{d}x - \\
&- \frac{1}{2}\int\limits_0^{\infty} \left\{ \int\limits_{-\infty}^{\infty} \sin\left[(\omega-\omega_0)\,t\right]\mathrm{e}^{-\omega_0 t x}\mathrm{d}t \right\}\mathrm{d}x - \\
&- \frac{\mathrm{i}}{2}\int\limits_0^{\infty} \left\{ \int\limits_{-\infty}^{\infty} \cos\left[(\omega-\omega_0)\,t\right]\mathrm{e}^{-\omega_0 t x}\mathrm{d}t \right\}\mathrm{d}x + \\
&+ \frac{\mathrm{i}}{2}\int\limits_0^{\infty} \left\{ \int\limits_{-\infty}^{\infty} \cos\left[(\omega+\omega_0)\,t\right]\mathrm{e}^{-\omega_0 t x}\mathrm{d}t \right\}\mathrm{d}x.
\end{aligned}
\tag{1.93}
$$

For real terms, we use the integral identities

$$
\int\limits_0^{\infty} \sin(at)\mathrm{e}^{-st}\mathrm{d}t = \frac{a}{a^2+s^2}, \tag{1.94}
$$

$$
\int\limits_0^{\infty} \cos(at)\mathrm{e}^{-st}\mathrm{d}t = \frac{s}{a^2+s^2}, \tag{1.95}
$$

where $a = \omega + \omega_0$, $s = \omega_0 x$. Hence

$$
\begin{aligned}
\mathcal{F}\left\{\operatorname{sinc}(\omega_0 t)\right\} = \frac{1}{2}\int\limits_{-\infty}^{\infty} \left(\frac{\omega+\omega_0}{(\omega+\omega_0)^2+\omega_0^2 x^2}\right)\mathrm{d}x - \frac{1}{2}\int\limits_{-\infty}^{\infty} \left(\frac{\omega-\omega_0}{(\omega-\omega_0)^2+\omega_0^2 x^2}\right)\mathrm{d}x - \\
- \frac{\mathrm{i}}{2}\int\limits_{-\infty}^{\infty} \left(\frac{\omega_0 x}{(\omega-\omega_0)^2+\omega_0^2 x^2}\right)\mathrm{d}x + \frac{\mathrm{i}}{2}\int\limits_{-\infty}^{\infty} \left(\frac{\omega_0 x}{(\omega+\omega_0)^2+\omega_0^2 x^2}\right)\mathrm{d}x.
\end{aligned}
\tag{1.96}
$$

For the real terms, we use

$$
\int\limits_{-\infty}^{\infty} \frac{a}{a^2+s^2}\mathrm{d}s = \frac{|a|}{a}\int\limits_{-\infty}^{\infty} \frac{1}{1+y^2}\mathrm{d}y = \operatorname{sgn}(a)\left[\arctan y\right]_{-\infty}^{\infty} = \operatorname{sgn}(a)\pi. \tag{1.97}
$$

For the imaginary term, the numerator is the derivative of the denominator, multiplied by a constant:

$$
\int\limits_{-\infty}^{\infty} \left[\frac{\omega_0 x}{(\omega-\omega_0)^2+\omega_0^2 x^2}\right]\mathrm{d}x = \frac{1}{2\omega_0}\left\{\ln\left[(\omega-\omega_0)^2+\omega_0^2 x^2\right]\right\}_{-\infty}^{\infty}, \tag{1.98}
$$

$$\int_{-\infty}^{\infty}\left[\frac{\omega_0 x}{(\omega+\omega_0)^2+\omega_0^2x^2}\right]\mathrm{d}x=\frac{1}{2\omega_0}\left\{\ln\left[(\omega-\omega_0)^2-\omega_0^2x^2\right]\right\}_{-\infty}^{\infty}, \tag{1.99}$$

$$\lim_{x\to\infty}\frac{1}{2\omega_0}\ln\frac{(\omega+\omega_0)^2+\omega_0^2x^2}{(\omega-\omega_0)^2+\omega_0^2x^2}+\lim_{x\to-\infty}\frac{1}{2\omega_0}\ln\frac{(\omega-\omega_0)^2+\omega_0^2x^2}{(\omega+\omega_0)^2+\omega_0^2x^2}=0. \tag{1.100}$$

Hence

$$\mathcal{F}\left\{\mathrm{sinc}(\omega_0 t)\right\}=\frac{\pi}{2}\left[\mathrm{sgn}(\omega+\omega_0)-\mathrm{sgn}(\omega-\omega_0)\right]. \tag{1.101}$$

The Fourier transform of a sinc function is a rectangular function, starting from the frequency $-\omega_0$ and ending at the frequency $+\omega_0$. One can see the general property that the time-domain and the frequency-domain representations are duals (see Eq. (1.86)).

Gauss function

$$g(t)=a\,\mathrm{e}^{-bt^2}, \tag{1.102}$$

$$\begin{aligned}\mathcal{F}\left\{g(t)\right\}&=\int_{-\infty}^{\infty}a\mathrm{e}^{-bt^2}\mathrm{e}^{-\mathrm{i}\omega t}\mathrm{d}t=a\int_{-\infty}^{\infty}\mathrm{e}^{-b\left(t^2+\frac{\mathrm{i}\omega t}{b}\right)}\mathrm{d}t=a\int_{-\infty}^{\infty}\mathrm{e}^{-b\left[\left(t+\frac{\mathrm{i}\omega}{2b}\right)^2-\left(\frac{\mathrm{i}\omega}{2b}\right)^2\right]}\mathrm{d}t=\\&=a\;\mathrm{e}^{-\frac{\omega^2}{4b}}\int_{-\infty}^{\infty}\mathrm{e}^{-b\left(t+\frac{\mathrm{i}\omega}{2b}\right)^2}\mathrm{d}t=\left|\begin{array}{l}u=t+\dfrac{\mathrm{i}\omega}{2b}\\ \mathrm{d}u=\mathrm{d}t\end{array}\right|=a\,\mathrm{e}^{-\frac{\omega^2}{4b}}\int_{-\infty}^{\infty}\mathrm{e}^{-bu^2}\mathrm{d}u=\\&=a\;\sqrt{\frac{\pi}{b}}\,\mathrm{e}^{-\frac{\omega^2}{4b}}.\end{aligned} \tag{1.103}$$

The Fourier transform of a Gauss function is a Gauss function.

Triangle

$$\begin{aligned}\mathcal{F}\left\{\Lambda(t)\right\}&=\int_{-\infty}^{\infty}\Lambda(t)\mathrm{e}^{-\mathrm{i}\omega t}\mathrm{d}t=\int_{-1}^{0}(1+t)\mathrm{e}^{-\mathrm{i}\omega t}\mathrm{d}t+\int_{0}^{1}(1-t)\mathrm{e}^{-\mathrm{i}\omega t}\mathrm{d}t=\\&=\int_{-1}^{0}\left[\mathrm{e}^{-\mathrm{i}\omega t}+t\mathrm{e}^{-\mathrm{i}\omega t}\right]\mathrm{d}t+\int_{0}^{1}\left[\mathrm{e}^{-\mathrm{i}\omega t}-t\,\mathrm{e}^{-\mathrm{i}\omega t}\right]\mathrm{d}t=\\&=\left|\begin{array}{ll}u=t & u'=1\\ v'=\mathrm{e}^{-\mathrm{i}\omega t} & v=-\dfrac{\mathrm{e}^{-\mathrm{i}\omega t}}{\mathrm{i}\omega}\end{array}\right|=\\&=\left[-\frac{\mathrm{e}^{-\mathrm{i}\omega t}}{\mathrm{i}\omega}-\frac{t\mathrm{e}^{-\mathrm{i}\omega t}}{\mathrm{i}\omega}+\frac{\mathrm{e}^{-\mathrm{i}\omega t}}{\omega^2}\right]_{-1}^{0}+\left[-\frac{\mathrm{e}^{-\mathrm{i}\omega t}}{\mathrm{i}\omega}+\frac{t\,\mathrm{e}^{-\mathrm{i}\omega t}}{\mathrm{i}\omega}-\frac{\mathrm{e}^{-\mathrm{i}\omega t}}{\mathrm{i}\omega}\right]_{0}^{1}=\\&=-\frac{1}{\mathrm{i}\omega}+\frac{1}{\omega^2}+\frac{\mathrm{e}^{\mathrm{i}\omega}}{\mathrm{i}\omega}-\frac{\mathrm{e}^{\mathrm{i}\omega}}{\mathrm{i}\omega}-\frac{\mathrm{e}^{\mathrm{i}\omega}}{\omega^2}-\frac{\mathrm{e}^{-\mathrm{i}\omega}}{\mathrm{i}\omega}+\frac{\mathrm{e}^{-\mathrm{i}\omega}}{\mathrm{i}\omega}-\frac{\mathrm{e}^{-\mathrm{i}\omega}}{\omega^2}+\frac{1}{\mathrm{i}\omega}+\frac{1}{\omega^2}=\\&=\frac{2}{\omega^2}-\frac{\mathrm{e}^{\mathrm{i}\omega}}{\omega^2}-\frac{\mathrm{e}^{-\mathrm{i}\omega}}{\omega^2}=-\frac{\left(\mathrm{e}^{\mathrm{i}\frac{\omega}{2}}-\mathrm{e}^{-\mathrm{i}\frac{\omega}{2}}\right)^2}{\omega^2}=-\frac{(2\mathrm{i})^2\sin^2\left(\frac{\omega}{2}\right)}{\omega^2}=\\&=\left(\frac{\sin(\frac{\omega}{2})}{\frac{\omega}{2}}\right)^2=\mathrm{sinc}^2\left(\frac{\omega}{2}\right).\end{aligned} \tag{1.104}$$

The Fourier transform of a triangle function corresponds to a squared sinc, in the frequency domain. The transform is real, symmetric, and decays faster than a single sinc.

Ellipse The characteristic function of an ellipse is

$$\frac{x^2}{a^2}+\frac{y^2}{b^2}\le 1,\quad \text{otherwise } 0. \tag{1.105}$$

The domain of integration is the region where for each

$$y\in[-b,b],\quad x\in\left[-a\sqrt{1-\frac{y^2}{b^2}},a\sqrt{1-\frac{y^2}{b^2}}\right].$$

The Fourier transform in two dimensions is

$$\mathcal{F}\{\text{elps}\}=\int\limits_{\frac{x^2}{a^2}+\frac{y^2}{b^2}\le 1}\int\limits \mathrm{e}^{2\pi \mathrm{i}ux}\,\mathrm{e}^{2\pi \mathrm{i}vy}\,\mathrm{d}x\,\mathrm{d}y=\int\limits_{-b}^{b}\mathrm{e}^{2\pi \mathrm{i}vy}\,\mathrm{d}y\int\limits_{-a\sqrt{1-\frac{y^2}{b^2}}}^{a\sqrt{1-\frac{y^2}{b^2}}}\mathrm{e}^{2\pi \mathrm{i}ux}\,\mathrm{d}x. \tag{1.106}$$

If we substitute

$$\left|\begin{array}{ll} y'=\dfrac{y}{b} & x'=\dfrac{x}{a}\\ \mathrm{d}y'=\dfrac{1}{b} & \mathrm{d}x'=\dfrac{\mathrm{d}x}{a}\end{array}\right|, \tag{1.107}$$

then

$$\mathcal{F}\{\text{elps}\}=ab\int\limits_{-1}^{1}\mathrm{e}^{2\pi \mathrm{i}vby'}\mathrm{d}y'\int\limits_{-\sqrt{1-y'^2}}^{\sqrt{1-y^2}}\mathrm{e}^{2\pi \mathrm{i}uax'}. \tag{1.108}$$

We evaluate the integral and convert the coordinates to polar ones as

$$\begin{aligned}
\mathcal{F}\{\text{elps}\}&=\frac{ab}{2\pi \mathrm{i}ua}\int\limits_{-1}^{1}\mathrm{e}^{2\pi \mathrm{i}vby'}\mathrm{d}y'\left[\mathrm{e}^{2\pi \mathrm{i}uax'}\right]_{-\sqrt{1-y'}}^{\sqrt{1-y'}}=\\
&=\frac{b}{2\pi \mathrm{i}u}\int\limits_{-1}^{1}\mathrm{e}^{2\pi \mathrm{i}vby'}\mathrm{d}y'\left[\mathrm{e}^{2\pi \mathrm{i}ua\ \sqrt{1-y'^2}}-\mathrm{e}^{-2\pi \mathrm{i}ua\ \sqrt{1-y'^2}}\right]=\\
&=\left|\begin{array}{l} y'=\sin\alpha\\ \mathrm{d}y'=\cos\alpha\,\mathrm{d}\alpha\end{array}\right|=\\
&=\frac{b}{2\pi \mathrm{i}u}\int\limits_{-\frac{\pi}{2}}^{\frac{\pi}{2}}\mathrm{e}^{2\pi \mathrm{i}vb\sin\alpha}\left[\mathrm{e}^{2\pi \mathrm{i}ua\ \cos\alpha}-\mathrm{e}^{-2\pi \mathrm{i}ua\ \cos\alpha}\right]\cos\alpha\,\mathrm{d}\alpha=\\
&=\frac{b}{\pi u}\int\limits_{-\frac{\pi}{2}}^{\frac{\pi}{2}}\mathrm{e}^{2\pi \mathrm{i}vb\sin\alpha}\ \sin(2\pi ua\cos\alpha)\cos\alpha\,\mathrm{d}\alpha=\\
&=\frac{b}{\pi u}\int\limits_{0}^{\frac{\pi}{2}}\mathrm{e}^{2\pi \mathrm{i}vb\sin\alpha}\ \sin(2\pi ua\cos\alpha)\cos\alpha\,\mathrm{d}\alpha+\\
&+\frac{b}{\pi u}\int\limits_{-\frac{\pi}{2}}^{0}\mathrm{e}^{2\pi \mathrm{i}vb\sin\alpha}\ \sin(2\pi ua\cos\alpha)\cos\alpha\,\mathrm{d}\alpha=
\end{aligned} \tag{1.109}$$

Let us substitute

$$\left| \begin{array}{c} \alpha = -\tau \\ \mathrm{d}\alpha = -\mathrm{d}\tau \\ \tau \equiv \alpha \end{array} \right| \tag{1.110}$$

Then, we obtain

$$\begin{aligned} \mathcal{F}\left\{\mathrm{elps}\right\} &= -\frac{b}{\pi a} \int\limits_{\frac{\pi}{2}}^{0} \mathrm{e}^{-2\pi \mathrm{i} v b \sin\alpha} \sin(2\pi u a \cos\alpha) \cos\alpha \, \mathrm{d}\alpha = \\ &= \frac{b}{\pi u} \int\limits_{0}^{\frac{\pi}{2}} \cos(2\pi v b \sin\alpha) \sin(2\pi u a \cos\alpha) \cos\alpha \, \mathrm{d}\alpha = \\ &= \left| 2 \sin x \cos x = \sin(x+y) + \sin(x-y) \right| = \\ &= \frac{b}{\pi u} \int\limits_{0}^{\frac{\pi}{2}} \Big\{ \sin\left[2\pi \left(u a \cos\alpha + v b \sin\alpha\right)\right] + \\ &+ \sin\left[2\pi \left(u a \cos\alpha - v b \sin\alpha\right)\right] \Big\} \cos\alpha \, \mathrm{d}\alpha. \end{aligned} \tag{1.111}$$

Let us assume a dimensionless amplitude $c \equiv \sqrt{(ua)^2 + (vb)^2}$. For the right-angle triangle, it holds that $\cos\beta = \frac{ua}{c}, \ \sin\beta = \frac{vb}{c}$

$$\begin{aligned} \mathcal{F}\left\{\mathrm{elps}\right\} &= \frac{b}{\pi u} \int\limits_{0}^{\frac{\pi}{2}} \Big\{ \sin\left[2\pi c \left(\sin\beta \sin\alpha + \cos\beta \cos\alpha\right)\right] + \\ &+ \sin\left[2\pi c \left(\cos\beta \cos\alpha - \sin\beta \sin\alpha\right)\right] \Big\} \cos\alpha \, \mathrm{d}\alpha = \\ &= \frac{b}{\pi u} \int\limits_{0}^{\frac{\pi}{2}} \left\{ \sin\left[2\pi c \cos\left(\alpha - \beta\right)\right] + \sin\left[2\pi c \cos\left(\alpha + \beta\right)\right] \right\} \cos \mathrm{d}\alpha. \end{aligned} \tag{1.112}$$

After changing the sign

$$\left| \begin{array}{c} \alpha = -\alpha \\ \mathrm{d}\alpha = -\mathrm{d}\alpha \end{array} \right|, \tag{1.113}$$

$$\begin{aligned} \mathcal{F}\left\{\mathrm{elps}\right\} &= -\frac{b}{\pi u} \int\limits_{0}^{-\frac{\pi}{2}} \Big\{ \sin\left[2\pi c \cos\left(-\alpha - \beta\right)\right] + \sin\left[2\pi c \cos\left(\beta - \alpha\right)\right] \Big\} \cos\alpha \, \mathrm{d}\alpha = \\ &= \frac{b}{\pi u} \int\limits_{-\frac{\pi}{2}}^{0} \left\{ \sin\left[2\pi c \cos\left(\alpha + \beta\right)\right] + \sin\left[2\pi c \left(\alpha - \beta\right)\right] \right\} \cos\alpha \, \mathrm{d}\alpha = \\ &= \frac{b}{2\pi u} \int\limits_{-\frac{\pi}{2}}^{\frac{\pi}{2}} \left\{ \sin\left[2\pi c \cos\left(\alpha + \beta\right)\right] + \sin\left[2\pi c \left(\alpha - \beta\right)\right] \right\} \cos\alpha \, \mathrm{d}\alpha = \end{aligned}$$

After subtracting a π from α as $|\alpha = \alpha - \pi|$, we get

$$\begin{aligned}
\mathcal{F}\{\text{elps}\} &= \frac{b}{2\pi u}\int_{\frac{3\pi}{2}}^{\frac{\pi}{2}}\Big\{\sin\left[2\pi c\cos\left(\alpha-\pi+\beta\right)\right]+\\
&+\sin\left[2\pi c\left(\alpha-\pi-\beta\right)\right]\Big\}\cos(\alpha-\pi)\,\mathrm{d}\alpha=\\
&=\frac{b}{2\pi u}\int_{\frac{3\pi}{2}}^{\frac{\pi}{2}}\left\{\sin\left[2\pi c\cos\left(\alpha+\beta\right)\right]+\sin\left[2\pi c\left(\alpha-\beta\right)\right]\right\}\cos(\alpha)\,\mathrm{d}\alpha=\\
&=\frac{b}{4\pi u}\int_{-\frac{\pi}{2}}^{\frac{3\pi}{2}}\left\{\sin\left[2\pi c\cos\left(\alpha+\beta\right)\right]+\sin\left[2\pi c\left(\alpha-\beta\right)\right]\right\}\cos\alpha\,\mathrm{d}\alpha=\\
&=\frac{b}{4\pi u}\int_{-\frac{\pi}{2}}^{\frac{3\pi}{2}}\sin\left[2\pi c\cos(\alpha+\beta)\right]\cos\alpha\,\mathrm{d}\alpha+\frac{b}{4\pi u}\int_{-\frac{\pi}{2}}^{\frac{3\pi}{2}}\sin\left[2\pi c\cos(\alpha-\beta)\right]\cos\alpha\,\mathrm{d}\alpha=\\
&=\frac{b}{4\pi u}\int_{-\frac{\pi}{2}+\beta}^{\frac{3\pi}{2}+\beta}\sin\left(2\pi c\cos\alpha\right)\cos\left(\alpha-\beta\right)\mathrm{d}\alpha+\\
&+\frac{b}{4\pi u}\int_{-\frac{\pi}{2}-\beta}^{\frac{3\pi}{2}-\beta}\sin\left(2\pi c\cos\alpha\right)\cos\left(\alpha+\beta\right)\,\mathrm{d}\alpha=\\
&=\frac{b}{4\pi u}\int_{-\frac{\pi}{2}+\beta}^{\frac{3\pi}{2}+\beta}\sin\left(2\pi c\cos\alpha\right)\cos\alpha\cos\beta\,\mathrm{d}\alpha+\\
&+\frac{b}{4\pi u}\int_{-\frac{\pi}{2}+\beta}^{\frac{3\pi}{2}+\beta}\sin\left(2\pi c\cos\alpha\right)\sin\alpha\sin\beta\,\mathrm{d}\alpha+\\
&+\frac{b}{4\pi u}\int_{-\frac{\pi}{2}-\beta}^{\frac{3\pi}{2}-\beta}\sin\left(2\pi c\cos\alpha\right)\cos\alpha\cos\beta\,\mathrm{d}\alpha-\\
&-\frac{b}{4\pi u}\int_{-\frac{\pi}{2}-\beta}^{\frac{3\pi}{2}-\beta}\sin\left(2\pi c\cos\alpha\right)\sin\alpha\sin\beta\,\mathrm{d}\alpha=\\
&=\frac{b}{4\pi u}\cos\beta\int_{0}^{2\pi}\sin\left(2\pi c\cos\alpha\right)\cos\alpha\mathrm{d}\alpha+\frac{b}{4\pi u}\sin\beta\int_{0}^{2\pi}\sin\left(2\pi c\cos\alpha\right)\sin\alpha\mathrm{d}\alpha+\\
&+\frac{b}{4\pi u}\cos\beta\int_{0}^{2\pi}\sin\left(2\pi c\cos\alpha\right)\cos\alpha\,\mathrm{d}\alpha-\frac{b}{4\pi u}\sin\beta\int_{0}^{2\pi}\sin\left(2\pi c\cos\alpha\right)\sin\alpha\,\mathrm{d}\alpha=\\
&=\frac{b}{\pi u}\cos\beta\int_{0}^{\pi}\sin(2\pi c\cos\alpha)\cos\alpha\,\mathrm{d}\alpha=\frac{b}{u}\cos\beta J_1(2\pi c)=\frac{ab}{c}\cos\beta\,J_1(2\pi c).
\end{aligned}$$

The Fourier transform of an ellipse is a scaled Airy pattern, stretched differently along a and b axes. It is a 2D version if the jinc function, but scaled. The magnitude of oscillations decreases with distance, as in J_1.

2. Orion complex

The Orion molecular cloud complex ('Orion complex' for short) is located between about 300 pc and 430 pc from Earth (Bally, 2008) and spans more than 200 deg^2 on the sky (i.e. ∼100 pc across). It is a star-forming region comprising gas, dust, H I and H II regions, emission nebulae, reflection nebulae, dark nebulae, even infrared dark clouds, and—most importantly—young stars, with ages ranging from literally 0 to 12 Myr.

Currently, star formation occurs in the central part of the Orion constellation (see Fig. 2.1 and Table 2.1), particularly within the Orion A and Orion B molecular clouds. Surrounding, embedded within, and located in front of these clouds lies the Orion OB1 association (Blaauw, 1964), a large stellar group composed of young, massive stars. While the region of massive star formation closest to Earth, the Orion Nebula M42, lies in front of Orion A, the most massive members of this association are in the Orion Belt: δ, ε, and ζ Ori, north of Orion A. The Orion OB1 association consists of a sequence of stellar groups of different ages, that are partially superimposed along our line-of-sight (Bally, 2008; Kounkel et al., 2018).

The feedback from the Orion OB1 association, i.e. several explosions of supernovæ, ionising UV radiation, and stellar wind of tens of massive stars, formed the Orion–Eridanus superbubble (Ochsendorf et al., 2015). It is a large, circular structure with a diameter close to 23° (see Fig. 2.6) that extends to the constellation of Eridanus. This superbubble has been studied at multiple wavelengths (Pon et al., 2016), serving as a benchmark for studies of bubbles and feedback in the process of star formation.

A final prominent feature visible in the Orion complex is located in the northern part of Orion: the molecular cloud and H II region around the λ Orionis Cluster (Barrado y Navascués et al., 2004), associated with the λ Orionis molecular ring (Maddalena & Morris, 1987). Its main star, λ Ori, is a blue giant responsible for the ionisation of the surrounding material.

For a list of individual objects and their membership to individual groups, see Table 2.1. This table includes the classical division of the Orion complex according to the position on the sky and age (Maddalena et al., 1986), but it also mentions three-dimensional groups with similar radial velocities (RV) and parallaxes (Kounkel et al., 2018). In this chapter, we will discuss individual groups and try to separately understand high-mass stars and low-mass stars, as well as their possible relations. First, we need to discuss the individual components of the Orion complex and understand their age distribution, kinematic properties, and dynamical state.

2.1 Gaia and APOGEE surveys

The mapping and analysis of the Orion complex are being done by using a 6D phase space with six key parameters: three spatial coordinates (position in space: X, Y, Z) and three velocity components in X, Y, Z directions, i.e. proper motions and radial velocities. Surveys like Gaia DR2, DR3 or APOGEE gathered lots of measurements for revealing this 6D structure of the Orion complex, which enables large-scale studies of this star-forming region and the possibility to understand its star formation history.

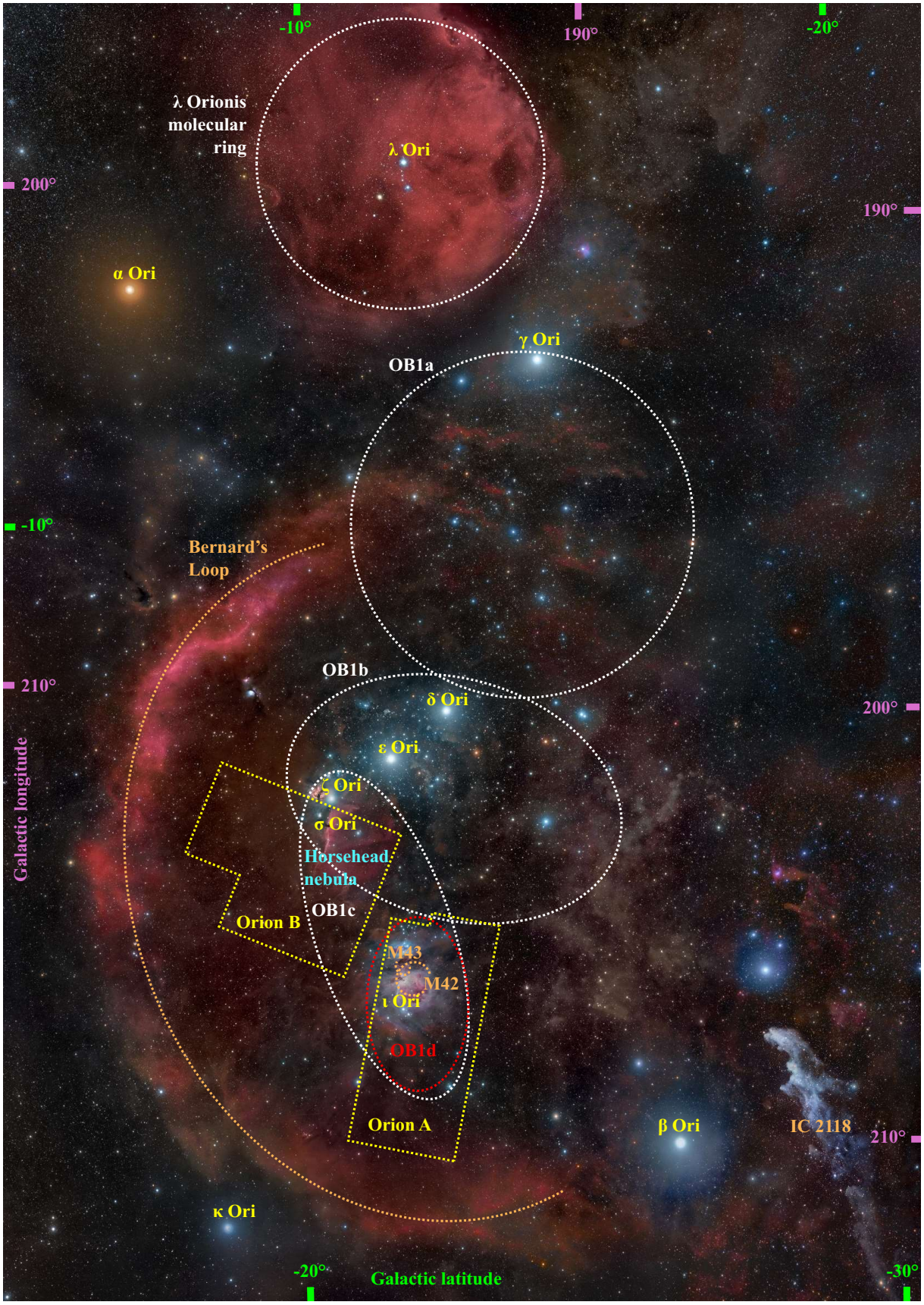

Figure 2.1: Orion complex in the galactic coordinates with the most prominent parts and stars marked (see Table 2.1). The background image taken from R. B. Andreo.

Table 2.1: Overview of objects located in the Orion complex (Maddalena et al., 1986; Kounkel et al., 2018). LSR stands for the local standard of rest (Schönrich et al., 2010).

Orion a molecular cloud	Orion Nebula (M42) M43 (to the north of M42) Sh2−279 (Sharpless 279) NGC 1980 Orion molecular clouds (OMC-1–OMC-4) NGC 1981 NGC 1999 Herbig–Haro objects HH 1-2, HH 34 Waterfall Nebula (HH 222) LDN 1641
Orion B molecular cloud	M78, a reflection nebula (NGC 2068) IC 434 Horsehead Nebula (B 33; in front of IC 434) Flame Nebula (NGC 2024) McNeil's Nebula Orion East Cloud (LDN 1621 + LDN 1622) HH 24-26, HH 111
Orion OB1 association	Orion's Belt (stars ζ, σ, ε, δ Ori) σ Ori Cluster 25 Ori Cluster
Orion–Eridanus superbubble	Barnard's Loop (Sh2-276) IC 2118 Eridanus Loop (Arc A, Arc B, Arc C)
λ Ori Cluster	λ Orionis molecular ring Barnard 30 Barnard 35 (Angelfish Nebula)
'Orion A' of Kounkel et al. (2018) $\mathrm{RV_{LSR}} \approx [0, 15]\,\mathrm{km\,s^{-1}}$, $\pi \approx [2.0, 2.8]$ mas	in Orion A, Orion Nebula M42, M43, part of OB1d
'Orion B' of Kounkel et al. (2018) $\mathrm{RV_{LSR}} \approx [8, 12]\,\mathrm{km\,s^{-1}}$, $\pi \approx [2.2, 2.6]$ mas	stars near the upper part of Barnard's Loop
'Orion C' of Kounkel et al. (2018) $\mathrm{RV_{LSR}} \approx [8, 17]\,\mathrm{km\,s^{-1}}$, $\pi \approx [2.2, 2.5]$ mas	Orion's Belt, OB1b association, faster in RV and more distant stars
'Orion D' of Kounkel et al. (2018) $\mathrm{RV_{LSR}} \approx [-0, 15]\,\mathrm{km\,s^{-1}}$, $\pi \approx [2.5, 3.7]$ mas	Orion's Belt, OB1b association, slower in RV and closer stars
'Orion λ' of Kounkel et al. (2018) $\mathrm{RV_{LSR}} \approx [13, 16]\,\mathrm{km\,s^{-1}}$, $\pi \approx [2.2, 2.7]$ mas	stars around λ Ori

The region is fragmented into several different populations with substantial differences in their phase space. Kounkel et al. (2018) published an analysis of spectroscopic and astrometric data from APOGEE and Gaia DR2, and identified spatially and/or kinematically distinct groups of young stellar objects with ages ranging from 1 to 12 Myr, see bottom of Table 2.1.

Zari et al. (2019) performed another analysis of the three-dimensional structure, kinematics, and age distribution of the Orion OB association based on Gaia DR3. They observed a correlation between stars and gas motions, stellar velocities closely follow the velocity gradients of the parental molecular gas, indicating that stars largely inherit the kinematics of their birth environment. However, some regions show deviations due to feedback and dynamical processes.

The Orion complex is not a single homogeneous entity but consists of multiple subgroups and clusters with distinct spatial and velocity distributions. Some groups show peculiar motions such as runaway stars or expansion from birthplaces, reflecting a history of hierarchical gravitational collapse, stellar feedback, and dynamical interactions (Getman et al., 2019; Zari et al., 2019).

2.2 Orion A

Most of the stars from 'Orion A' as identified by Kounkel et al. (2018) are located within the Orion A molecular cloud. Großschedl et al. (2018) came with a new view of Orion A after investigating its 3D shape using Gaia DR2 data (Brown et al., 2018). In 2D, the cloud extends over a projected length of approximately 45 pc. However, in 3D, Großschedl et al. (2018) found that the structure is cometary-like (possibly due to feedback from nearby OB stars), with its 'head' at a distance of 400 pc and its 'tail' reaching out to 470 pc, see Fig. 2.4.

The most prominent part is the young, dense Orion Nebula Cluster (ONC; see Fig. 2.2). Kounkel et al. (2022) concluded that even though the ONC is gravitationally bound, it weakly expands. This behaviour can be attributed to the low-velocity ejection of stars, resulting from dynamically unstable N-body interactions within the cluster. These ejected stars tend to be more spherically distributed around the cluster and exhibit higher velocity dispersions compared to the cluster's core population.

South of the ONC lies the dark molecular cloud Lynds Dark Nebula 1641 (LDN 1641), which continues into the Integral-Shaped Filament (ISF). The filament has its 'lower limit' in OMC 4, extends through M42 and M43, and reaches its "upper limit" in OMC 3, see Fig. 2.2 (left). The ISF is a dense filamentary structure of gas and dust (see Fig. 2.2, right panel). It is amongst the most prominent nearby star-forming regions in the Milky Way. Kounkel et al. (2022) concluded that there is a significant signature of young stars infalling along the ISF. This means that young stars (or protostars) are moving parallel to the filament's long axis, sliding down the gravitational potential toward denser regions like the ONC. Such a behaviour is often interpreted as gravitationally driven flows along the filament. It indicates that parts of the complex are still dynamically collapsing. Kounkel et al. (2022) cloncluded that the ONC shows organised rotation signatures, but only in stars younger than about 2 Myr. Older stars do not show this rotation, suggesting that angular momentum evolves during cluster formation and dynamical evolution.

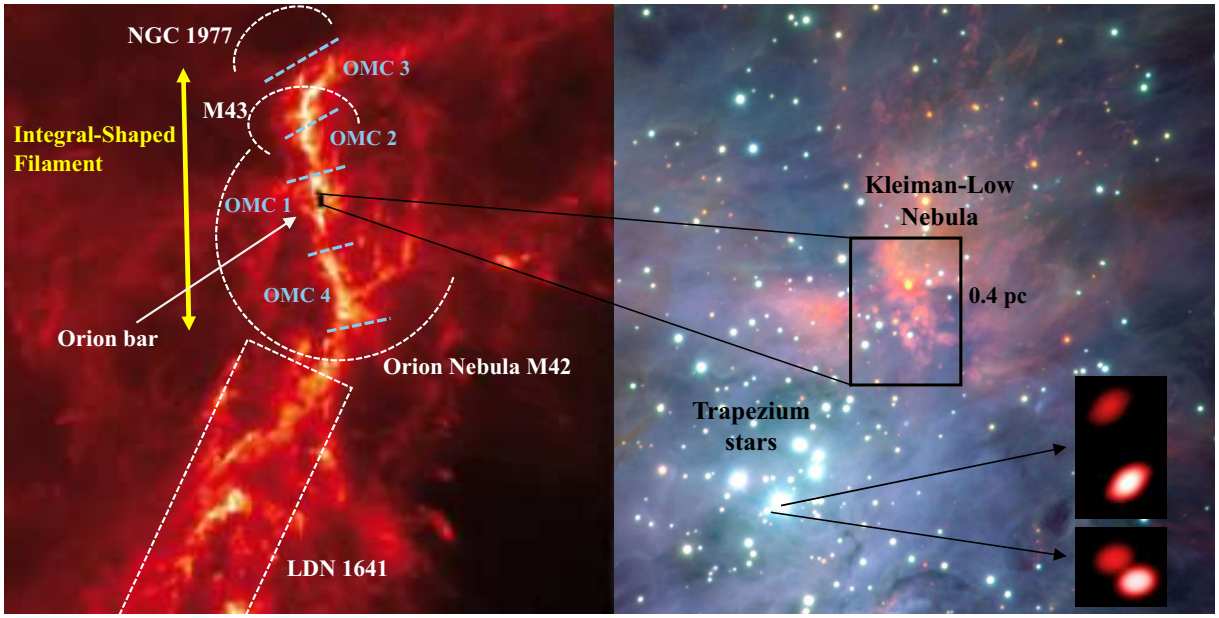

Figure 2.2: Part of Orion A. Left: a near-infrared image of Kleiman-Low nebula and Trapezium cluster obtained with the ISAAC instrument at the 8.2-m VLT telescope. the images of double stars show θ^1 Ori C (above) and θ^1 Ori F (bottom) in the Trapezium Cluster. These observations were among the first made with the new VLTI/GRAVITY instrument. Even from this early data, GRAVITY achieved a breakthrough: it revealed for the first time that θ^1 Ori F is a double star. Credit: ESO/GRAVITY consortium/NASA/ESA/M. McCaughrean. Right: Herschel image of LDN 1641 and Integral-Shaped Filament, going through the ONC. Note that the nebula is saturated (black) in the image from Herschel. Credit: A. M. Stutz / MPIA.

At the heart of the Orion nebula and at the centre of the filament lies the Kleinmann–Low Nebula[1]. It is surrounded by optically thick dust and is therefore observed primarily in far-infrared light, see the left panel of Fig. 2.2. Bally (2008) found that the region exhibits a wide-angle, high-velocity molecular outflow. They estimated that the outflowing material has a mass of $8\,M_\odot$, the bulk of the gas is moving at around $20\,km\,s^{-1}$, and individual clumps or streamers have velocities exceeding $100\,km\,s^{-1}$.

They provided observational and theoretical evidence for a dynamical interaction between massive stars (close three-body interactions, binary formation, or stellar mergers) that occurred around 1475 in a compact region of approximately 500 au within the KL (Kleiman-Low). This event triggered the explosive molecular outflow (see Fig. 2.3), birth of stars, and ejection of three massive stars: BN (Becklin–Neugebauer object), Source I, and Source n. They are called after their roles. BN is the ejected massive young stellar object (YSO) moving northwest at high velocity ($\approx 30\,km\,s^{-1}$). It was likely not the most massive object. Source I is possibly the most massive component (15-20 $M_\odot$), a protostar or YSO, surrounded by a rotating disk and bipolar outflow. The star is currently located near the centre of the explosion. Source n as a less massive YSO (3-6 $M_\odot$) was also ejected and moved southwest. Its role was to destabilise the original configuration. Bally (2008) suggested that such explosive events are an important self-regulating mechanism in the process of massive star formation. It naturally limits the further growth of massive

[1]also known as Becklin–Neugebauer/Kleinmann–Low (BN/KL; Wynn-Williams et al., 1984)

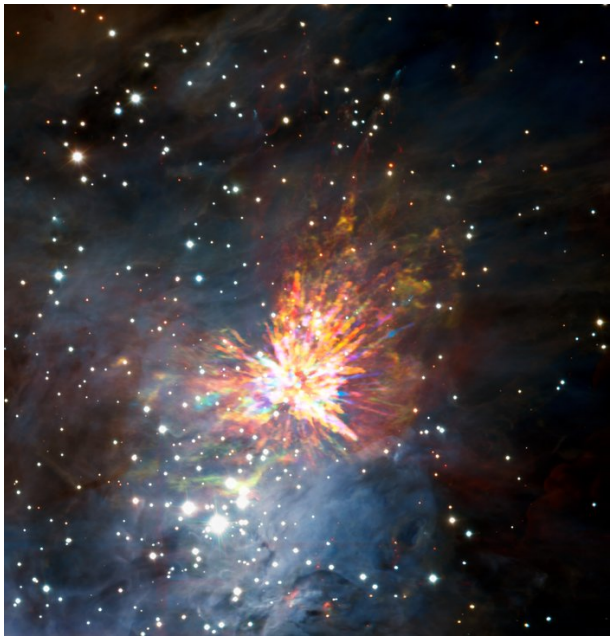

Figure 2.3: Outflows during the birth of stars in the Kleinmann–Low nebula. Colours correspond to the ALMA data and represent the relative Doppler shift; blue represents gas approaching at the highest speeds; red is from gas moving toward us more slowly. The background image includes optical and near-infrared imaging from both the Gemini South and ESO Very Large Telescope. Credit: ALMA (ESO/NAOJ/NRAO), J. Bally/H. Drass et al.

stars and regulates their immediate environment through feedback, triggered by their own formation.

Runaway stars Also dynamically ejected from the ONC were three runaway stars: μ Col (Blaauw & Morgan, 1954), AE Aur (Blaauw & Morgan, 1953), and 53 Ari (Blaauw, 1956). The first two are moving in nearly opposite directions with space velocities of $v_{\rm space}$ of 107.8 km s^{-1} and 113.3 km s^{-1} in LSR and with RVs of 109.0 km s^{-1} and 57.5 km s^{-1}, respectively (Hoogerwerf et al., 2001). Stickland et al. (1987) traced proper motions and radial velocities in 3D space and found that the past trajectories of AE Aur and μ Col intersect on the sky near the location of the massive, highly-eccentric ($e = 0.764$), double-lined spectroscopic binary ι Ori (Bagnuolo et al., 2001). This suggested that the two runaways resulted from a dynamical interaction also involving ι Ori. Hoogerwerf et al. (2001) simulated and verified this possibility. All stars share a common origin, approximately 2.5 Myr ago, and have consistent nominal observed properties. The high velocities of the runaways and the high eccentricity of the ι Ori binary are consistent with a binary–binary encounter, as suggested by Gies & Bolton (1986). 53 Arietis appears to have originated in the Orion association about 4.8 Myr ago and is moving away from it at a speed of $v_{\rm space} = 39.1$ km s^{-1} in LSR and RV = 21.2 km s^{-1} (Hoogerwerf et al., 2001). It is thus the third known high-velocity star originating from this region.

The ONC is still active and serves as a natural laboratory for investigating the formation, early evolution, and feedback of massive stars, dynamical processes and events such as those described above. In total, it hosts around 2 600 pre-main sequence stars, 3 000 young stellar objects, including approximately 190 protostars (Großschedl et al., 2019) that are particularly concentrated in the ONC. In contrast, Orion B tends to host a higher proportion of more evolved objects Gezer et al. (2025).

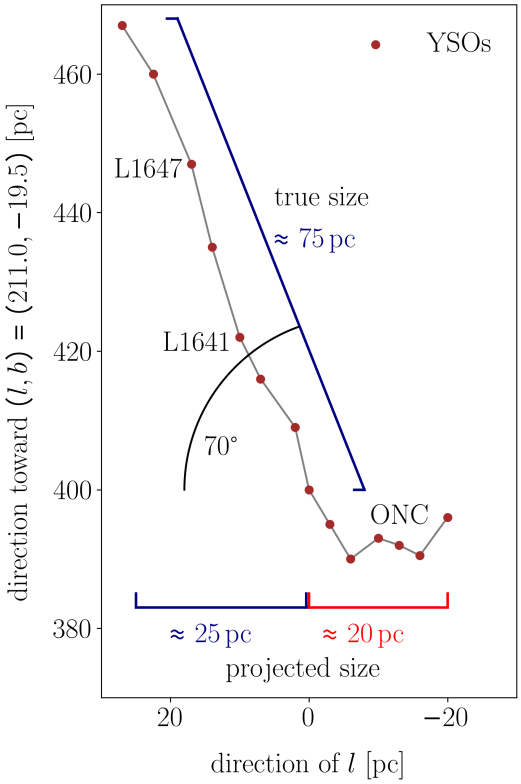

Figure 2.4: True size of Orion A molecular cloud. The points are the YSOs in Orion A according to Großschedl et al. (2018). The y-axis in parsecs is oriented toward the galactic coordinates $(l, b) = (211.0°, -19.5°)$. The x-axis corresponds to the direction of decreasing galactic longitude l. The z-axis (not displayed) would correspond to the galactic coordinate b. The Sun is placed at the origin, (0,0), and serves as the reference point for the distance scale. The figure illustrates that in galactic coordinate, we see the projected size of Orion A as ≈ 20 pc for the 'head' (red) and as ≈ 25 pc for the 'tail' (navy) as denoted by Großschedl et al. (2018). However, the true size of the 'tail' is 75 pc as Großschedl et al. (2018) revealed in his 3D study.

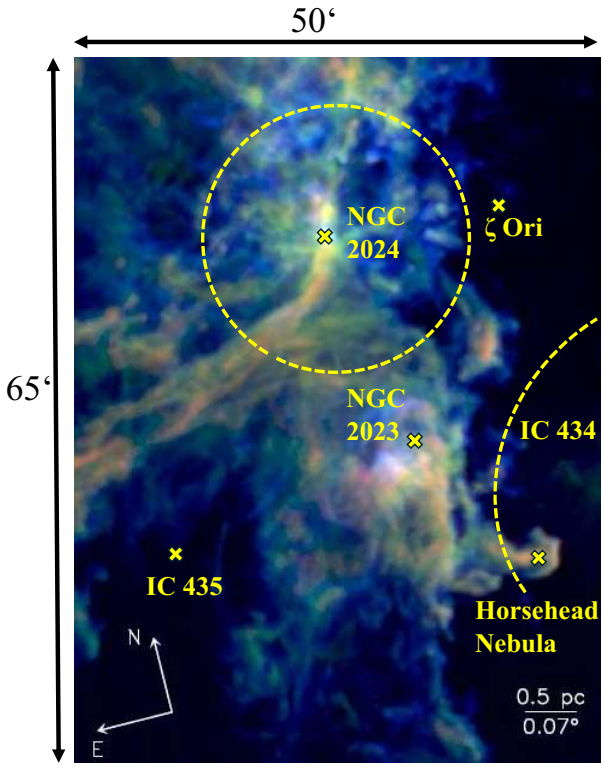

Figure 2.5: Orion B. Column density map of H_2 derived from dust emission, using Herschel data. At the centre lies NGC 2024 (Flame Nebula) that is east of ζ Ori. To the south is NGC 2023, the brightest nebula in the near-infrared sky. IC 434, excited by σ Ori (located 0.5° to the east), and IC 435 appear dark in the molecular hydrogen map, because they are primarily regions of ionised or atomic gas and scattered starlight, respectively. Background from Pety et al. (2017), adapted.

2.3 Orion B

The second giant molecular cloud, Orion B, serves as a laboratory for investigating the later evolutionary phases, such as their influence on the environment, feedback, and cloud structure. At the same time, Orion B is rich in cold gas and dust, which makes the cloud ideal for forming new stars. The cloud is located 400–420 pc away from Earth and extents of approximately 6° × 8° on the sky (Pety et al., 2017). Orion B is home to several well-known star-forming regions, including the Flame Nebula (NGC 2024), the Horsehead Nebula (B 33), the Reflection Nebula (IC 435), IC 434, NGC 2023, and others; see Fig. 2.5.

Orion B also exhibits a complex internal structure, with varying levels of turbulence, magnetic field influence, and feedback from nearby OB stars in the Orion OB1 association. Studies using Herschel and ALMA have revealed fragmented filaments and cores, many of which appear to be gravitationally bound and capable of collapsing to form stars (Könyves et al., 2020). The presence of external irradiation from nearby massive stars likely shapes the cloud's morphology and affects its star formation efficiency, which is lower on average than in Orion A (Lada et al., 2017). Observations show that the motions in Orion B are predominantly solenoidal (divergence-free) rather than compressive, which tends to suppress star formation. However, in the main star-forming regions within Orion B (such

as NGC 2023 and NGC 2024), the turbulence is strongly compressive, promoting star formation (Orkisz et al., 2017).

Orion B is characterised by a higher fraction of more evolved YSOs, particularly of Class II and III. (Gezer et al., 2025) suggested that star formation in Orion B may have started earlier, or proceeded more efficiently in some regions, compared to Orion A. To remain consistent with Lada et al. (2017), the better efficiency is possible only locally, where compressive turbulence dominates and star formation is more active.

Kounkel et al. (2022) found that the distance and motions of stars show an age gradient, with older stars closer (around 385 pc) and younger stars farther away (around 395 pc), implying that star formation is propagating into the molecular cloud over time.

2.4 OB1 association

The OB1 association is home to one of the largest and best-studied associations of O and B stars. It is divided into subgroups denoted from OB1a to OB1d (Blaauw, 1964). The subgroups in Orion OB1 are believed to have formed sequentially due to stellar feedback, including UV radiation, winds, and supernovæ, beginning with the currently dust-free 1a subgroup and ending with dust-embedded 1d subgroup around the Orion Nebula (Blaauw, 1964; Kubiak et al., 2017):

- **OB1a** is located in the northwest of Orion's Belt, in front of clouds. the region includes little gas and massive stars have evolved beyond the main sequence. the members are mostly low-mass pre-main sequence stars; B stars are sparse. the age of the association is approximately 10 Myr and the disk fraction is as low as 10%.

- **OB1b** with the age of 5 Myr is centred on Orion's Belt stars (ζ, ε, δ Ori), which is associated with Orion B. The subgroup includes many B stars. The region consists of diffuse gas and remining dust, exhibiting low extinction. Main star formation activity is declining and the occurrence of disks is moderate (30–40%).

- **OB1c** is estimated to be from 3 to 5 Myr old and is centered around NGC 1980. The association includes O and B stars, dense filaments, and clumps. The extinction is higher. the formation of the most massive stars is still ongoing. The disk fraction is estimated to approximately 50%.

- **OB1d** is the youngest group, <1 Myr old, in the vicnity of the ONC, and is deeply embedded in Orion A. the members are relatively often massive stars and protostars. The region is filled with dense, active, star-forming gas with very high disk fraction (more than 70%).

Blaauw (1964) found 56 O and B stars in the full Orion OB1 association, while Bally (2008) calculated that Orion should have formed between 30 and 100 stars more massive than 8 $M_\odot$ over the past 12 Myr and concludes that 10–20 supernovæ likely exploded in the Orion region over this time interval. The effects of supernovæ are well-observed across the Orion constellation, especially in the Orion–Eridanus superbubble (Soler et al., 2018), see Sect. 2.7.

2.5 Orion's Belt

The Orion Belt, including stars from the OB1b association, hosts our closest massive stars and is an ideal region for investigating questions related to the birth of OB stars and their evolution. The region, spannig an angular distance of about 2.3° is dominated by one single star and three multiple systems:

- **δ Ori** (Mintaka, HD 36486, HR 1852/1851) studied in this work (Oplištilová et al., 2023), see Sect. 3, or previously by, e.g., Mayer et al. (2010), Corcoran et al. (2015), Nichols et al. (2015), Pablo et al. (2015), and Shenar et al. (2015);

- **ε Ori** (Alnilam, 46 Ori, HD 37128) also studied in this work (Oplištilová et al., 2025), see Sect. 4, or previously by Puebla et al. (2016) or Thompson & Morrison (2013);

- **ζ Ori** (Alnitak, 50 Ori, HR 1948/1949) studied by Hummel et al. (2000, 2013);

- **σ Ori** (48 Ori, HD 37468, HR 1931) studied by Simón-Díaz et al. (2015); Schaefer et al. (2016).

Each of these systems hosts one or more stars more massive than $8\,M_\odot$, which are known to evolve on short timescales (< 12 Myr) and will eventually end their lives as supernovæ, enriching the interstellar medium.

South of the Orion Belt lies the well-known young stellar cluster centred on σ Ori. Caballero (2008) provided a comprehensive compilation of stellar and brown dwarf members in this cluster. The massive stars in this system are responsible for ionising the surrounding region and driving strong feedback, which likely influences the evolution of nearby protoplanetary disks. The σ Orionis Cluster contains hundreds of confirmed members, including classical and weak-line T Tauri stars, brown dwarfs, and even several free-floating planet candidates Caballero (2008). Many of these objects exhibit infrared excesses or H_α emission, indicating ongoing accretion or the presence of circumstellar material.

Kubiak et al. (2017) studied the foreground population of the Orion molecular clouds. They focused on a region covering about 25 square degrees, covering the Orion Belt asterism. They concluded that the Orion Belt population is likely a less massive counterpart of Ori OB1b. Furthermore, they suggested that the Orion Belt population could represent an evolved stage of a cluster similar to the Orion Nebula Cluster.

2.6 λ Ori Cluster

The λ Ori Cluster, also referred to as Collinder 69, is a young open cluster centred on the massive O8 III star λ Ori (HD 36861), see Fig. 2.1, which is embedded in a large ring of molecular gas (mostly H_2, H I, H II, and dust known as the λ Ori ring (Cunha & Smith, 1996). The cluster lies at a distance of approximately 400 pc and has an estimated age of about 5 Myr. Its relatively low extinction and rich stellar population make it an important site for studying the formation and early evolution of stars and substellar objects in environments influenced by high-mass stars.

The λ Ori Cluster exhibits a wide mass spectrum, from massive OB-type stars to planetary-mass objects. Several photometric and spectroscopic surveys such as Bouy et al. (2009) and Barrado y Navascués et al. (2004) have confirmed the presence of numerous pre-main sequence stars, including both classical and weak-line T Tauri stars, substellar objects, and potential planetary-mass companions (i.e. objects with masses $M < 13\,\mathrm{M_{Jup}}$). The presence of infrared excesses among many low-mass members suggests that circumstellar disks are still present in a significant fraction, although at somewhat lower rates compared to denser regions such as the Orion Nebula Cluster. The effect of the ionising radiation and stellar winds from λ Ori may be contributing to disk dispersal, rendering the cluster a valuable case study for environmental feedback processes.

A prominent feature of the λ Ori Cluster is the λ Ori ring, a molecular ring approximately $5 \times 5\,\mathrm{deg}$ in size. Cunha & Smith (1996) explored the hypothesis that the expanding molecular ring around λ Ori was produced by a Type-II supernova, approximately 0.3–0.4 Myr ago. Based on its current size and expansion velocity of $14\,\mathrm{km\,s^{-1}}$ (Maddalena & Morris, 1987), they argue that a supernova explosion within a flattened molecular cloud could explain the ring—possibly originating from the former companion of λ Ori itself. Later studies, such as Ansdell et al. (2020), supported the idea that the λ Ori ring was created by a supernova, but estimated that the explosion occurred about 1 Myr ago.

2.7 Orion–Eridanus superbubble

The most prominent nearby example of a profound impact that massive stars may have on the interstellar medium is the Orion–Eridanus superbubble. The bubble spans about 300 pc, and its near side lies approximately at the distance of 180 pc; see Fig. 2.6. The bubble is shaped by the cumulative energy released through stellar winds and multiple supernova explosions. Many clouds now forming stars are located along the inner walls of the superbubble, indicating a feedback-driven, 'sweep-compress-trigger' scenario (Bally, 2008). The expanding superbubble sweeps up surrounding gas, the gas gets compressed as it is pushed together by the expansion, and this compression leads to gravitational collapse, initiating a new sequence of star formation.

The visible part of the Orion–Eridanus superbubble is Barnard's Loop (Ochsendorf et al., 2015), an arc of extended filaments of H_α emission. It is named after the astrophotographer E. E. Barnard, who photographed it and published a description in 1894. The loop is spanning up to 20 deg on the sky and is situated at a distance of 400 pc, which corresponds to a physical diameter of roughly 100 pc. O'Dell et al. (2011) used high-resolution spectrophotometry to study the physical conditions in Barnard's Loop and determined the temperature $T \approx 6\,000\,\mathrm{K}$ and electron density $n_e \approx 2.0\,\mathrm{cm^{-3}}$.

(Kounkel, 2020) explained the origin of Barnard's loop as a remnant of a single supernova that exploded 6 Myr ago. The centre of the expansion is consistent with the geometrical centre of the H II bubble. This is similar to the H II bubble and the ballistic expansion associated with λ Ori, see Sect. 2.6. Foley et al. (2023) found that the expansion of Barnard's Loop is propelled by a combination of feedback from Orion X (which is a label for the centre of Barnard's Loop) and OBP-B1. OBP-B1, identified by Swiggum et al. (2021), is a combined population of two subclusters, Briceño-1 and OBP-Near, that are subgroups of Orion OB1a and OB1b, respectively. Foley et al. (2023) also found that just OBP-B1 likely produced one to a few supernovæwithin the past few million years.

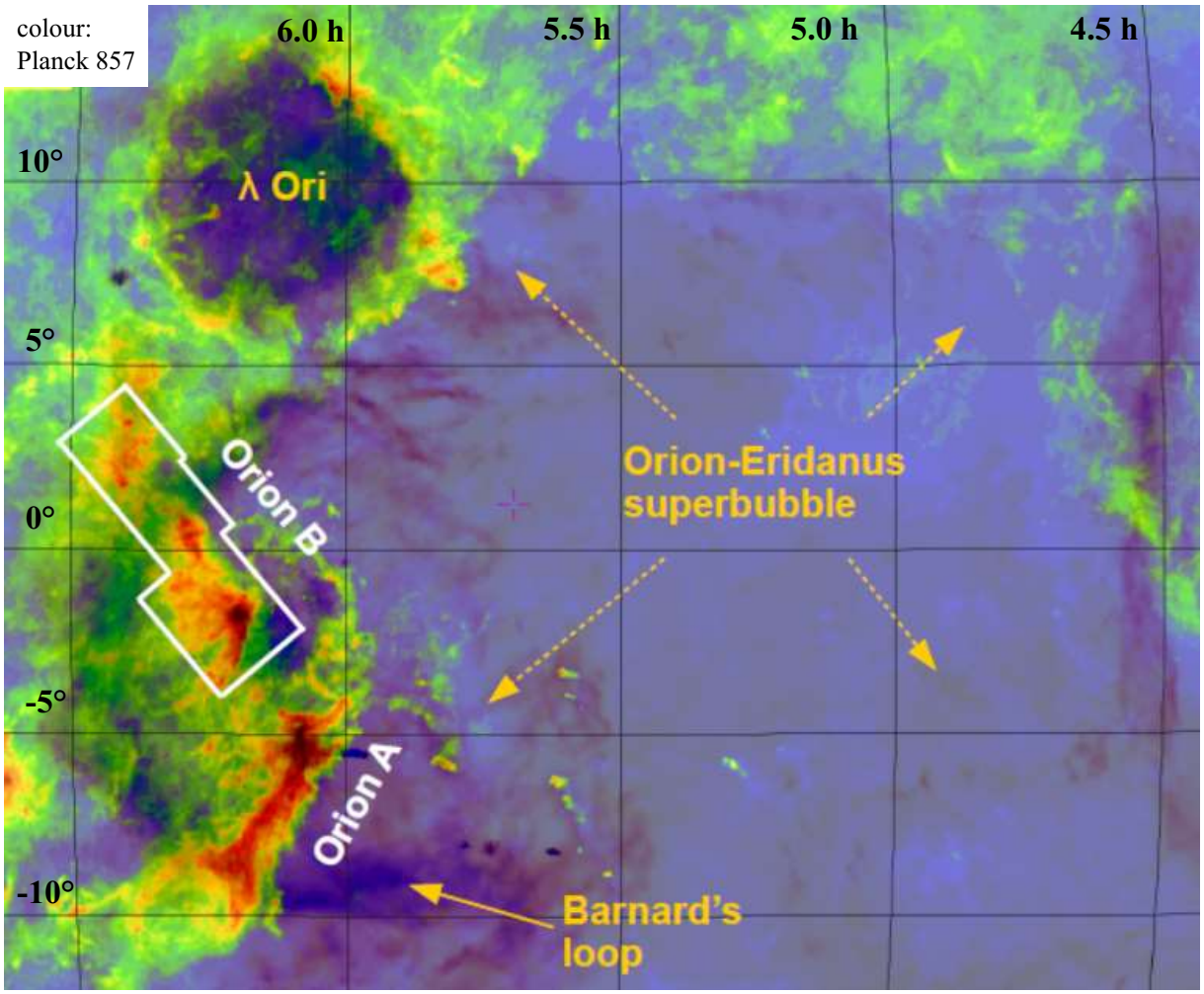

Figure 2.6: Orion–Eridanus superbubble in a wide-angle view. Note the star-forming clouds along its walls. The background image is emission from Planck at 857 GHz (350 μm); background from Könyves et al. (2020), adapted.

Barnard's Loop may thus be directly related to several known runaway stars, including AE Aur, μ Col, and 53 Ari, discussed in Sect. 2.2.

2.8 Low-mass stars

We shall discuss low-mass stars ($M < 8\,\mathrm{M}_\odot$) and high-mass stars separately, even though low-mass stars play an important role in the evolution and star formation history of the Orion complex. They allow us to understand the complex interplay of star formation, feedback, and cluster evolution. Their key functions are i) to trace star formation history, ii) to allow studying protoplanetary disks and planet formation, iii) to contribute to the stellar population and total mass, iv) to influence feedback processes, chemical enrichment, and v) to partialy drive dynamical evolution and cluster dispersal.

Low-mass stars are numerous and form over more extended periods of time. Their ages and spatial distribution help to reconstruct the star formation timeline and the propagation of star formation across the complex. Because they live longer than massive stars ($\gg 12\,\mathrm{Myr}$), they serve as a 'fossil record' of past star formation episodes (e.g. Levine, 2006).

In addition to tracing the history, many low-mass stars in Orion retain protoplanetary disks, especially around the Trapezium Cluster. Studying these disks gives insight into the early stages of planet formation in an m'adverse' star environment, when UV radiation from massive stars affects disk survival (e.g. Mann, 2010).

Despite their faintness, low-mass stars dominate the total number of stars in Orion and contribute substantially to the total mass. This contributes to the gravitational potential of the cluster and the dynamical evolution of the region (e.g. Rivilla et al., 2013).

While massive stars dominate, low-mass stars also contribute to the dynamic environment via outflows and jets, as manifested by the Herbig-Haro (HH) objects (Herbig, 1950; Haro, 1952), compact patches of nebulosity. These outflows can regulate star formation locally by dispersing gas and triggering or suppressing collapse in nearby regions (e.g. Bally & Reipurth, 2001).

Over longer timescales, 100 Myr to $\approx$1 Gyr, low-mass stars further influence their environment through chemical enrichment. As they evolve—eventually becoming asymptotic giant branch stars—they return processed material to the interstellar medium (e.g. D'Orazi et al., 2009).

Finally, motions and mutual interactions with massive stars shape the evolution of Orion's stellar populations. These dynamical processes influence cluster stability and contribute to the eventual dispersal of clusters (Kroupa et al., 2018).

2.8.1 T Tau

Low mass stars dominates among YSOs (Gezer et al., 2025), a broader class, including deeply embedded stages: i) class 0, protostars, mostly with envelope, very young; ii) class I, embedded protostars with disks and envelopes; iii) class II, disk-bearing stars, typically classical T Tauri stars (CTTS); iv) class III, disk-less stars, typically weak-lined T Tauri stars (WTTS). All YSOs exhibit variability, active accretion, and outflows

(Schwartz, 1983). In particular, they have narrow jets of partially ionised gas, which are ejected by young stars, and collide at high speeds (hundreds of $\mathrm{km\,s^{-1}}$) with nearby clouds of gas forming HH objects.

T Tauri stars, i.e. class II and class III, are pre-main-sequence (PMS) stars, which creates the largest group of low-mass stars in the Orion complex. They are named after the prototype T Tauri located in the neighbouring star-forming region Taurus. Also, some brown dwarfs show CTTS/WTTS-like behaviour.

CTTS (Bertout, 1989) are young ($< 10\,\mathrm{Myr}$) stars with masses less than $2\,\mathrm{M_\odot}$. They still accrete material from a circumstellar disk, contract toward the main sequence, and have not yet started stable hydrogen fusion in their cores. Because of active accretion, they have strong emission lines (e.g. $\mathrm{H_\alpha}$, Li). CTTS exhibit infrared excess, caused by warm dust in the disk and variability in brightness. They are often associated with jets and outflows. We can find them in the youngest parts of Orion, especially in the ONC, L1641 in Orion A, NGC 2024, NGC 2068/2071 in Orion B.

WTTS have a weak or absent emission lines (Gras-Velázquez & Ray, 2005). They exhibit little or no accretion but are still contracting toward the main sequence. Their disks have mostly dissipated. They were identified in slightly older parts of the Orion complex, compared to CTTS, i.e. outer regions of ONC and subgroups OB1a, OB1b, OB1c of the Orion OB1 association.

Older PMS, still moving toward the main sequence, which do not belong to YSOs, are called post-T Tauri stars (Jensen, 2001). Observationally, they are often indistinguishable from WTTS. They were found in more dispersed populations, such as Orion OB1a or OB1b, with ages between 5 Myr and 10 Myr. Another group of objects that show CTTS-/WTTS-like behaviour, but on a smaller scale, is brown dwarfs (Burrows & Liebert, 1993). Many are found in Orion, especially in the ONC.

2.8.2 FU Ori

The transition phase of low-mass YSOs between class I and class II is represented by FU Orionis; its prototype star FU Ori located in the northern part of the Orion complex, at a distance of about 416 pc (Vallenari et al., 2023). FU Ori became historically significant in 1936, when it brightened from approximately 16 mag to 9.6 mag in the V-band over a few months. This dramatic outburst marked the new class of variable stars, now informally called 'FUors'. They are characterised by episodic eruptive events. These events are believed to be initiated by increased accretion from $\approx 10^{-7}$ up to $\approx 10^{-4}\,\mathrm{M_\odot\,yr^{-1}}$. During such outbursts, FUors typically change their spectral type. In the visible range, their spectra resemble those of F- and G-type supergiants, while in the infrared, they are similar to K- and M-type stars. The brightening is followed by a slow decline over decades.

FU Ori itself is a binary system (as probably all of them) with a primary mass of $0.6\,\mathrm{M_\odot}$. Its faint, infrared companion, FU Ori S, was discovered ≈ 0.5 arcsec away. The star represents a critical phase in early stellar evolution, likely linked to episodic accretion events that influence mass build-up, disk evolution, and possibly planet formation. Lykou et al. (2022) resolved its accretion disk in the mid-infrared using VLTI/MATISSE in L-, M- and N-band. The authors concluded that the disk is compact, and of moderate mass, supporting a picture of steady viscous accretion with declining disk size over time.

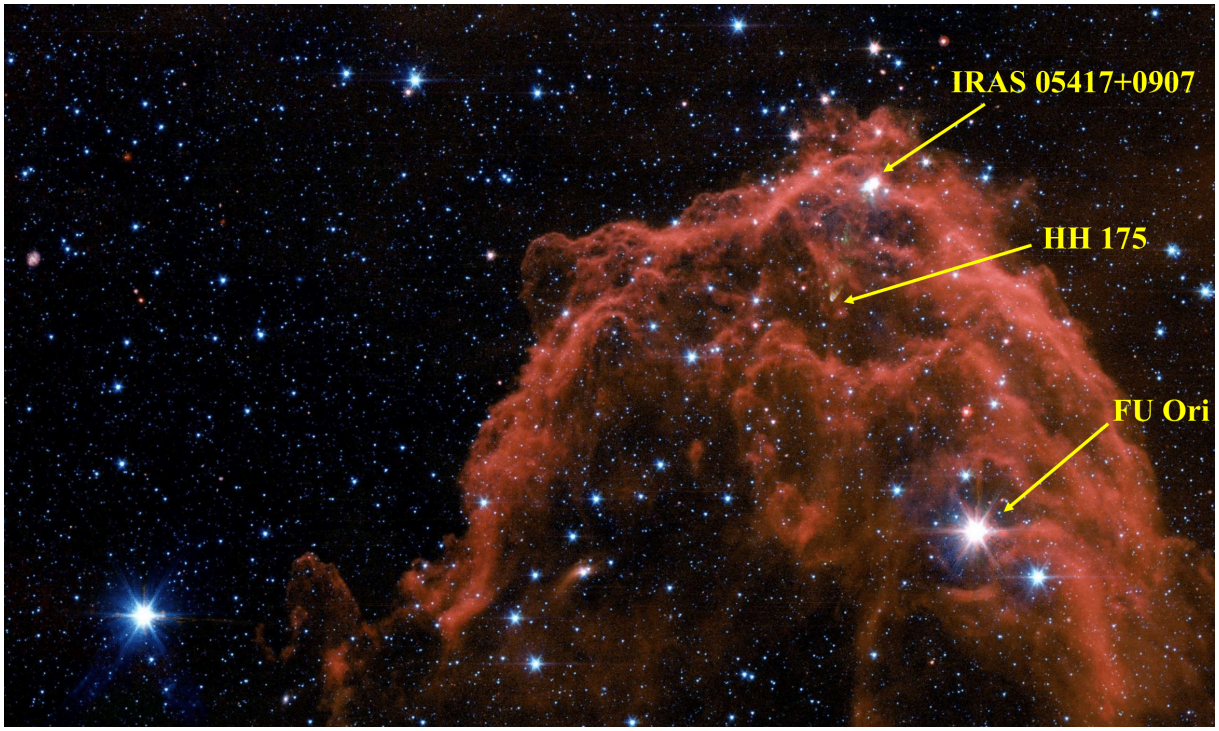

Figure 2.7: FU Ori (the brightest star bottom right) and Barnard 35 Nebula, located in the λ Orionis Cluster. The nebula is dark, but in infrared, it appears bright. It contains Herbig-Haro object HH 175 (light conical shape) related to protostar IRAS 05417+0907. The image was captured by the Spitzer Space Telescope with the following filters: 3.6 μm (blue), 4.5 μm (green), 8.0 μm (orange), 24 μm (red). Credit: NASA/JPL-Caltech.

2.8.3 Low-mass star surveys

Scholz & Eislöffel (2005) studied targets belonging to the OB1b subgroup near ε Ori, containing a mixture of very low-mass stars and brown dwarfs. In total, they observed 143 objects, with masses between 0.02 and 0.66 $M_\odot$ to characterize rotational properties, magnetic activity, and accretion behaviour through photometric monitoring. Each object was observed in the I-band over four nights, resulting in more than 100 measurements per object. Regarding periodic variability, 30 objects (9 brown dwarfs) showed clear periodicity (4–100 h), interpreted as rotation periods. Irregular, high-amplitude variability was confirmed for 5 objects that vary by up to 1 mag. The analysis of trends showed that lower-mass stars rotate faster.

Caballero & Solano (2008) identified new sites rich in substellar objects, analogous to the σ Ori Cluster. They focused on fields with 45' radius around ε Ori and δ Ori. Both regions have low extinction. Their resulting samples included ϵ Ori field with 89 confirmed stars and δ Ori field with 47 confirmed stars. The conclusion was that the ζ Ori region is a broad distribution without central concentration. It might be a widely dispersed cluster or not a cluster. On the other hand, δ Ori region exhibits a clear radial concentration and suggests the δ Ori cluster, but likely in a more evolved stage than the σ Ori Cluster. Both fields show approximately 40–70% lower substellar surface density than σ Ori.

Karim et al. (2016) filled an observational gap for T Tauri, because they studied T Tauri stars with ages between 4 Myr and 10 Myr, while the most of existing surveys focused on stars younger than 3 Myr. They found that older T Tauri stars (closer to

10 Myr) rotate significantly faster than younger ones (approximately 4 Myr). T Tauri stars clearly undergo a sudden spin-up, marking the end of disk-locked rotation and the start of contraction-driven rotation. Their findings align well with angular momentum transfer models, which predict a spin-up once a circumstellar disks dissipate (at approximately 5 Myr).

Großschedl et al. (2019) measured motions of gas in the southern part of the Orion complex and found that the clouds of gas were closest about 6 Myr ago. This is consistent with a feedback event called the 'Orion-BB' (big blast), associated with the position 'Orion X'. Although it is unlikely that an event in the 'Orion X' has been the sole feedback in the region. They argue that motion of most YSOs corresponds to gas, because they record a feedback-driven star formation history in Orion and that the majority of the young stars in this complex are a product of large-scale triggering, which can raise the star formation rate by at least an order of magnitude, as seen in the head of Orion A.

Noroozi et al. (2024) carried out a ground-based photometric survey covering a $6\,\mathrm{deg}^2$ area centred on NGC 1980. The aim was to identify and characterise YSOs. They found that short-period (< 1 d) variables are 2–4 times more common than previously reported, and 10% of the periodic sample are rapid rotators (< 1 d), predominantly weak-line T Tauri stars. Generally, WTTSs rotate faster (< 4 d), while CTTSs cluster at longer periods (> 4 d), in agreement with previous studies. The authors also identified ultra-fast rotators, a distinct subgroup with P as low as ≈ 0.2 d, rotating at $\approx 60\%$ of their critical velocity.

2.9 Massive stars

Massive stars ($M > 8\,\mathrm{M}_\odot$) play a central, transformative role in the Orion complex (the list of the most massive stars in the Orion complex is in Table 2.2). Since the time that a star spends on the main sequence is inversely proportional to the power of mass $m^{-2.5}$, they are short-lived; however, their influence outlasts their lives. Their key roles include (Bally, 2008): i) shaping the structure of the Orion complex, ii) feedback and regulation of star formation, iii) chemical enrichment and iv) turbulence, and driving large-scale kinematics.

Massive stars, particularly O- and early B-type stars, exert strong winds, ionising radiation, and supernova explosions that shape their broader environment. Winds and radiation pressure create bubbles and cavities, like those in Barnard's Loop and Orion–Eridanus superbubble. The expansion of these bubbles compresses nearby molecular clouds, potentially triggering new star formation via 'collect and collapse' or radiation-driven implosion mechanisms. Moreover, massive stars radiate UV photons that ionise the surrounding hydrogen gas, giving rise to H II regions, such as the Orion Nebula (M42).

Through these processes, massive stars provide both positive and negative feedback to the star formation process. The negative feedback refers to the dispersion of gas by radiation and winds, which halt further formation in the immediate vicinity. Conversely, positive feedback involves the compression of gas via pressure waves, creating new dense cores that may eventually collapse into stars.

Table 2.2: List of selected massive stars in the Orion complex and their properties. In the case of multiple systems, the spectral type corresponds to primaries.

Star	Spectral type	Mass [$M_\odot$]	RV [km s^{-1}]	Notes
δ Ori A	O9.5 II	≈ 25	18.5 ± 2.0	multiple system
ε Ori	B0 Ia	≈ 35	25.0 ± 1.5	supergiant
ζ Ori A	O9.5 Iab	≈ 40	20.6 ± 1.3	multiple system
θ^1 Ori C	O7 Vp	≈ 45	25.1 ± 1.2	ONC's main ionizing source
θ^1 Ori A	B0.5 V	≈ 20	28.0 ± 2.0	eclipsing binary
θ^1 Ori B	B1 V	≈ 10	29.1 ± 2.5	multiple system
θ^2 Ori A	O9.5 V	≈ 25	31.3 ± 1.5	strong X-ray emission
θ^2 Ori B	B1 V	≈ 12	27.5 ± 1.2	companion system
σ Ori A	O9.5 V	≈ 20–25	30.9 ± 0.5	quintuple system
σ Ori E	B2 Vp	≈ 9	32.0 ± 1.0	magnetic, helium-strong
25 Ori	B1 V	≈ 12	19.7 ± 1.0	centre of 25 Ori Cluster
λ Ori A	O8IIIf	≈ 33	30.1 ± 0.3	binary
α Ori	M2Iab	≈ 17	21.91 ± 3	red supergiant
β Ori	B8 Ia	≈ 28	19.0 ± 1.0	multiple system
γ Ori	B2 V	≈ 8	18.2 ± 0.3	single star
η Ori	B1 V	≈ 36	23.0 ± 0.5	multiple system
ι Ori	O9 III	≈ 41	21.5 ± 0.5	multiple system

In addition to regulating star formation, massive stars contribute to the chemical enrichment and turbulence of the interstellar medium. They end their lives in supernovae explosions, injecting heavy elements (e.g. O, Si, Fe, Co, Ni, C, Ne, Mg, S, Ca, and Ti) into the ISM and driving turbulent motions that affect subsequent episodes of star formation.

These energetic outputs also influence the kinematics of star-forming regions. The energy from massive stars contributes to the bulk motions and expansion of gas in the complex. The velocity structure of gas and stars in Orion reveals sequential star formation (such as OB1 association, see Sect. 2.4) likely driven by earlier generations of massive stars.

2.9.1 Multiplicity

A defining characteristic of massive stars is their multiplicity. Already Duchêne & Kraus (2013) concluded that at least 60% of stars with 8–16 $M_\odot$ are members of a multiple system, and for stars with masses $\geq 16\,M_\odot$, at least 80% were found in multiple systems. Later studies such as Sana et al. (2014); Sota et al. (2014); Maíz Apellániz et al. (2019); Pauwels et al. (2023) raised this number to 90% of massive, hot OB stars, which possess at least one companion.

Stellar multiplicity is a ubiquitous outcome of star formation. The higher number of companions and their prevalence among massive stars suggest that multiplicity is closely linked to initial conditions of star formation or to subsequent evolution (Duchêne & Kraus, 2013). However, massive stars are so short-lived that it is unlikely that they assemble all of their companions through random interactions in a reasonable timescale.

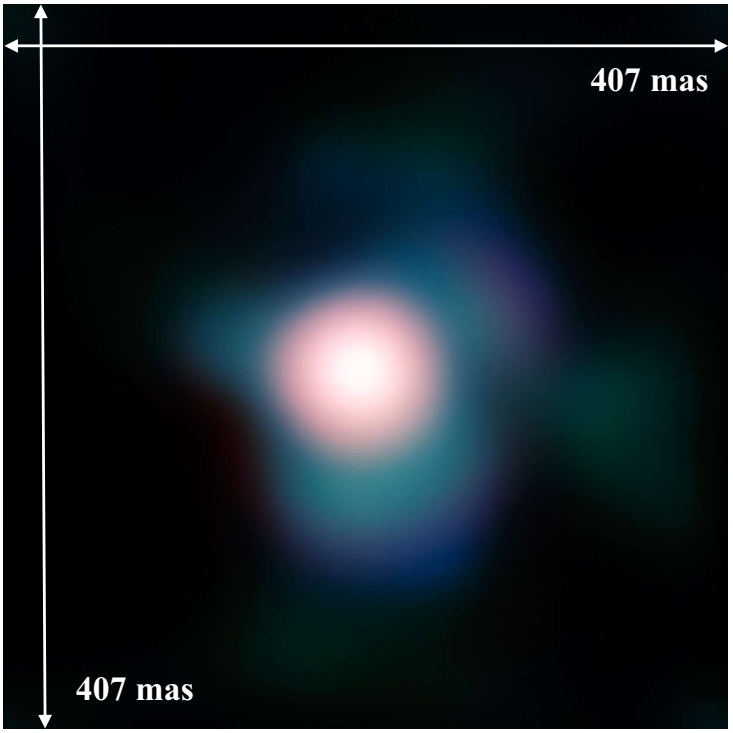

Figure 2.8: Betelgeuse (α Ori) with the NACO adaptive-optics instrument on ESO's Very Large Telescope. The use of NACO combined with a lucky-imaging technique, allowed obtaining the sharpest ever image of Betelgeuse. The image, ∼400 mas across, is based on data obtained in the near-infrared, through different filters. From (Kervella et al., 2009), adapted.

Yet, some stars in the Orion complex are single, particularly massive supergiants such as α Ori, Betelgeuse (see Fig. 2.8), ε Ori, Alnilam (see Sect. 4), Rigel (β Ori), or Bellatrix (γ Ori). Betelgeuse is a semiregular variable red supergiant approaching the end of its life. It raises a question whether these stars are future evolutionary states of multiple systems.

Trapezium stars A remarkable example of multiplicity is provided by Trapezium stars, see Fig. 2.2. Karl et al. (2018) conducted an interferometric survey of the massive binaries in the Trapezium Cluster with VLTI/GRAVITY focused on 16 stars. They are primarily of O, B spectral types. The GRAVITY instrument filled the gap between adaptive optics (wide binaries) and spectroscopic methods (close binaries) to clarify the structure of θ Ori. They i) identify three previously unknown companions for θ^1 Ori B, θ^2 Ori B, and θ^2 Ori C; ii) measured the separation of 3.6 au for a previously suspected companion of θ^2 Ori B; iii) confirmed four companions to θ^1 Ori A, θ^1 Ori C, θ^1 Ori D, and θ^2 Ori A, providing improved astrometry and photometric mass estimates; iv) refined the orbit of the high-mass binary θ^1 Ori C with $P = (11.4 \pm 0.2)$ yr; v) determined a new orbit for the close binary θ^1 Ori D with a system mass of 21.7 $M_\odot$, a period of 53 d.

Another important result is multiplicity statistics. Including companions detected in previous studies, 11 stars of 16 are multiple systems. They concluded that the average companion fraction was approximately 2, which is significantly higher than in previous studies of OB stars associations. Duchêne & Kraus (2013) found 0.22 ± 0.06 companions for stars with masses $\leq 0.1\,M_\odot$ and 1.3 ± 0.2 companions for primary stars with masses $\geq 16\,M_\odot$.

Duchêne & Kraus (2013) also found 22 companions around those 16 primaries in the studied sample. The separations were a bimodal distribution that included peaks at 0.5 au and 50 au. Such a distribution suggests two different formation mechanisms, namely, disk fragmentation for close companions (accretion) and dynamical capture or core fragmentation (competitive accretion) for wide companions. However, the authors rules out stellar collisions as the dominant formation mechanism.

Regarding the mass ratio and the IMF, Duchêne & Kraus (2013) concluded that there was no excess at the mass ratio $q = 1$, which implies that there is no significant population banaries with equal masses. The mass-ratio distribution follows a standard power-law with a steep slope of 1.7 ± 0.1. This contradicts earlier findings of flat mass ratio distributions in OB associations, such as the O-type population in 30 Doradus of the Large Magellanic Cloud (Shenar et al., 2022).

2.9.2 Infrared dark clouds

Infrared dark clouds (IRDCs) are prime sites for massive star formation. They comprise cold regions of interstellar gas and dust that appear as dark patches against the bright background of the mid-infrared Galactic plane. In the Orion complex, IRDCs are less abundant and prominent than in more massive regions along the Galactic plane, such as near the Galactic Center (Genzel et al., 2010) or Cygnus X (Beuther et al., 2022). Classic IRDCs are more challenging to detect here due to the low Galactic background at Orion's latitude ($b \approx -20°$), and the closer distance, causing them to blend with surrounding emission. Yet, several cold, dense, high-column-density filaments and cores in Orion exhibit IRDC-like properties such as the Integral-Shaped Filament in Orion A (see Sect. 2.2). The ISF contains several dense clumps and cores (e.g. OMC-2/3, OMC-4) that appear dark in Spitzer 8 μm and MSX 8.28 μm images, especially where the background is sufficient. Megeath et al. (2012) and Stutz & Kainulainen (2015) point out absorption spectral lines at mid-IR wavelengths in these regions. These features are analogous to IRDCs: they are cold ($\approx$ 10–15 K), dense ($> 10^{22}\,\mathrm{cm}^{-2}$), and filamentary.

A key question that IRCD might reveal is whether the birth of massive and low-massive stars is contemporary. Cyganowski et al. (2017) and Pillai et al. (2019) analysed ALMA observations of IRDCs (G11.92−0.61, G11.11−0.12, and G28.34+0.06) and concluded that low- and high-mass stars form simultaneously. On the other hand, there are extreme cases in which either only low-mass cores are present, or a single high-mass core dominates Beuther et al. (2018). For instance, G17.64+0.16 is an example of a single O-type YSO with mass exceeding $> 30\,\mathrm{M}_\odot$ (Maud et al., 2018), while G28.23−0.19 is a massive IRDC without any massive core (Sanhueza et al., 2017).

2.9.3 Supernovæ

Recent studies suggest that the Orion complex has been significantly shaped by supernova activity in the past. The Orion–Eridanus superbubble has been attributed to multiple supernova explosions or to strong winds from past OB stars in Orion OB1 association (see Sect. 2.7). These supernovæ very likely played a critical role in shaping the large-scale gas morphology and may even have triggered subsequent star formation in nearby molecular clouds (Lee et al., 2015; Feddersen, 2020).

Figure 2.9: Artist's impression of a supernova explosion leaving behind a compact object. The image is based on the aftermath of the explosion of supernova SN 2022jli, as seen by ESO's VLT and NTT telescopes (Chen et al., 2024). Credit: ESO/L. Calçada.

Several studies such as Hoogerwerf et al. (2001) have linked a past supernova to the observed proper motions of runaway stars (see Sect. 2.2), suggesting a supernova-driven ejection from a binary system in the Orion region around 2.5 million years ago. The identification of radioactive ^{26}Al emission in the region supports the existence of recent core-collapse supernovæ, which is also consistent with the evolutionary timescales of massive stars in the Orion OB association (Voss et al., 2010).

One particularly noteworthy future event in the Orion complex is the anticipated explosion of Betelgeuse (α Ori). Saio et al. (2023) analysed multiple pulsation periods of α Ori and interpreted them, via pulsation models, as evidence that this star is in its late stages of core carbon burning. They argue that once carbon is exhausted, Betelgeuse is expected to explode in a few decades to a few hundred years, making it a strong candidate for the next Type-II Galactic supernova. Altogether, supernova feedback in Orion appears to be a major driver of both cloud dispersal and subsequent star formation, connecting the death of massive stars to the birth of new stellar generations.

References

Akiyama, K., Alberdi, A., Alef, W., et al. 2022, First Sagittarius A* Event Horizon Telescope Results. I. The Shadow of the Supermassive Black Hole in the Center of the Milky Way, ApJ, 930, L12

Akiyama, K., Alberdi, A., Alef, W., et al. 2019, First M87 Event Horizon Telescope Results. I. The Shadow of the Supermassive Black Hole, ApJ, 875, L1

Ansdell, M., Haworth, T. J., Williams, J. P., et al. 2020, An ALMA Survey of λ Orionis Disks: From Supernovae to Planet Formation, AJ, 160, 248

Anugu, N., Le Bouquin, J.-B., Monnier, J. D., et al. 2020, MIRC-X: A Highly Sensitive Six-telescope Interferometric Imager at the CHARA Array, AJ, 160, 158

Anugu, N., ten Brummelaar, T. A., Lanthermann, C., et al. 2024, CHARA/Silmaril Instrument Software and Data Reduction Pipeline: Characterization of the Instrument in the Lab and On-Sky

Armstrong, J. T., Mozurkewich, D., Rickard, L. J., et al. 1998, The Navy Prototype Optical Interferometer, ApJ, 496, 550

Bagnuolo, Jr., W. G., Riddle, R. L., Gies, D. R., & Barry, D. J. 2001, ι Orionis-Evidence for a Capture Origin Binary, ApJ, 554, 362

Balick, B. & Brown, R. L. 1974, Intense sub-arcsecond structure in the galactic center., ApJ, 194, 265

Bally, J. 2008, in Handbook of Star Forming Regions, Volume I, ed. B. Reipurth, Vol. 4, 459

Bally, J. & Reipurth, B. 2001, Irradiated Herbig-Haro Jets in the Orion Nebula and near NGC 1333, ApJ, 546, 299

Barrado y Navascués, D., Stauffer, J. R., Bouvier, J., Jayawardhana, R., & Cuillandre, J.-C. 2004, The Substellar Population of the Young Cluster λ Orionis, ApJ, 610, 1064

Bely, P. Y., Burrows, C. J., & Roddier, F. J. 1990, in Amplitude and Intensity Spatial Interferometry, ed. J. B. Breckinridge, Vol. 1237, International Society for Optics and Photonics (San Diego, CA: SPIE), 198 – 205

Bertout, C. 1989, T Tauri stars: wild as dust., ARA&A, 27, 351

Beuther, H., Mottram, J. C., Ahmadi, A., et al. 2018, Fragmentation and disk formation during high-mass star formation. IRAM NOEMA (Northern Extended Millimeter Array) large program CORE, A&A, 617, A100

Beuther, H., Wyrowski, F., Menten, K. M., et al. 2022, The Cygnus Allscale Survey of Chemistry and Dynamical Environments: CASCADE. Overview and first results toward DR20 from the Max Planck IRAM Observatory program (MIOP), A&A, 665, A63

Blaauw, A. 1956, On the Luminosities, Motions, and Space Distribution of the Nearer Northern O-B5 Stars., ApJ, 123, 408

Blaauw, A. 1964, The O Associations in the Solar Neighborhood, ARA&A, 2, 213

Blaauw, A. & Morgan, W. W. 1953, Note on the motion and possible origin of the O-type star HD 34078 = AE Aurigae and the emission nebula IC 405., Bull. Astron. Inst. Netherlands, 12, 76

Blaauw, A. & Morgan, W. W. 1954, The Space Motions of AE Aurigae and μ Columbae with Respect to the Orion Nebula., ApJ, 119, 625

Bouy, H., Huélamo, N., Barrado Y Navascués, D., et al. 2009, A deep look into the core of young clusters. II. λ-Orionis, A&A, 504, 199

Brož, M. 2017, An Advanced N-body Model for Interacting Multiple Stellar Systems, ApJS, 230, 19

Brož, M., Ďurech, J., Carry, B., et al. 2022a, Observed tidal evolution of Kleopatra's outer satellite, A&A, 657, A76

Brož, M., Harmanec, P., Zasche, P., et al. 2022b, Towards a consistent model of the hot quadruple system HD 93206 = QZ Carinæ. II. N-body model, A&A, 666, A24

Brož, M., Marchis, F., Jorda, L., et al. 2021, An advanced multipole model for (216) Kleopatra triple system, A&A, 653, A56

Brown, A. G. A., Vallenari, A., Prusti, T., et al. 2018, Gaia Data Release 2. Summary of the contents and survey properties, A&A, 616, A1

Brož, M. & Wolf, M. 2017, Astronomická měření (Univerzita Karlova. Matematicko-fyzikální fakulta)

Brož, M., Prša, A., Conroy, K. E., & Abdul-Masih, M. 2025a, Physics Of Eclipsing Binaries. IX. Spectroscopic module, A&A in prep.; `https://arxiv.org/abs/2506.20868` [[arXiv]2506.20868]

Brož, M., Prša, A., Conroy, K. E., Oplištilová, A., & Horvat, M. 2025b, Physics Of Eclipsing Binaries. VII. Interferometric module, A&A in prep.; `https://arxiv.org/abs/2506.20865` [[arXiv]2506.20865]

Burrows, A. & Liebert, J. 1993, The science of brown dwarfs, Reviews of Modern Physics, 65, 301

Buscher, D. F. 2015, Practical Optical Interferometry: Imaging at Visible and Infrared Wavelengths, Cambridge Observing Handbooks for Research Astronomers (Cambridge University Press)

Caballero, J. A. 2008, Stars and brown dwarfs in the σ Orionis cluster: the Mayrit catalogue, A&A, 478, 667

Caballero, J. A. & Solano, E. 2008, Young stars and brown dwarfs surrounding Alnilam (ε Orionis) and Mintaka (δ Orionis), A&A, 485, 931

Carpenter, K. G., Boyajian, T., Buzasi, D., et al. 2025, NASA Innovative Advanced Concepts Phase I Final Report – A Lunar Long-Baseline UV/Optical Imaging Interferometer: Artemis-enabled Stellar Imager (AeSI)

Che, X., Sturmann, L., Monnier, J. D., et al. 2013, Optical and Mechanical Design of the CHARA Array Adaptive Optics, Journal of Astronomical Instrumentation, 2, 1340007

Chen, P., Gal-Yam, A., Sollerman, J., et al. 2024, A 12.4-day periodicity in a close binary system after a supernova, Nature, 625, 253

Ciurlo, A. & Morris, M. R. 2025, Sagittarius A* – The Milky Way Supermassive Black Hole, arXiv e-prints, arXiv:2503.20081

Colavita, M. M., Wallace, J. K., Hines, B. E., et al. 1999, The Palomar Testbed Interferometer, ApJ, 510, 505

Conrady, A. 2013, Applied Optics and Optical Design, Part One, Dover Books on Physics (Dover Publications)

Conroy, K. E., Kochoska, A., Hey, D., et al. 2020, Physics of Eclipsing Binaries. V. General Framework for Solving the Inverse Problem, ApJS, 250, 34

Corcoran, M. F., Nichols, J. S., Pablo, H., et al. 2015, A Coordinated X-Ray and Optical Campaign of the Nearest Massive Eclipsing Binary, δ Orionis Aa. I. Overview of the X-Ray Spectrum, ApJ, 809, 132

Cunha, K. & Smith, V. V. 1996, Is the expanding molecular cloud surrounding λ Orionis caused by a Supernova?, A&A, 309, 892

Cyganowski, C. J., Brogan, C. L., Hunter, T. R., et al. 2017, Simultaneous low- and high-mass star formation in a massive protocluster: ALMA observations of G11.92-0.61, MNRAS, 468, 3694

Davis, J. 1994, The Sydney University Stellar Interferometer (SUSI), Symposium - International Astronomical Union, 158, 135–142

Domiciano de Souza, A., Kervella, P., Jankov, S., et al. 2003, in SF2A-2003: Semaine de l'Astrophysique Francaise, ed. F. Combes, D. Barret, T. Contini, & L. Pagani, 515

D'Orazi, V., Randich, S., Flaccomio, E., et al. 2009, Metallicity of low-mass stars in Orion, A&A, 501, 973

Duchêne, G. & Kraus, A. 2013, Stellar Multiplicity, ARA&A, 51, 269

Edlén, B. 1966, The Refractive Index of Air, Metrologia, 2, 71

Eisenhauer, F., Perrin, G., Brandner, W., et al. 2011, GRAVITY: Observing the Universe in Motion, The Messenger, 143, 16

Feddersen, J. R. e. a. 2020, The Past and Future of Orion's Star-forming Regions, ApJ, 895, 126

Fizeau, H. 1868, Remarques sur la relation remarquable et nécessaire entre les dimensions des franges d'interférence et celles de la source lumineuse, Comptes Rendus de l'Académie des Sciences de Paris, 66, 1005

Foley, M. M., Goodman, A., Zucker, C., et al. 2023, A 3D View of Orion. I. Barnard's Loop, ApJ, 947, 66

Freudling, W., Romaniello, M., Bramich, D. M., et al. 2013, Automated data reduction workflows for astronomy. The ESO Reflex environment, A&A, 559, A96

Galilei, G. 1613, Istoria E dimostrazioni intorno alle macchie solari E loro accidenti comprese in tre lettere scritte all'illvstrissimo signor Marco Velseri ...

Garcia, E., van Belle, G., Muterspaugh, M. W., & Swihart, S. 2014, in American Astronomical Society Meeting Abstracts, Vol. 223, American Astronomical Society Meeting Abstracts #223, 154.26

Genzel, R., Eisenhauer, F., & Gillessen, S. 2010, The Galactic Center massive black hole and nuclear star cluster, Rev. Mod. Phys., 82, 3121

Getman, K. V., Feigelson, E. D., Kuhn, M. A., & Garmire, G. P. 2019, Gaia stellar kinematics in the head of the Orion A cloud: runaway stellar groups and gravitational infall, Monthly Notices of the Royal Astronomical Society, 487, 2977

Gezer, I., Marton, G., Roquette, J., et al. 2025, SED Modelling of Young Stellar Objects in the Orion Star Formation Complex, A&A, 696, A196

Gies, D. R. & Bolton, C. T. 1986, The Binary Frequency and Origin of the OB Runaway Stars, ApJS, 61, 419

Glindemann, A. 2013, VLTI School: Introduction to Spatial Interferometry, `https://www.eso.org/sci/facilities/paranal/telescopes/vlti/tuto/tutorial_spatial_interferometry.pdf`, european Southern Observatory, VLTI School Tutorial

Gras-Velázquez, À. & Ray, T. P. 2005, Weak-line T Tauri stars: circumstellar disks and companions. I. Spectral energy distributions and infrared excesses, A&A, 443, 541

Großschedl, J. E., Alves, J., Meingast, S., et al. 2018, 3D shape of Orion A from Gaia DR2, A&A, 619, A106

Großschedl, J. E., Alves, J., Teixeira, P. S., et al. 2019, VISION - Vienna survey in Orion. III. Young stellar objects in Orion A, A&A, 622, A149

Gu, M. 2000, Imaging with Aberration (Berlin, Heidelberg: Springer Berlin Heidelberg), 177–198

Hanbury Brown, R. 1956, A Test of a New Type of Stellar Interferometer on Sirius, Nature, 178, 1046

Hanbury Brown, R., Davis, J., & Allen, L. R. 1974, The Angular Diameters of 32 Stars, MNRAS, 167, 121

Haniff, C. A., Baldwin, J. E., Baron, F., et al. 2006, in Society of Photo-Optical Instrumentation Engineers (SPIE) Conference Series, Vol. 6268, Advances in Stellar Interferometry, ed. J. D. Monnier, M. Schöller, & W. C. Danchi, 626805

Haro, G. 1952, Herbig's Nebulous Objects Near NGC 1999., ApJ, 115, 572

Hecht, E. 2002, Optics, Pearson education (Addison-Wesley)

Herbig, G. H. 1950, Spectra of Variable Stars in the Orion Nebula., ApJ, 111, 15

Ho, P. T. P., Moran, J. M., & Lo, K. Y. 2004, The Submillimeter Array, ApJ, 616, L1

Hoogerwerf, R., de Bruijne, J. H. J., & de Zeeuw, P. T. 2001, On the origin of the O and B-type stars with high velocities. II. Runaway stars and pulsars ejected from the nearby young stellar groups, A&A, 365, 49

Horvat, M., Conroy, K. E., Pablo, H., et al. 2018, Physics of Eclipsing Binaries. III. Spin-Orbit Misalignment, ApJS, 237, 26

Huang, B., Bates, M., & Zhuang, X. 2009, Super-Resolution Fluorescence Microscopy, Annual Review of Biochemistry, 78, 993

Hummel, C. A., Rivinius, T., Nieva, M. F., et al. 2013, Dynamical mass of the O-type supergiant in ζ Orionis A, A&A, 554, A52

Hummel, C. A., White, N. M., Elias, N. M., I., Hajian, A. R., & Nordgren, T. E. 2000, ζ Orionis A is a Double Star, ApJ, 540, L91

Huygens, C. 1690, Traité de la lumière: Où sont expliquées les causes de ce qui luy arrive dans la reflexion & dans la refraction (Leiden: Pierre van der Aa, marchand libraire), first edition of Huygens's foundational work on the wave theory of light

Jennison, R. C. 1958, A phase sensitive interferometer technique for the measurement of the Fourier transforms of spatial brightness distributions of small angular extent, MNRAS, 118, 276

Jensen, E. L. N. 2001, in Astronomical Society of the Pacific Conference Series, Vol. 244, Young Stars Near Earth: Progress and Prospects, ed. R. Jayawardhana & T. Greene, 3

Jones, D., Conroy, K. E., Horvat, M., et al. 2020, Physics of Eclipsing Binaries. IV. The Impact of Interstellar Extinction on the Light Curves of Eclipsing Binaries, ApJS, 247, 63

Kalari, V. M., Horch, E. P., Salinas, R., et al. 2022, Resolving the Core of R136 in the Optical, ApJ, 935, 162

Karim, M. T., Stassun, K. G., Briceño, C., et al. 2016, THE ROTATION PERIOD DISTRIBUTIONS OF 4–10 Myr T TAURI STARS IN ORION OB1: NEW CONSTRAINTS ON PRE-MAIN-SEQUENCE ANGULAR MOMENTUM EVOLUTION, AJ, 152, 198

Karl, M., Pfuhl, O., Eisenhauer, F., et al. 2018, Multiple star systems in the Orion nebula, A&A, 620, A116

Kervella, P., Verhoelst, T., Ridgway, S. T., et al. 2009, The close circumstellar environment of Betelgeuse. Adaptive optics spectro-imaging in the near-IR with VLT/NACO, A&A, 504, 115

Khodadi, M., Vagnozzi, S., & Firouzjaee, J. T. 2024, Event Horizon Telescope observations exclude compact objects in baseline mimetic gravity, Scientific Reports, 14, 26932

Kitchin, C. R. 2020, Astrophysical Techniques, 7th edn. (Boca Raton, London, New York: CRC Press), 466

Könyves, V., André, P., Arzoumanian, D., et al. 2020, Properties of the dense core population in Orion B as seen by the Herschel Gould Belt survey, A&A, 635, A34

Kounkel, M. 2020, Supernovae in Orion: The Missing Link in the Star-forming History of the Region, ApJ, 902, 122

Kounkel, M., Covey, K., Suárez, G., et al. 2018, The APOGEE-2 Survey of the Orion Star-forming Complex. II. Six-dimensional Structure, AJ, 156, 84

Kounkel, M., Stassun, K. G., Covey, K., & Hartmann, L. 2022, A gravitational and dynamical framework of star formation: the Orion nebula, Monthly Notices of the Royal Astronomical Society, 517, 161

Krips, M., Castro-Carrizo, A., Neri, R., & Pietu, V. 2022, in Astronomical Society of the Pacific Conference Series, Vol. 532, Astronomical Data Analysis Software and Systems XXX, ed. J. E. Ruiz, F. Pierfedereci, & P. Teuben, 313

Kroupa, P., Jeřábková, T., Dinnbier, F., Beccari, G., & Yan, Z. 2018, Evidence for feedback and stellar-dynamically regulated bursty star cluster formation: the case of the Orion Nebula Cluster, A&A, 612, A74

Kubiak, K., Alves, J., Bouy, H., et al. 2017, Orion revisited. III. The Orion Belt population, A&A, 598, A124

Labeyrie, A. 1975, Interference fringes obtained on Vega with two optical telescopes., ApJ, 196, L71

Lada, C. J., Lewis, J. A., Lombardi, M., & Alves, J. 2017, HP2 survey. III. The California Molecular Cloud: A sleeping giant revisited, A&A, 606, A100

Le Bouquin, J. B., Berger, J. P., Lazareff, B., et al. 2011, PIONIER: a 4-telescope visitor instrument at VLTI, A&A, 535, A67

Lee, Y.-H., Murray, N. W., & Rahman, M. 2015, Triggered Star Formation in Orion via Superbubble Compression, ApJ, 798, 115

Leinert, C., Graser, U., Waters, L. B., et al. 2000, Society of Photo-Optical Instrumentation Engineers (SPIE) Conference Series, Vol. 4006, 10-um interferometry on the VLTI with the MIDI instrument: a preview, ed. P. Léna & A. Quirrenbach, 43–53

Levine, J. L. 2006, PhD thesis, University of Florida

Longinotti, A., Bickert, K., Cautain, R., et al. 2002, The VINCI instrument software in the very large telescope environment, IEEE Transactions on Nuclear Science, 49, 483

Lopez, B., Lagarde, S., Petrov, R. G., et al. 2022, MATISSE, the VLTI mid-infrared imaging spectro-interferometer, A&A, 659, A192

Lykou, F., Ábrahám, P., Chen, L., et al. 2022, The disk of FU Orionis viewed with MATISSE/VLTI. First interferometric observations in L and M bands, A&A, 663, A86

Maddalena, R. J. & Morris, M. 1987, An Expanding System of Molecular Clouds Surrounding lambda Orionis, ApJ, 323, 179

Maddalena, R. J., Morris, M., Moskowitz, J., & Thaddeus, P. 1986, The Large System of Molecular Clouds in Orion and Monoceros, ApJ, 303, 375

Maestro, V., Kok, Y., Huber, D., et al. 2012, Society of Photo-Optical Instrumentation Engineers (SPIE) Conference Series, Vol. 8445, Imaging rapid rotators with the PAVO beam combiner at CHARA, ed. F. Delplancke, J. K. Rajagopal, & F. Malbet, 84450G

Maíz Apellániz, J., Trigueros Páez, E., Negueruela, I., et al. 2019, MONOS: Multiplicity Of Northern O-type Spectroscopic systems. I. Project description and spectral classifications and visual multiplicity of previously known objects, A&A, 626, A20

Mann, R. M. 2010, PhD thesis, University of Hawaii, Manoa

Maud, L. T., Cesaroni, R., Kumar, M. S. N., et al. 2018, Chasing discs around O-type (proto)stars. ALMA evidence for an SiO disc and disc wind from G17.64+0.16, A&A, 620, A31

Mayer, P., Harmanec, P., Wolf, M., Božić, H., & Šlechta, M. 2010, Physical elements of the eclipsing binary δ Orionis, A&A, 520, A89

Megeath, S. T., Gutermuth, R., Muzerolle, J., et al. 2012, The Spitzer Space Telescope Survey of the Orion A and B Molecular Clouds. I. A Census of Dusty Young Stellar Objects and a Study of Their Mid-infrared Variability, AJ, 144, 192

Menu, J., Perrin, G., Choquet, E., & Lacour, S. 2012, Kalman-filter control schemes for fringe tracking. Development and application to VLTI/GRAVITY, A&A, 541, A81

Michelson, A. A. & Pease, F. G. 1921, Measurement of the Diameter of α Orionis with the Interferometer., ApJ, 53, 249

Millour, F. 2008, All you ever wanted to know about optical long baseline stellar interferometry, but were too shy to ask your adviser, New Astronomy Reviews, 52, 177, circumstellar Disks and Planets at Very High Angular Resolution

Monnier, J. D., Le Bouquin, J.-B., Anugu, N., et al. 2018, in Society of Photo-Optical Instrumentation Engineers (SPIE) Conference Series, Vol. 10701, Optical and Infrared Interferometry and Imaging VI, ed. M. J. Creech-Eakman, P. G. Tuthill, & A. Mérand, 1070122

Monnier, J. D., Pedretti, E., Thureau, N., et al. 2006, in Advances in Stellar Interferometry, ed. J. D. Monnier, M. Schöller, & W. C. Danchi, Vol. 6268, International Society for Optics and Photonics (SPIE), 62681P

Monnier, J. D., Zhao, M., Pedretti, E., et al. 2007, Imaging the Surface of Altair, Science, 317, 342

Mourard, D., Berio, P., Pannetier, C., et al. 2022, in Optical and Infrared Interferometry and Imaging VIII, ed. A. Mérand, S. Sallum, & J. Sanchez-Bermudez (SPIE), 7

Mourard, D., Bério, P., Perraut, K., et al. 2017, SPICA, Stellar Parameters and Images with a Cophased Array: a 6T visible combiner for the CHARA array, Journal of the Optical Society of America A, 34, A37

Mourard, D., Clausse, J. M., Marcotto, A., et al. 2009, VEGA: Visible spEctroGraph and polArimeter for the CHARA array: principle and performance, A&A, 508, 1073

Mourard, D., Tallon-Bosc, I., Blazit, A., et al. 1994, The GI2T interferometer on Plateau de Calern, A&A, 283, 705

Mugnier, L. M., Fusco, T., & Conan, J.-M. 2004, MISTRAL: a myopic edge-preserving image restoration method, with application to astronomical adaptive-optics-corrected long-exposure images, Journal of the Optical Society of America A, 21, 1841

Nichols, J., Huenemoerder, D. P., Corcoran, M. F., et al. 2015, A Coordinated X-Ray and Optical Campaign of the Nearest Massive Eclipsing Binary, δ Orionis Aa. II. X-Ray Variability, ApJ, 809, 133

Noroozi, S., Chen, Z., García-Díaz, M. T., & González-Buitrago, D. H. 2024, Variability of young stellar objects in the Orion nebula, A&A, 691, A358

Ochsendorf, B. B., Brown, A. G. A., Bally, J., & Tielens, A. G. G. M. 2015, Nested Shells Reveal the Rejuvenation of the Orion-Eridanus Superbubble, ApJ, 808, 111

O'Dell, C. R., Ferland, G. J., Porter, R. L., & van Hoof, P. A. M. 2011, Physical Conditions in Barnard's Loop, Components of the Orion-eridanus Bubble, and Implications for the Warm Ionized Medium Component of the Interstellar Medium, ApJ, 733, 9

Oplištilová, A., Mayer, P., Harmanec, P., et al. 2023, Spectrum of the secondary component and new orbital elements of the massive triple star δ Ori A, A&A, 672, A31

Oplištilová, A., Brož, M., Hummel, C. A., Harmanec, P., & Barlow, B. 2025, VLTI observations of the Orion Belt stars: I. eps Orionis

Orkisz, J. H., Pety, J., Gerin, M., et al. 2017, Turbulence and star formation efficiency in molecular clouds: solenoidal versus compressive motions in Orion B, A&A, 599, A99

Pablo, H., Richardson, N. D., Moffat, A. F. J., et al. 2015, A Coordinated X-Ray and Optical Campaign of the Nearest Massive Eclipsing Binary, δ Orionis Aa. III. Analysis of Optical Photometric (MOST) and Spectroscopic (Ground-based) Variations, ApJ, 809, 134

Pannetier, C., Mourard, D., Berio, P., et al. 2020, in Society of Photo-Optical Instrumentation Engineers (SPIE) Conference Series, Vol. 11446, Optical and Infrared Interferometry and Imaging VII, ed. P. G. Tuthill, A. Mérand, & S. Sallum, 114460T

Pauwels, T., Reggiani, M., Sana, H., Rainot, A., & Kratter, K. 2023, The multiplicity of massive stars in the Scorpius OB1 association through high-contrast imaging, A&A, 678, A172

Pease, F. G. 1931, Interferometer Methods in Astronomy, Ergebnisse der exakten Naturwissenschaften, 10, 84

Pepe, F., Cristiani, S., Rebolo, R., et al. 2021, ESPRESSO at VLT. On-sky performance and first results, A&A, 645, A96

Petrov, R. G., Malbet, F., Weigelt, G., et al. 2007, AMBER, the near-infrared spectro-interferometric three-telescope VLTI instrument, A&A, 464, 1

Pety, J., Guzmán, V. V., Orkisz, J. H., et al. 2017, The anatomy of the Orion B giant molecular cloud: A local template for studies of nearby galaxies, A&A, 599, A98

Pillai, T., Kauffmann, J., Zhang, Q., et al. 2019, Massive and low-mass protostars in massive "starless" cores, A&A, 622, A54

Pon, A., Ochsendorf, B. B., Alves, J., et al. 2016, Kompaneets Model Fitting of the Orion-Eridanus Superbubble. II. Thinking Outside of Barnard's Loop, ApJ, 827, 42

Pretheesh Kumar, V. C. & Ganesan, A. R. 2022, Shack-Hartmann wavefront sensor with enhanced dynamic range and reference-free operation, Optical Engineering, 61, 054108

Prša, A., Conroy, K. E., Horvat, M., et al. 2016, Physics Of Eclipsing Binaries. II. Toward the Increased Model Fidelity, ApJS, 227, 29

Puebla, R. E., Hillier, D. J., Zsargó, J., Cohen, D. H., & Leutenegger, M. A. 2016, X-ray, UV and optical analysis of supergiants: ε Ori, MNRAS, 456, 2907

Rivilla, V. M., Martín-Pintado, J., Jiménez-Serra, I., & Rodríguez-Franco, A. 2013, The role of low-mass star clusters in massive star formation. The Orion case, A&A, 554, A48

Sahlmann, J., Ménardi, S., Abuter, R., et al. 2009, The PRIMA fringe sensor unit, A&A, 507, 1739

Saio, H., Nandal, D., Meynet, G., & Ekström, S. 2023, The evolutionary stage of Betelgeuse inferred from its pulsation periods, MNRAS, 526, 2765

Sana, H., Le Bouquin, J. B., Lacour, S., et al. 2014, Southern Massive Stars at High Angular Resolution: Observational Campaign and Companion Detection, ApJS, 215, 15

Sanhueza, P., Jackson, J. M., Zhang, Q., et al. 2017, A Massive Prestellar Clump Hosting No High-mass Cores, ApJ, 841, 97

Schaefer, G. H., Hummel, C. A., Gies, D. R., et al. 2016, Orbits, Distance, and Stellar Masses of the Massive Triple Star σ Orionis, AJ, 152, 213

Schneider, F. R. N., Sana, H., Evans, C. J., et al. 2018, An excess of massive stars in the local 30 Doradus starburst, Science, 359, 69

Schöller, M. 2007, The Very Large Telescope Interferometer: Current facility and prospects, New A Rev., 51, 628

Scholz, A. & Eislöffel, J. 2005, Rotation and variability of very low mass stars and brown dwarfs near ε Ori, A&A, 429, 1007

Schönrich, R., Binney, J., & Dehnen, W. 2010, Local kinematics and the local standard of rest, MNRAS, 403, 1829

Schwartz, R. D. 1983, Herbig-haro objects., ARA&A, 21, 209

Shao, M., Colavita, M. M., Hines, B. E., et al. 1988, The Mark III stellar interferometer, A&A, 193, 357

Shenar, T., Oskinova, L., Hamann, W. R., et al. 2015, A Coordinated X-Ray and Optical Campaign of the Nearest Massive Eclipsing Binary, δ Orionis Aa. IV. A Multiwavelength, Non-LTE Spectroscopic Analysis, ApJ, 809, 135

Shenar, T., Sana, H., Mahy, L., et al. 2022, The Tarantula Massive Binary Monitoring. VI. Characterisation of hidden companions in 51 single-lined O-type binaries: A flat mass-ratio distribution and black-hole binary candidates, A&A, 665, A148

Simón-Díaz, S., Caballero, J. A., Lorenzo, J., et al. 2015, Oorbital and physical properties of the σ Ori Aa, Ab, B triple system, ApJ, 799, 169

Smith, W. J. 2008, Modern Optical Engineering: The Design of Optical Systems, Fourth Edition

Soler, J. D., Bracco, A., & Pon, A. 2018, The magnetic environment of the Orion-Eridanus superbubble as revealed by Planck, A&A, 609, L3

Sota, A., Maíz Apellániz, J., Morrell, N. I., et al. 2014, The Galactic O-Star Spectroscopic Survey (GOSSS). II. Bright Southern Stars, ApJS, 211, 10

Stephan, E. J.-M. 1874, Sur la mesure des diamètres apparents des étoiles par la méthode des interférences, Comptes Rendus de l'Académie des Sciences, 78, 1005, first aperture masking interferometry experiment on the 80-cm Marseille telescope

Stickland, D. J., Pike, C. D., Lloyd, C., & Howarth, I. D. 1987, A study of the massive O-type binary IOTA Orionis., A&A, 184, 185

Stutz, A. M. & Kainulainen, J. 2015, Evolution of column density distributions within Orion A$\star$, A&A, 577, L6

Surdej, J. 2019, Introduction to Optical/IR Interferometry: history and basic principles

Swiggum, C., D'Onghia, E., Alves, J., et al. 2021, Evidence for Radial Expansion at the Core of the Orion Complex with Gaia EDR3, ApJ, 917, 21

Tallon-Bosc, I., Bonneau, D., Labeyrie, A., et al. 1994, in IAU Symposium, Vol. 158, Very High Angular Resolution Imaging, ed. J. G. Robertson & W. J. Tango, 155

ten Brummelaar, T. A., McAlister, H. A., Ridgway, S. T., et al. 2005, First Results from the CHARA Array. II. A Description of the Instrument, ApJ, 628, 453

ten Brummelaar, T. A., Sturmann, J., Ridgway, S. T., et al. 2013, The Classic/climb Beam Combiner at the CHARA Array, Journal of Astronomical Instrumentation, 2, 1340004

Thompson, G. B. & Morrison, N. D. 2013, Variability in optical spectra of ε Orionis, AJ, 145, 95

Trégon, B. 2020–2025, Interférométrie Astronomie Amateur, `https://www.btregon-astro.org/`, accessed: 2025-07-10

Vallenari, A., Brown, A. G. A., Prusti, T., et al. 2023, Gaia Data Release 3. Summary of the content and survey properties, A&A, 674, A1

van Belle, G. T., Ciardi, D., Hillsberry, D., et al. 2024, MoonLITE: a CLPS-delivered NASA Astrophysics Pioneers lunar optical interferometer for sensitive, milliarcsecond observing

van Cittert, P. 1934, Die Wahrscheinliche Schwingungsverteilung in Einer von Einer Lichtquelle Direkt Oder Mittels Einer Linse Beleuchteten Ebene, Physica, 1, 201

Vernazza, P., Ferrais, M., Jorda, L., et al. 2021, VLT/SPHERE imaging survey of the largest main-belt asteroids: Final results and synthesis, A&A, 654, A56

Voss, R., Diehl, R., Vink, J. S., & Hartmann, D. H. 2010, Probing the evolving massive star population in Orion with kinematic and radioactive tracers, A&A, 520, A51

Whitmore, B. C., Chandar, R., Schweizer, F., et al. 2010, The Antennae Galaxies (NGC 4038/4039) Revisited: Advanced Camera for Surveys and NICMOS Observations of a Prototypical Merger, AJ, 140, 75

Wootten, A. & Thompson, A. R. 2009, The Atacama Large Millimeter/Submillimeter Array, Proceedings of the IEEE, 97, 1463

Wynn-Williams, C. G., Genzel, R., Becklin, E. E., & Downes, D. 1984, The Kleinmann-Low nebula : an infrared cavity., ApJ, 281, 172

Young, T. 1804, The Bakerian Lecture: Experiments and Calculations Relative to Physical Optics, Philosophical Transactions of the Royal Society of London Series I, 94, 1

Zari, E., Brown, A. G. A., & de Zeeuw, P. T. 2019, Structure, kinematics, and ages of the young stellar populations in the Orion region, A&A, 628, A123

Zernike, F. 1938, The concept of degree of coherence and its application to optical problems, Physica, 5, 785

3. Spectrum of the secondary component and new orbital elements of the massive triple star δ Ori A

In the following study, we analysed one of the brightest members of the Orion OB1 association, namely δ Ori. To constrain the complex models, we used a wide range of observables: photometry, astrometry, radial velocities, eclipse timings, eclipse durations, spectral line profiles, and spectral energy distributions. We used two codes for modelling, for the triple system Xitau (Brož, 2017; Brož et al., 2021, 2022a,b), and for the inner eclipsing binary PHOEBE2 (Prša et al., 2016; Horvat et al., 2018; Jones et al., 2020; Conroy et al., 2020; Brož et al., 2025a,b). Each of them has its own advantages (and disadvantages).

Astronomy & Astrophysics manuscript no. output
July 5, 2025

Spectrum of the secondary component and new orbital elements of the massive triple star δ Ori A ⋆,⋆⋆

A. Opštilová[1], P. Mayer⋆⋆⋆[1], P. Harmanec[1], M. Brož[1], A. Pigulski[2], H. Božić[3], P. Zasche[1], M. Šlechta[4], H. Pablo[5], P. A. Kołaczek-Szymański[2], A. F. J. Moffat[5], C. C. Lovekin[6], G. A. Wade[7], K. Zwintz[8], A. Popowicz[9], and W. W. Weiss[10]

[1] Charles University, Faculty of Mathematics and Physics, Astronomical Institute, V Holešovičkách 2, CZ-180 00 Praha 8-Trója, Czech Republic
[2] Uniwersytet Wrocławski, Instytut Astronomiczny, Kopernika 11, 51-622 Wrocław, Poland
[3] Hvar Observatory, Faculty of Geodesy, Zagreb University, Kačićéva 26, 10000 Zagreb, Croatia
[4] Czech Academy of Sciences, Astronomical Institute, CZ-25165 Ondřejov, Czech Republic
[5] Université de Montréal, Département de physique, C.P.6128, Succursale center-Ville, Montréal, Québec, H3C 3J7, Canada
[6] Department of Physics, Mount Allison University, Sackville, NB, E4L1E6, Canada
[7] Department of Physics and Space Science, Royal Military College of Canada, Kingston, Ontario K7K 7B4, Canada
[8] Institut für Astro- und Teilchenphysik, Universität Innsbruck, Technikerstraße 25, A-6020 Innsbruck, Austria
[9] Department of Electronics, Electrical Engineering and Microelectronics, Silesian University of Technology, Akademicka 16, 44-100 Gliwice, Poland.
[10] University of Vienna, Institute for Astrophysics, Türkenschanzstraße 17, 1180 Vienna, Austria

Received 23 October 2022 / Accepted 9 January 2023

ABSTRACT

δ Orionis is the closest massive multiple stellar system and one of the brightest members of the Orion OB association. The primary (Aa1) is a unique evolved O star. In this work, we applied a two-step disentangling method to a series of spectra in the blue region (430 to 450 nm), and we detected spectral lines of the secondary (Aa2). For the first time, we were able to constrain the orbit of the tertiary (Ab) – to 55 450 d or 152 yr – using variable γ velocities and new speckle interferometric measurements, which have been published in the Washington Double Star Catalogue. In addition, the Gaia DR3 parallax of the faint component (Ca+Cb) constrains the distance of the system to (381 ± 8) pc, which is just in the centre of the Orion OB1b association, at (382 ± 1) pc. Consequently, we found that the component masses according to the three-body model are 17.8, 8.5, and 8.7 $M_\odot$, for Aa1, Aa2, and Ab, respectively, with the uncertainties of the order of 1 $M_\odot$. We used new photometry from the BRITE satellites together with astrometry, radial velocities, eclipse timings, eclipse duration, spectral line profiles, and spectral energy distribution to refine radiative properties. The components, classified as O9.5 II + B2 V + B0 IV, have radii of 13.1, 4.1, and 12.0 $R_\odot$, which means that δ Ori A is a pre-mass-transfer object. The frequency of 0.478 cycles per day, known from the Fourier analysis of the residual light curve and X-ray observations, was identified as the rotation frequency of the tertiary. δ Ori could be related to other bright stars in Orion, in particular, ζ Ori, which has a similar architecture, or ε Ori, which is a single supergiant, and possibly a post-mass-transfer object.

Key words. Stars: close – Stars: massive – Stars: binaries: eclipsing – Stars: fundamental parameters – Stars: individual: δ Ori – Techniques: spectroscopic

1. Introduction

The bright star δ Ori (HR 1852, HD 36486, HIP 25930, ADS 4134) is a multiple stellar system consisting of six components: Aa1, Aa2, Ab, B, Ca, and Cb, more specifically, the eclipsing binary Aa1+Aa2, the interferometric binary (Aa1+Aa2)+Ab, the faint visual companion B, and the spectroscopic binary Ca+Cb (see Fig. 1). Their properties can be summarised as follows:

- Aa1+Aa2 ($V_{\rm Aa1}$ = 2.55 mag, $V_{\rm Aa2} \simeq$ 5.5 mag)[1] is a detached eclipsing binary with a negligible mass transfer, the orbital period P_1 = 5.732436 d (Mayer et al. 2010), a slightly eccentric orbit (0.08), and apsidal motion (1.45° $\rm yr^{-1}$) (Pablo et al. 2015).
- Ab ($V_{\rm Ab}$ = 3.7 mag) is a nearby companion, which forms an interferometric pair with Aa1+Aa2. It was discovered by

Send offprint requests to: A.O., e-mail: betsimsim@seznam.cz

⋆ Based on spectroscopic CCD observations with a coudé spectrograph attached to the 2m reflector of the Astronomical Institute AS ČR at Ondřejov, archival Haute Provence and ESO La Silla spectra, ground-based *UBV* photometry from Hvar, and data collected by the BRITE Constellation satellite mission, designed, built, launched, operated, and supported by the Austrian Research Promotion Agency (FFG), the University of Vienna, the Technical University of Graz, the University of Innsbruck, the Canadian Space Agency (CSA), the University of Toronto Institute for Aerospace Studies (UTIAS), the Foundation for Polish Science & Technology (FNiTP MNiSW), and National Science Centre (NCN).

⋆⋆ Tables B.1 and B.2 are also available in electronic form at the CDS via anonymous ftp to cdsarc.cds.unistra.fr (130.79.128.5) or via https://cdsarc.cds.unistra.fr/...+A/

⋆⋆⋆ Pavel Mayer passed away on November 7, 2018.

[1] $\alpha_{\rm J2000} = 5^{\rm h}\,32^{\rm m}\,0.398^{\rm s}$ and $\delta_{\rm J2000} = -00°\,17'\,56.69''$

Heintz (1980), confirmed by speckle interferometry (Mason et al. 1999) and by *Hipparcos* astrometry (Perryman & ESA 1997) of the (Aa1+Aa2)+Ab system. The corresponding orbital period P_2 must be of the order of tens of thousands of days.

- B ($V_B \simeq 14$ mag) is a very faint distant companion[2] that is probably not associated with the system. Assuming that the component is a main-sequence star, its absolute magnitude of 6.7 mag corresponds to the spectral type K.
- Ca+Cb ($V_{Ca+Cb} = 6.85$ mag) is another distant companion[3] to (Aa1+Aa2)+Ab that is a spectroscopic, non-eclipsing binary with a period of 29.96 d and of spectral types B3 V + A0 V (Leone et al. 2010).

In the present paper, we focus on the triple sub-system δ Ori (Aa1+Aa2)+Ab, with $V_{Aa1+Aa2+Ab} = 2.223$ mag (from the differential photometry at the Hvar Observatory), $\alpha_{J2000} = 5^h\,32^m\,00.400^s$, and $\delta_{J2000} = -00°\,17'\,56.74''$. Hereinafter, the parameters corresponding to the inner orbit Aa1+Aa2 and to the outer orbit (Aa1+Aa2)+Ab are denoted by indices 1 and 2, respectively. The parameters of the components Aa1, Aa2, and Ab are denoted by indices 1, 2, and 3, respectively.

Many researchers have studied the system since the end of the 19th century. For a detailed summary of the early investigation of δ Ori, we refer readers to our earlier study of the system (Mayer et al. 2010). As far as studies of the 21st century are concerned, Harvin et al. (2002) carried out a tomographic separation of the ultraviolet and optical spectra into two systems of spectral lines, interpreted them as the lines of the primary and secondary of the eclipsing subsystem, and concluded that the components have unexpectedly low masses ($m_1 = 11.2\,M_\odot$ and $m_2 = 5.6\,M_\odot$). However, Mayer et al. (2010), showed that the optical spectra are dominated by the spectral lines of the O9.5 II primary (Aa1; Walborn 1972) and the similarly hot tertiary (Ab), and that the system has normal masses for O and early-B stars (Harmanec 1988). The previous solution of the light curves (LCs) led Mayer et al. (2010) to the conclusion that the faint secondary (Aa2) contributes only a few percent to the total flux. Although they carried out disentangling of the spectra, they were unable to find its spectral lines convincingly, and could only rely on an indirect estimate of the mass ratio m_2/m_1.

Five in-depth studies of δ Ori were published in 2015 (the first four are a series): Corcoran et al. (2015) presented an overview of deep Chandra HETGS X-ray observations that covered nearly the entire binary (Aa1+Aa2) orbit. The observed X-ray emission was dominated by wind shocks from the primary (Aa1). Nichols et al. (2015) discussed the time-resolved and phase-resolved variability seen in the Chandra spectra. For the first time, they found phase-dependent variability in the X-ray emission line widths. They identified two periods in the total X-ray flux: 4.76 ± 0.30 and 2.04 ± 0.05 days. Pablo et al. (2015) carried out a detailed analysis of space-based photometry from Microvariability and Oscillations of STars (MOST) and simultaneously secured ground-based spectroscopy in the residuals of the orbital LC, with periods ranging from 0.7 to 29 days. Shenar et al. (2015) carried out a multi-wavelength non-local thermodynamic equilibrium (NLTE) analysis of spectra. The determined parameters led to a O9.5 II, B1 V, and B0 IV spectral classification for Aa1, Aa2, and Ab, respectively, with evolved primary (Aa1) and tertiary (Ab) components. They also found wind-driven mass loss by the Aa1 component at $4 \cdot 10^{-7}\,M_\odot\,yr^{-1}$. Richardson et al. (2015) used cross-correlation of the ultraviolet spectra from HST to obtain stellar parameter estimates for the primary, secondary, and the tertiary that was angularly resolved in the observations.

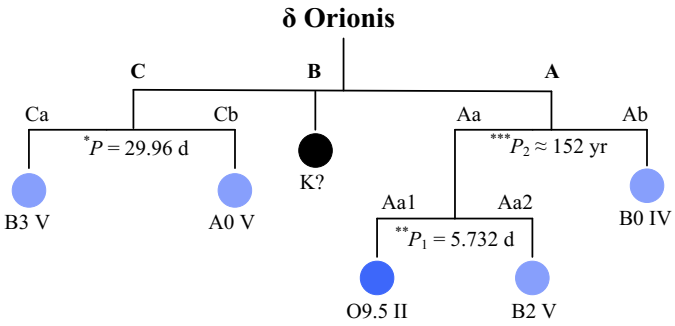

Fig. 1. Scheme of the multiple system δ Ori (HD 36486, ADS 4134, Mintaka). Orbital periods were taken from * Leone et al. (2010), ** Mayer et al. (2010), and *** this paper.

In this work, we continue our earlier analysis (Harmanec et al. 2013), which was devoted to the detection of very weak He I 6678 Å lines of the secondary in the red spectral region. Hereinafter, we focus on the blue spectral region. This study was also motivated by the tentative evidence of the secondary reported by Richardson et al. (2015), namely in the ultraviolet region, observed by the Hubble Space Telescope (Space Telescope Imaging Spectrograph).

However, a robust detection of the secondary (Aa2) spectrum is still lacking. Now, we have a larger set of spectra in the blue part of the optical spectrum and procedures to successfully detect the secondary's spectrum. Moreover, new Gaia DR3 parallax measurements have been published. This provides the possibility to estimate the distance of bright stars, saturated in the Gaia images, from the measured distances of their faint companions. We also have new high-resolution astrometric measurements at our disposal, which enables us to constrain the long-period orbit of (Aa1+Aa2)+Ab.

2. Observational data

In this section, only the spectroscopic and photometric data sets are described as these data sets are new and fundamental to our analysis. Details of other data sets (astrometry, spectral energy distribution SED, speckle interferometry, etc.) are described in the following sections (Sects. 4, 8, 9).

2.1. Spectroscopy

We used digital spectra covering the blue spectral region secured at the coudé focus of the Ondřejov 2m reflector (Škoda et al. 2002). We supplemented these data sets with spectra from the public archives of the ELODIE echelle spectrograph (Moultaka et al. 2004) at the Haute Provence Observatory, and the FEROS echelle spectrograph (Kaufer et al. 1999) at the ESO La Silla Observatory. The journal of the observations is presented in Table 1 (see Table B.1 for more details). The coverage of orbital phase φ_1 is illustrated in Fig. 2. The short period P_1 of 5.732436 d is well covered. The mean signal-to-noise ratio (S/N) is 208.5 (S/N values of individual spectra are given in Tables B.1 and B.2), which was sufficient for spectral disentangling. We normalised

[2] $\alpha_{J2000} = 5^h\,31^m\,58.745^s$ and $\delta_{J2000} = -00°\,18'\,18.65''$
[3] $\alpha_{J2000} = 5^h\,32^m\,00.406^s$ and $\delta_{J2000} = -00°\,17'\,04.38''$

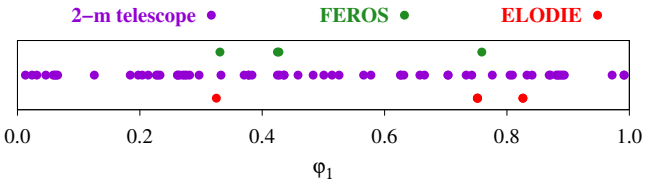

Fig. 2. Coverage of the orbital period P_1 by blue spectra. Phases are determined with respect to time T_0 = HJD 2454002.8735 (time of periastron passage determined by KOREL) for the eclipsing binary.

Table 1. Journal of digital spectra covering the blue spectral region.

Time interval [HJD – 2400000]	No. of spectra	Detector	Resolution [Å]
50031.68–50435.40	4	ELODIE	0.05
54136.58–54953.46	6	FEROS	0.03
55836.57–58405.57	65	Site-5 CCD	0.13

Notes. For more details, see Tables B.1 and B.2.

the spectra using polynomials of degree at least 4, with the program reSPEFO2[4] (written by Adam Harmanec).

2.2. Photometry

We used space-based photometric data from instruments on board the BRITE (BRIght Target Explorer; Pablo et al. 2016) and the MOST (Carroll et al. 1998) satellites and ground-based photometric data obtained at the Hvar Observatory with the 0.65m telescope. The time coverage is illustrated in Fig. 3. We did not use the saturated photometry from the Transiting Exoplanet Survey Satellite (TESS).

Each BRITE nanosatellite hosts a telescope, which has a 3 cm aperture. The BTr, BHr, and UBr satellites are equipped with a red filter (with effective wavelength 620 nm); BAb and BLb have a blue filter (420 nm). We have eliminated instrumental effects from the raw BRITE data by removing outliers and worst orbits, and by decorrelations. For more information on BRITE data processing, see Pigulski (2018).

The MOST passband covers the visible range of the spectrum (350–750 nm). The satellite performs high-precision optical photometry of single bright stars. It is equipped with a Maksutov telescope with an aperture of 15 cm and a custom broadband filter. It can point with an error of less than 1 arcsec. Other information can be found in Table 2.

The δ Ori LC from MOST continuously covers 3 weeks of observation. During calibration, we numerically shifted the measured magnitude to the V magnitude from the differential photometry at the Hvar Observatory. Then, we constructed normal points by centring the errors on the satellite orbital periods from Table 2, omitting the points with larger than the average uncertainty (0.5 mmag).

The Cassegrain 0.65m $f/11$ telescope at the Hvar observatory is equipped with a photoelectric detector (Božić 1998). This telescope was constructed at the Ondřejov Observatory of the Czechoslovak Academy of Sciences and brought to the Hvar Observatory at the beginning of 1972. A monitoring programme of bright variable stars has continued until today. The Hvar all-sky photometry provides accurate UBVR magnitudes in the Johnson system. For δ Ori A, we used UBV differential magnitudes obtained between October 2006 and October 2008 and UBVR between January 2019 and March 2021.

[4] https://astro.troja.mff.cuni.cz/projects/respefo/

Table 2. Information on satellites.

Satellite	Height [km]	Inclination [°]	Period [d]
MOST	825–840	98.7	0.07042
UBr (UniBRITE)	775–790	98.6	0.06972
BAb (BRITE-Austria)	775–790	98.6	0.06972
BLb (BRITE-Lem)	600–890	97.7	0.06917
BTr (BRITE-Toronto)	620–643	97.9	0.06819
BHr (BRITE-Heweliusz)	612–640	98.0	0.06743

Notes. Sources Pablo et al. (2016), Carroll et al. (1998), Webb et al. (2006).

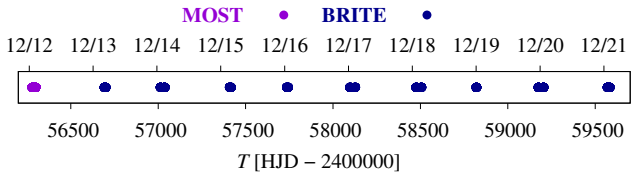

Fig. 3. Photometric data from MOST and BRITE displayed with respect to time. The BRITE data covers six consecutive seasons between 2013 and 2021.

3. Parallax and distance of δ Ori

In Gaia DR3 (Gaia Collaboration et al. 2016, 2021; Vallenari 2022), the parallaxes of the faint components of bright stars in the Orion OB1 association were measured (see Table 3). The parallax of δ Ori Ca+Cb, π = (2.6244 ± 0.0538) mas implies a distance d = (381 ± 8) pc and a distance modulus μ = (7.90 ± 0.04) mag. Hereinafter, we assume that the components (Aa1+Aa2)+Ab as well as Ca+Cb are located at the same distance. Statistically, they are located close to each other. The number of stars brighter than Ca+Cb (6.62 mag) is limited, there is only 15 of them within 7200″. Given the separation of 52″, the probability that stars are physically unrelated is low, $p < 10^{-3}$.

To the contrary, δ Ori B, which is also a formal member of the multiple visual system ADS 4134, is located at a substantially smaller distance (by almost 100 pc). It is therefore not physically related to δ Ori A. Either way, it is too faint (14 mag) to affect our results.

The Orion OB1 stellar association is usually divided into four subgroups, OB1a, OB1b, OB1c, and OB1d (Brown et al. 1994). The system δ Ori belongs to OB1b. We used the distances of 131 members from the Gaia DR3 catalogue and estimated the median distance to be (382 ± 1) pc, using a cumulative distribution function that is sensitive to the local number density of stars (see Fig. 4). We obtained the same distance as the distance of δ Ori Ca+Cb, within the respective intervals. We consider this to be an independent estimate for the δ Ori A system since massive stars are often located in the centre of the given association.

Other bright stars in the Orion belt are also located at very similar distances (Table 3). For instance, the faint components of ζ Ori C, σ Ori C, D, and E all have precise parallaxes. Moreover, the single star ε Ori has a similar spectroscopic distance modulus. Again, this is an independent confirmation for the δ Ori system.

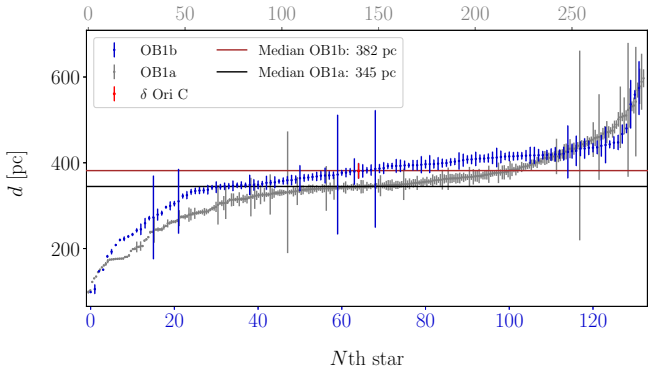

Fig. 4. Sorted distances of objects from the Orion OB1b (blue) and OB1a (grey) associations (Brown et al. 1994). Parallax data were taken from the Gaia DR3 catalogue (Vallenari 2022). The median values of distance for OB1b and OB1a are (382 ± 1) pc (brown) and (345 ± 1 pc) (black), respectively. The distance of δ Ori C (red), (381 ± 8) pc, is very close to the median distance of the OB1b distribution.

For comparison, the dispersion of distance in the radial direction (1σ) of the OB1b subgroup is only 15 pc, as seen in Fig. 4, while the angular dispersion (1σ) is about 0.5°, which corresponds to 3 pc, at the distance of 382 pc. In other words, 1′ corresponds to 0.11 pc, and 1″ to 0.0018 pc; this is a range of separations for the faint components discussed above.

The age of the OB1b association is estimated between 4 and 5 Myr (Maucó et al. 2018).[5] The OB1a subgroup (north-west) is older and at a smaller distance (by approximately 37 pc), while the OB1c and OB1d subgroups (north-east), including the Trapezium, are younger and at larger distances.

4. Visual orbit of (Aa1+Aa2)+Ab

To determine the parameters of the long-period (P_2) orbit of the (Aa1+Aa2)+Ab system, we constructed a simplified two-body model in the `Xitau` program (Brož 2017; Brož et al. 2021, 2022a,b)[6]. We used astrometric data from the Washington Double Star (WDS) Catalogue (Mason et al. 2001). If uncertainties were not available, we assumed the uncertainties of the separation ρ and the position angle measured from v, +DE direction as follows: $\sigma_\theta = 1.0°$, $\sigma_\rho = 0.01$ mas, or $\sigma_\theta = 0.2°$, $\sigma_\rho = 0.005$ mas for measurements before and after 2013, respectively. After removing 8 outliers due to poor resolution, incorrect plate scale, or calibration (from 1879.12[7] , 1978.10, 1979.06, 1980.02, 1981.01, 1985.74, 1995.05, 1999.78), we used $N = 74$ data points (both ρ, θ).

Another data set incorporated into the model included values of the systemic velocities γ_1 of δ Ori (Harvey et al. 1987; Harvin et al. 2002), which vary between approximately 12 and 23 km s^{-1} (see Table 5). This should correspond to the radial velocity of the (Aa1+Aa2) component. We did not take into account data points with possible systematic errors in γ_1, that is, blending with Ab (1910, 1948), low amplitude of RV curve K_1 (1951, 1969, 1981), and different γ_1 for Aa2 (1987, 1997). In some cases, also the RV of Ab was measured.

In total, we had $N = 88$ data points and $M = 8$ free parameters, which means $N-M = 80$ degrees of freedom. The model resulted in the best-fit with $\chi^2 = 95$, with contributions $\chi^2_{\rm SKY} = 60$ for astrometry and $\chi^2_{\rm RV} = 35$ for RVs. Although $\chi^2 > N - M$, the fit is still acceptable. The RV amplitude is in agreement, as well as directly measured RV values of Ab, which is lower than γ_1.

The resulting parameters and parameters that were fixed are shown in Table 4. We fixed the mass of the (Aa1+Aa2) components based on the phoebe2 model (Sect. 7) and the distance d based on the parallax (Sect. 3). The orbit is illustrated in Fig. 5. The fit of RVs is shown in Fig. 6.

We estimated the uncertainties of parameters using χ^2 mapping and verified the MCMC method. According to the χ^2 statistics, a 1σ level corresponds to $\chi^2 \doteq 101$. Since the distance was fixed, the uncertainties are relatively small (1% for the period, 10% for the mass). We determined the mass of the Ab component to be 11.0 $M_\odot$. Therefore, the total mass of the (Aa1+Aa2)+Ab system is around 37.5 $M_\odot$.

Mirror solution. We are aware of the existence of a mirror solution, with the opposite sign of inclination i_2. It exhibits higher total mass (up to 52 $M_\odot$), higher eccentricity (0.95), shorter period (40000 d), closer periastron passage. The RV curve of (Aa1+Aa2) component is also opposite, with a 'spike' due to the eccentricity. According to our throughout testing, it always has a worse best-fit χ^2, especially the $\chi^2_{\rm rv}$ contribution. Moreover, in the mirror solution, the RVs of Ab are larger than γ_1, which is incorrect. A more complex model is needed to test other constraints (see Sect. 9).

5. Spectral disentangling of residuals

After obtaining the reliable value of the long-period (P_2) of δ Ori Aa and Ab, we searched for the secondary's lines in the spectra. Our experience with the disentangling technique is that the result is often sensitive to the choice of initial values of the parameters. This is understandable since the χ^2 sum based on all data points of all spectra is a complicated function of the orbital elements, and it is easy to end up in a local minimum.

Moreover, the rotationally broadened spectral lines of the primary (Aa1) and tertiary (Ab) blend with each other at all orbital phases and altogether dominate the spectrum. Consequently, the contribution of the faint secondary (Aa2) to the χ^2 sum is almost comparable to the noise. The mass ratio q_1 of the Aa2 and Aa1 components is therefore poorly constrained. Nevertheless, the lines of the secondary can be detected in the residuals by a procedure called a two-step disentangling.

To disentangle the spectra, we used the `KOREL` program developed by Hadrava (1995, 1997, 2004, 2005). Rebinning of the spectra to a linear scale in RV, needed as input for `KOREL`, was carried out using the `HEC35D` program written by P.H. [8] The relative fluxes for the new wavelength points were derived using the `INTEP` program (Hill 1982), which is a modification of the Hermite interpolation formula. It is possible to choose both boundaries of the desired spectral region, and the program smoothly

[5] Some of the outliers seen in Fig. 4 might actually be former members of the OB1b association. If they were ejected at the typical speed of 10 km s^{-1}, they may travel 50 pc or 7.5° in the radial or tangential directions. The same is true for δ Ori B.

[6] http://sirrah.troja.mff.cuni.cz/~mira/xitau/

[7] Niesten (1904) reported micrométriques measures by 15cm Merz refractor, with two position angles 162° and a note 'en contact'. However, it is unlikely that it corresponds to δ Ori Ab, because its separation at that epoch was only 0.11″; separations in other binaries were 1″ or more. This observation is not compatible with our model, which indicates $\theta \doteq 127°$.

[8] The program `HEC35D` with User's Manual is available at http://astro.troja.mff.cuni.cz/hec/HEC35.

Table 3. Information about bright stars and their companions in Orion.

HD	Name	V [mag]	Spectral type	A_V [mag]	V_0 [mag]	M_V	V_0-M_V	Gaia DR3 parallax [mas]	Notes
36486	δ Ori	2.22*	O9.5 II	0.13	2.09	−5.81	7.90		OB1b association, multiple
37128	ε Ori	1.68*	B0 Ia	0.14	1.54	−6.25**	7.79		OB1b, single, variable 0.05 mag
37742	ζ Ori	1.75*	O9.5 Ib	0.17	1.58	−6.28**	7.92		OB1b, multiple
37468	σ Ori	3.82*	O9.5 V	0.17	3.65	−4.14	7.79		OB1b, multiple
37043	ι Ori	2.75	O8.5 III	0.09	2.66	−5.13	7.79		OB1d (Trapezium), multiple
36486 Aa1	δ Ori Aa1	2.55	O9.5 II		2.42	−5.7**	8.12		cf. this work
36486 Aa2	δ Ori Aa2	5.5?	B2 V		5.4?	−2.5?			0.00052″ from Aa1, Shenar et al. (2015)
36486 Ab	δ Ori Ab	3.83	B0 IV		3.70	−4.0***	7.70		0.32″
36486 B	δ Ori B	14.0	K?		13.9	+6.6		3.5002 ± 0.0119	33″, UCAC3 180-24383
36485 Ca	δ Ori Ca	6.62	B3 V		6.49	−1.6***	8.09	2.6244 ± 0.0538	52″, helium star, Leone et al. (2010)
36485 Cb	δ Ori Cb	9.8?	A0 V		9.7?	+1.8?			0.0012″ from Ca
37742 Aa	ζ Ori Aa	2.1	O9.5 Ib						Hummel et al. (2000)
37742 Ab	ζ Ori Ab	4.3	B0.5 IV						0.042″
37743	ζ Ori B	4.0	B0 III						2.4″
37742 C	ζ Ori C	9.54	A?					2.5876 ± 0.0387	57″
37468 Aa	σ Ori Aa	4.61	O9.5 V						Simón-Díaz et al. (2015)
37468 Ab	σ Ori Ab	5.20	B0.5 V						0.00042″
37468 B	σ Ori B	5.31	B?						0.25″
37468 C	σ Ori C	8.79	B0.5 V					2.4720 ± 0.0292	11″
37468 D	σ Ori D	6.62	B2 V					2.4744 ± 0.0621	13″
37468 E	σ Ori E	6.66	B2 V					2.3077 ± 0.0646	42″, helium star
37043 Aa1	ι Ori Aa1	2.8?	O8.5 III						Bagnuolo et al. (2001)
37043 Aa2	ι Ori Aa2		B0.8 III						0.0015″, eccentric
37043 Ab	ι Ori Ab		B2 IV						0.15″
37043 B	ι Ori B	7.00	B8 III					2.7869 ± 0.0476	11″
37043 C	ι Ori C	9.76	A0 V					2.6057 ± 0.0241	49″, Parenago (1954), Brun 731

Notes. * Hvar all-sky photometry; ** Martins et al. (2005); *** Schmidt-Kaler (1982); spectral types from Maíz Apellániz et al. (2019); Burssens et al. (2020) and absorption from Lallement et al. (2019). The visual magnitude including absorption is denoted by V; the absorption, by A_V; the visual magnitude without absorption, by V_0; and the distance modulus computed from visual magnitude, by M_V.

Table 4. Parameters of the orbit (Aa1+Aa2)+Ab, for the model with unreduced $\chi^2 = 95$.

Parameter	Value	Unit
T_0	2458773.1886 ± 0.1	HJD
$(m_1 + m_2)^{\mathrm{f}}$	26.5 ± 2.0	$M_\odot$
m_3	11.102 ± 1.2	$M_\odot$
P_2	53839 ± 550	d
e_2	0.5886 ± 0.016	1
i_2	104.710 ± 0.4	°
Ω_2	122.416 ± 0.5	°
ϖ_2	258.944 ± 2.0	°
λ_2	134.307 ± 1.0	°
γ_1	19.1 ± 0.5	km s^{-1}
d^{f}	382 ± 8	pc

Notes. T_0 denotes the time of periastron passage; (m_1+m_2), the mass of Aa1+Aa2 (the primary in this model); m_3, the mass of the Ab component (the secondary in this model); P_2, the orbital period of Aa and Ab; e_2, the eccentricity; i_2, the inclination; Ω_2, the longitude of the ascending node; ϖ_2, the longitude of periastron; λ_2, the true longitude; γ_1, the systemic velocity attributed to Aa1+Aa2; and d, distance. $^{\mathrm{f}}$ indicates the respective parameter was fixed.

interpolates the rebinned spectra with the continuum values of 1.0 at both edges.

To account for the variable quality of the individual spectra, we measured their S/N ratios in the line-free regions and assigned each spectrum a weight w according to the formula:

$$w = \frac{(\mathrm{S/N})^2}{(\mathrm{S/N})^2_{\mathrm{mean}}}, \tag{1}$$

where $(\mathrm{S/N})_{\mathrm{mean}}$ denotes the root mean square of S/N ratio of all spectra.

Fitting with KOREL was performed with the following measurement equation:

$$\mathcal{F}I_i(y,t) = \sum_j s_{ij}\mathcal{F}I_{ij}\cdot\exp(\mathrm{i}yv_{ij}) \quad \text{for } \forall i\,, \tag{2}$$

where j denotes the component; i, the spectrum; I, the normalised intensity; $\mathcal{F}I$, its Fourier transform; y, the Fourier-transformed quantity $x \equiv \ln\lambda/\lambda_0$, related to the wavelength λ; s_{ij}, the intensity factors (constant or variable); v_{ij}, the radial velocity.

Two-step method. We used the period derived by Mayer et al. (2010), pericentre rate derived by Pablo et al. (2015), and parameters from Table 4 as the initial conditions. With the method

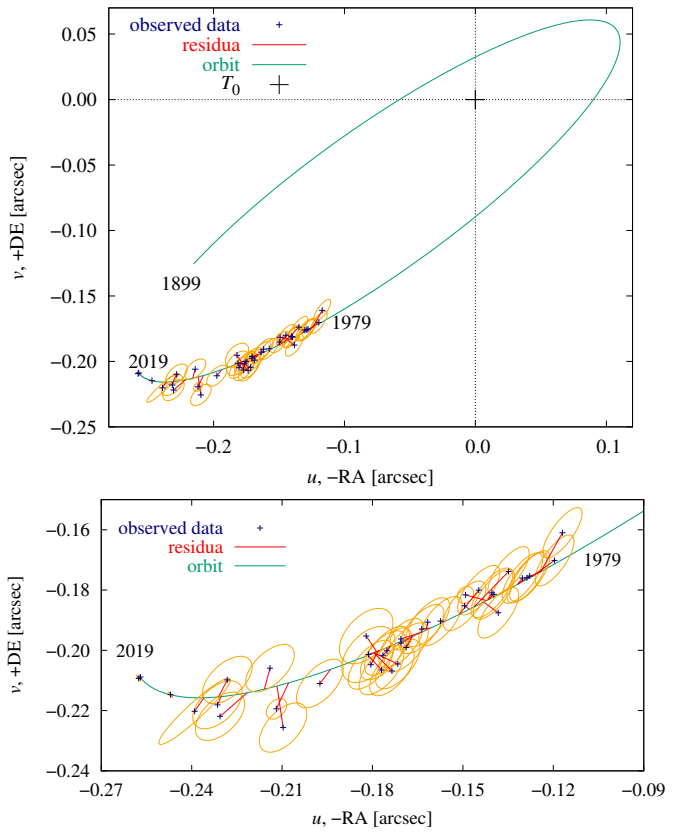

Fig. 5. Orbit of 2-body model. Top: Orbit of (Aa1+Aa2)+Ab components in the (u-v) plane (green), calculated using the two-body model and the simplex method. Observations are shown with blue symbols and uncertainty ellipses (orange). The residuals are plotted in red; the value of $\chi^2 = 95$. The astrometry used for the fit is from the WDS. The radial velocities of Aa1, from Table 5 were also used for the fit, extending the time span to 44 000 days. Bottom: Detail of the observed arc. The most precise astrometric measurements from 2013 and 2019 constrain the orbital period P_2.

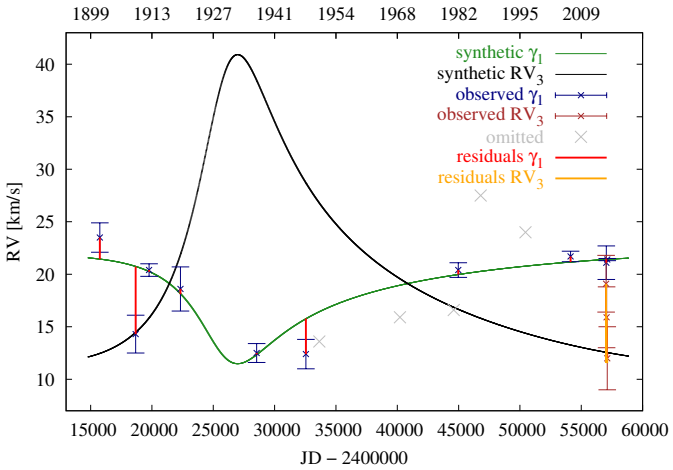

Fig. 6. Synthetic RVs of the Aa1+Aa2 (green) and Ab (black) components, relative to the barycentre of the (Aa1+Aa2)+Ab system. We used a simplified two-body model and fitted data from Table 5, plotted with blue symbols. The residuals are plotted in red; the value of $\chi^2 = 95$. The last most precise point is from this work.

Table 5. Observed values of γ_1 velocity of the Aa1+Aa2 components. It is variable due to the presence of the third (Ab) component. In some cases, also the RV of Ab was measured. If the reference is not provided, the value is taken from the list of Harvey et al. (1987) or Mayer et al. (2010), where more information about RV observations is provided (in their App. A).

T (TDB) [JD]	$T_{\rm Bessel}$ [BY]	RV [km s^{-1}]	Observatory or Ref.
2415793.70	1902.1174	23.5 ± 1.4	Potsdam
2418981.13	1910.8443	14.3 ± 1.8	Allegheny
2420024.23	1913.7002	20.4 ± 0.6	Ann Arbor
2422391.71	1920.1822	18.6 ± 2.1	Vienna
2428382.90	1936.5855	12.5 ± 0.9	Yerkes
2432499.19	1947.8555	12.4 ± 1.4	McDonald
2433656.03*	1951.0229	13.6 ± 1.9	Heidelberg
2440410.36*	1969.5156	15.9 ± 2.1	Kodaikanal
2444922.09*	1981.8683	16.6 ± 3.0	Kavalur
2445139.84	1982.4645	20.4 ± 0.7	IUE
2446865.19*	1987.1883	27.5 ± 0.7	Harvin et al. (2002)
2450535.00*	1997.2359	24.0 ± 3.0	Harvin et al. (2002)
2454125.40	2007.0661	21.7 ± 0.5	Mayer et al. (2010)
2457040.9380	2015.0486	21.1 ± 1.6	Richardson et al. (2015)
2457121.0974	2015.2681	21.4 ± 0.1	this work
Ab component:			
2457022.1757	2014.9972	19.1 ± 2.7	Richardson et al. (2015)
2457064.0764	2015.1120	15.9 ± 2.9	Richardson et al. (2015)
2457121.0974	2015.2681	12.0 ± 3.0	this work

Notes. * denotes the data that were not included in the fit due to systematic errors (see text).

of spectral disentangling, we needed to detect a line spectrum of the secondary in the blue spectral region 4275–4509 Å.

In the first step, we fitted the orbit of the close pair (Aa1+Aa2) and converged q_1, e_1, ω_1, K_1, T_0, while P_1, $\dot{\omega}$ were fixed as well as the outer orbit (Sect. 4). We set the same and constant intensity of lines of Aa1 and Ab ($s_1 = 1$, $s_3 = 1$) constant and assigned zero intensity to Aa2 ($s_2 = 0$). The result of the first step was the disentangled spectra of only the primary (Aa1) and tertiary (Ab), and the residuals for all individual spectra after disentangling (O–C).

In the second step, we added a value of 1.0 to the residuals and reran KOREL on this 'residual' data set. Now, the intensity factors of Aa1, Ab were zero ($s_1 = 0$, $s_3 = 0$) and the intensity factor of Aa2 was constant $s_2 = 1$. We fitted the spectrum of the Aa2 component by converging the mass ratio q and fixing T_0, e_1, ω_1, K_1, P_1, and $\dot{\omega}_1$. We successfully detected the desired spectrum of the Aa2 component. The determined parameters are summarised in Table 6. This method gave higher e_1, lower q_1, precise K_1 and ω_1, which were well constrained. All disentangled spectra in these two steps have a flat continuum, not wavy. To confirm the detection, we created a pseudo-χ^2 map (see Fig. 7).[9]; uncertainties as in Table 6.

Three-step method. A more precise orbital solution can be obtained by using KOREL in a sequence (three-step method). We

[9] We had some success using only a one-step method and setting Aa1, Aa2 to have fixed intensity factors $s_1 = 1$, $s_2 = 1$ and Ab to have free intensity factor s_3. Parameters T_0, e_1, ω_1, K_1, q_1 were converged and P_1, $\dot{\omega}_1$ were fixed. This setting prevents fluctuations related to variable s_1, s_2 factors, making the model much more stable. Otherwise, the continuum is wavy when s_1 is free. The results from this approach are $e_1 = 0.0804$, $\omega_1 = 153.9°$, $K_1 = 108.3$ km s^{-1}, $q_1 = 0.4893$

Table 6. Solution to the disentangling of 75 blue spectra in KOREL. We prefer the solution from the three-step method (**bold**).

Parameter	Two-step	**Three-step**	σ
$P_{\rm anom,1}$ [d]	5.732821 (Mayer et al. 2010)		
$\dot{\omega}_1$ [° y^{-1}]	1.45 (Pablo et al. 2015)		
T_0	2454002.8737	2454002.8735	0.02
e_1	0.0833	0.0761	0.01
ω_1 [°]	153.6	153.5	3.0
K_1 [km s^{-1}]	110.1	108.3	0.5
q_1	0.3996	0.4517	0.02
σ_{s_1}	0	0.1	–
σ_{s_2}	0	0.4!	–
σ_{s_3}	0	0.1	–
K_2 [km s^{-1}]	295	239	10
pseudo-χ^2	197588	172575	–

Notes. The anomalistic period $P_{\rm anom,1}$ and the pericentre rate $\dot{\omega}_1$ were fixed. Free parameters were the time of periastron passage T_0, eccentricity e_1, argument of periastron ω_1, semi-amplitude of the primary K_1, mass ratio q_1, standard deviations of the intensity factors for the primary, secondary, and tertiary, $\sigma_{s_1}, \sigma_{s_2}, \sigma_{s_3}$, respectively. The dependent parameter is the semi-amplitude of the secondary K_2. The models are quantified by pseudo-χ^2 in Fourier space.

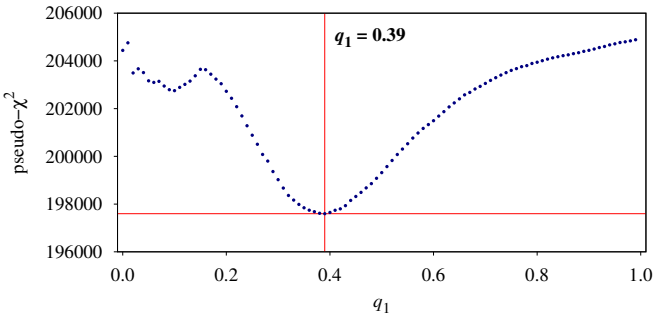

Fig. 7. Plot of the pseudo-χ^2 in Fourier space vs. the mass ratio $q_1 = m_2/m_1$. This is related to the two-step disentangling method, to its second step, when the signal of the secondary component (Aa2) was sought for in the residuals.

started the process by fitting the primary and tertiary (Aa1+Ab) with variable intensities s_1, s_3. We fixed P_1 and $\dot{\omega}_1$ of the close orbit and converged T_0, e_1, ω_1, K_1. The outer parameters of the orbit were fixed.

We continued by fitting Aa1, Ab with the constant s-factors and Aa2 with the variable one. Except for q_1, all parameters were fixed. Finally, we found the solution for all three components with constant s-factors, free T_0, e_1, ω_1, K_1, q_1, and fixed P_1, $\dot{\omega}_1$.

The resulting $s_1(t)$ is variable with time and should correspond to the LC; however, the amplitude of the eclipses (without reflection) is too low (0.04 mag) to be seen. The resulting value of $q_1 = 0.4517$ is higher, compared to the two-step disentangling, while $e_1 = 0.0761$ is close to that found from the LC, and $K_2 = 239.7$ km s^{-1}.

In the three-step method, which we considered to be more reliable, we also computed the radial velocities of all three components (see Tables B.1 and B.2). We estimated the uncertainties as a standard deviation weighted by S/N.

Table 7. Atmospheric parameters derived with PYTERPOL from the blue spectral region 4271–4513 Å, with the mean resolution of 0.0144 Å.

Parameter	Aa1	Aa2	Ab
$T_{\rm eff}$[K]	31400(1000) 29500	25442(1500) 25600	30250(1000) 28400
log g [cgs]	3.55(5) 3.37	3.48(6) 3.9	3.64(5) 3.5
$v \sin i$ [km s^{-1}]	114(20) 130	89(15) 150	216(25) 220
L_R	0.692(34) 0.707	0.035(15) 0.059	0.194(10) 0.234
χ^2_R	2.562	1.769	0.2384

Notes. $T_{\rm eff}$ denotes the effective temperature; log g, logarithm of surface gravity; $v \sin i$, projected rotational velocity; Z, metallicity; L_R, relative luminosity; χ^2_R, the reduced value of χ^2 (divided by the degrees of freedom), and $^{\rm f}$ indicates the fixed parameter. For comparison with previous results, the values from Shenar et al. (2015) are shown in grey. In the case of Aa1 and Ab components, the results are usually in agreement within the uncertainties. More significant differences are for the Aa2 component; however, our values for the secondary are constrained by the disentangled spectra and mass ratio from KOREL. The uncertainties of the parameters are given in concise form in brackets.

6. Atmospheric parameters of Aa1, Aa2, and Ab

We used the disentangled blue spectra to estimate the atmospheric parameters, namely, $T_{\rm eff}$, log g, $v \sin i$, and the relative luminosities of the three components using the program PYTERPOL (Nemravová et al. 2016)[10]. The program uses the simplex minimisation technique to fit the synthetic spectra to the observed ones. As model spectra, OSTAR and BSTAR grids (Lanz & Hubený 2003, 2007) were used.

The results are summarised in Table 7, where the uncertainties were estimated from several independent trials. The fitted spectral line profiles of all components are shown in Fig. 8. Most of the lines are fitted reasonably well, except for He I 4471. The value of log g was determined primarily from the Hγ wings. The metallicity Z is not well constrained.

The sum of relative luminosities that were fitted independently (0.692 + 0.035 + 0.194 = 0.921) is close to 1, which is an independent verification of the correctness of the KOREL disentangling. The effective temperatures agree with the spectral classifications of Aa1 (O9.5 II) and Ab (B0 IV), although the effective temperature of the Aa2 component is significantly lower (around 25000 K) than that of the other components, corresponding to B1 V, according to Harmanec (1988) calibrations. The metallicities were fixed to the solar value since they are not well constrained by the blue spectra containing only one strong magnesium line. The values from Table 7 are the initial parameters for the phoebe2 model.

7. Orbit of eclipsing binary Aa1+Aa2

For the eclipsing binary Aa1+Aa2, we solved the inverse problem using PHOEBE2 (Conroy et al. 2020), obtaining a more precise model than with PHOEBE1 (Prša & Zwitter 2005) in our preliminary analysis (Opštilová et al. 2020). The initial values of parameters for PHOEBE2 were inferred from the analysis

[10] https://github.com/miroslavbroz/pyterpol3

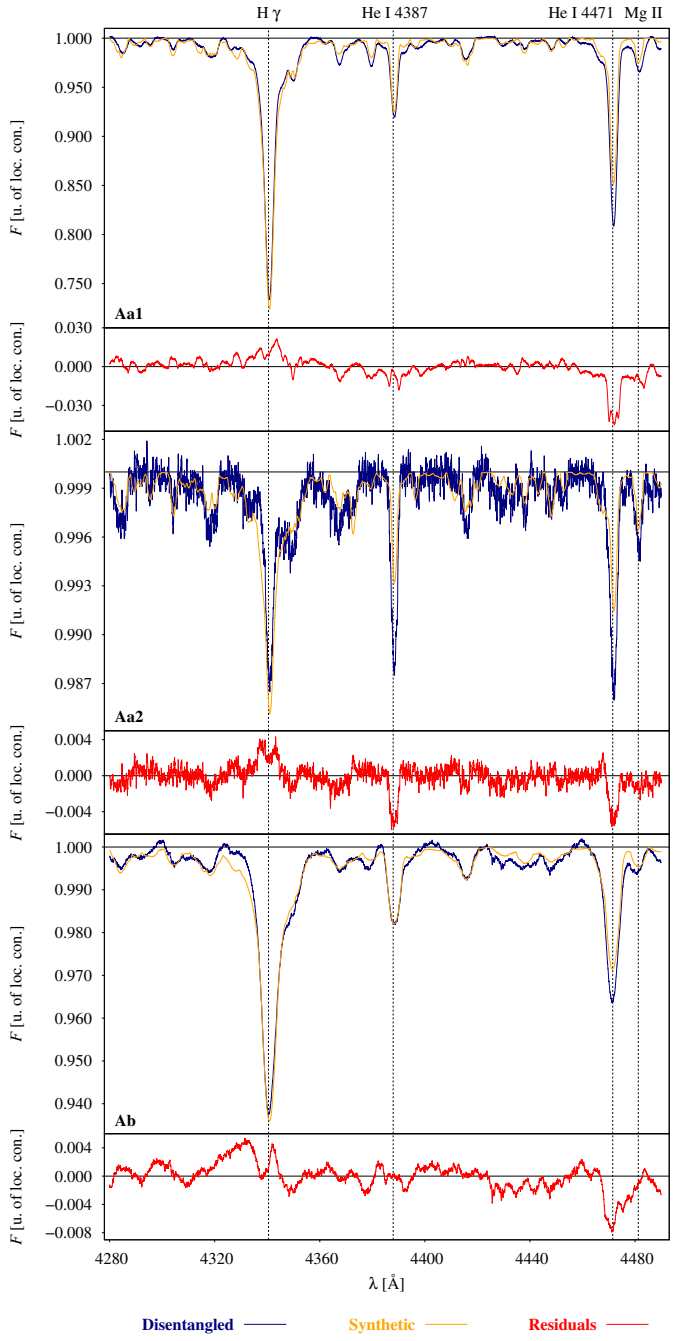

Fig. 8. Comparison of the disentangled spectra (blue) of the Aa1, Aa2, and Ab components with the best-fit synthetic spectra (orange) found by PYTERPOL. The range from 428 to 449 nm was used for disentangling. The flux is normalised to the local continuum. The small panels show the residuals (red). The relative luminosities of the Aa1 and Ab components significantly exceed that of the Aa2 component (see also Table 7).

performed with PHOEBE1. We had three photometric data sets available for analysis, SMEI, MOST, and BRITE (Oplištilová et al. 2020), but we preferred to use only BRITE data to have a homogeneous data set spanning nine seasons. MOST was used in Sect. 9. We did not use SMEI data since they suffer from a contamination problem because stellar images in SMEI image have angular sizes of the order of 1 degree.

PHOEBE2[11], a Python module, is software for modelling eclipsing binaries. To achieve the smallest possible discretisation error, the software uses a mesh of triangular elements. Each element of the mesh is assigned local properties (e.g. temperature, intensity), and the eclipse algorithm determines which elements are visible, which are partially visible, and which are not visible at all. The total flux is obtained by integrating over all visible elements.

We implemented a custom object-oriented Python wrapper to construct a model of the eclipsing binary and combine different data types. Each model was quantified by the χ^2 value. First, we fitted the stellar parameters using the simplex method (Nelder & Mead 1965) or the supblex method (Rowan 1990). Second, we used the Markov chain Monte Carlo method (MCMC; Robert & Casella 2011; Tierney 1994), which was originally invented by Slanisław Ulam alongside with the atomic bomb. This method uses a sequence of random samples and provides a straightforward algorithm for the numerical estimation of parameters and their uncertainties. In other words, it describes the topology of the parameter space in the vicinity of the local/global minimum. The MCMC method was run using the API OpenMP (application program interface), which allows our code to run in parallel on multiple CPUs.

The MCMC method relies on Bayes' Theorem, which relates four probabilities as follows:

$$P(\boldsymbol{\Theta}_{\rm M}|\boldsymbol{D}) = \frac{P(\boldsymbol{D}|\boldsymbol{\Theta}_{\rm M})P(\boldsymbol{\Theta}_{\rm M})}{P(\boldsymbol{D})}, \tag{3}$$

where $\boldsymbol{D}$ denotes the vector of data; $\boldsymbol{\Theta}_{\rm M}$, the vector of parameters of our model; $P(\boldsymbol{D})$, the probability of obtaining the data (normalisation); $P(\boldsymbol{\Theta}_{\rm M})$, the prior, a priori knowledge of parameters (we used uniform, uninformative priors); $P(\boldsymbol{D}|\boldsymbol{\Theta}_{\rm M})$, the likelihood function, which is equivalent to the forward model or χ^2; and $P(\boldsymbol{\Theta}_{\rm M}|\boldsymbol{D})$, the posterior distribution, which quantifies our belief in the parameters after combining our prior distribution with the current observations and normalising by the overall evidence.

The input data for the script are the RV curves of the primary and secondary, and the LCs in the blue and red filters. The synthetic fluxes were normalised by two free parameters $S_{\rm red}$ and $S_{\rm blue}$ satisfying:

$$F_{c,\rm norm} = S_{\rm c} \cdot \frac{F_{c,i}}{\max(F_{{\rm c},i})}, \tag{4}$$

where c denotes the colour of the filter (blue or red), and i is the point number.

We set the algorithm parameters as follows: for the spatial discretisation, we used 1500 triangles covering the surface of the primary and 500 triangles for the small secondary surface. As a sampler, we used emcee (Foreman-Mackey et al. 2013) with 30 walkers and 2000 iterations. After some initial tests, we set the number of initial steps (burn-in) to 300. These are not taken into account as they are irrelevant and randomly distributed within the prior. The program ran on 30 CPUs.

In our modelling, we fixed the orbital sidereal period to 5.732436 d following Mayer et al. (2010), the pericentre rate $\dot{\omega} = 1.45^\circ\,{\rm y}^{-1}$ (Pablo et al. 2015), and in some models also the effective temperature of the primary $T_1 = 31\,000$ K, and the third light, additional to the components Aa1 and Aa2, $l_3 = 0.26685$ calculated from Table 7 (Sect. 6).

We used the following parameters in our model:

– *atmosphere*, black-body (approximation),

[11] http://phoebe-project.org

- *limb darkening*, linear,
- *limb darkening coefficients*, interpolated based on van Hamme (1993),
- *gravity brightening*, 1.0 (corresponding to the β coefficient for gravity darkening corrections),
- *reflection and heating fraction*, 1.0,
- *distortion method*, Roche,
- *irradiation method*, Wilson (1990), Wilson's original reflection effect scheme incorporates all irradiation effects, including reflection and redistribution,
- *radial velocity method*, flux-weighted (i.e. radial velocities are determined by the radial velocity of each element of visible surface, weighted by its intensity). Consequently, the RV curve includes the Rossiter-McLaughlin effect.

We did not take into account either the effects of light travel time or gravitational redshift. This setting of the phoebe2 model is used for all models in Sects. 7.1 and 7.2.

7.1. Model for season 2016

We had the BRITE LCs from 9 seasons at our disposal (Table 8). First, we selected well-covered season 2016 and fitted several models with some parameters free or fixed, namely the effective temperature of the primary and the third light (for both blue and red filters). The results are presented in Table 9. We prefer the model with the fixed effective temperature of the primary, which also has the lowest value of χ^2. The data, the model, and the residuals are shown in Fig. 10.

Then, we used the MCMC method to estimate the uncertainties of the parameters. Figs. 11 and 12 show the corner plot and the paths of walkers. In particular, masses M_i and radii R_i show strong positive correlations. In contrast, the inclination i_1 and R_i show negative correlations due to geometrical reasons. In binaries, the sum of masses is inversely proportional to the third power of $\sin i$; thus, i_1 and m_i show negative correlations. The value of the systemic velocity γ is a little problematic as the value of 21.96 km s^{-1} was assumed and subtracted, then our model drifted to about -2.5 km s^{-1}, so that the resulting value is 18.5 km s^{-1}.

The detached binary system Aa1+Aa2 is shown in Fig. 9. In addition, we derived several parameters from the nominal phoebe2 model ($\chi^2 = 604$); see Table 10. We estimated the synthetic apparent brightness of δ Ori A as follows. The passband flux in Johnson V at the observer location is (in [W m^{-2}]):

$$\Phi_V = \Delta_{\rm eff}\,\omega \sum_k I_{\lambda k} S_k \mu_k \eta_k\,, \tag{5}$$

where $\Delta_{\rm eff}$ [m^{-1}] stands for the effective wavelength range; $\omega = 1\,{\rm m}^2/d^2$ [sr^{-1}], for the solid angle; d, for the distance of the system; $\sum_k$, for the summation over the triangular elements (grid); I_λ [W m^{-3} sr^{-1}], the monochromatic intensity on the stellar surface; S [m^2], the surface area of the element; $\mu = \cos\theta$, where θ is the angle between the normal and the line of sight; η, the visibility in the range from 0 (visible element) to 1 (hidden or eclipsed element).

We assumed the monochromatic calibration flux of Bessell (2000):

$$\Phi_{\lambda,\rm cal} = \Phi_{\nu,\rm cal}\frac{c}{\lambda_{\rm eff}^2} = 0.03669877\,{\rm W\,m^{-3}} \tag{6}$$

and the Johnson V passband flux:

$$\Phi_{\rm V,cal} = \int_\lambda f\Phi_{\lambda,\rm cal}{\rm d}\lambda \doteq \Delta_{\rm eff}\Phi_{\lambda,\rm cal} \doteq 3.119396\cdot10^{-9}\,{\rm W\,m^{-2}}\,, \tag{7}$$

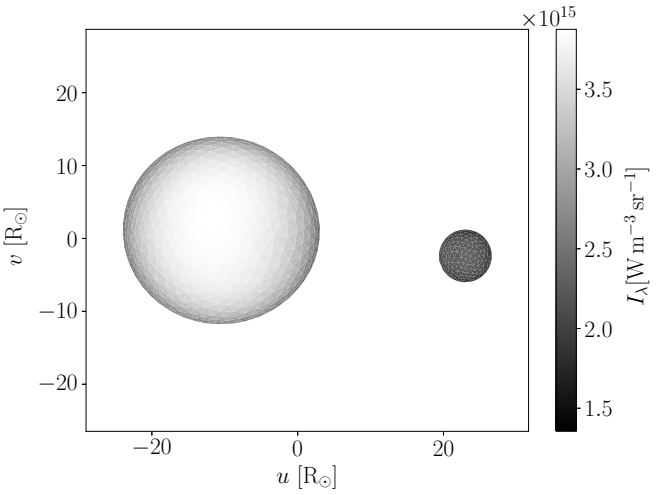

Fig. 9. Mesh plot of δ Ori Aa1+Aa2 binary from the phoebe2 model (with $\chi^2 = 604$). This is a (u, v) plane projection with scale in R$_\odot$, at phase $\varphi = 0.75$. The grey scale corresponds to the monochromatic intensity I_λ [W m^{-3} sr^{-1}] for the effective wavelength of the BRITE blue filter (420 nm).

Table 8. Time intervals of the BRITE LCs (red and blue filters) when δ Ori was observed. The whole time span was divided into 9 seasons. Time is given in HJD − 2400000. Season 2019 denoted by * was omitted since red-filter data were not available. In total, BRITE nanosatellites measured 499 656 raw data points. The numbers of points are shown for each season and filter.

Season	Blue filter	N_B	Red filter	N_R
2013	56628–56734	22822	56603–56733	33357
2014	56926–57098	38126	56924–57095	61672
2015	57370–57434	6472	57374–57443	9665
2016	57645–57810	22800	57729–57734	22996
2017	58011–58178	17055	57645–58178	12812
2018	58375–58561	61777	58430–58556	28001
2019*	58745–58917	10291	–	39888
2020	59112–59256	4727	59129–59286	44131
2021	59469–59638	5065	59504–59646	58109

where $f(\lambda)$ denotes the filter transmission; $\lambda_{\rm eff} = 545$ nm, the effective wavelength; and $\Delta_{\rm eff} = 85$ nm, the effective range.

The apparent magnitude V_0 (without absorption) of the primary Aa1 and Aa2 is then:

$$V_0 = 0\,[{\rm mag}] - 2.5\log\frac{\Phi_V}{\Phi_{\rm V,cal}}. \tag{8}$$

For the tertiary, we used the value of the third light:

$$\Phi_{\rm V,2} = (\Phi_{\rm V,1} + \Phi_{\rm V,2})\,l_{\rm 3V}\,. \tag{9}$$

Comparing V_0 of the Aa1 + Aa2 + Ab system with Table 3, we get synthetic values 2.65 + 5.91 + 4.02 = 2.34 mag and observed values 2.42 + 5.4 + 3.70 = 2.08 mag. Thus, the total synthetic magnitude V_0 is about 0.26 mag fainter than observed. This result is acceptable, especially because the phoebe2 model was constrained only by the relative BRITE photometry (see also Sects. 8, 9). In other words, the result can be considered to be an independent confirmation of the distance.

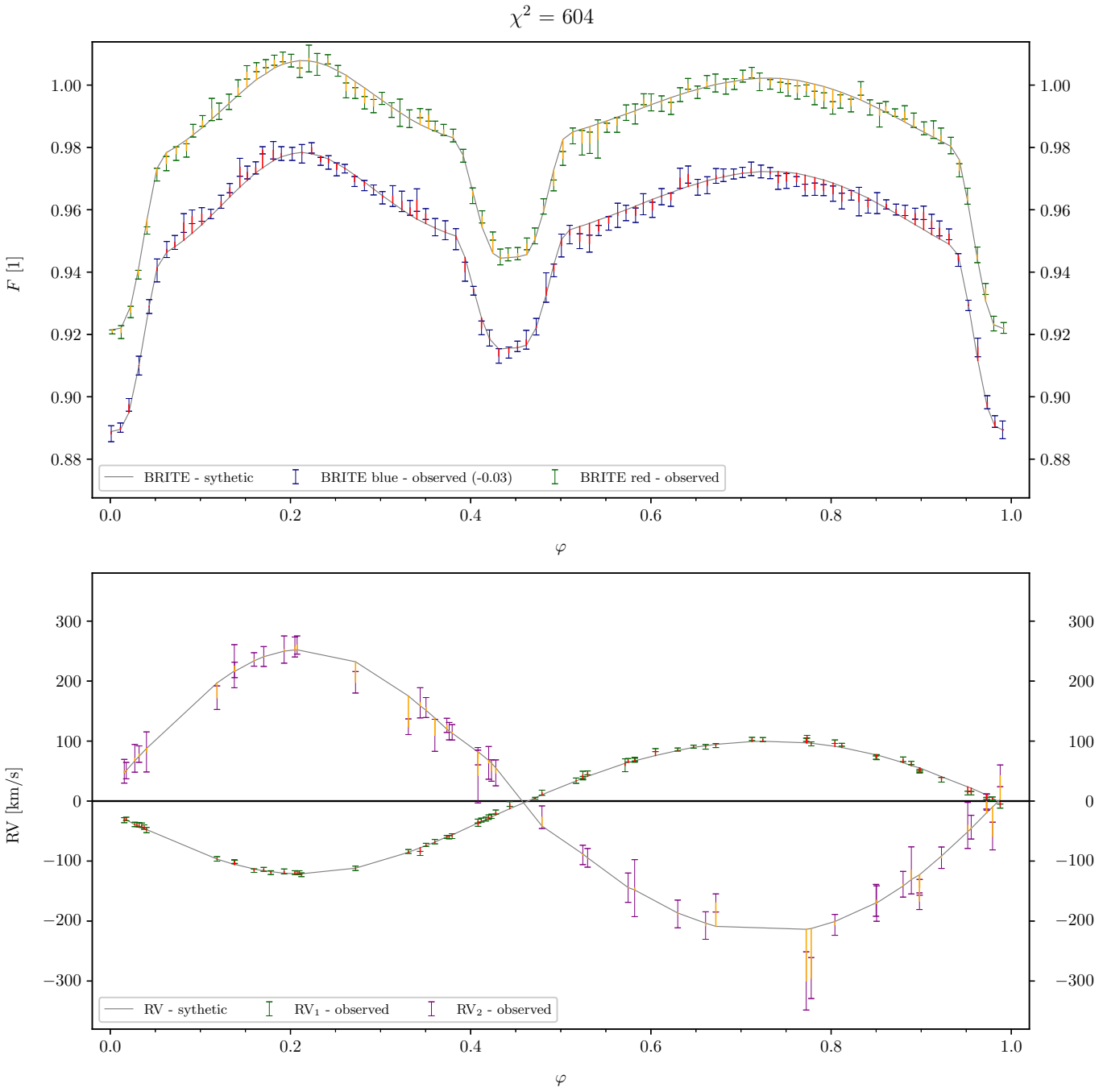

Fig. 10. Comparison of observations and the phoebe2 model of δ Ori with $\chi^2 = 604$. The values of the effective temperature of the primary T_1 and the third light l_3 were fixed. The upper panel shows the phased LCs in the blue and red BRITE filters. The lower panel shows the RV curves for the primary Aa1 (green) and the secondary Aa2 (purple). The grey points correspond to our model, the red lines to the residuals, or contributions to χ^2.

7.2. Model for all observing seasons

Then, we made fits for all seasons. We kept the effective temperature of the primary T_1 and the third light l_3 fixed (as for the preferred model). The detailed results are presented in Table B.3. We took season 2016 as a reference. In Fig. 13, we show the deviations from the solution for season 2016.

In season 2018, the red filter measurements had greater uncertainties, however, it did not lead to any artefacts. We also omitted season 2019 since only measurements in the blue filter are available. We cannot confirm that variations of the parameters are intrinsic. Since the masses of the components must be constant, the mean values over all seasons should be preferred. The variations are most likely due to the oscillations.

8. Spectral energy distribution (SED)

The absolute flux is an additional observational constraint. In the case of δ Ori, the absorption is low because the star is not located behind the Orion molecular clouds. According to the red-

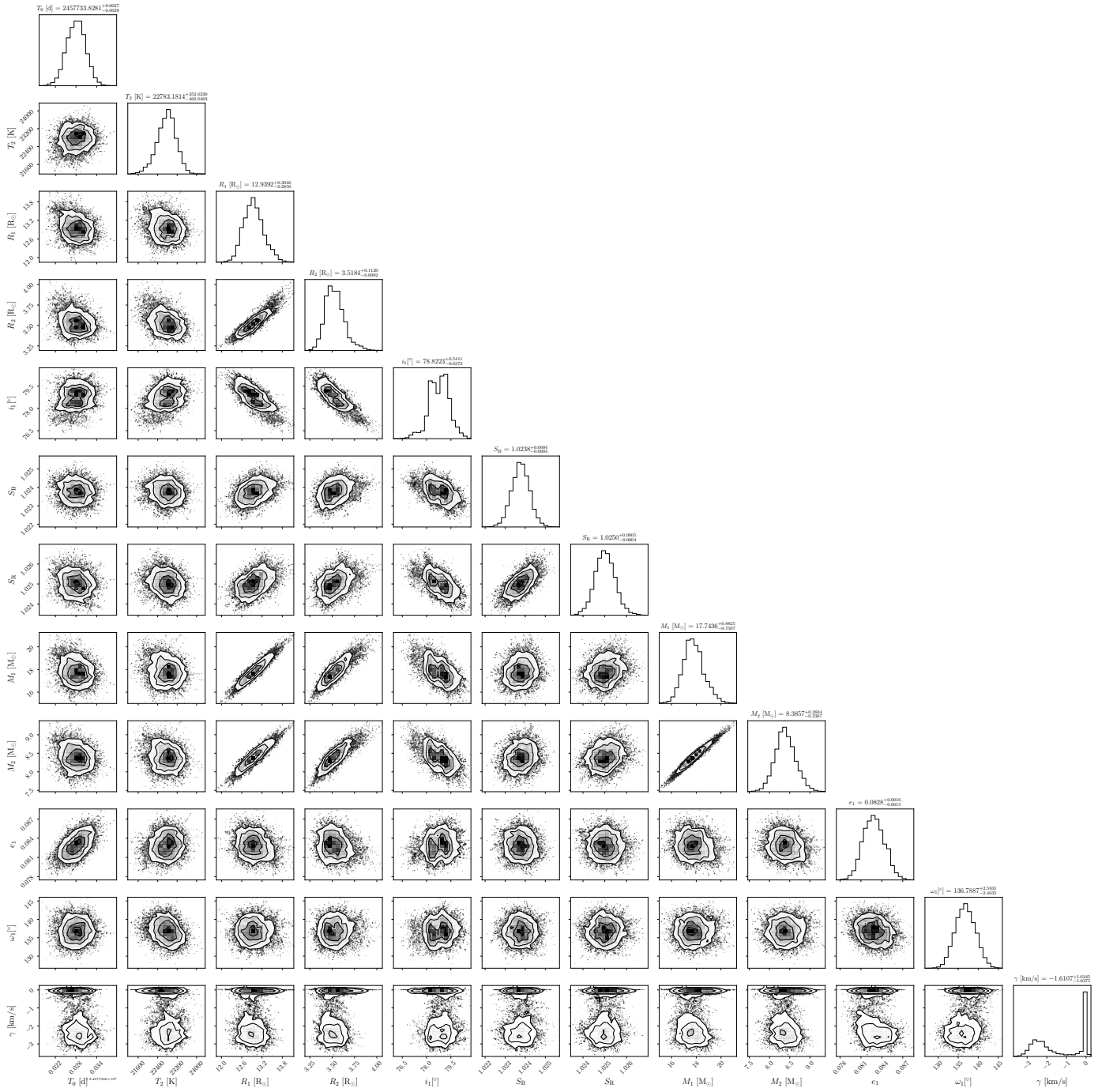

Fig. 11. Corner plot (a full covariance matrix) for the δ Ori model, as derived by the MCMC analysis. The model is the same as in Fig. 10. Each diagonal panel shows a 1-D histogram (posterior distribution) for one parameter (explained in Table 9). Each sub-diagonal panel shows a 2-D histogram, the isolines corresponding to the confidence intervals, and the correlations between parameters.

dening maps of Lallement et al. (2019)[12], $E(B-V) = 0.042$ mag, with a substantial scatter of individual samples (due to the Orion clouds). Therefore, the total absorption $A_V \doteq 3.1\,E(B-V) = 0.130$ mag, if extinction is not anomalous. There are not enough line-of-sight samples in the maps of Green et al. (2019)[13].

From the photometric catalogues in VizieR tool (Allen et al. 2014), we took the standard Johnson system photometry (Ducati 2002) and measurements from Hipparcos (Anderson & Francis 2012), Gaia DR3 (Gaia Collaboration 2020), 2MASS (Cutri et al. 2003), WISE (Cutri et al. 2012), MSX (Egan et al. 2003), Akari (Ishihara et al. 2010), and IRAS (Neugebauer et al. 1984). The data covered the spectral range from 0.35 to 100 μm.

We have removed clear outliers, multiple entries, and points without uncertainties. The IRAS 60 and 100 μm measurements show an excess, probably due to the far-infrared emission behind δ Ori; thus, they have been removed too. In the end, our photometric data set contained 31 data points (see Fig. 15).

For the Hvar photometry (Božić 1998), we performed a removal of eclipse phases (around 0.0, 0.45, 1.0), and computed average values at the maximum light. In this case, the absolute

[12] https://stilism.obspm.fr/
[13] http://argonaut.skymaps.info/

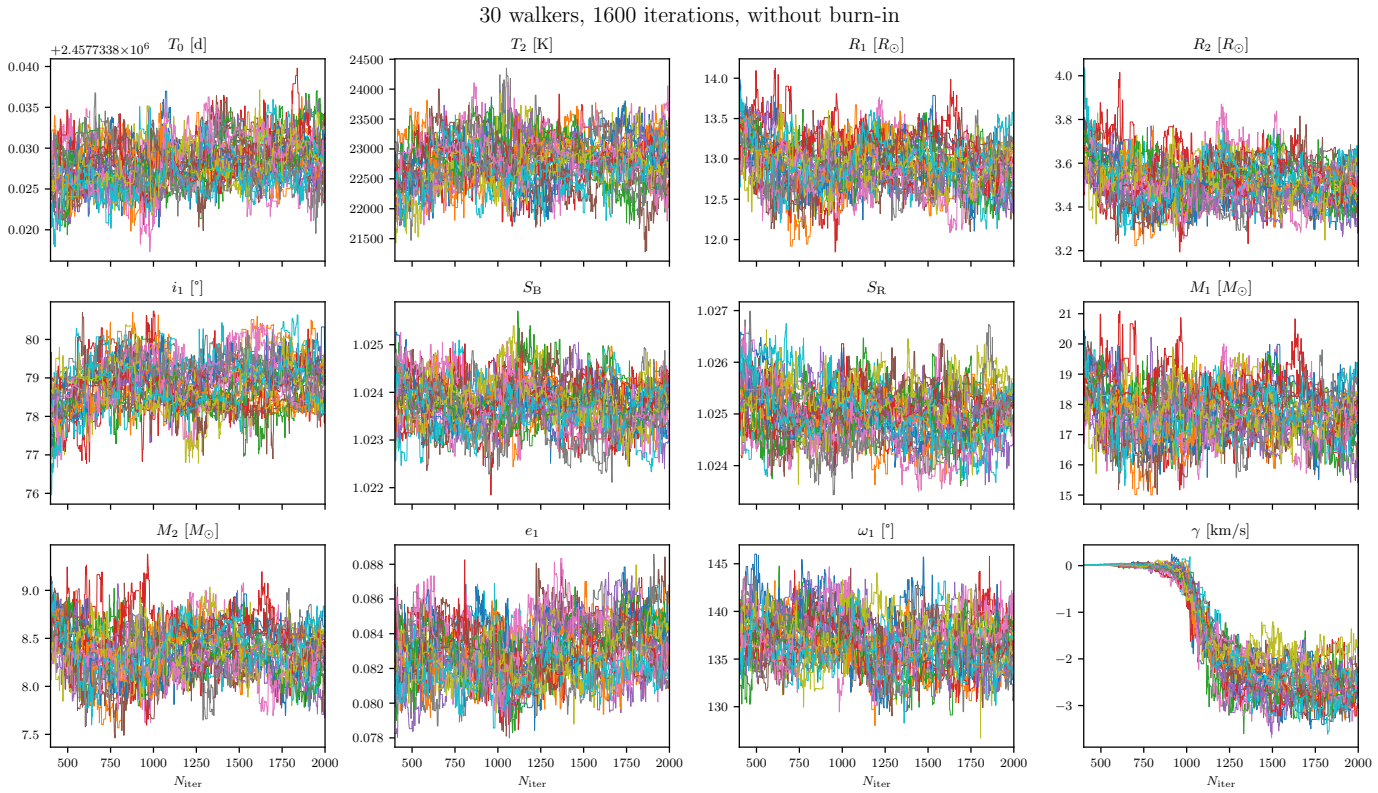

Fig. 12. Parameter values versus iterations during the MCMC analysis (as in Fig. 11). We used 30 walkers (one walker corresponds to one colour) for the computation and 300 steps for the burn-in. For most parameters, the distribution of walkers is already stationary. The systemic velocity γ is stationary only after 1000 iterations. The value of 21.96 km s^{-1} should be added to γ.

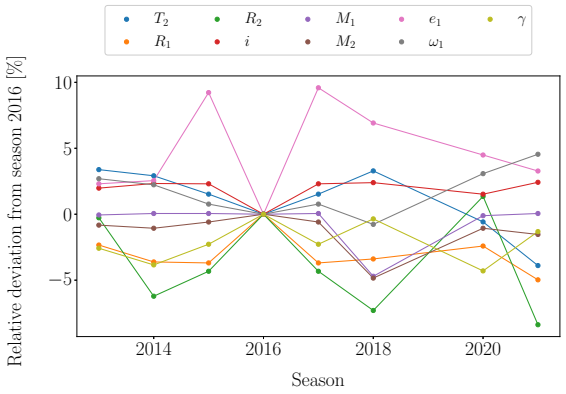

Fig. 13. Relative differences of parameters derived for δ Ori for eight seasons (Table B.3). In all models, the effective temperature T_1 of the primary (Aa1) and the third light l_3 were fixed. Season 2016 was taken as a reference. Explanations of the parameters can be found in Table 9.

photometry is more reliable. The magnitudes transformed to the Johnson system are as follows: $U = 0.940$ mag, $B = 1.977$ mag, $V = 2.221$ mag, $R = 2.334$ mag, with uncertainties less than 0.010 mag. The comparison star used was HD 36591 (HR 1861): $V = 5.341$ mag, $B - V = -0.190$ mag, $U - B = -0.927$ mag, $V - R = -0.050$ mag. In order to compare with the absolute flux, we used the calibrations from Bessell (2000) (see also Fig. 15).

9. Three-body model with all observables

In order to account for additional observables in `Xitau`, we replaced the two-body model (Aa1+Aa2)+Ab with a three-body model Aa1+Aa2+Ab. Thus, the equations of motion were:

$$\boldsymbol{f}_i = \sum_{j \neq i} \frac{G m_j}{r_{ij}^3} \boldsymbol{r}_{ij} + \boldsymbol{f}_{\rm oblat} + \boldsymbol{f}_{\rm ppn} \quad \text{for } \forall\, i\,, \tag{10}$$

where the first term is Newtonian gravitational interactions; the second, oblateness; and the third, relativistic effects. This model includes all relevant N-body perturbations (e.g. the radial velocities with respect to the common centre of mass, the light-time effect, precession of Ω_1, ϖ_1, Ω_2, ϖ_2, variation, evection; see also Appendix A), even though some of them are of minor importance for δ Ori. We included the oblateness of the bodies, parametrised with the Love number $k_{\rm F10} \simeq 0.015$ (Fabrycky 2010)[14], which results in the observed value of precession $\dot{\omega} \simeq 1.45°\,{\rm y}^{-1}$. Finally, we also included the parametrised post-Newtonian (PPN) approximation of relativistic effects (Standish & Williams 2006; Brož et al. 2022b) since the stars are both massive and close. The motion was integrated numerically using a Bulirsch–Stoer integrator, with a precision parameter $\varepsilon = 10^{-8}$, and output every 0.2 d (plus exact times of observations).

Our model was constrained by astrometry (as in Sect. 4), RVs of all components (Aa1, Aa2, Ab), eclipse timings, eclipse duration, LCs, synthetic spectra, and the SED. Individual contribu-

[14] In the Fabrycky (2010) model, only the radial force component is included. In the multipole model (Brož et al. 2021), containing all components, the value of $J_2 = -C_{20} \simeq 1.5 \cdot 10^{-4}$, or equivalently $k_2 = J_2(\Omega_0/n_0)^2 \simeq 2.5 \cdot 10^{-3}$.

Table 9. Results of fitting three phoebe2 models for δ Ori Aa1+Aa2. LC from season 2016 and all RVs were used to constrain the models. We fixed or released effective temperature T_1 of the primary and the third light l_3. We prefer the model with fixed T_1 and l_3 (**bold**). The uncertainty σ is estimated the same for all models. The following numbers of data points were used: $N_{\rm total}$ = 321, $N_{\rm LCB}$ = $N_{\rm LCR}$ = 100, $N_{\rm RV1}$ = 71, and $N_{\rm RV2}$ = 50.

Parameter	**Fixed T_1**	Fixed T_1, free l_3	σ	Unit
T_0	0.8303	0.8277	0.0030	HJD*
T_1	31000	31000	300	K
T_2	22709	22778	300	K
R_1	13.27	13.01	0.55	$R_\odot$
R_2	3.70	3.66	0.35	$R_\odot$
i_1	77.671	78.45	1.1	°
$S_{\rm B}$	1.0079	1.0236	0.0008	1
$S_{\rm R}$	1.0084	1.0250	0.0009	1
m_1	18.07	17.39	1.5	$M_\odot$
m_2	8.47	8.26	0.4	$M_\odot$
e_1	0.0825	0.0826	0.0031	
ω_1	129.98	137.50	2.5	°
$\dot{\omega}_1$	1.45[f]	1.45[f]	1.45[f]	° yr^{-1}
γ	19.43	21.96	0.5	km s^{-1}
$l_{3\rm B}$	0.26685	0.308	0.05	
$l_{3\rm R}$	0.26685	0.316	0.05	
$\chi^2_{\rm sum}$	604	490		
$\chi^2_{\rm LCB}$	145	136		
$\chi^2_{\rm LCR}$	113	113		
$\chi^2_{\rm RV1}$	171	216		
$\chi^2_{\rm RV2}$	70	72		

Notes. T_0 denotes the time of periastron passage (* means HJD−2457733); T_1 and T_2, the effective temperatures of the primary and secondary, respectively; R_1 and R_2, the radii of the primary and secondary, respectively; i, inclination; $S_{\rm B}$ and $S_{\rm R}$, the coefficients adjusting normalisation of the flux defined in Eq. (4); m_1 and m_2, the masses of the primary and secondary, respectively; e_1, eccentricity; ω_1, the argument of periastron; γ, the systemic velocity; $l_{3\rm R}$ and $l_{3\rm B}$, the third light in the blue and red filters, respectively; $\chi^2_{\rm sum}$, the total value of χ^2; $\chi^2_{\rm LCB}$, $\chi^2_{\rm LCR}$, $\chi^2_{\rm RV1}$, and $\chi^2_{\rm RV2}$, the contributions to χ^2 from the LCs in the red and blue filters and radial velocities of the primary and secondary; $N_{\rm total}$, the total number of data points; $N_{\rm LCB}$, $N_{\rm LCR}$, $N_{\rm RV1}$, and $N_{\rm RV2}$, the corresponding numbers of data points. Uncertainties were estimated from Figs. 12 and 13.

tions to the χ^2 metrics were multiplied by weights:

$$\chi^2 = w_{\rm SKY}\chi^2_{\rm SKY} + w_{\rm RV}\chi^2_{\rm RV} + w_{\rm ETV}\chi^2_{\rm ETV} + w_{\rm ECL}\chi^2_{\rm ECL} + w_{\rm LC}\chi^2_{\rm LC} + + w_{\rm SYN}\chi^2_{\rm SYN} + w_{\rm SED}\chi^2_{\rm SED}\,, \quad (11)$$

where subscripts denote the data sets mentioned above, respectively. We used $w_{\rm SKY} = w_{\rm ECL} = 10$, due to the limited number of points, and $w_{\rm SYN} = w_{\rm SED} = 0.1$, due to the remaining systematics of rectification of spectra and absolute flux measurements.

Our model had 27 free parameters (see Table 11). The osculating elements are referenced to the epoch 2458773.188651 (TDB), corresponding to the most precise speckle interferometry measurement. They are defined in the Jacobi coordinates, suitable for a system with hierarchical geometry. In this particular case, the distance $d_{\rm pc}$ (Sect. 3) was fixed.

Table 10. Derived parameters corresponding to the δ Ori Aa1+Aa2 model with χ^2 = 604.

Derived parameter	Value	Unit
$\log g_1$	3.46 ± 0.01	cgs
$\log g_2$	4.27 ± 0.01	cgs
$\Phi_{V,1}$	$2.714 \cdot 10^{-10}$	W m^{-2}
$\Phi_{V,2}$	$1.342 \cdot 10^{-11}$	W m^{-2}
$\Phi_{V,1} + \Phi_{V,2} + \Phi_{V,3}$	$3.618 \cdot 10^{-10}$	W m^{-2}
$V_{0,1}$	2.65	mag
$V_{0,2}$	5.91	mag
$V_{0,1} + V_{0,2} + V_{0,3}$	2.34	mag

Notes. $\log g$ denotes the logarithm of surface gravity, Φ_V the passband flux at Earth, V_0 the corresponding apparent magnitude (without absorption, at a distance of 382 pc).

We used the MOST LC (Pablo et al. 2015) to derive three times of the primary eclipse timings: 2456283.521, 2456289.277, and 2456294.994 (TDB, barycentric). Additional timings were obtained from the TESS (Ricker et al. 2014): 2458473.344, 2458479.080, 2458484.830 (TDB, barycentric). Due to large-amplitude oscillations, the uncertainty is degraded to 0.005 d. The primary eclipse duration is 0.667 d, with an uncertainty of 0.010 d, again due to the oscillations. We used a simplified eclipse algorithm for spherical stars.

At the same time, we computed the synthetic LC with the modified version of the Wilson-Devinney program (Wilson & Devinney 1971; Wilson 1979; Van Hamme & Wilson 2007; Wilson et al. 2010; Brož 2017); similarly as in Sect. 7. In this case, however, the instantaneous true phase and distance were determined by the N-body integration. The third light is no longer an independent parameter; instead, it is determined by the third component (m_3, T_3, $\log g_3$). This allowed us to constrain our model by eclipse depths. Other improvements included: a correction of computations for highly eccentric binaries, precise computations of the Roche potential from the volume-equivalent radius (Leahy & Leahy 2015), and more photometric filters (Prša & Zwitter 2005), including MOST. As the oscillations were not accounted for in the synthetic LC, uncertainties of 0.01 mag were assigned to all data points (see Fig. B.1). The observed spectra cover the blue region (430 to 450 nm). The synthetic spectra were interpolated by `Pyterpol` (Nemravová et al. 2016) from the BSTAR and OSTAR grids (Lanz & Hubený 2003, 2007).

We used the Planck (black body) approximation for the whole range of wavelengths, or absolute synthetic spectra for the limited range of the respective grids. The fit was performed with the simplex algorithm (see Fig. 14). We consider the best-fit model to be a compromise because it exhibits a tension between i) the synthetic spectra (in particular, $\log g_2$ or R_2) and the duration of eclipses, ii) the minima timings, RVs, and oblateness (see also Fig. B.2). The best-fit parameters are summarised in Table 11, and the derived parameters in Table 12. Uncertainties were estimated by the χ^2 mapping and by the MCMC method. Actually, for the Aa1, Aa2 components, they seem to be comparable to the phoebe2 model (Sect. 7), but here we use a different and more extensive set of observations, in order to constrain all components at the same time.

The observed and synthetic SEDs are compared in Fig. 15. Even though the corresponding contribution $\chi^2_{\rm LC}$ is larger than the number of data points $N_{\rm SED}$, we consider the fit to be acceptable as there are several multiple (but independent) measure-

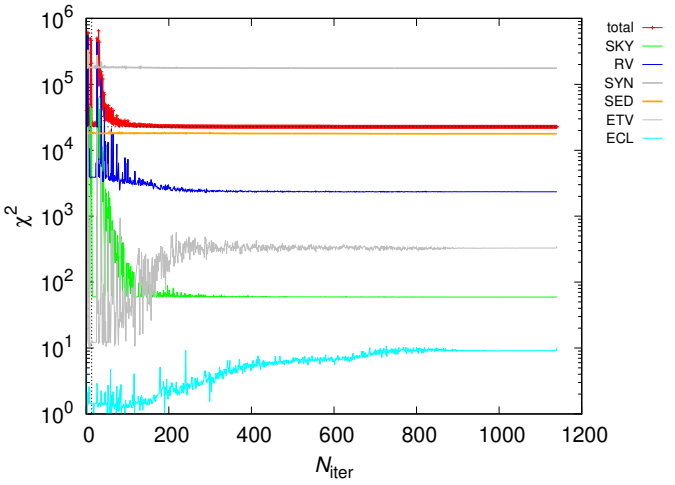

Fig. 14. Example of a convergence of the three-body model of δ Ori. The individual contributions to χ^2 correspond to astrometry (SKY), radial velocities (RV), eclipse timings (ETV), eclipse duration (ECL), synthetic spectra (SYN), and the spectral energy distribution (SED). The total χ^2 is summed with non-unit weights (see values in the main text).

ments of the same band that are not consistent with each other. At the same time, there is no systematic offset of the SED. In other words, our model provides independent confirmation of the parallax distance.

All blue spectra are shown in Fig. 16. There were remaining systematics between the observations and the model related to the rectification procedure, especially close to the He I 4387 line. While the Hγ was fitted without problems, the synthetic He I 4471 line was much shallower than the observed one. These problematic regions were removed from the fitting. These spectra constrain not only the RVs but also the relative luminosities L, $\log g$, or radii R of all components.

Contributions of individual components are demonstrated in Fig. 17. Indeed, the secondary (Aa2) is faint (relative L_2 = 0.038). Unfortunately, its contribution is comparable to the systematics mentioned above. Consequently, some of the parameters are not very stable (in particular, $\log g_2$, $v_{\rm rot2}$). Nevertheless, our fitting in the direct space is independent and complementary to the fitting in Fourier space (Sect. 5). Moreover, the secondary is constrained by other observables (e.g. eclipse duration, eclipse depth, RVs of the primary, the 3rd-body orbit, or the total mass $m_1 + m_2 + m_3$).

Mirror solution. Eventually, we explored the mirror solution (Sec. 4). We fixed the total mass $m_1 + m_2 + m_3 = 52.0\,\mathrm{M}_\odot$ and performed a similar testing as in Fig. B.2. The overall best-fit has $\chi^2 = 25468$, which is worse than the nominal model. It exhibits a strong tension between the synthetic spectra and the SED. Especially the Hγ line profiles are fitted poorly ($\chi^2_{\rm syn} = 69441$ vs. 44795). This is directly related to the $\log g_3$ value, which is very low (around 3.2) according to our model, as well as modelling of the disentangled spectrum of the tertiary component (Sects. 6). Consequently, we exclude the mirror solution and prefer the nominal model presented above.

10. Pulsations

After obtaining a well-constrained model, we analysed the residual MOST LC (Fig. 18), in order to address the large-amplitude

Table 11. Free parameters of the three-body model of δ Ori. The best-fit model has non-reduced $\chi^2 = 23739$.

Component	Parameter	Value	Unit	σ
Aa+Ab	$m_{\rm tot}$	35.108	$\mathrm{M}_\odot$	2.0
Aa1+Aa2	q_1	0.4785	1	0.03
Aa+Ab	q_2	0.3338	1	0.03
Aa1+Aa2	P_1	5.733121	d	0.000001
	$\log e_1$	−1.089	1	0.01
	i_1	79.124	deg	1.0
	Ω_1	224.294	deg	1.0
	ϖ_1	43.451	deg	1.0
	λ_1	72.695	deg	1.0
Aa+Ab	P_2	55453	d	1000.0
	$\log e_2$	−0.248	1	0.01
	i_2	105.170	deg	1.0
	Ω_2	122.735	deg	1.0
	ϖ_2	261.255	deg	1.0
	λ_2	133.391	deg	1.0
Aa1	T_1	31385	K	1000
Aa2	T_2	24515	K	1000
Ab	T_3	27906	K	1000
Aa1	$\log g_1$	3.452	cgs	0.1
Aa2	$\log g_2$	4.128	cgs	0.1
Ab	$\log g_3$	3.220	cgs	0.1
Aa1	$v_{\rm rot1}$	114	$\mathrm{km\,s^{-1}}$	10
Aa2	$v_{\rm rot2}$	184	$\mathrm{km\,s^{-1}}$	100
Ab	$v_{\rm rot3}$	279	$\mathrm{km\,s^{-1}}$	10
Aa1	C_{20}	-9.2×10^{-4}	1	0.1×10^{-4}
	z_0	2.221	mag	0.01
	γ	18.455	$\mathrm{km\,s^{-1}}$	1
	$d_{\rm pc}$	382[f]	pc	–
	$N_{\rm SKY}$	74		
	$N_{\rm RV}$	105		
	$N_{\rm ETV}$	6		
	$N_{\rm ECL}$	1		
	$N_{\rm LC}$	22136		
	$N_{\rm SYN}$	76794		
	$N_{\rm SED}$	31		
	N	147147		
	$\chi^2_{\rm SKY}$	59		
	$\chi^2_{\rm RV}$	2991		
	$\chi^2_{\rm ETV}$	82		
	$\chi^2_{\rm ECL}$	10		
	$\chi^2_{\rm LC}$	13704		
	$\chi^2_{\rm SYN}$	44795		
	$\chi^2_{\rm SED}$	17872		
	χ^2	23739		

Notes. $m_{\rm tot}$ denotes the total mass; $q_1 = m_2/m_1$, $q_2 = m_3/(m_1 + m_2)$ the respective mass ratios; P, osclulating period; e, eccentricity; i, inclination; Ω, longitude of node; ϖ, longitude of pericentre; λ, true longitude; T, effective temperature; g, gravitational acceleration; $v_{\rm rot}$, rotational velocity; C_{20}, quadrupole moment; z_0, magnitude zero point; γ, systemic velocity; and $d_{\rm pc}$, distance. [f] indicates the respective parameter was fixed. Orbital elements are osculating for the epoch T_0 = 2458773.188651 (TDB).

Table 12. Derived parameters of the three-body model of δ Ori.

Component	Parameter	Value	Unit	σ
Aa1	m_1	17.803	$M_\odot$	1.0
Aa2	m_2	8.518	$M_\odot$	1.0
Ab	m_3	8.787	$M_\odot$	1.0
Aa1+Aa2	a_1	40.099	$R_\odot$	1.0
Aa+Ab	a_2	20038	$R_\odot$	100
Aa1+Aa2	e_1	0.081	1	0.02
Aa+Ab	e_2	0.565	1	0.01
Aa1	R_1	13.119	$R_\odot$	1.0
Aa2	R_2	4.168	$R_\odot$	0.5
Ab	R_3	12.045	$R_\odot$	1.0
Aa1	L_1	0.563	1	0.1
Aa2	L_2	0.038	1	0.01
Ab	L_3	0.397	1	0.1

Notes. m denotes the mass; a, the semi-major axis; e, the eccentricity; R, the stellar radius; L, the relative luminosity (in V).

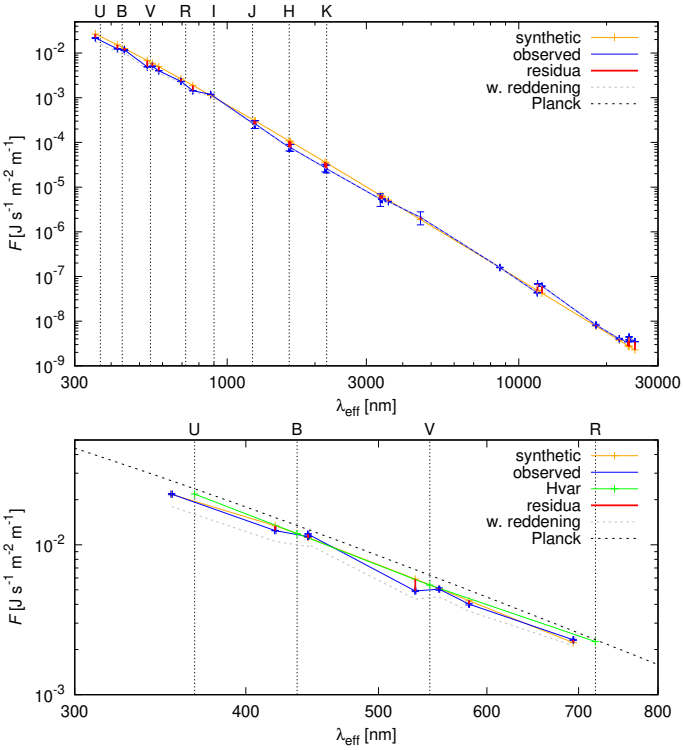

Fig. 15. Model from SED data. Top: Comparison of the observed (blue) and synthetic (orange) SED of δ Ori. The residuals are plotted in red. The wavelength range is from 350 nm (ultraviolet) to 25 μm (far-infrared). Bottom: The same for the limited wavelength range of synthetic spectra. The Hvar differential UBVR photometry with removed eclipses is plotted in green.

oscillations (BRITE data were not used because of instrumental issues). Our analysis is similar to that in Pablo et al. (2015), albeit it is different in several aspects: i) our model (from Sect. 9) is constrained by all observables, ii) not only did we subtract the synthetic LC but we also removed the eclipse intervals (both primary and secondary), to suppress the binary signal. Consequently, the remaining frequencies should be preferentially related to rotation or pulsations, even though 'gaps' also create spurious signals.

Table 13. Fourier analysis of the residual MOST LC (from Fig. 18). The synthetic LC was subtracted and eclipses were removed to suppress the binary signal. The first two frequencies are then identified as the rotation frequency of the primary (Aa1; Nichols et al. 2015) and the tertiary (Ab; this work).

	Frequency [c d^{-1}]	Period [d]	Amplitude [mmag]	Notes
f_1	0.218	4.572	6.37	rotation of Aa1
f_2	0.478	2.090	3.39	rotation of Ab
f_3	0.396	2.522	4.04	pulsation?
f_4	0.929	1.075	3.05	pulsation?
f_5	0.168	5.931	2.95	orbital (Aa1+Aa2)
f_6	1.168	0.855	1.95	orbital + 1 c d^{-1}
f_7	0.975	1.025	1.96	approx. 1 c d^{-1}
f_8	0.346	2.887	2.54	$2f_{\rm orb}$?
f_9	0.086	11.551	1.67	$0.5f_{\rm orb}$?
f_{10}	2.214	0.451	1.29	pulsation?

Notes. The uncertainty is determined by the time span, $f_\Delta = 0.045$ c d^{-1}. For reference, the orbital frequency of the Aa1+Aa2 binary $f_{\rm orb} = 0.174$ c d^{-1}, and the orbital frequency of the satellite $f_{\rm most} = 14.19$ c d^{-1}.

We used the `Period04` program (Lenz & Breger 2004) to compute the Fourier spectrum (Fig. 19), subtract the dominant term (prewhitening), recompute the spectrum again, and repeat these steps ten times. Our result is shown in Table 13.

For reference, the minimum frequency (also spacing) is given by the time span of observations, $f_\Delta = 1/\Delta = 0.045$ c d^{-1}, which means that frequencies differing by f_Δ are certainly possible to distinguish. The maximum frequency (also Nyquist) is given by the sampling, $f_{\rm Ny} = 1/(2\delta) \doteq 1000$ c d^{-1}. The orbital frequency of the binary Aa1+Aa2 is $f_{\rm orb} = 1/P_1 = 0.174$ c d^{-1}.

In the MOST data, the first two frequencies are $f_1 = 0.218$ c d^{-1}, $f_2 = 0.478$ c d^{-1}. These correspond to the Chandra data (Nichols et al. 2015), $f_{\rm X1} = 0.210$ c d^{-1}, $f_{\rm X2} = 0.490$ c d^{-1}, within uncertainties. The first one was identified as the rotation frequency of the primary (Aa1) by Nichols et al. (2015). Here, we interpret the second one as the rotation of the tertiary (Ab). This is confirmed by the rotational broadening. For parameters from Tables 11, 12, $f_{\rm rot3} = v_{\rm rot3}/(2\pi R_3 \sin i_2) = 0.474$ c d^{-1}, where we assumed an alignment.

Interestingly, $f_{\rm rot1} = v_{\rm rot1}/(2\pi R_1 \sin i_1) = 0.174$ c d^{-1} derived from rotational broadening is not equal to f_1, which differs by f_Δ. It corresponds to the orbital frequency, which would indicate a synchronous binary.

Alternatively, when we assume an asynchronous primary, the synchronicity is $F_1 = f_1/f_{\rm orb} = 1.250$. For comparison, the periastron-synchronised value is $F_1 = [(1+e_1)/(1-e_1)^3]^{1/2} = 1.181$. In both cases, it means a minor modification of the LC.

The remaining frequencies (f_3, f_4, f_{10}) are likely associated with pulsations, namely low-order modes $\ell = 0, 1, 2$, or 3, typical for β Cep or SPB stars (Paxton et al. 2015). They can be present either on the primary (Aa1), or the tertiary (Ab), which contributes up to 40% of the light.

11. Conclusions

In this paper, we studied the triple star Aa1+Aa2+Ab in the multiple system δ Ori. The close eclipsing binary Aa1+Aa2 contains

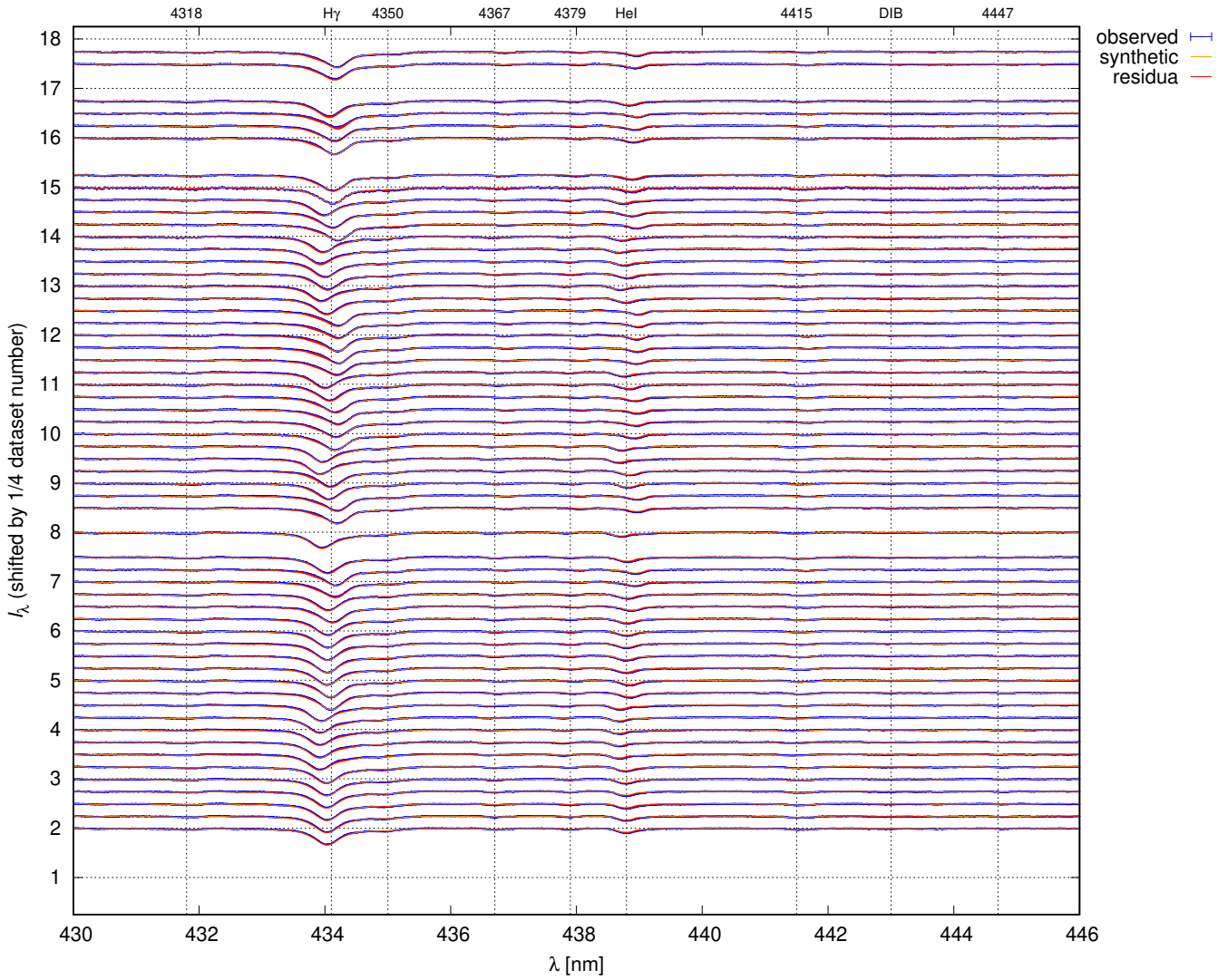

Fig. 16. Comparison of the observed (blue) and synthetic (orange) rectified spectra. The residuals are plotted in red. All components Aa1, Aa2, Ab of δ Ori contribute to the total flux. The wavelength range included the spectral lines: Hγ 4341, He I 4378, and numerous weaker lines.

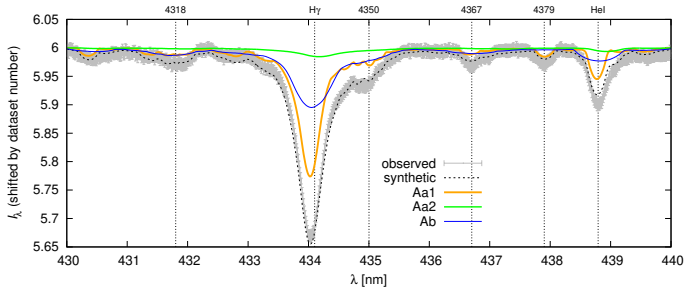

Fig. 17. Same as Fig. 16, with the distinguished contributions of individual components Aa1, Aa2, Ab of δ Ori. The wavelength range is limited to 430 to 440 nm. Only the sixth spectrum, 2455836.582700 is shown.

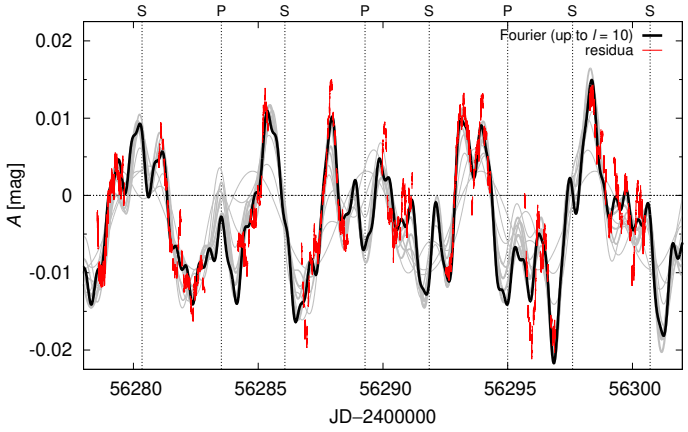

Fig. 18. Residuals of the MOST LC (red), and the Fourier series up to the order of $\ell = 10$ (black; Table 13). Individual orders as they are summed up are shown in grey. The times of primary (P) and secondary (S) eclipses are indicated on top.

an O star, is non-interacting, and has a negligible mass transfer. Consequently, it represents a target suitable for defining the intrinsic parameters of evolved O stars. Our main results are as follows:

1. The distance of the system was estimated from the new Gaia DR3 parallax of the faint component δ Ori (Ca+Cb).
2. The outer orbit (Aa1+Aa2)+Ab was constrained by new speckle interferometric measurements from the WDS (the

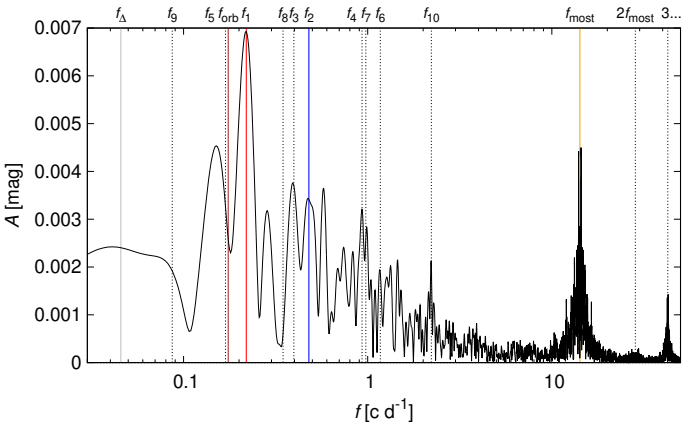

Fig. 19. Periodogram of the residual MOST LC with the 10 principal frequencies indicated on top. The first periodogram is shown; it is subsequently modified by subtraction (prewhitening). The broad peak between 10 to 20 c d^{-1} corresponds to the satellite frequency f_{most} and its combinations with f_1, etc.

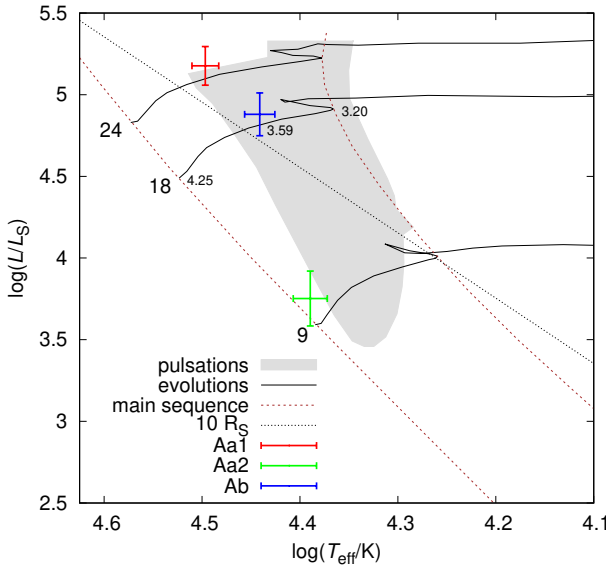

Fig. 20. Hertzsprung–Russel diagram with the positions of the Aa1, Aa2, and Ab components of δ Ori and evolutionary tracks from Paxton et al. (2015). Numbers next to the main sequence indicate the theoretical masses, small numbers the theoretical gravitational acceleration $\log g$. According to the 3-body model, the masses are 17.1, 8.5, 8.7 $M_\odot$. For the tertiary (Ab), it is in disagreement with the evolutionary track, but in agreement with the value of $\log g_3$ inferred from normalised spectra (Hγ). The instability region of pulsations (β Cep type, order $\ell = 0$) is indicated as grey area. Other modes ($\ell = 1, 2, 3$) can be found in a very similar region (Paxton et al. 2015). Both Aa1, Ab components are located here, and they can exhibit photometric variability attributed to pulsations.

period of approximately 152 years and eccentricity 0.58) and by γ velocities.
3. The secondary (Aa2) spectrum in the blue spectral region was detected by the two- and three-step disentangling.
4. The RV curve of the secondary was obtained by cross-correlation with a disentangled template spectrum.
5. The two-body model of the eclipsing binary was constructed in `PHOEBE2`.
6. The three-body model in `Xitau` was constrained by all observables.

Compared to previous studies, we obtained significantly lower masses than Pablo et al. (2015), in their low-mass model $(23.81+8.54)\,M_\odot$. In contrast to the study of Shenar et al. (2015), where models were calculated for two distances, 212 and 380 pc, we adopted the latter. Our results give lower radii of Aa1, Aa2; Shenar et al. (2015) have $[(16.5\pm1)+(6.5\pm2)]\,R_\odot$. Nevertheless, the radius of Ab is in agreement with Shenar et al. (2015) who reported $(10.4\pm2)\,R_\odot$. We also obtained low $\log g_3$ similarly as Shenar et al. (2015).

Hertzprung–Russel diagram. Given the spectral types of Aa1 + Aa2 + Ab, O9.5 II + B2 V + B0 IV (Pablo et al. 2015 and this work), the primary has evolved from the main sequence; however, it has not reached the overflow yet. The Hertzsprung–Russel diagram (Fig. 20) with the positions of Aa1, Aa2, Ab components indicates an interesting problem — the Ab component is very offset from a normal position. This offset is either related to its $\log g_3$ value (3.2) or to its m_3 value (8.7 $M_\odot$). However, it is not easy to modify these values, because they are well constrained by observations. To put Ab on the evolutionary track, either $\log g_3 \simeq 3.7$, or $m_3 \simeq 18\,M_\odot$. If all components were normal, the sum of masses should be about $(24 + 18 + 10)\,M_\odot = 52\,M_\odot$. Interestingly, this is similar to the mirror solution, which was excluded (see the discussion in Sects. 4 and 9). Consequently, we are left with an unusual stellar component. Actually, it is not unusual — see for example δ Ori Ca, or σ Ori E which are both helium-rich, with Hα emission (Tab. 3). Detailed stellar-evolution models with possible mass transfer between (some of) the components shall be computed in future work. Additionally, long-baseline optical or near-infrared interferometry may be able to measure precisely the angular diameters of the component stars (e.g. (Shabun et al. 2008)) and the separation of the inner orbit in the sky, giving direct constraints on the size of the orbit, helping to resolve any discrepancies in the masses measured between this study and other similar studies of δ Ori.

A comparison of δ Ori with other bright stars in the Orion belt (see Table 3) shows that σ Ori has a similar architecture (((Aa+Ab)+B)+C)+D+E, and even a very similar angular scale (Simón-Díaz et al. 2015). All of its components seem to be less evolved.[15] On the other hand, ζ Ori exhibits an angular scale about 10 times larger and has the primary evolved in an O supergiant (Hummel et al. 2000). In this sense, ε Ori, which seems to be a single variable B supergiant (Puebla et al. 2016), may represent an even more evolved object.

Given the fact that all these stars (δ, ε, ζ, σ) are the most massive within the Orion OB1b association, they might have encountered and perturbed (destabilised) each other. Again, a possible convergence of their proper motions will be analysed in future work.

Acknowledgements. This research was supported by the grants P209/10/0715, GA15-02112S, and GA19-01995S of the Czech Science Foundation. M.B. was supported by the Czech Science Foundation grant GA21-11058S. We acknowledge the support from the Research Programmes MSM0021620860 "Physical study of objects and processes in the solar system and in astrophysics" of the Ministry of Education of the Czech Republic and the grant AV0Z10030501 of the Academy of Sciences of the Czech Republic. Thanks to Dr. Rachel Matson for providing the data from Washington Double Star Catalogue. H.B. acknowledges financial support from the Croatian Science Foundation under the project 6212 "Solar and Stellar Variability". We gratefully acknowledge the use of the program `KOREL` written by Petr Hadrava, `PYTERPOL` by Jana Nemravová, and `reSPEFO2` by Adam Harmanec. This research has made use of the

[15] ι Ori is located farther away, in the Trapezium region.

AMBER data reduction package of the Jean-Marie Mariotti Center[16]. Our thanks are due to Š. Dvořáková, D. Korčáková, J. Kubát, J. Nemravová, M. Oksala, P. Škoda, and V. Votruba who obtained some of the Ondřejov blue spectra in this study. We also acknowledge the use of the electronic database from CDS Strasbourg and the electronic bibliography maintained by the NASA/ADS system. CCL and GAW acknowledge Discovery Grant support by the Natural Science and Engineering Research Council (NSERC) of Canada. Last but not least, we would like to thank our anonymous referee for the constructive useful comments that helped to improve the paper.

References

Allen, M. G., Ochsenbein, F., Derriere, S., et al. 2014, in Astronomical Society of the Pacific Conference Series, Vol. 485, Astronomical Data Analysis Software and Systems XXIII, ed. N. Manset & P. Forshay, 219
Anderson, E. & Francis, C. 2012, Astronomy Letters, 38, 331
Bagnuolo, William G., J., Riddle, R. L., Gies, D. R., & Barry, D. J. 2001, ApJ, 554, 362
Bessell, M. 2000, in Encyclopedia of Astronomy and Astrophysics, ed. P. Murdin, 1939
Božić, H. 1998, Hvar Observatory Bulletin, 22, 1
Breiter, S. & Vokrouhlický, D. 2015, MNRAS, 449, 1691
Brož, M. 2017, ApJS, 230, 19
Brož, M., Ďurech, J., Carry, B., et al. 2022a, A&A, 657, A76
Brož, M., Harmanec, P., Zasche, P., et al. 2022b, A&A, 666, A24
Brož, M., Marchis, F., Jorda, L., et al. 2021, A&A, 653, A56
Brown, A. G. A., de Geus, E. J., & de Zeeuw, P. T. 1994, A&A, 289, 101
Burssens, S., Simón-Díaz, S., Bowman, D. M., et al. 2020, A&A, 639, A81
Carroll, K., Zee, R., & Matthews, J., eds. 1998, The MOST Microsatellite Mission: Canada's First Space Telescope
Conroy, K. E., Kochoska, A., Hey, D., et al. 2020, ApJS, 250, 34
Corcoran, M. F., Nichols, J. S., Pablo, H., et al. 2015, ApJ, 809, 132
Cutri, R. M., L., W. E., & Conrow, T. 2012, VizieR Online Data Catalog, II/311
Cutri, R. M., Skrutskie, M. F., van Dyk, S., et al. 2003, VizieR Online Data Catalog, II/246
Ducati, J. R. 2002, VizieR Online Data Catalog
Egan, M. P., Price, S. D., Kraemer, K. E., et al. 2003, VizieR Online Data Catalog, V/114
Fabrycky, D. C. 2010, in Exoplanets, ed. S. Seager, 217–238
Fitzpatrick, R. 2012, An Introduction to Celestial Mechanics
Foreman-Mackey, D., Hogg, D. W., Lang, D., & Goodman, J. 2013, PASP, 125, 306
Gaia Collaboration. 2020, VizieR Online Data Catalog, I/350
Gaia Collaboration, Brown, A. G. A., Vallenari, A., et al. 2021, A&A, 649, A1
Gaia Collaboration, Prusti, T., de Bruijne, J. H. J., et al. 2016, A&A, 595, A1
Green, G. M., Schlafly, E., Zucker, C., Speagle, J. S., & Finkbeiner, D. 2019, ApJ, 887, 93
Hadrava, P. 1995, A&AS, 114, 393
Hadrava, P. 1997, A&AS, 122, 581
Hadrava, P. 2004, Publ. Astron. Inst. Acad. Sci. Czech Rep., 92, 15
Hadrava, P. 2005, Ap&SS, 296, 239
Harmanec, P. 1988, Bulletin of the Astronomical Institutes of Czechoslovakia, 39, 329
Harmanec, P., Mayer, P., & Šlechta, M. 2013, in Massive Stars: From alpha to Omega, 70
Harvey, A. S., Stickland, D. J., Howarth, I. D., & Zuiderwijk, E. J. 1987, The Observatory, 107, 205
Harvin, J. A., Gies, D. R., Bagnuolo, William G., J., Penny, L. R., & Thaller, M. L. 2002, ApJ, 565, 1216
Heintz, W. D. 1980, ApJS, 44, 111
Hill, G. 1982, Publ. Dominion Astrophys. Obs. Victoria, 16, 67
Hummel, C. A., White, N. M., Elias, N. M., I., Hajian, A. R., & Nordgren, T. E. 2000, ApJ, 540, L91
Ishihara, D., Onaka, T., Kataza, H., et al. 2010, A&A, 514, A1
Kaufer, A., Stahl, O., Tubbesing, S., et al. 1999, The Messenger, 95, 8
Lallement, R., Babusiaux, C., Vergely, J. L., et al. 2019, A&A, 625, A135
Lanz, T. & Hubený, I. 2003, ApJS, 146, 417
Lanz, T. & Hubený, I. 2007, ApJS, 169, 83
Leahy, D. A. & Leahy, J. C. 2015, Computational Astrophysics and Cosmology, 2, 4
Lenz, P. & Breger, M. 2004, in The A-Star Puzzle, ed. J. Zverko, J. Ziznovsky, S. J. Adelman, & W. W. Weiss, Vol. 224, 786–790
Leone, F., Bohlender, D. A., Bolton, C. T., et al. 2010, MNRAS, 401, 2739
Maíz Apellániz, J., Trigueros Páez, E., Negueruela, I., et al. 2019, A&A, 626, A20
Martins, F., Schaerer, D., & Hillier, D. J. 2005, A&A, 436, 1049
Mason, B. D., Martin, C., Hartkopf, W. I., et al. 1999, AJ, 117, 1890
Mason, B. D., Wycoff, G. L., Hartkopf, W. I., Douglass, G. G., & Worley, C. E. 2001, AJ, 122, 3466
Maucó, K., Briceño, C., Calvet, N., et al. 2018, ApJ, 859, 1
Mayer, P., Harmanec, P., Wolf, M., Božić, H., & Šlechta, M. 2010, A&A, 520, A89
Moultaka, J., Ilovaisky, S. A., Prugniel, P., & Soubiran, C. 2004, PASP, 116, 693
Nelder, J. A. & Mead, R. 1965, The Computer Journal, 7, 308
Nemravová, J. A., Harmanec, P., Brož, M., et al. 2016, A&A, 594, A55
Neugebauer, G., Habing, H. J., van Duinen, R., et al. 1984, ApJ, 278, L1
Nichols, J., Huenemoerder, D. P., Corcoran, M. F., et al. 2015, ApJ, 809, 133
Niesten, L. 1904, Annales de l'Observatoire Royal de Belgique Nouvelle serie, 8, 1
Oplištilová, A., Harmanec, P., Mayer, P., et al. 2020, Contributions of the Astronomical Observatory Skalnate Pleso, 50, 585
Pablo, H., Richardson, N. D., Moffat, A. F. J., et al. 2015, ApJ, 809, 134
Pablo, H., Whittaker, G. N., Popowicz, A., et al. 2016, PASP, 128, 125001
Parenago, P. P. 1954, Trudy Gosudarstvennogo Astronomicheskogo Instituta, 25, 3
Paxton, B., Marchant, P., Schwab, J., et al. 2015, ApJS, 220, 15
Perryman, M. A. C. & ESA. 1997, The HIPPARCOS and TYCHO catalogues (Publisher: Noordwijk, Netherlands: ESA Publications Division, Series: ESA SP Series 1200)
Pigulski, A. 2018, in 3rd BRITE Science Conference, ed. G. A. Wade, D. Baade, J. A. Guzik, & R. Smolec, Vol. 8, 175–192
Prša, A. & Zwitter, T. 2005, ApJ, 628, 426
Prša, A. & Zwitter, T. 2005, ApJ, 628, 426
Puebla, R. E., Hillier, D. J., Zsargó, J., Cohen, D. H., & Leutenegger, M. A. 2016, MNRAS, 456, 2907
Richardson, N. D., Moffat, A. F. J., Gull, T. R., et al. 2015, ApJ, 808, 88
Ricker, G. R., Winn, J. N., Vanderspek, R., et al. 2014, in Society of Photo-Optical Instrumentation Engineers (SPIE) Conference Series, Vol. 9143, Space Telescopes and Instrumentation 2014: Optical, Infrared, and Millimeter Wave, ed. J. Oschmann, Jacobus M., M. Clampin, G. G. Fazio, & H. A. MacEwen, 914320
Robert, C. & Casella, G. 2011, Statistical Science, 26, 102
Rowan, N. 1990, Ph.D. thesis, Univ. Texas Austin
Schmidt-Kaler, T. 1982, Bulletin d'Information du Centre de Donnees Stellaires, 23, 2
Shabun, K., Richichi, A., Munari, U., Siviero, A., & Paczynski, B. 2008, in A Giant Step: from Milli- to Micro-arcsecond Astrometry, ed. W. J. Jin, I. Platais, & M. A. C. Perryman, Vol. 248, 118–119
Shenar, T., Oskinova, L., Hamann, W. R., et al. 2015, ApJ, 809, 135
Simón-Díaz, S., Caballero, J. A., Lorenzo, J., et al. 2015, ApJ, 799, 169
Škoda, P., Šlechta, M., & Honsa, J. 2002, Publications of the Astronomical Institute of the Czechoslovak Academy of Sciences, 90
Standish, E. M. & Williams, J. G. 2006, Orbital Ephemerides of the Sun, Moon, and Planets, ed. P. Seidelmann (University Science Books)
Tierney, L. 1994, The Annals of Statistics, 1701
Vallenari, A. 2022, A&A
van Hamme, W. 1993, AJ, 106, 2096
Van Hamme, W. & Wilson, R. E. 2007, ApJ, 661, 1129
Walborn, N. R. 1972, AJ, 77, 312
Webb, D., Mizuno, D., Buffington, A., et al. 2006, Journal of Geophysical Research, 111
Wilson, R. E. 1979, ApJ, 234, 1054
Wilson, R. E. 1990, ApJ, 356, 613
Wilson, R. E. & Devinney, E. J. 1971, ApJ, 166, 605
Wilson, R. E., Van Hamme, W., & Terrell, D. 2010, ApJ, 723, 1469

[16] http://www.jmmc.fr/amberdrs

Appendix A: Secular rates for δ Ori A

We used the standard Gauss equations to estimate the secular rates for the δ Ori A system. A perturbation due to the quadrupole moment $J_2 \equiv -C_{20}$ of the primary induces a precession of the argument of pericentre:

$$\dot{\omega}_1 = +3 n_1 J_2 \left(\frac{R_1}{a_1}\right)^2 \frac{5\cos^2\tilde{i}_1 - 1}{4\eta_1^4}\,, \tag{A.1}$$

and the longitude of the node:

$$\dot{\Omega}_1 = -\frac{3}{2} n_1 J_2 \left(\frac{R_1}{a_1}\right)^2 \frac{\cos\tilde{i}_1}{\eta_1^4}\,, \tag{A.2}$$

where $n_1 = \sqrt{G(m_1+m_2)/a_1^3}$, $\eta_1 \equiv \sqrt{1-e_1^2}$, and $\tilde{i}_1$ is the inclination with respect to the primary equator. Otherwise, the notation is the same as in Table 11. For $\tilde{i}_1 \to 0$, $e_1 \to 0$, $J_2 > 0$, we would have $\dot{\omega}_1 > 0$, $\dot{\Omega}_1 < 0$, $\dot{\omega}_1 = -2\dot{\Omega}_1$.

The quadrupole moment is determined by the internal structure:

$$J_2 = -\frac{1}{m_1 R_1^2} \int_V \rho |\boldsymbol{r}|^2 P_2(\cos\theta)\,\mathrm{d}V\,, \tag{A.3}$$

where the Legendre polynomial $P_2(x) = \frac{1}{2}(3x^2-1)$. For a homogeneous body, it would be related to the ellipticity (Fitzpatrick 2012)[17]:

$$J_2 = -\frac{2}{5}\varepsilon_0\,. \tag{A.4}$$

For a rotating body, it is related to the Love number[18]:

$$J_2 \simeq k_2 \left(\frac{\Omega_0}{n_0}\right)^2\,, \tag{A.5}$$

where Ω_0 is the angular rotation frequency; n_0, the mean motion at the surface. Assuming $J_2 = 1.8 \cdot 10^{-4}$ results in $\dot{\omega} = 1.47\,\mathrm{deg\,y^{-1}}$, $\dot{\Omega} = -0.73\,\mathrm{deg\,y^{-1}}$, where the node circulates with respect to the primary equator, but it only librates with respect to the observer plane.

For the binary Aa1+Aa2 (acting on a mass-less particle), the equations should be modified as follows:

$$\dot{\omega}_2 = +3 n_2 J_2 \left(\frac{a_1}{a_2}\right)^2 \frac{5\cos^2\tilde{i}_2 - 1}{4\eta_2^4}\,, \tag{A.6}$$

$$\dot{\Omega}_2 = -\frac{3}{2} n_2 J_2 \left(\frac{a_1}{a_2}\right)^2 \frac{\cos\tilde{i}_2}{\eta_2^4}\,, \tag{A.7}$$

where the inclination $\tilde{i}_2$ is with respect to the binary. The effective quadrupole moment is:

$$J_2 = \frac{1}{2}\frac{m_1 m_2}{(m_1+m_2)^2}\,, \tag{A.8}$$

because the respective radius ($|\boldsymbol{r}| = a_1$) is the same as the reference radius ($R = a_1$). Given that $J_2 = 0.109$, and the ratio of $a_1/a_2 = 0.002$, the precession rates should be of the order of $10^{-6}\,\mathrm{deg\,y^{-1}}$.

[17] $r(\vartheta) = R(1 - 2/3\varepsilon_0 P_2(\cos\vartheta))$

[18] approximately, 0.02 for the Sun; 0.3 for the Earth, Jupiter, or an M-dwarf; up to 0.75 for incompressible fluid

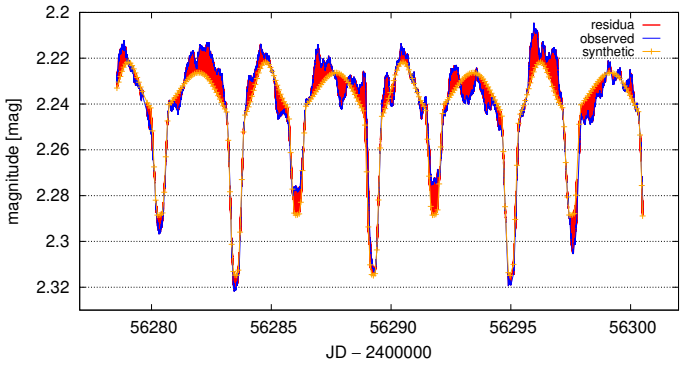

Fig. B.1. Comparison of the observed MOST (blue) and synthetic (orange) light curve. The residuals are plotted in red. Apart from the eclipses, the light curve contains large-amplitude oscillations (not included in our model); uncertainties 0.01 mag were thus assigned to all data points.

However, for the massive triple system (Aa1+Aa2)+Ab, we used the theory of Breiter & Vokrouhlický (2015); for the longitudes of pericentre and node:

$$\dot{\varpi}_2 = \frac{3}{8}\frac{n_2}{\eta_2^3}\frac{m_3}{m_1+m_2+m_3}\frac{n_2}{n_1}\gamma\,\cdot \\ \cdot\left[3\cos^2 J - 1 - \frac{\gamma\sin J\sin 2J}{1+\gamma\cos J+\sqrt{1+\gamma^2+2\gamma\cos J}}\right], \tag{A.9}$$

$$\dot{\Omega}_2 = \frac{3}{4}\frac{n_2}{\eta_2^3}\frac{m_3}{m_1+m_2+m_3}\frac{n_2}{n_1}\cos J\sqrt{1+\gamma^2+2\gamma\cos J}\,, \tag{A.10}$$

where $m_1' = m_1 m_2/(m_1+m_2)$, $m_2' = (m_1+m_2)\,m_3/(m_1+m_2+m_3)$ denote the reduced masses; $L_1 = m_1' n_1 a_1^2$, $L_2 = m_2' n_2 a_2^2$, the angular momenta; $\cos J = \cos i_1 \cos i_2 + \sin i_1 \sin i_2 \cos(\Omega_1 - \Omega_2)$, the mutual inclination; and $\gamma = L_1/(L_2\eta_2)$. Assuming parameters from Table 11, $\dot{\varpi}_2 = 3.4 \cdot 10^{-6}\,\mathrm{deg\,y^{-1}}$, $\dot{\Omega}_2 = 8.5 \cdot 10^{-5}\,\mathrm{deg\,y^{-1}}$, which is negligible on the observational time span. All these effects were nevertheless included in our numerical N-body model (Sect. 9).

Appendix B: Supplementary figures and tables

In Tables B.1 and B.2, we present more details on the spectral data sets discussed in Sect. 2.1. In Table B.3, we report parameters derived for the 8 seasons observed by the BRITE satellites. The LC from our three-body model (Sect. 9) is shown in Fig. B.1. Individual contributions to χ^2 computed for an extensive set models of δ Ori is shown in Fig. B.2.

Table B.1. Details on spectra from the coudé focus of the Ondřejov 2m reflector in the blue region. The RVs were determined during the spectral disentangling (three-step method) in KOREL.

T [HJD − 2400000]	Exposure time [s]	S/N	Heliocentric correction [km s^{-1}]	RV_1 [km s^{-1}]	σ_{RV_1} [km s^{-1}]	RV_2 [km s^{-1}]	σ_{RV_2} [km s^{-1}]	RV_3 [km s^{-1}]	σ_{RV_3} [km s^{-1}]
55836.5692	1113	235.3	26.2335	−13.03	1.73	101.44	1.48	17.25	1.72
55836.5827	1131	268.3	26.2097	−13.29	1.52	100.76	1.30	16.46	1.51
55836.5963	1129	217.3	26.1849	−13.97	1.87	104.81	1.60	17.91	1.86
55836.6137	1250	238.0	26.1517	−14.86	1.71	108.90	1.46	17.19	1.70
55836.6287	1265	236.2	26.1222	−17.11	1.72	115.37	1.47	17.70	1.71
55836.6434	1174	254.2	26.0929	−19.88	1.60	113.68	1.37	15.16	1.59
55837.5877	1124	214.3	26.0588	−94.63	1.90	278.78	1.63	16.35	1.88
55837.6016	1134	239.5	26.0328	−96.07	1.70	280.05	1.45	13.32	1.69
55837.6152	1150	232.7	26.0064	−95.62	1.75	279.59	1.50	14.24	1.74
55837.6294	1218	237.1	25.9784	−98.09	1.71	278.48	1.47	13.54	1.70
55871.5969	1999	217.1	16.9755	−79.45	1.87	251.90	1.60	17.42	1.86
55893.4601	1662	226.5	7.9171	36.33	1.79	−31.61	1.54	17.48	1.78
55893.4820	2003	225.8	7.8667	36.04	1.80	−25.90	1.54	11.27	1.79
55953.4009	1916	224.9	−19.2387	−11.07	1.81	91.43	1.55	15.22	1.80
55953.4226	1766	243.8	−19.2836	−9.87	1.67	87.03	1.43	12.58	1.66
55953.4508	1599	250.2	−19.3381	−7.24	1.62	79.34	1.39	14.11	1.61
55953.4692	1503	252.0	−19.3704	−5.12	1.61	75.37	1.38	14.21	1.60
55953.4871	1468	216.3	−19.3992	−1.59	1.88	71.30	1.61	14.07	1.87
55956.3498	3561	230.1	−20.1601	58.08	1.77	−72.93	1.51	11.98	1.75
55959.2469	2134	230.6	−20.9128	4.46	1.76	68.90	1.51	14.61	1.75
55977.3276	2165	209.0	−25.6205	86.76	1.95	−121.98	1.67	14.70	1.93
55990.3318	4872	206.6	−27.3138	96.47	1.97	−152.94	1.69	14.40	1.95
55991.2779	1466	258.1	−27.2883	−5.95	1.58	77.34	1.35	14.43	1.56
55992.2949	1415	199.3	−27.3830	−93.85	2.04	278.69	1.75	18.81	2.03
56003.3328	1200	186.8	−27.6165	−72.08	2.18	231.46	1.86	12.62	2.16
56011.3498	1361	142.0	−27.1206	54.90	2.86	−52.75	2.45	17.89	2.84
56167.6213	2054	154.9	26.1472	118.69	2.62	−195.80	2.25	15.19	2.61
56241.4709	2405	199.5	15.4295	112.55	1.86	−178.56	1.59	6.27	1.85
56257.4224	2287	219.6	8.5701	13.12	1.85	42.02	1.59	16.01	1.84
56257.6273	3324	227.7	8.1164	35.28	1.79	−5.17	1.53	13.21	1.77
56330.3789	1399	245.5	−22.8962	−91.20	1.66	271.45	1.42	16.21	1.64
56354.3038	3112	241.5	−27.1587	−50.33	1.54	180.31	1.32	5.28	1.53
56357.3761	1138	170.5	−27.5049	88.62	2.38	−124.65	2.04	15.73	2.37
56596.5631	1415	212.4	19.1204	98.83	1.91	−147.64	1.64	17.80	1.90
56608.6423	2196	181.0	14.3991	121.15	2.25	−201.59	1.92	13.34	2.23
56609.4312	3840	166.5	14.4441	93.94	2.44	−153.01	2.09	19.46	2.43
56621.6375	6298	264.2	8.7784	22.16	1.54	14.69	1.32	14.10	1.53
56629.6451	5211	232.3	5.0123	−30.90	1.75	135.90	1.50	15.84	1.74
56642.5644	2340	236.0	−1.1527	103.79	1.72	−163.06	1.48	14.29	1.71
56643.3817	2365	218.8	−1.2259	121.57	1.86	−196.79	1.59	12.93	1.85
56643.6078	4554	246.3	−1.7159	110.68	1.51	−198.65	1.29	19.58	1.50
56666.3166	2968	197.2	−11.9535	120.06	2.06	−196.17	1.77	16.15	2.05
56666.4940	5013	237.6	−12.3482	120.37	1.56	−187.88	1.34	8.33	1.55
56704.3508	2793	279.8	−24.9170	−15.22	1.45	90.44	1.25	13.73	1.44
56714.2672	2292	260.6	−26.4964	−77.91	1.56	246.02	1.34	16.17	1.55
56719.3096	3214	240.8	−27.1475	−1.73	1.69	79.65	1.45	18.73	1.68
56721.3496	2993	256.5	−27.3779	−32.32	1.59	140.09	1.36	16.81	1.57
56737.3202	629	226.3	−27.4373	−93.55	1.80	265.23	1.54	15.84	1.78
56738.3020	2404	184.0	−27.3532	−58.28	2.21	194.34	1.89	15.57	2.19
56746.2894	1392	199.8	−26.5682	120.01	2.03	−201.76	1.74	16.48	2.02
56928.5832	1652	221.9	26.6856	59.66	1.83	−64.14	1.57	14.96	1.82
57105.2900	1986	205.6	−27.2198	−45.65	1.98	170.70	1.69	12.24	1.96
57106.2877	565	118.5	−27.1303	60.16	3.43	−62.99	2.94	14.03	3.41
57106.3182	1784	166.9	−27.1696	63.36	2.44	−69.25	2.09	16.40	2.42
57116.3066	1651	156.0	−25.8607	−88.80	2.61	254.62	2.23	11.35	2.59
57128.2762	1434	158.1	−23.3452	−39.86	2.57	158.43	2.20	14.13	2.55
57297.5482	3202	187.7	26.2886	83.80	2.17	−113.55	1.86	20.79	2.15
57364.5793	2224	219.8	2.9803	85.92	1.85	−124.80	1.58	14.50	1.84
57445.3477	3194	218.4	−26.6982	114.68	1.86	−185.19	1.60	16.60	1.85
57464.3540	6102	211.3	−27.6372	18.76	1.92	28.03	1.65	15.26	1.91
58389.5221	2398	176.3	26.7622	−29.27	2.31	132.85	1.98	16.06	2.29
58390.6224	161	79.9	26.4953	81.98	5.09	−114.83	4.36	15.47	5.05
58390.6416	3001	174.5	26.4581	85.89	2.33	−118.96	2.00	17.81	2.31
58402.5225	2556	171.8	24.7883	108.15	2.37	−177.53	2.03	16.77	2.35
58405.5661	2701	193.3	24.0578	−89.81	1.92	273.70	1.65	6.62	1.91

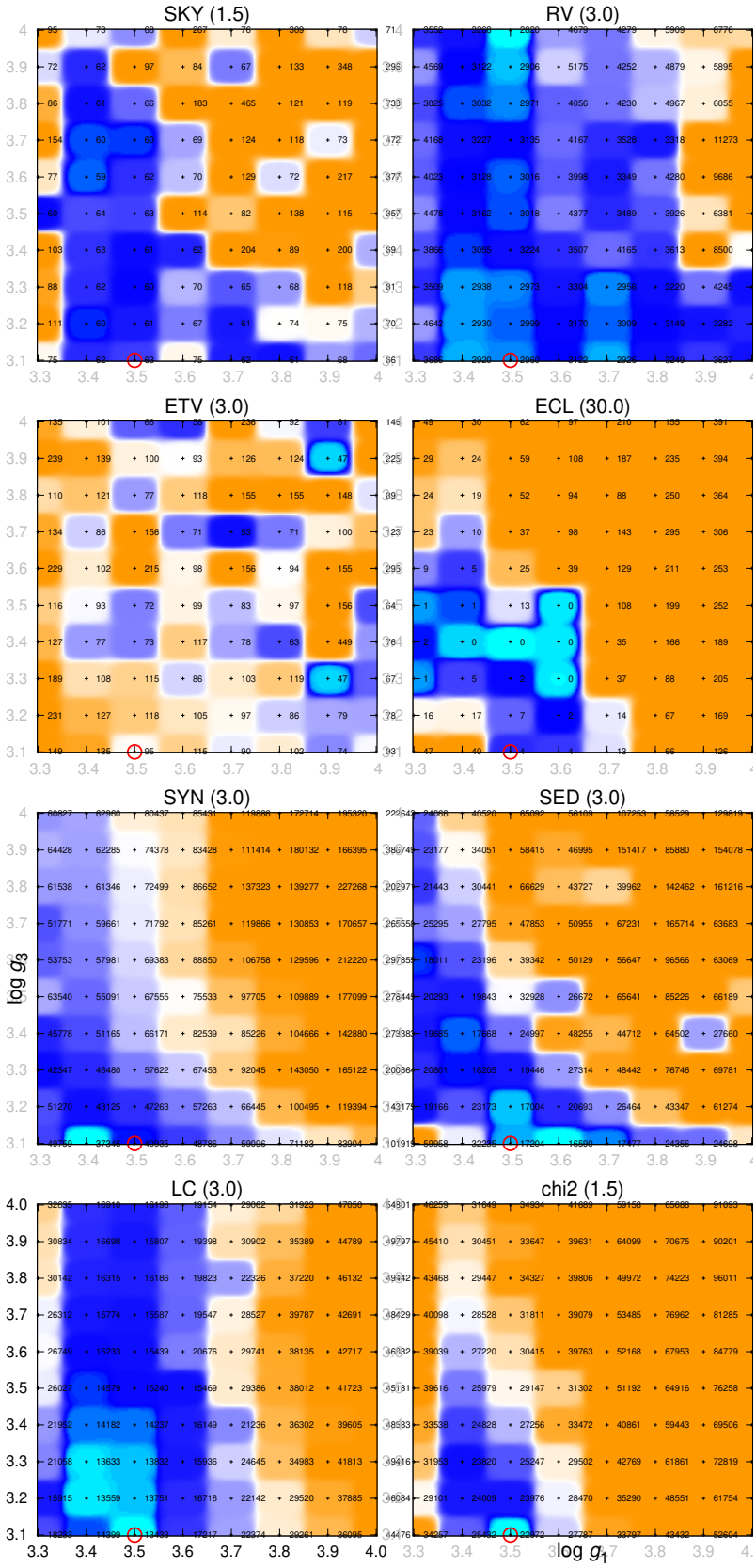

Fig. B.2. Contributions to χ^2 for a set 100 best-fit models of δ Ori. Individual contributions are shown in the panels (from top left): astrometry (SKY), RV, eclipse timings (ETV), eclipse duration (ECL), normalised spectra (SYN), SED, light curve (LC), and total. Every simplex was initialised with a different combination of the gravitational accelerations $\log g_1$, $\log g_3$, which were kept fixed to obtain a regular grid. All other parameters were free. The number of convergence steps was limited to 2000, consequently, 200000 models were computed in total. Axes correspond to the values of $\log g_1$, $\log g_3$, colours to χ^2 (see also tiny numbers). The colour scale was adjusted as follows: cyan the very best fit for a given data set, blue acceptable fits (<3.0 min χ^2), orange poor fits (≥3.0 min χ^2). The factor was 1.5 for the SKY, total; and 30.0 for the ECL data set. 'Forbidden regions' can be seen, in particular, large $\log g_1$, $\log g_3$ due to the SYN, SED, or large $\log g_1$ due to the ECL, LC. The weighted very best fit is denoted by the red circle.

Table B.2. Details on ELODIE and FEROS spectra in the blue region. ELODIE is at the upper part of the table, FEROS at the lower part. The RVs were determined during the spectral disentangling (three-step method) in KOREL.

T [HJD − 2400000]	Exposure time [s]	S/N	Heliocentric correction [km s^{-1}]	RV_1 [km s^{-1}]	σ_{RV_1} [km s^{-1}]	RV_2 [km s^{-1}]	σ_{RV_2} [km s^{-1}]	RV_3 [km s^{-1}]	σ_{RV_3} [km s^{-1}]
50033.5779	187.13	86.9	14.76	126.27	4.27	−206.96	3.66	18.15	4.24
50033.5920	333.78	99.6	14.72	123.38	3.73	−206.12	3.19	16.55	3.70
50435.4013	120.50	102.9	−1.87	112.98	3.61	−184.64	3.09	20.89	3.58
54136.5830	30	295.3	−22.15	22.27	1.26	4.33	1.08	14.51	1.25
54809.7226	20	216.8	2.19	76.14	1.71	−101.90	1.47	15.43	1.70
54809.7238	20	213.4	2.19	76.02	1.74	−101.64	1.49	15.43	1.73
54809.7255	20	219.8	2.19	72.08	1.69	−100.56	1.45	12.72	1.68
54953.4599	30	232.0	−18.33	27.82	1.60	6.80	1.37	15.67	1.59
54953.4615	30	216.8	−18.33	27.35	1.71	10.92	1.47	10.76	1.70

Table B.3. Results of eight phoebe2 models of δ Ori. LCs from eight individual seasons S. (Table 8) and all RVs were used to constrain the models. We assumed a fixed value of the temperature T_1 and the third light l_3. The uncertainties are the same as in Table 9.

Parameters	S. 2013	S. 2014	S. 2015	**S. 2016**	S. 2017	S. 2018	S. 2020	S. 2021	All seasons
T_0 [HJD]	733.8355*	733.8355*	733.8412*	773.3830*	733.8412*	733.8359*	733.8343*	733.8447*	733.8340*
T_1 [K]	31000^f	31000^f	31000^f	31000^f	31000^f	31000^f	31000^f	31000^f	31000^f
T_2 [K]	23477	23371	23055	22709	23055	23455	22577	21825	22940
R_1 [$R_\odot$]	12.96	12.79	12.78	13.27	12.78	12.82	12.95	12.61	12.87
R_2 [$R_\odot$]	3.69	3.47	3.54	3.70	3.54	3.43	3.75	3.39	3.56
i_1 [°]	79.21	79.48	79.46	77.67	79.46	79.53	78.85	79.55	79.15
S_B	1.00631	1.00489	1.00556	1.00786	1.00872	1.02264	1.00430	1.00455	var
S_R	1.00375	1.00355	1.00872	1.00841	1.00361	1.02431	1.00342	1.00640	var
m_1 [$M_\odot$]	18.06	18.08	18.08	18.07	18.08	17.22	18.05	18.08	17.97
m_2 [$M_\odot$]	8.40	8.38	8.42	8.47	8.42	8.06	8.38	8.34	8.35
e_1	0.0843	0.0845	0.0900	0.0824	0.0903	0.0881	0.0861	0.0851	0.0864
ω_1 [°]	133.5	132.9	131.0	130.0	131.0	129.0	134.0	135.91	129.86
$\dot{\omega}_1$ [° yr^{-1}]	1.45^f	1.45^f	1.45^f	1.45^f	1.45^f	1.45^f	1.45^f	1.45^f	-
γ [km s^{-1}]	19.27	19.02	19.33	19.78	19.33	19.71	18.93	19.52	19.36
l_{3B}	0.273^f	0.273^f	0.273^f	0.273^f	0.273^f	0.273^f	0.273^f	0.273^f	-
l_{3R}	0.273^f	0.273^f	0.273^f	0.273^f	0.273^f	0.273^f	0.273^f	0.273^f	-
χ^2_{sum}	661	683	1051	604	1003	877	1310	1176	
χ^2_{LCB}	195	174	598	153	280	392	895	61	
χ^2_{LCR}	201	254	180	200	463	217	160	284	
χ^2_{RV1}	197	188	206	184	192	200	186	207	
χ^2_{RV2}	68	66	67	67	68	68	69	77	

Notes. * −2457000 HJD. The explanation of variables is the same as in Table 9. ^{f} indicates the respective parameter was fixed. var denotes variable values for each season (they were between 1.004 and 1.010). For each season, the numbers of data points were: N_{total} = 321, N_{LCB} = N_{LCR} = 100, N_{RV1} = 71, and N_{RV2} = 50.

4. VLTI observations of the Orion Belt stars: I. ε Orionis

In the following study, we obtained, reduced, and calibrated interferometric measurements from our successful ESO proposal (ID: 112.25JX, PI A. Opli$\check{\text{s}}$tilová) for the VLTI. We chosed an extended configuration ($\approx 130\,\text{m}$) that is available from 2020. We constructed a single star model for $\varepsilon\,$Ori using PIONIER interferometry, alongside high-resolution spectroscopy. The interferometric data imply that the star has a very oblate shape, similar to Achernar ($\alpha\,$Eri; Domiciano de Souza et al., 2003) or Altair (α Aql; Monnier et al., 2007), less massive stars from the neighbouring constellation.

Astronomy & Astrophysics manuscript no. output
July 8, 2025

VLTI observations of the Orion Belt stars: I. ε Orionis ⋆

A. Opličtilová[1], M. Brož[1], C. A. Hummel[2], P. Harmanec[1], and B. N. Barlow[3]

[1] Charles University, Faculty of Mathematics and Physics, Astronomical Institute, V Holešovičkách 2, CZ-180 00 Praha 8-Trója, Czech Republic
[2] European Southern Observatory, Karl-Schwarzschild-Str. 2, D-85748 Garching, Germany
[3] Department of Physics and Astronomy, University of North Carolina at Chapel Hill, Chapel Hill, NC 27599, USA

Received 27 June 2025

ABSTRACT

Context. Massive stars play a decisive role in the evolution of the Universe. They are the primary sources of ionising radiation, generate strong stellar winds affecting the interstellar medium, and ultimately end their lives as supernovæ, ejecting synthesised, r-process elements.
Aims. In order to constrain their current state and structure, we need sufficiently complex models, constrained by astrometric, interferometric, and spectroscopic observations. However, they are not available for distant stars. Instead, we focused on the nearest massive stars in the Orion Belt.
Methods. We obtained VLTI interferometric observations of Orion Belt stars and calibrated visibility data from the GRAVITY and PIONIER instruments. Additionally, we obtained spectroscopic data from the CFHT and CTIO observatories. For modelling, we used a modified version of PHOEBE2, extended with new interferometric and spectroscopic modules. To describe non-spherical, rotating, or Roche-like stars, integrals over triangular meshes have to be computed, using extensive grids of synthetic spectra (OSTAR, BSTAR, ATLAS). For fitting, we used the simplex algorithm and χ^2 mapping of the parameter space.
Results. In this paper, the first in a series, we present single-star models of the B0 Ia supergiant ε Ori. Interferometric visibilities indicate that the star is not spherical but rotating close to its critical velocity. The preferred distance, $d = (384 \pm 8)$ pc, corresponds to the median of distances for the Orion OB1b association. Specifically, we obtained the following parameters: mass $m = (28.4 \pm 2.0)\,\mathrm{M}_\odot$, equivalent radius $R = (27.6 \pm 1.5)\,\mathrm{R}_\odot$ (the polar and equatorial values were $22.3\,\mathrm{R}_\odot$ and $33.6\,\mathrm{R}_\odot$, respectively), effective temperature $T_\mathrm{eff} \simeq 25\,000$ K, inclination of the rotation axis $i \simeq 45$ deg, longitude of the ascending node (of the equator), $\Omega \simeq 300$ deg, and period $P_\mathrm{rot} = 4.3^{+1.0}_{-0.0}$ d. This 'compromise' model provides a reasonable fit to wind-free Balmer line profiles (Hγ, Hδ, Hε, etc.), but there is still some tension between interferometric and spectroscopic datasets, corresponding to a faster- vs. slower-rotating star.
Conclusions. Our fast-rotating model implies that circumstellar matter should be naturally present, in the form of wind or disk, and contribute to continuum radiation. The fast rotation of ε Ori is compatible with a merger, formed from a multiple system of comparable mass, like δ, ζ, or σ Ori.

Key words. Stars: massive – Techniques: interferometric – Stars: individual: ε Ori – Stars: individual: Orion's Belt

1. OB stars in the Orion Belt

OB stars live relatively short—only a few millions or tens of millions of years, yet they are crucial cosmic engines with influence on the Universe that outlasts their lifetimes. They exert strong feedback on their environment; not only as sources of energy, ionising photons, chemical elements—through winds or core-collapse supernovæ explosions (Clayton 1983)—but also as precursors of neutron stars, black holes, and consequently gravitational wave sources (Marchant et al. 2021).

Most likely precursors include overcontact binaries (Almeida et al. 2015), X-ray binaries (Atri et al. 2019), quiescent binaries (Shenar et al. 2022), or pair-instability supernovae (Renzo et al. 2022). Various formation channels must be constrained by photonic observations. The distribution of black hole masses (Abbott et al. 2021) indicates a hierarchical merging. This is complicated by 'kicks' of the order of 100 km/s, during explosions (Wongwathanarat et al. 2013) or mergers (Shenar et al. 2022). The kicks can be compensated by the escape velocity from nuclear clusters or the escape velocity from multiple systems, where the radial velocities (RVs) of components are comparable to the kick velocities.

The very characteristic of massive stars is multiplicity; 90% of massive hot OB stars possess at least one stellar companion (Sana et al. 2014; Sota et al. 2014; Maíz Apellániz et al. 2019; Pauwels et al. 2023), which influences their evolution throughout their lives. Yet, some stars remain single (e.g. ε Ori), even though they share the same birth environment with multiple systems. Considering the possible interactions among stars, they might be the result of a more complicated evolutionary process, including mass transfer or mergers resulting from close encounters between stars.

The evolution of massive stars still remains poorly constrained by observations. The primary kind of observation constraining diameters is long-baseline interferometry. While the most massive stars in the Large Magellanic Cloud, e.g. BAT99-98 with $M \approx 200\,\mathrm{M}_\odot$ located in the Tarantula nebula (30 Dor) (Hainich et al. 2014; Kalari et al. 2022), are too distant (50 kpc) for interferometric measurements, the Orion OB1 association at about 400 pc from us seems to be a perfect region for the inves-

Send offprint requests to: A.O.,
e-mail: alzbeta.oplistilova@gmail.com
⋆ Based on ESO proposal Programme ID: 112.25JX, PI A. Opličtilová

tigation of questions related to the birth of OB stars and their evolution.

The brightest stars in the Orion Belt, members of the OB1b Orion association, δ Ori, ζ Ori, σ Ori, and ε Ori with individual component masses of up to 35 $M_\odot$ (Hummel et al. 2013; Schaefer et al. 2016a; Puebla et al. 2016a; Opluštilová et al. 2023) represent massive stars that are accessible to the most advanced optical interferometers. The parallaxes of faint stars surrounding the aforementioned bright stars were measured in Gaia DR3 (Gaia Collaboration et al. 2021); the corresponding distances are all around 0.38 kpc (Opluštilová et al. 2023). It is thus possible to measure their angular separations and angular diameters.

In this first paper, we focus on ε Ori (Alnilam, 46 Ori, HD 37128), which is the largest and brightest star in the Orion Belt. Based on photometric measurements taken at the Hvar Observatory (Božić & Harmanec 2023), its standard magnitudes are: $V = 1.691$ mag, $B = 1.509$ mag, and $U = 0.495$ mag. It is classified as a B0 Ia blue supergiant and represents the only massive single star in Orion's Belt. Its mass of about 30 $M_\odot$ (Puebla et al. 2016a) is similar to the total masses of the other multiple systems in Orion. Also, it has an intense wind (Puebla et al. 2016a) and a mass-loss rate of up to $\dot{M} = 5.25 \cdot 10^{-6}\,M_\odot\,\mathrm{yr}^{-1}$ (Repolust et al. 2005). It might be the case that ε Ori is a post-mass-transfer object, and represents a future evolved state of multiple stellar systems in Orion. For this reason, we include a brief discussion of the relevant systems, δ, ζ, and σ Ori, to enable comparison of their masses, radii, spectral types, etc.

δ Ori (Mintaka, HD 36486, HR 1852/1851) is our closest massive multiple system consisting of five components in total: [(Aa1 + Aa2) + Ab] + (Ca +Cb). The triple star A (O9.5 II + B2 V +B0 IV) has the periods $P_1 = 5.732436$ d, $P_2 = 55\,450$ d and the mass 17.8 + 8.5 + 8.7 $\simeq$ 35 $M_\odot$ (Opluštilová et al. 2023). The primary (Aa1) is an unusually evolved O-type star. The star has been studied in a series of papers by Corcoran et al. (2015), Pablo et al. (2015), Nichols et al. (2015), and Shenar et al. (2015). We have already constructed a model of δ Ori A (Opluštilová et al. 2023), based on diverse observational data (photometry, astrometry, radial velocities, eclipse timings, eclipse duration, spectral line profiles, and spectral-energy distribution), with the exception of interferometry, as previous VLTI/AMBER data were not usable. One conclusion from that study was that the compact binary Aa1+Aa2 is a pre-mass-transfer object, while the tertiary seems to be unusually inflated (according to its log g and the HR diagram).

ζ Ori (Alnitak, 50 Ori, HR 1948/1949) consists of four components [((Aa + Ab) + B] + C, also includes a triple star O9.7 Ib + B0.5 IV + B0 III and, in particular, a double-lined spectroscopic binary with the mass 33 + 14 $\simeq$ 47 $M_\odot$ (Hummel et al. 2000). The 2 mag fainter companion Ab with the period $P_1 \approx 2687$ d, mean separation of 45 mas, and eccentricity $e_1 = 0.338$ was discovered by Hummel et al. (2000). The primary Aa is the only known magnetic O-type supergiant. Tertiary B has a fast rotation of 350 km/s, separation of 2.4 arcsec, period $P_2 = 1509$ yr, and eccentricity $e_2 = 0.07$.

Finally, σ Ori (48 Ori, HD 37468, HR 1931) has six components [(Aa + Ab) + B] + C + D + E of spectral types [(O9.5 V + B0.5 V) + A2V] + B2V + B2V+ ?. The triple star has masses of 17 + 13 + 12 $\simeq$ 42 $M_\odot$. Binary A ($P_1 \approx 143$ d) and component B form a visual pair with $P_2 \approx 160$ yr. The angular separations of all components are 4.3 mas, 260 mas, 11 arcsec, 13 arcsec, and 42 arcsec, respectively. Unlike δ Ori, the inner orbit of σ Ori is eccentric, while the outer is circular (Schaefer et al. 2016b). According to Schaefer et al. (2016b), the expected angular diameters are 0.27 and 0.21 mas for Aa and Ab, respectively. The system has already been observed by interferometers such as CHARA/MIRC, NPOI, and VLTI/AMBER; however, the diameters were unresolved.

In 2023, we succeeded with the ESO proposal (Programme ID: 112.25JX) to observe ε, δ, ζ, and σ Ori with the Very Large Telescope Interferometer (VLTI). The main goal was to resolve the angular diameters of individual components to constrain complex models of the stellar systems.

2. Observational data

Hereinafter, we describe the observational datasets, including interferometry from VLTI instruments, spectroscopy from CFHT and CTIO, together with other datasets used for modelling ε Ori.

2.0. VLTI/GRAVITY interferometry

In our two runs of Programme ID: 112.25JX, (PI A. Opluštilová, 12 h + 1 h) – in phase 112, running between 1/10/23 and 31/3/24 at Cerro Paranal in northern Chile, we obtained observations of ζ, σ, and δ Ori with the GRAVITY instrument (Eisenhauer et al. 2011; GRAVITY Collaboration et al. 2017) and observations of ε Ori with the PIONIER instrument (Le Bouquin et al. 2011).

Both runs were performed in service mode. Such data should enable us to fit stars' angular diameters and angular positions with up to 10-microarcsecond accuracy.

For observations with GRAVITY, we requested 12 concatenations, each including 2 observing blocks (OBs), science target and calibrator (CAL-SCI). Each concatenation lasted 1 h; thus, we obtained observations on four different nights for each target, 12 hours of observations in total, We chose the extended configuration, which made these observations possible for the first time, and the high spectrometer resolution. The observations (snapshots) were in on-axis mode, with automatic fringe tracking, adaptive optics with Coude guiding, and standard calibration. For δ and σ Ori, we set the Wollaston spectrometer out and for ζ Ori, in. Otherwise, the brightest object ζ Ori would be saturated. All our three targets were very bright; therefore, we used the auxiliary telescopes (ATs) and allowed for the worst weather conditions when observations are possible, which were a seeing <1.4 arcsecs, variable sky with thin cirrus, and an air mass of 1.6.

We performed the calibration using the EsoReflex GRAVITY pipeline (Freudling et al. 2013). The essence of calibration is to compare the visibilities of calibrators (see Table 1) with the theoretical visibilities of a uniform disk, which is described by

$$\mu(u, v) = \frac{2\,J_1(\pi\,\theta\,\sqrt{u^2 + v^2})}{\pi\,\theta\,\sqrt{u^2 + v^2}}, \tag{1}$$

where J_1 is the Bessel function of the first order, the square root $\sqrt{u^2 + v^2}$ corresponds to the length of a baseline, and θ is the angular diameter of a star. The visibility function for a uniform disk is the simplest model, but it is sufficient for the calibration process. The larger the diameter, the faster the visibility drops. The comparison of theoretical and observed visibilities is expressed by a transfer function as the ratio of the calibrator's squared visibilities and theoretical squared visibilities for a uniform disk

$$\mathrm{TF} = \frac{V^2_{\mathrm{cal}}}{V^2_{\mathrm{UD}}} \tag{2}$$

The transfer function is used to reduce raw uncalibrated data; the reduced data V^2_* are the ratio of raw data and the transfer function

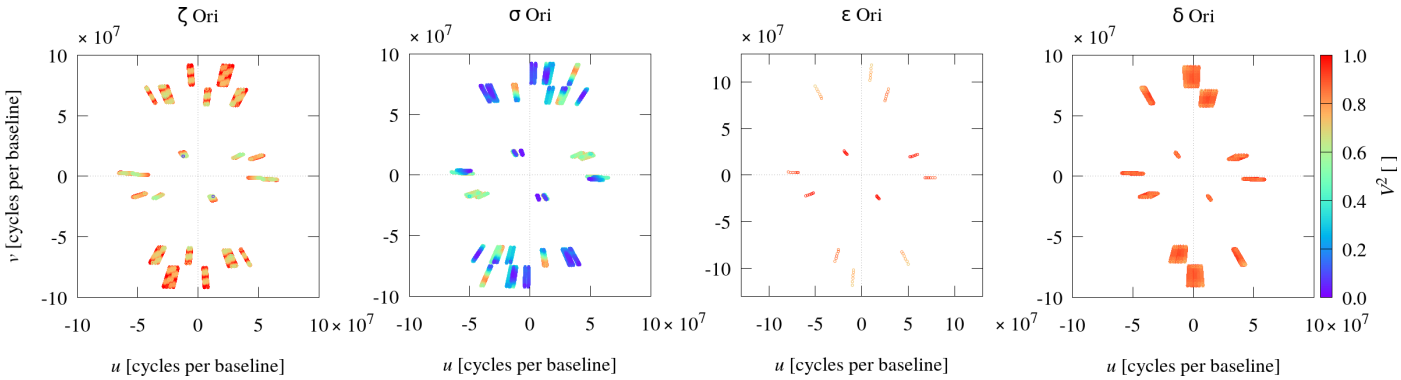

Fig. 1. Coverage for interferometric measurements showing the squared visibility V^2 vs. baselines $(u, v) \equiv \mathbf{B}/\lambda$ in cycles per baseline. Individual panels show four stars in Orion's Belt (ζ, σ, ε, and δ Ori). For each star, all nights are plotted. Colours correspond to visibility values.

$$V^2_* = \frac{V^2_{\rm raw}}{\rm TF}. \quad (3)$$

For all three objects, we obtained squared visibilities measured on six baselines, covering the wavelength range from 1.95 μm to 2.45 μm. The coverage of measurements in uv-planes for each target is shown in Fig. 1, and examples of reduced squared visibilities V^2 and the corresponding calibrators' visibilities are in Fig. 2. We also obtained closure phases for four triangles composed of those six baselines. We checked the closure phases of calibrators; they were close to zero as expected.

In the case of ζ Ori and its calibrator, we obtained two polarisation directions, P_1 and P_2, thanks to the Wollaston prism. However, since the object does not have a strong magnetic field, we cannot use the polarimetric data to determine any properties. The Wollaston prism was used just to prevent saturation of this bright target.

Table 1. Epochs of interferometric observations and uniform-disk diameters (UDD) of calibrators. The values were taken from the VLTI or PIONIER pipelines, or recalibrated by us in the case of ζ Ori.

Star	T [HJD]	Calibrators	$\mathrm{UDD_{cal}}$ [mas]
δ Ori	2460268.66081427 2460270.66197214 2460271.64182168 2460300.59365039	HIP 26149	0.6658
ζ Ori	2460269.65275756 2460271.75297908 2460300.67146289 2460317.64698373	HIP 26108	1.9350
σ Ori	2460268.82653117 2460271.72554332 2460317.61074530 2460318.55852424	HIP 26174	0.6419
ε Ori	2460268.50080073	ζ Lep	0.7950

2.1. VLTI/PIONIER interferometry

With the PIONIER instrument, we proposed a single concatenation composed of three observing blocks (CAL-SCI-CAL) and obtained six interferometric measurements of ε Ori on six baselines, within one hour of observing time. This resulted in a total of 36 squared visibility and 24 closure phase measurements. To get this snapshot, we applied for the grism as the disperser for PIONIER. The PIONIER instrument works in the H-band (1.52–1.76) μm, which delivers a better angular resolution than GRAVITY for measuring a single star. The target is very bright; thus, observations could be conducted under relaxed weather constraints: seeing <1.15 arcsec, variable sky with thin cirrus, and an air mass of 2.0. Data reduction was performed using the `Pndrs` software (Le Bouquin et al. 2011). The uv-plane coverage is shown in Fig. 1, and the reduced squared visibilities V^2 together with those of the calibrator ζ Lep are in Fig. 2.

2.2. CTIO/CHIRON and CFHT Spectroscopy

We obtained four echelle spectra of spectral range (4504–8900) Å at the Cerro Tololo Inter-American Observatory (CTIO) with the 1.5-m reflector using the highly stable cross-dispersed echelle spectrometer CHIRON. We used the fibre mode with the resolution of $R \approx 25\,000$. A preliminary reduction to 1-D spectra was carried out at CTIO (Tokovinin et al. 2013). We performed rectification using the `reSPEF02` software written by A. Harmanec[1].

Additionally, we used four spectra measured by the 3.6-m Canada-France-Hawaii Telescope (CFHT), located near the summit of Mauna Kea on Hawaii. The spectra from the ESPaDOnS instrument cover the region of (3815–6600) Å and have the resolution of 68 000. These archival spectra have relatively low uncertainties in the normalised intensity, less than 0.01, corresponding to photon noise for bright stars. Due to remaining rectification systematics, we added a value of 0.01 to uncertainties.

2.3. Spectral-energy distribution (SED)

To compute SED, we downloaded absolute fluxes from the photometric catalogues in the VizieR tool (Allen et al. 2014). We selected all measurements within the wavelength range of the BSTAR absolute synthetic spectra. Specifically, we obtained measurements between 0.353 and 2.1 μm in the standard Johnson photometric system (Ducati 2002), and measurements from Gaia DR3 (Gaia Collaboration 2020), and 2MASS (Cutri et al. 2003). We omitted clear outliers and multiple entries. For mea-

[1] `https://astro.troja.mff.cuni.cz/projects/respefo`

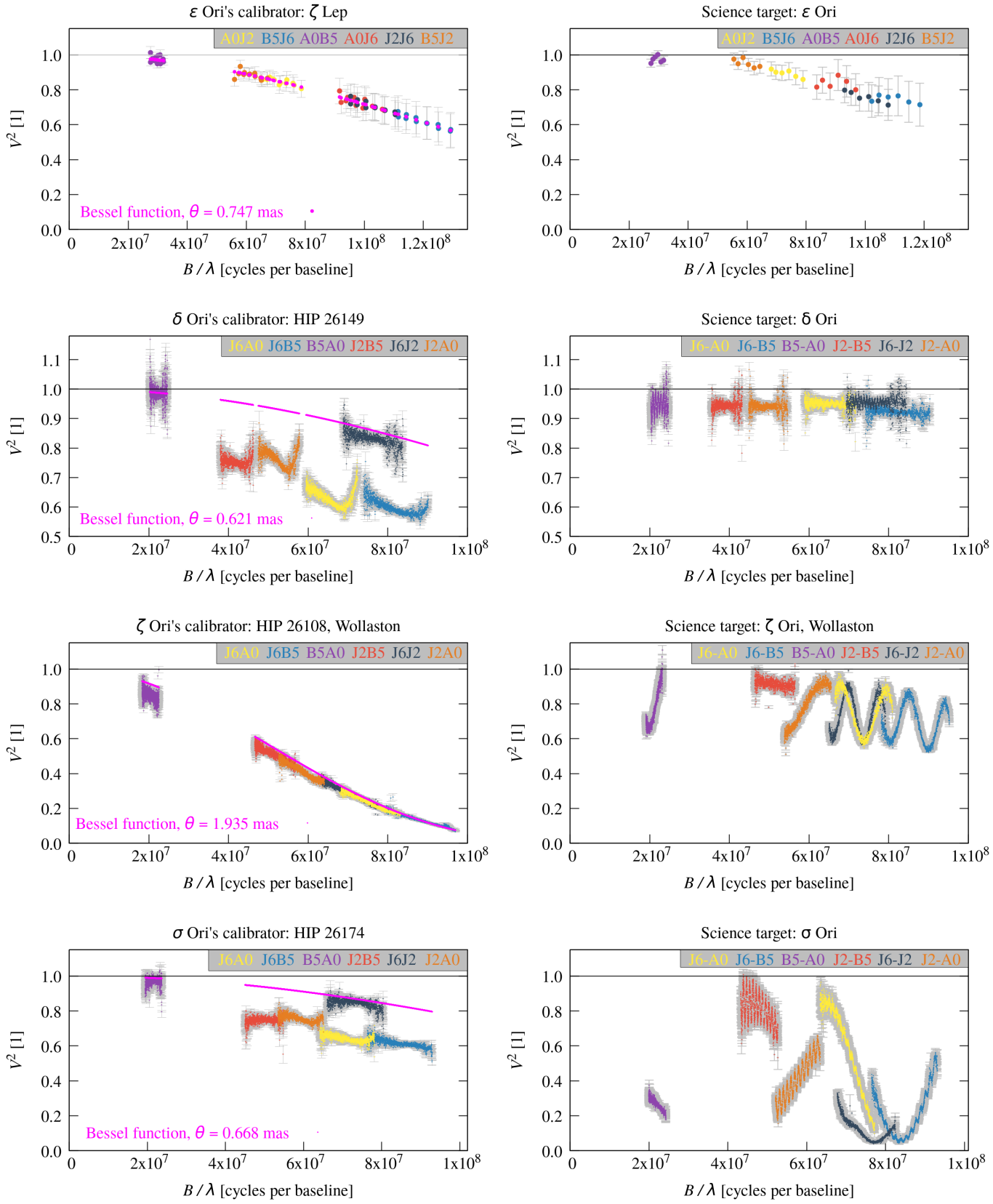

Fig. 2. Examples of raw visibilities of the calibrators and reduced squared visibilities V^2 of the science targets, ε, δ, ζ, and σ Ori. Measurements are from nights: 20 November 2023, 22 November 2023, 8 January 2024, 23 November 2023, respectively. Left column: calibrators and the corresponding Bessel functions with the calibrator's diameters plotted for reference (magenta). Right column: science targets with obvious signals from companions. For the single star ε Ori, the signal suggests an elongated or non-spherical shape, unlike the calibrator ζ Lep, which exhibits a perfectly spherical shape. Colours correspond to individual baselines.

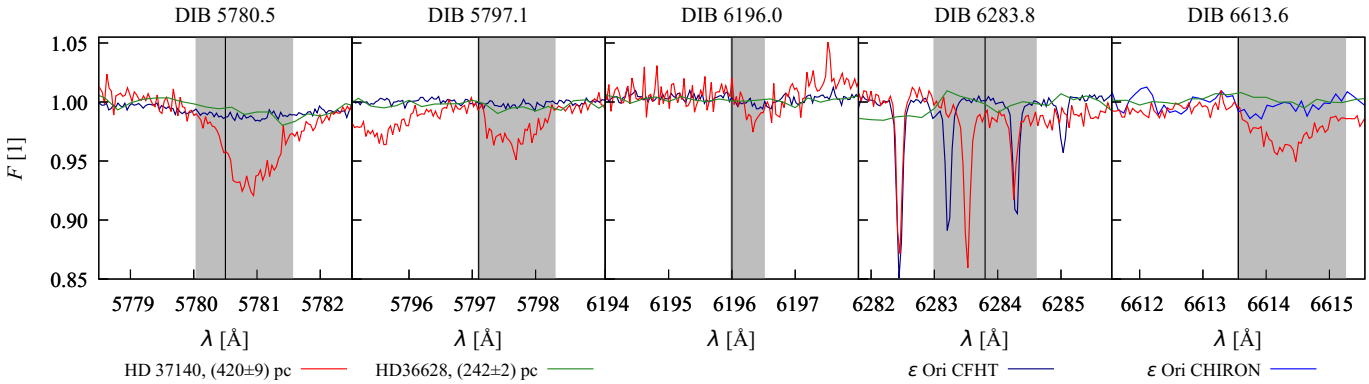

Fig. 3. Comparison of DIBs' intensities for ε Ori and stars which are close on the sky. (HD 37140, and HD 36628). The most distant star has the deepest DIBs, while the star with the lowest distance has very weak DIBs. The spectrum of ε Ori also shows weak DIBs, which suggests its distance is lower than 420 pc. The spectra were taken from public archives of CFHT and ESO.

surements without reported uncertainties, we assumed the value of 0.02 mag. Hipparcos measurements were not used due to underestimated systematic uncertainties. The final dataset contained 13 data points see Table C.1.

To compute the reddening E_{B-V} for ε Ori, we used the differential photometry measured in October 2006 and February 2024 (2454015.6–2460362.4 HJD) at the Hvar Observatory (Božić & Harmanec 2023), namely, the observed colour index $(B-V)_0 = -0.192$ mag. For the corresponding spectral type B0Ia, the intrinsic colour is $(B-V) = -0.240$, according to (Golay 1974), consequently, $E_{B-V} = 0.05$ mag and $A_V = 0.155$ mag, which is in agreement with Fan et al. (2017) and negligible in the infrared.

For the construction of SED, we also used calibrated UBV photometry from the Hvar differential archive. It contains 21 observations secured in 2006 by Petr Harmanec, Domagoj Ružđjak and Davor Sudar, and 4 observations secured during one night in 2024 by Hrvoje Božić. We use the mean values of all 25 observations, $U = 0.479 \pm 0.025$, $B = 1.487 \pm 0.034$, and $V = 1.679 \pm 0.018$. The SED data were calculated using the wavelengths from Bessell (2000) and calibration fluxes from Wilson et al. (2010). The resulting values of SED are in Table C.1.

2.4. Parallax

As ε Ori is too bright, it saturates Gaia's detector, designed primarily for stars fainter than $G = 6$ mag, and its parallax measurements are not reliable. Hipparcos parallaxes were less precise; Perryman et al. (1997) estimated the distance of 412 pc, while van Leeuwen (2007) 606 pc. Instead, in Opštilová et al. (2023), we used Gaia DR3 parallaxes of the faint stars in the same stellar association (Orion OB1b). We assumed that the most massive stars are located close to the median distance. Then the distance of ε Ori should be close to $d \simeq 384$ pc, which is just intermediate between the other Orion Belt stars, ζ Ori (386 pc) and δ Ori (381 pc).

As a verification, we checked diffuse interstellar bands (DIBs). Their strength depends on the interstellar medium, not on a spectral type, and is correlated with the colour excess E_{B-V}, which quantifies the amount of dust/reddening along the line of sight (Friedman et al. 2011). We assumed that the interstellar medium in the direction of ε Ori has similar properties to other stars close on the sky. We used the same methodology as Guinan et al. (2012); we selected two stars (Table 2) that are not in a dusty region according to the WISE map (Baumann et al. 2022) and have both Gaia parallaxes and high-resolution spectra in public archives. Then, we compared the strengths of their DIBs (Fig. 1). The star HD 37140 shows significant DIBs at the distance of (420 ± 9) pc, while HD 36628 shows no DIBs at (242 ± 2) pc. Thus, we verified that ε Ori is likely located at the distance <420 pc, and our previous estimate seems to be reasonable.

Similarly, the colour excess E_{B-V} is closely related to the distance. We thus computed E_{B-V} according to Johnson & Morgan (1953), using U, B, and V magnitudes from Blanco et al. (1970) and Mermilliod (1994), see Table 2. The colour excess of ε Ori is computed in Sect. 2.3 Moreover, according to Green et al. (2019)[2], there is a sudden 'jump' in reddening in this direction, occurring at a distance of 400 pc.

We conclude that the previous distance estimate of about 600 pc is certainly incorrect. The relation of E_{B-V}, the strengths of DIBs, and distance of ε Ori corresponds to our estimate, (384 ± 8) pc.

Table 2. Distances and reddening of stars, which are close to ε Ori on the sky. The corresponding DIBs observations are shown in Fig. 1.

Star	d [pc]	E_{B-V} [mag]	Spectral type
HD 37140	420 ± 9	0.256	B8 II*
ε Ori	384 (assumed)	0.050	B0 Ia
HD 36628	242 ± 2	0.030	B9 IV/V*

Notes. * Houk & Swift (1999)

3. ε Ori as a single star

We constructed a single-star model of the B0 Ia supergiant ε Ori using PHOEBE2[3] (Prša et al. 2016; Horvat et al. 2018; Jones et al. 2020; Conroy et al. 2020). PHOEBE2 employs seamless triangular meshes, closely following the generalised Roche potential. Each triangular element of the mesh is assigned local quantities (e.g. temperature, surface gravity, intensity, directional cosine). The total flux is then computed by integrating over visible elements. PHOEBE2 incorporates various stellar atmosphere models, which enables a realistic, self-consistent treatment of limb darkening, gravity darkening, as well as rotational

[2] http://argonaut.skymaps.info/
[3] http://phoebe-project.org

Table 3. Grid of almost spherical models for ε Ori assuming a fixed value of $v \sin i = 70\,\mathrm{km\,s^{-1}}$. Except for the temperature T, all the parameters were determined from interferometry. The values of χ^2_{VIS} do not exhibit a significant minimum, because the model is too constrained by $v \sin i$. Then, we kept the determined parameters fixed and fitted the temperature according to the spectroscopic data to find χ^2_{SPE}. However, synthetic line profiles were in all cases deeper than the observed ones. The model with the lowest χ^2_{VIS} and χ^2_{SPE} is in bold.

i [deg]	m [$\mathrm{M_\odot}$]	Ω [deg]	R_{equiv} [$\mathrm{R_\odot}$]	θ_{equiv} [mas]	P_{rot} [d]	v [km s^{-1}]	$v \sin i$ [km s^{-1}]	χ^2_{VIS} [1]	T [K]	χ^2_{SPE} [10^3]
14	**22.90**	**289.7**	**24.68**	**0.598**	**4.31**	**289**	**70**	**11.451**	**25384**	**13.4**
15	23.99	289.9	25.26	0.612	4.72	270	70	11.532	25363	14.7
20	26.06	289.9	26.32	0.638	6.51	205	70	11.658	26366	17.0
30	27.12	290.5	26.85	0.650	9.70	140	70	11.715	26718	18.5
40	27.43	299.4	27.00	0.654	12.55	109	70	11.732	26929	18.9
50	27.58	290.2	27.08	0.656	14.99	91	70	11.740	27962	20.1
60	27.66	299.1	27.12	0.657	16.97	81	70	11.743	27956	20.3
70	27.68	290.5	27.13	0.657	18.43	74	70	11.745	27198	19.3
80	27.68	290.1	27.13	0.657	19.31	71	70	11.747	28041	20.4
90	27.71	290.0	27.14	0.657	19.62	70	70	11.746	28050	20.4

Notes. i denotes the inclination of the spin axis with respect to the sky plane; m, mass; Ω, the orientation of star's equator, as seen by the observer; R_{equiv}, equivalent radius; θ_{equiv}, angular diameter; P_{rot}, rotational period; v, circumference velocity. For models based on interferometry, the parameters i, $\log g = 3.0$, $v \sin i = 70\,\mathrm{km\,s^{-1}}$, $T = 25\,000$ K were fixed, while m, Ω were free.

Table 4. Grid of non-spherical models of ε Ori without a $v \sin i$ constraint. Otherwise, χ^2_{VIS} and χ^2_{SPE} were computed as in Table 3. The best-fit model based on interferometry is shown in Fig. 6, while the one based on spectroscopy is in Fig. 7.

i [deg]	m [$\mathrm{M_\odot}$]	Ω [deg]	R_{equiv} [$\mathrm{R_\odot}$]	θ_{equiv} [mas]	P_{rot} [d]	v [km s^{-1}]	$v \sin i$ [km s^{-1}]	χ^2_{VIS} [1]	T [K]	χ^2_{SPE} [10^3]
0	23.75	306.1	25.20	0.610	4.85	None	0	12.188	25300	71.7
10	23.87	307.2	25.26	0.612	4.80	266	46	11.949	25283	31.7
20	**21.47**	**290.2**	**23.96**	**0.580**	**3.99**	**304**	**104**	**10.273**	**24537**	**1.9**
30	23.46	300.6	25.04	0.607	4.07	311	155	8.734	23970	15.4
40	24.96	308.1	25.83	0.626	4.14	316	203	7.363	23378	43.0
50	26.73	300.8	26.73	0.648	4.21	321	246	6.959	22747	68.1
60	**28.18**	**301.3**	**27.45**	**0.665**	**4.27**	**325**	**282**	**6.929**	**22282**	**85.8**
70	28.58	300.7	27.64	0.669	4.28	326	307	6.967	21997	96.1
80	28.27	298.6	27.49	0.666	4.36	319	314	7.222	22018	100.0
90	28.16	298.1	27.44	0.665	4.44	312	312	7.339	22192	100.0

Notes. The parameters i (range of value), $\log g = 3.011$, and $T = 24985$ were fixed, while m, Ω, P_{rot} free.

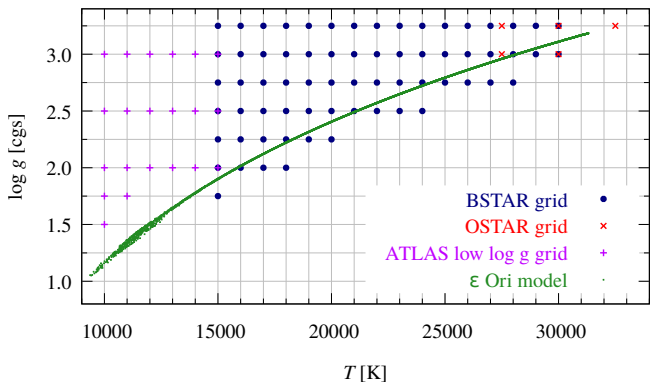

Fig. 4. Grids of synthetic spectra BSTAR and OSTAR (Lanz & Hubený 2003; Lanz & Hubený 2007), used in our spectroscopic models. Each spectrum is parametrised by $\log g$ and T. In order to describe also critically rotating stars (cf. green points), it was necessary to compute additional ATLAS spectra (Castelli & Kurucz 2003) for low values of $\log g$ and T.

distortion. It is a powerful tool for solving an inverse problem, constrained by light curves and radial velocity curves, and recently, it was extended to include interferometry, spectra, and SED.

A new interferometric module of PHOEBE2[4] (Brož et al. 2025b) enables computations of interferometric observables—squared visibility (V^2), closure phase ($\arg T_3$), and amplitude ($|T_3|$)—by means of the Fourier transform approach. Additionally, a new spectroscopic module (Brož et al. 2025a) utilises interpolations in grids of synthetic spectra, assigning one spectrum to each element. Again, the total spectrum is obtained by integrating over all elements, weighted by appropriate passband intensities. It allows fitting of detailed spectral line profiles.

Visibility. First, we modelled ε Ori as a spherical star with fixed radiative parameters according to Puebla et al. (2016a), namely, $T = (27\,000 \pm 500)$ K and $\log g = (3.00 \pm 0.05)$ that they estimated by the fitting of line profiles of H_β, H_γ, H_δ, H_ε. In PHOEBE2, we set the Kurucz atmospheres, but linear limb darkening coefficient $c_1 = 0.01621$ interpolated from van Hamme (1993) tables for comparison purposes (see below). We assumed the distance $d \simeq 384$ pc, as discussed in Sect. 2.4. We verified the computation of V^2 using the independent implementation of Brož (2017). The fitting of V^2 from PIONIER and the convergence of one

[4] https://github.com/miroslavbroz/phoebe2

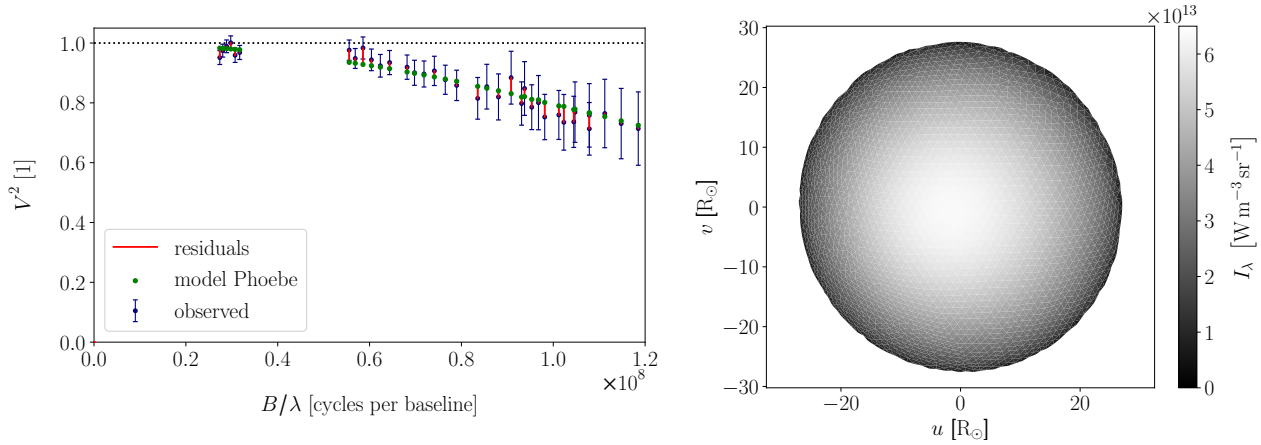

Fig. 5. Almost spherical model of ε Ori based on PIONIER observations in passband Johnson:H. Left: squared visibility vs. projected baseline B/λ; right: corresponding triangular mesh with the passband intensities (grayscale). fixed $v \sin i$ (Puebla et al. 2016b) The model was converged starting with the parameters from Table 3 (bold line). The best-fit was with $\chi^2_{\rm VIS} = 11.23$. The free parameters were $i = 13.6$ deg, $m = 20.3\,{\rm M}_\odot$, $\Omega = 293.7$ deg, $P_{\rm rot} = 4.01$ d; the fixed parameters, $v \sin i = 70\,{\rm km\,s^{-1}}$, $T = 25\,000$ K, $\gamma = 25.9\,{\rm km\,s^{-1}}$; and the derived parameters, $v = 298\,{\rm km\,s^{-1}}$, $R_{\rm equiv} = 22.43\,{\rm R}_\odot$ (derived), $R_{\rm pole} = 22.29\ {\rm R}_\odot$ (derived), $R_{\rm equ} = 22.46\ {\rm R}_\odot$ (derived), $\theta_{\rm equiv} = 0.543$ mas. The star is close to critical rotation and has almost pole-on orientation in order to decrease projected rotation (cf. $v \sin i$).

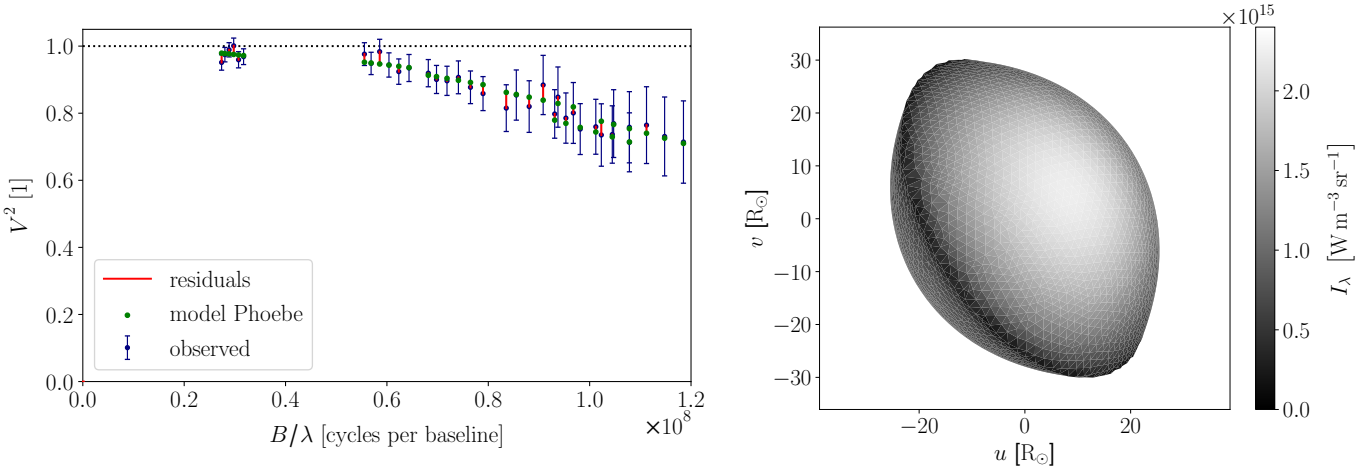

Fig. 6. The same as Fig. 5, but with free $v \sin i$. The model was converged starting with the parameters from Table 4. The best fit model was with $\chi^2_{\rm VIS} = 6.928$. The free parameters were $i = 58.3°$, $m = 28.0\,{\rm M}_\odot$, $\Omega = 301.5$ deg, $P_{\rm rot} = 4.26$ d; the fixed parameters, $T = 27\,000$ K, $\gamma = 25.9\,{\rm km\,s^{-1}}$; and the derived parameters, $v \sin i = 277\,{\rm km\,s^{-1}}$, $v = 325\,{\rm km\,s^{-1}}$, $R_{\rm equiv} = 27.37\,{\rm R}_\odot$, $R_{\rm pole} = 22.29\,{\rm R}_\odot$, $R_{\rm equ} = 33.61\,{\rm R}_\odot$, $\theta_{\rm equiv} = 0.667$ mas, $\theta_{\rm pole} = 0.540$ mas, and $\theta_{\rm equ} = 0.814$ mas. Again, the star is close to the critical rotation, but with an oblique orientation. This model better explains the visibilities along different baselines $\boldsymbol{B}/\lambda$. The meaning of Ω is illustrated.

free parameter (m) using the simplex method (Nelder & Mead 1965) resulted in exactly the same $\chi^2_{\rm VIS} = 12.1$ in both codes (Fig. D.3). The χ^2 value is smaller than the number of degrees of freedom $\nu = N - M = 35$, which most likely indicates overestimated uncertainties of PIONIER observations. In fact, previous PIONIER observations were more precise (Pietrzyński et al. 2019). If the uncertainties are properly rescaled, the best-fit mass is $m = (23.5 \pm 0.5)\,{\rm M}_\odot$, corresponding to the angular diameter $\theta = (0.615 \pm 0.007)$ mas and physical radius $R = (25.4 \pm 0.3)\,{\rm R}_\odot$.

Second, we modelled a rotating, almost spherical star. For simplicity, we used black-body atmospheres to avoid problems with too low $\log g$ values, occurring when the star is close to the critical rotation (cf. Fig. 4). Nevertheless, we derived the limb darkening coefficients from the Kurucz atmospheres and set them manually, with a power-law prescription (Prša et al. 2016)

$$\frac{I}{I_0} = 1 - c_1(1-\mu^{\frac{1}{2}}) - c_2(1-\mu) - c_3(1-\mu^{\frac{2}{3}}) - c_4(1-\mu^2)\,, \quad (4)$$

where $c_1 = 1.698$, $c_2 = -4.151$, $c_3 = 5.887$, $c_4 = -2.525$ are suitable for the temperature $T = 27\,000\,K$ and $\log g = 3.0$ (Puebla et al. 2016a). We set the bolometric gravity brightening exponent $\beta = 1.0$, which corresponds to hot stars ($T > 8000$ K), assuming that the local temperature is proportional to

$$T = T_{\rm pole}\,(g/g_{\rm pole})^{0.25\beta}\,, \quad (5)$$

where g is the local gravitational acceleration. To reveal all possible minima of χ^2, we computed a more detailed grid in inclination of the rotation axis (hereafter only 'inclination') i. The orientation of the star is also determined by Ω, longitude of the ascending node (of the equator). We made the parameters m and Ω free, the parameters $\log g$, d, $v \sin i$ (and i) fixed, while the dependent parameters $P_{\rm rot}$, $R_{\rm equiv}$, $\theta_{\rm equiv}$ were constrained by the following relations

$$P_{\rm rot} = \frac{2\pi R_{\rm equiv}}{v \sin i}\sin i\,, \quad (6)$$

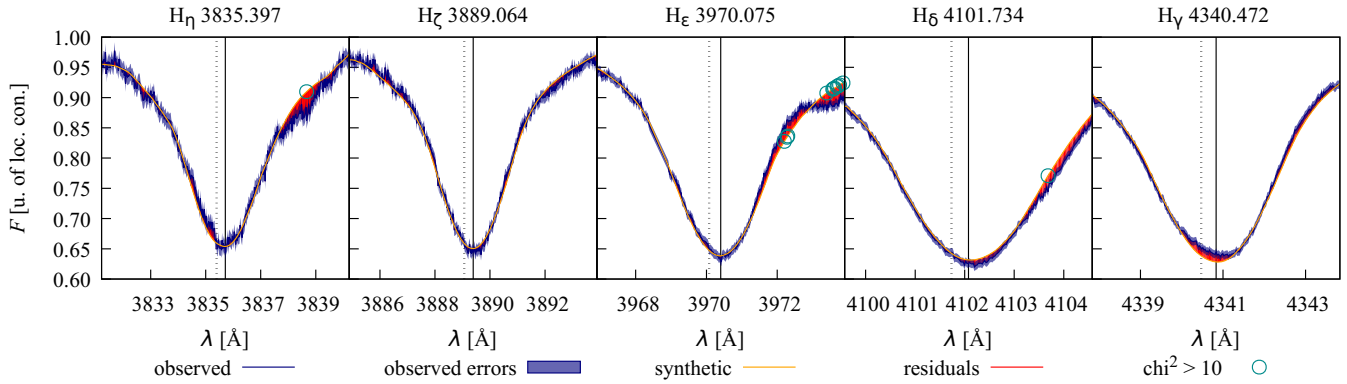

Fig. 7. Almost spherical model of ε Ori based on CFHT spectroscopy. Hydrogen Balmer lines were fitted using 1443 data points, excluding H_α and H_β, which are 'filled' by wind-induced emission. An interstellar calcium 3968 Å for H_ε was masked. The best fit resulted in $\chi^2_{\rm SPE} = 1770$. Free parameters were $P_{\rm rot} = 4.551$ d, $T = 25037$ K, $\log g = 3.016$, $i = 21.40$ deg, and $\gamma = 25.00\,{\rm km\,s^{-1}}$. Other parameters were fixed and set according to interferometry. The derived parameters were $v \sin i = 111\,{\rm km\,s^{-1}}$ and $v = 305\,{\rm km\,s^{-1}}$. The dotted lines show laboratory wavelengths, while the solid vertical lines indicate the Doppler-shifted line centres, corresponding to the resulting γ. The teal circles denote the points that contributed to χ^2 with values greater than 10. This model explains reasonably well the Balmer lines, with a few systematics remaining in H_ε, H_η, possibly due to different metal abundances. The temperature was constrained, and $\log g$ was slightly adjusted. However, due to the difference in inclination ($i = 21$ vs. 62 deg), the interferometric model would become worse, with $\chi^2_{\rm VIS} = 16.04$.

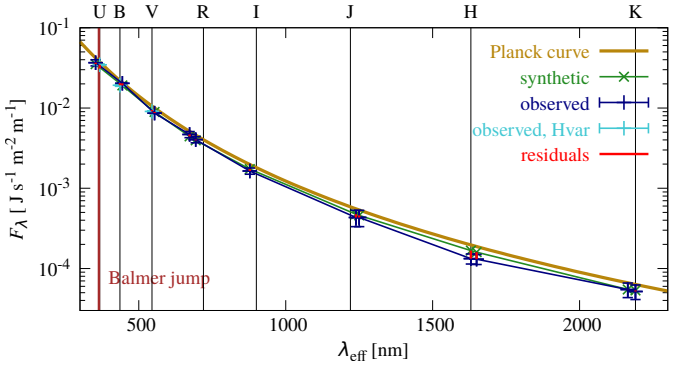

Fig. 8. SED model of ε Ori based on data from the Hvar Observatory and Vizier—the monochromatic flux F_λ vs. wavelength λ. The best-fit value was $\chi^2_{\rm SED} = 52$ with the following parameters: $T_{\rm eff} = 24\,654$ K (fitted), $d = 384$ pc (fixed), $M = 28.43\,{\rm M}_\odot$ (fixed), $R = 27.45\,{\rm R}_\odot$ (derived); other parameters were fixed and set according to interferometry. This model served as an independent verification of the temperature from the spectroscopic model.

$$R_{\rm equiv} = \sqrt{\frac{Gm}{g}}\,, \tag{7}$$

$$\theta_{\rm equiv} = \frac{2R_{\rm equiv}}{d}\,, \tag{8}$$

where the value of $v \sin i$ was set up to $70\,{\rm km\,s^{-1}}$ (Puebla et al. 2016a).

The converged models for fixed values of i are listed in Table 3. Unfortunately, the models were too constrained by the fixed value of $v \sin i$; the $\chi^2_{\rm VIS}$ dependence on i remained flat over the full range of i. Formally, the lowest $\chi^2_{\rm VIS}$ value is for the lowest inclination, $i = 14$ deg. Lower values of i cause problems in modelling of edges. For the best-fit model, converged from parameters with the lowest $\chi^2_{\rm VIS}$, see Fig. 5. It is a almost spherical star close to critical rotation, with almost pole-on orientation.

To obtain a model that best corresponds to the measured squared visibilities, we relaxed the $v \sin i$ constraint and computed another grid in i, using still only the interferometric data. In this case, there were three free parameters, m, Ω, and $P_{\rm rot}$. Our results are summarised in Tab. 4. Fortunately, $\chi^2_{\rm VIS}$ substantially decreased, from 12.2 down to 6.9, and the best-fit model is again a critically rotating star, seen at an oblique inclination of $i = (58 \pm 20)$ deg (see Fig. 6). On the other hand, the nominal projected velocity, $v \sin i = 277^{+30}_{-80}\,{\rm km\,s^{-1}}$, seems to be too high.

Spectroscopy. To constrain radiative parameters, which were only assumed in the previous interferometric models, we used the spectra from CFHT. First, we checked the influence of i, i.e. $v \sin i$, on synthetic line profiles, by computing forward models for the Balmer lines, H_γ, H_δ, H_ε, H_ζ, H_η, that are not much influenced by the wind (Puebla et al. 2016a). We used narrow ranges of wavelengths ($\pm 3, \pm 2.5, \pm 4, \pm 5, \pm 5$) Å, respectively, in order to eliminate neighbouring lines. Also, we masked one remaining interstellar calcium line 3968 Å near H_ε. In PHOEBE2, we set `spe_method` to 'integrate' and set the interpolation to nearest-neighbour, to remain within the respective grid (Fig. 4) and prevent excessive extrapolation. Furthermore, we computed additional ATLAS synthetic spectra (Castelli & Kurucz 2003)[5] for low values of $\log g$ and T, to describe critically rotating stars.

The resulting $\chi^2_{\rm SPE}$ values for fixed $v \sin i$ are listed in Table 3 and for relaxed $v \sin i$, in Table 4. The $\chi^2_{\rm SPE}$ contribution to the total χ^2 is more than 3 orders of magnitude larger than $\chi^2_{\rm VIS}$ because of the number of measurements. While $\chi^2_{\rm SPE}$ and $\chi^2_{\rm VIS}$ are the lowest for $i = 14$ deg in the models with fixed $v \sin i$, there is a tension between spectra and visibilities for models with relaxed $v \sin i$, which describes the interferometric data much better.

For comparison, we reconverged a model based only on spectroscopy, starting from the parameters with the lowest $\chi^2_{\rm SPE}$ in Tab. 4 (bold); again with relaxed $v \sin i$. The best-fit model is shown in Fig. 7, corrsponding to $\chi^2_{\rm SPE} = 1797$. The free parameters and their resulting values were $P_{\rm rot} = 4.535$ d, $T = 24915$ K, $\log g = 3.01$, $i = 21.0$ deg. Other parameters were fixed and set according to interferometry. The derived projected velocity,

[5] https://github.com/RozanskiT/vidmapy

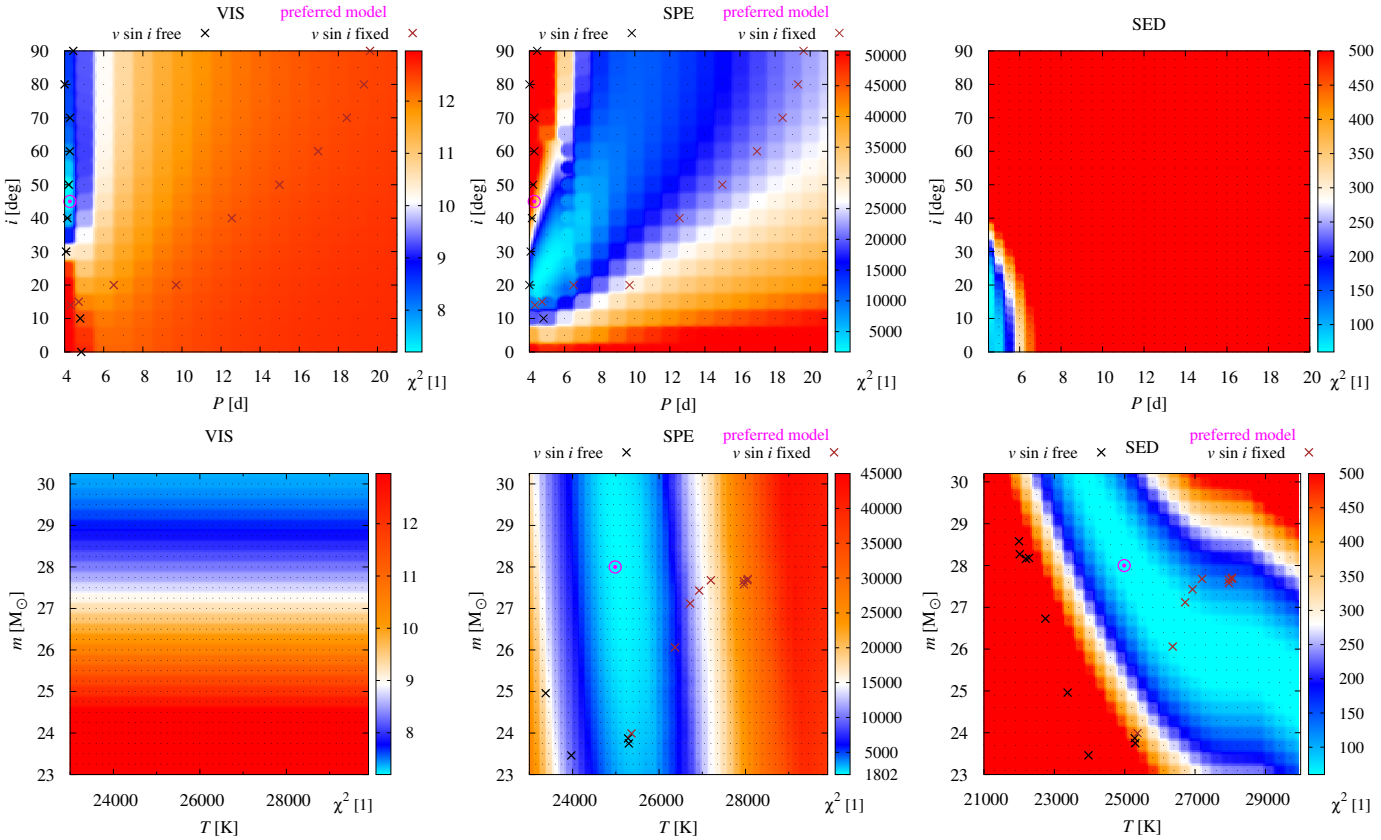

Fig. 9. Maps of χ^2 for the ε Ori model. We performed 2D mapping of χ^2 across different datasets: squared visibilities (VIS), spectral lines of Balmer series (SPE), and spectral energy distribution (SED). We systematically varied two parameters to create a regular grid ($P_{\rm rot}$ vs. i in the first row, T vs. m in the second row). The remaining parameters were held fixed. The colour scale was adjusted as follows: cyan—the best fit for a given data set, blue—acceptable fits, white—poor fits, orange—unacceptable fits, red—forbidden regions. In the first row, the fixed parameters are those resulting from the best fit of interferometric data in Fig. 6: d, m, and Ω; other fixed parameters are $T = 25\,000$ K, $\log g = 3.011$, and $\gamma = 25.9$ km s^{-1}. The dependent parameters were $R_{\rm equiv}$ and $v \sin i$. In the second row, we set $P_{\rm rot}$ and i according to the best fit in the first row. The individual panels, from the upper left, are as follows: I) VIS dataset shows a preference for a critically rotating star and i around 45 deg. II) SPE dataset (H lines) shows a preference for a fast-rotating star, $P_{\rm rot} = 5$ d, $i = 25$ deg. The correlation between $P_{\rm rot}$ and i is due to rotation and $v \sin i$. III) SED dataset also allows a critically or fast-rotating star for i close to 20 deg. However, it is possible to re-fit T, R, or d to achieve improved SED fits in other regions of the parameter space. IV) VIS dataset shows a flat dependence on temperature and the preferred mass. V) SPE dataset for H lines demonstrates a weak correlation between T and m, the best-fit of T is around 25 000 K. VI) SED dataset is strongly correlated between T and m due to the Stefan–Boltzmann law and Eq. (7). The crosses mark the models from Tables 3 and 4.

$v \sin i = 111$ km s^{-1}, is substantially lower. A forward model based on parameters from interferometry, with higher $v \sin i$, gives smeared lines, while the observed lines are sharper.

Closure phase. Unfortunately, even though closure phases are very useful to detect photocentre offsets, the observed amplitude from PIONIER seems to be too high (up to 4 deg) compared to any of our models. Even critically rotating stars, which have the largest differences of polar-to-equatorial temperatures, exhibit synthetic amplitudes less than 0.1 deg (Fig. D.4). Nevertheless, taking into account only the signs and trends of arg T_3 vs. λ, synthetic closure phases should change in the same sense as observed ones, which allowed us to resolve the Ω ambiguity (120 vs. 300 deg) in Sect. 3.

SED. As an independent check, we computed the PHOEBE2 model for the SED (using again the new module). As synthetic spectra, we used the absolute fluxes from the BSTAR, OSTAR, and ATLAS grids. The observed SED values were discussed in Sect. 2.3. We converged only the effective temperature $T_{\rm eff}$. Other parameters were fixed according to the model based on interferometry (from Fig. 6). The resulting value was $T_{\rm eff} = 24\,880$ K, which is very close to the value inferred from the fitting of Balmer lines. Our model was in good agreement with the observed SED; see Fig. 8.

Compromise model. Finally, we computed two-dimensional χ^2 maps to better understand mutual relations between datasets (see Fig. 9). We always distinguished individual contributions to χ^2, namely from interferometry (VIS), spectroscopy (SPE) and SED (SED). In each panel, we were changing only two parameters to get a regular grid, while others parameters are kept fixed. For mapping, we chose the period $P_{\rm rot}$ from 4 d to 20 d with the step of 0.5 d vs. the inclination i from 0 deg to 90 deg with the step of 5 deg. Alternatively, we chose the temperature T from 21 000 K to 30 000 K with the step of 500 K vs. the mass m from 21 $M_\odot$ to 32 $M_\odot$ with the step of 0.5 $M_\odot$. Let us recall that m is always related to $R_{\rm equiv}$ (Eq. (7)).

The VIS maps with squared visibility measurements show a preference for a critically rotating, oblate star, seen at an oblique angle (40 to 60 deg). On the other hand, there is a negligible dependence on temperature. A higher mass (28 to 30 $M_\odot$) is preferred, but this is certainly correlated with the distance (Eq. (8)).

The SPE maps with Balmer lines demonstrate that only lower inclinations can appropriately fit the depth and width of spectral lines. There is a weak correlation between the mass and temperature, indicating the appropriate temperature is around 25 000 K and not well-constrained mass.

The SPE maps based on He I lines (Fig. 10) is quite similar. Although there is a correlation of good fits between i and $P_{\rm rot}$, we see a possible solution for a fast-rotating star, with a similar inclination to that derived from the Balmer lines. Again, the mass and temperature are weakly correlated, indicating the temperature 25 000 K. (The fits around 28 000 K resulted in poorer line depths.)

The SED maps are, of course, strongly influenced by the fixed temperature and mass, but show good solutions for a critically rotating star, with a similar inclination as for spectra. The mass and temperature are strongly correlated.

We conclude that the inclination is the only uncertain parameter, for which the results differ according to interferometry (40 to 60 deg) vs. spectroscopy (10 to 30 deg). Other parameters correspond to all three kinds of observations. As a compromise, we prefer the value around 40 deg, which partly explains both the interferometry and the spectroscopy. The resulting parameters of ε Ori are summarised in Table 5.

4. Discussion

Our interferometry of ε Ori can be compared to Abeysekara et al. (2020), who acquired intensity interferometry in B band. Their limb-darkened angular diameter, $\theta_{\rm LD} = (0.660 \pm 0.018)$ mas, is in perfect agreement with our measurements in H band (Tab. 5).

However, as discussed in Sect. 3, the observed closure phases are high (up to 4 deg) compared to our model. This raises the question: what could be missing in our model?

Possible binarity. Such a modest amplitude in closure phases indicates a flux asymmetry with low contrast, up to $4° = 0.07$ rad $= 7\%$, in the Johnson:H passband. For this estimate, we assumed a maximally asymmetric object (i.e. a binary) and used the following closure phase approximation, $\arg T_3 \approx F_2/F_1 \sin\left(2\pi\frac{B\phi}{\lambda}\right)$, where F_1, F_2 denote the fluxes of the two stars and ϕ the angular scale. Based on this, we estimated the mass of the companion, assuming that it is on the main sequence, to $\sim$12 $M_\odot$. To explain the observed dependence on B/λ, the angular scale should be of the order of 0.5 mas, corresponding to $\sim$40 $R_\odot$. From this, we estimated the orbital period, $P = 2\pi\sqrt{a^3/(GM)} \approx 6$ d, assuming the total mass $\sim$30 $M_\odot$, i.e. of the same order as the primary. RV amplitudes for the primary and secondary are of the order of a hundred km s^{-1}, but these could be suppressed by orbit orientation (e.g. for $i = 5°$, 15 km s^{-1}). In the dataset of Thompson & Morrison (2013), there are RV variations of this order observed in the He I 5876 Å line. However, they are not persistent, and they cannot be phased with a fixed period. Only for one season, Thompson & Morrison (2013) reported a period of about 5 d. In the context of our model, this could correspond to the rotation period of the primary, or even more likely, to the variability of circumstellar material.

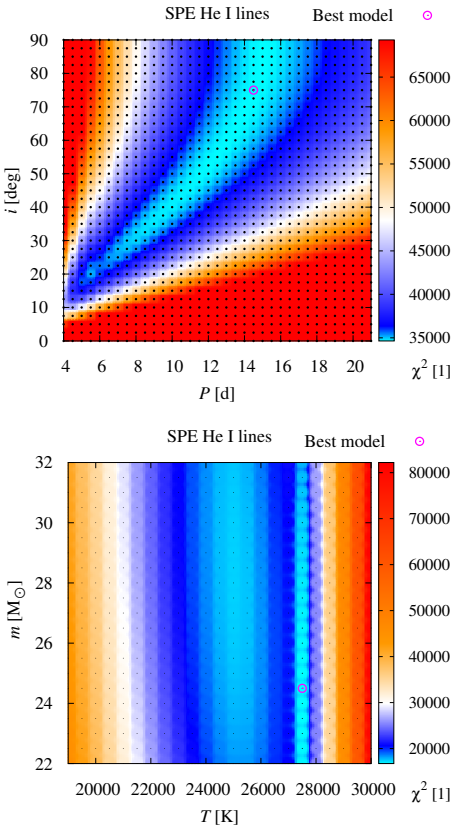

Fig. 10. The same as Fig. 9, but for the spectroscopic dataset based on He I lines. Top: SED dataset for He I lines exhibits results very similar to spectroscopy based on Balmer lines. The higher $P_{\rm rot}$ and i values are excluded because of other datasets. Bottom: SED dataset for He I lines, indicating two possible solutions at $T = 25\,000$ K or 27 500 K due to systematic offsets in some lines. The model with $T = 25\,000$ K fits better the depths of He I lines. The map also shows no preference for the mass.

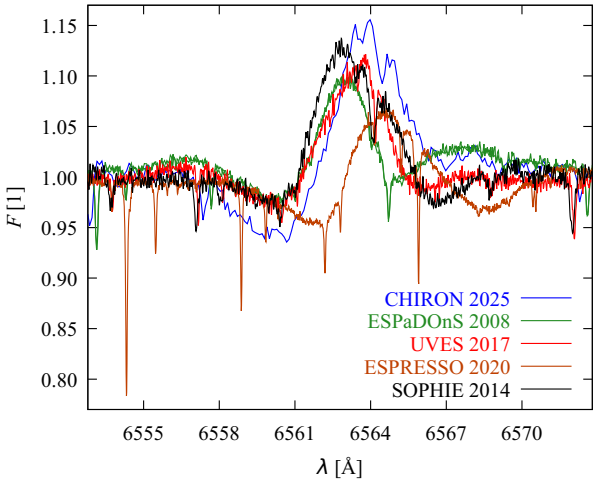

Fig. 11. Spectroscopy of ε Ori showing the H_α line profile that is highly variable and can be in several morphologies, like P Cygni profile, inverse P Cygni profile, double emission, or pure emission (Thompson & Morrison 2013). It implies an intense wind (e.g. Puebla et al. 2016b), or a deccretion disk fed by mass loss from the star. This variable line was not used in our modelling.

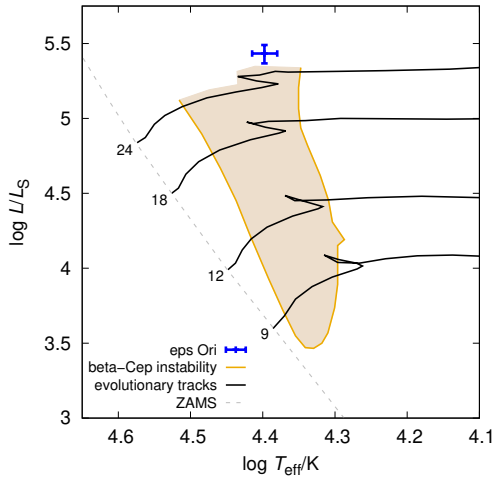

Fig. 12. Hertzsprung–Russel diagram showing the position of ε Ori (blue) in comparison to the β-Cep instability region ($\ell = 0$; orange) and several evolutionary tracks (black) from Paxton et al. (2015). Note that the instability was computed only up to 24 $M_\odot$, but the region most likely continues upwards, and the instability also occurs for the luminosity class Ia ($\log L/L_\odot \geq 5.3$).

Table 5. Resulting parameters of ε Ori based on a compromise among interferometry, spectroscopy, and SED.

Parameter	Value	Uncertainty	Unit	Note
m	28.42	2.0	$M_\odot$	fitted
$P_{\rm rot}$	4.27	$^{+1.0}_{-0.0}$	d	fitted
i	45	20	deg	fitted
Ω	301.6	30	deg	fitted
d	384	8	pc	fixed
$T_{\rm eff}$	24985	1000	K	fixed
$\log g$	3.011	0.1	cgs	fixed
β	1.0	0.1	1	fixed
γ	25.0	0.9	km s^{-1}	derived
$\gamma_{\rm LSR}$	8.2	0.7	km s^{-1}	derived
$R_{\rm equiv}$	27.36	1.5	$R_\odot$	derived
$R_{\rm pole}$	22.29	1.2	$R_\odot$	derived
$R_{\rm equ}$	33.61	1.8	$R_\odot$	derived
$\theta_{\rm equiv}$	0.667	0.035	mas	derived
$\theta_{\rm pole}$	0.540	0.064	mas	derived
$\theta_{\rm equ}$	0.814	0.073	mas	derived
L	271 000	38 000	$L_\odot$	derived
$v \sin i$	220	$^{+40}_{-100}$	km s^{-1}	derived
v	326	$^{+50}_{-120}$	km s^{-1}	derived
f	1.47	0.35	rad/d	derived

Notes. m denotes the mass; $P_{\rm rot}$, the rotation period; i, the inclination of the stellar rotation axis with respect to the sky; Ω, the longitude of the ascending node of the star (i.e. equator); d, the distance; $T_{\rm eff}$, the effective temperature; $\log g$, the logarithm of surface gravity; β, bolometric gravity brightening exponent; γ, the systemic velocity; $\gamma_{\rm LSR}$, the systemic velocity with respect to the local standard of rest; $R_{\rm equiv}$, the equivalent radius; $R_{\rm pole}$, the pole radius; $R_{\rm equ}$, the equatorial radius; $\theta_{\rm equiv}$, the equivalent angular diameter; $\theta_{\rm pole}$, the polar angular diameter; $\theta_{\rm equ}$, the equatorial angular diameter; L, the luminosity; $v_{\rm rot} \sin i$, the projected rotation velocity; $v_{\rm rot}$, the rotation velocity; and f, the rotation frequency.

Wind. Another asymmetry could be related to wind (Puebla et al. 2016b), if the material expelled from ε Ori is not evenly distributed, but concentrated in relatively dense clumps. This phenomenon is especially relevant for hot, massive stars like B supergiants, O-type stars, or Wolf-Rayet stars (Puls et al. 2008; Krtička et al. 2021). Only if clumps are locally optically thick in the Johnson:H passband, they contribute to the respective continuum flux and the closure phase signal observed by PIONIER. Otherwise, wind is observed in H_α line (Fig. 11), which is highly variable and exhibits a range of morphologies, from a classical P Cygni profile, an inverse P Cygni profile, double emission, to pure emission (see also Thompson & Morrison 2013, Fig. 1).

Disk. An additional asymmetry might be produced by an unresolved disk, fed by mass loss from the star, and partially eclipsed by the star. If this is the source of the double emission sometimes observed in the wings of H_α (Fig. 11), the redshift and the blueshift, $\Delta\lambda \simeq 6$ Å, are interpreted as rotation, $\Delta v = \Delta\lambda/\lambda\, c = 274\,{\rm km\,s^{-1}}$. This is surprisingly similar to the projected velocity $v \sin i$ in our models of ε Ori. Finally, if the star is close to critical rotation, as indicated by the PIONIER observations, we naturally expect an ongoing outflow from the equator.

Pulsations. Moreover, ε Ori is close to the β Cep instability region (Paxton et al. 2015) for low-order modes $\ell = 0, 1, 2$ (see Fig. 12). Photometric observations of ε Ori seem to be compatible with typical periods ranging from 0.1 to 0.6 d, and the amplitudes ~0.1 mag for β Cep variables (Lesh & Aizenman 1978). Such pulsations can enhance mass loss, especially if the star is rotating near its critical velocity. On the other hand, the periodograms for BRITE light curves or for RVs do not exhibit distinct peaks Krtička & Feldmeier (2018); Thompson & Morrison (2013), so their interpretation is stochastic, episodic activity due to mass loss.

Stellar evolution. If we—for the moment—assume a standard stellar evolution model for a 28.4 $M_\odot$, rotating star, it takes ~7.3 My to evolve from the zero-age main sequence to B0Ia (Ekström et al. 2012; Paxton et al. 2013). This is about 25% longer than for a non-rotating star due to enhanced mixing and homogenised composition. For comparison, there are two groups of low-mass, young stellar objects (YSOs) observed in the vicinity of ε Ori, denoted 'Orion C' and 'Orion D' (Kounkel et al. 2018). Their ages span from approximately 0.3 to 5.5 My. They were classified as Class II or III, as some are still accreting and associated with translucent gas clouds (Briceño et al. 2005). This implies either that the stellar evolution for ε Ori was non-standard, e.g. with extreme mass loss, or the formation of low- and high-mass stars was not *eodem loco et tempore*. Additionally, both the distance and the systemic velocity of ε Ori (384 pc and 8 km s^{-1}; measured with respect to the local standard of rest) seem to be in the middle, between Orion C and Orion D groups (Kounkel et al. 2018, Fig. 11). This relation might suggest that high-mass stars form either a bit earlier than low-mass stars or elsewhere (Sanhueza et al. 2017; Maud et al. 2018).

5. Conclusions

We obtained and calibrated VLTI/GRAVITY and PIONIER interferometric data for the brightest stars in the Orion Belt, the closest star-forming region. In this first paper, we modelled the supergiant ε Ori based on VLTI/PIONIER visibility data, CFHT and CTIO spectra, and absolute fluxes. While the models based on interferometry indicate an oblate, critically rotating star, the models based on spectroscopy indicate a fast-rotating, less oblate star. The fast rotation might imply that ε Ori is a merger.

We also discussed the possibility of binarity, based on the asymmetry visible in closure phase data. However, due to the lack of consistent radial velocity variations, we excluded this binary model. We rather attributed the asymmetry to the clumped stellar wind or possibly to a deccretion disk. To better constrain its properties, it is necessary to observe ε Ori with a spectro-interferometer such as CHARA/SPICA (Mourard et al. 2024), which is capable of scanning across the H_α line.

In a forthcoming second paper, we will focus on the multiple stellar systems in the Orion Belt.

Acknowledgements. A.O. was supported by GA UK grant no. 113224 of the Grant Agency of Charles University. M.B. was supported by GA ČR grant no. 25-16507S of the Czech Science Foundation. We thank other observers at the Hvar Observatory, Hrvoje Božić, Domagoj Ruždjak, and Davor Sudar for securing data for ε Ori.

References

Abbott, R., Abbott, T. D., Abraham, S., et al. 2021, ApJ, 913, L7
Abeysekara, A. U., Benbow, W., Brill, A., et al. 2020, Nature Astronomy, 4, 1164
Allen, M. G., Ochsenbein, F., Derriere, S., et al. 2014, in Astronomical Society of the Pacific Conference Series, Vol. 485, Astronomical Data Analysis Software and Systems XXIII, ed. N. Manset & P. Forshay, 219
Almeida, L. A., Sana, H., de Mink, S. E., et al. 2015, ApJ, 812, 102
Anderson, E. & Francis, C. 2012, Astronomy Letters, 38, 331
Atri, P., Miller-Jones, J. C. A., Bahramian, A., et al. 2019, MNRAS, 489, 3116
Baumann, M., Boch, T., Pineau, F.-X., et al. 2022, in Astronomical Society of the Pacific Conference Series, Vol. 532, Astronomical Data Analysis Software and Systems XXX, ed. J. E. Ruiz, F. Pierfedereci, & P. Teuben, 7
Bessell, M. 2000, in Encyclopedia of Astronomy and Astrophysics, ed. P. Murdin, 1939
Blanco, M., Demers, S., & Douglass, G. G. 1970, Photoelectric catalogue - Magnitudes and colors or stars in the U, B, V and Uc, B, V systems
Božić, H. & Harmanec, P. 2023, Highlights of a half century of the UBV photometry at Hvar
Briceño, C., Calvet, N., Hernández, J., et al. 2005, AJ, 129, 907
Brož, M. 2017, ApJS, 230, 19
Brož, M., Prša, A., Conroy, K. E., & Abdul-Masih, M. 2025a, A&A in prep.; https://arxiv.org/abs/2506.20868 [arXiv:2506.20868]
Brož, M., Prša, A., Conroy, K. E., Opištilová, A., & Horvat, M. 2025b, A&A in prep.; https://arxiv.org/abs/2506.20865 [arXiv:2506.20865]
Castelli, F. & Kurucz, R. L. 2003, in IAU Symposium, Vol. 210, Modelling of Stellar Atmospheres, ed. N. Piskunov, W. W. Weiss, & D. F. Gray, A20
Clayton, D. D. 1983, Principles of stellar evolution and nucleosynthesis
Conroy, K. E., Kochoska, A., Hey, D., et al. 2020, ApJS, 250, 34
Corcoran, M. F., Nichols, J. S., Pablo, H., et al. 2015, ApJ, 809, 132
Cutri, R. M., L., W. E., & Conrow, T. 2012, VizieR Online Data Catalog, II/311
Cutri, R. M., Skrutskie, M. F., van Dyk, S., et al. 2003, VizieR Online Data Catalog, II/246
Ducati, J. R. 2002, VizieR Online Data Catalog
Egan, M. P., Price, S. D., Kraemer, K. E., et al. 2003, VizieR Online Data Catalog, V/114
Eisenhauer, F., Perrin, G., Brandner, W., et al. 2011, The Messenger, 143, 16
Ekström, S., Georgy, C., Eggenberger, P., et al. 2012, A&A, 537, A146
Fan, H., Welty, D. E., York, D. G., et al. 2017, ApJ, 850, 194
Freudling, W., Romaniello, M., Bramich, D. M., et al. 2013, A&A, 559, A96
Friedman, S. D., York, D. G., McCall, B. J., et al. 2011, ApJ, 727, 33
Gaia Collaboration. 2020, VizieR Online Data Catalog, I/350
Gaia Collaboration, Brown, A. G. A., Vallenari, A., et al. 2021, A&A, 649, A1
Golay, M. 1974, Introduction to astronomical photometry
GRAVITY Collaboration, Abuter, R., Accardo, M., et al. 2017, A&A, 602, A94
Green, G. M., Schlafly, E., Zucker, C., Speagle, J. S., & Finkbeiner, D. 2019, ApJ, 887, 93
Guinan, E. F., Mayer, P., Harmanec, P., et al. 2012, A&A, 546, A123
Hainich, R., Rühling, U., Todt, H., et al. 2014, A&A, 565, A27
Horvat, M., Conroy, K. E., Pablo, H., et al. 2018, ApJS, 237, 26
Houk, N. & Swift, C. 1999, Michigan Spectral Survey, 5, 0
Hummel, C. A., Rivinius, T., Nieva, M. F., et al. 2013, A&A, 554, A52
Hummel, C. A., White, N. M., Elias, N. M., I., Hajian, A. R., & Nordgren, T. E. 2000, ApJ, 540, L91
Ishihara, D., Onaka, T., Kataza, H., et al. 2010, A&A, 514, A1
Johnson, H. L. & Morgan, W. W. 1953, ApJ, 117, 313
Jones, D., Conroy, K. E., Horvat, M., et al. 2020, ApJS, 247, 63
Kalari, V. M., Horch, E. P., Salinas, R., et al. 2022, ApJ, 935, 162
Keller, S. C., Schmidt, B. P., Bessell, M. S., et al. 2007, PASA, 24, 1
Kounkel, M., Covey, K., Suárez, G., et al. 2018, AJ, 156, 84
Krtička, J. & Feldmeier, A. 2018, A&A, 617, A121
Krtička, J., Kubát, J., & Krtičková, I. 2021, A&A, 647, A28
Lanz, T. & Hubený, I. 2003, ApJS, 146, 417
Lanz, T. & Hubený, I. 2007, ApJS, 169, 83
Le Bouquin, J. B., Berger, J. P., Lazareff, B., et al. 2011, A&A, 535, A67
Lesh, J. R. & Aizenman, M. L. 1978, ARA&A, 16, 215
Maíz Apellániz, J., Trigueros Páez, E., Negueruela, I., et al. 2019, A&A, 626, A20
Marchant, P., Pappas, K. M. W., Gallegos-Garcia, M., et al. 2021, A&A, 650, A107
Maud, L. T., Cesaroni, R., Kumar, M. S. N., et al. 2018, A&A, 620, A31
Mermilliod, J. C. 1994, Bulletin d'Information du Centre de Donnees Stellaires, 45, 3
Mourard, D., Meilland, A., Ibañez Bustos, R., et al. 2024, in Society of Photo-Optical Instrumentation Engineers (SPIE) Conference Series, Vol. 13095, Optical and Infrared Interferometry and Imaging IX, ed. J. Kammerer, S. Sallum, & J. Sanchez-Bermudez, 1309503
Nelder, J. A. & Mead, R. 1965, The Computer Journal, 7, 308
Neugebauer, G., Habing, H. J., van Duinen, R., et al. 1984, ApJ, 278, L1
Nichols, J., Huenemoerder, D. P., Corcoran, M. F., et al. 2015, ApJ, 809, 133
Opištilová, A., Mayer, P., Harmanec, P., et al. 2023, A&A, 672, A31
Pablo, H., Richardson, N. D., Moffat, A. F. J., et al. 2015, ApJ, 809, 134
Pauwels, T., Reggiani, M., Sana, H., Rainot, A., & Kratter, K. 2023, A&A, 678, A172
Paxton, B., Cantiello, M., Arras, P., et al. 2013, ApJS, 208, 4
Paxton, B., Marchant, P., Schwab, J., et al. 2015, ApJS, 220, 15
Perryman, M. A. C., Lindegren, L., Kovalevsky, J., et al. 1997, A&A, 323, L49
Pietrzyński, G., Graczyk, D., Gallenne, A., et al. 2019, Nature, 567, 200
Prša, A., Conroy, K. E., Horvat, M., et al. 2016, ApJS, 227, 29
Puebla, R. E., Hillier, D. J., Zsargó, J., Cohen, D. H., & Leutenegger, M. A. 2016a, MNRAS, 456, 2907
Puebla, R. E., Hillier, D. J., Zsargó, J., Cohen, D. H., & Leutenegger, M. A. 2016b, MNRAS, 456, 2907
Puls, J., Vink, J. S., & Najarro, F. 2008, A&A Rev., 16, 209
Renzo, M., Hendriks, D. D., van Son, L. A. C., & Farmer, R. 2022, Research Notes of the American Astronomical Society, 6, 25
Repolust, T., Puls, J., Hanson, M. M., Kudritzki, R. P., & Mokiem, M. R. 2005, A&A, 440, 261
Sana, H., Le Bouquin, J. B., Lacour, S., et al. 2014, ApJS, 215, 15
Sanhueza, P., Jackson, J. M., Zhang, Q., et al. 2017, ApJ, 841, 97
Schaefer, G. H., Hummel, C. A., Gies, D. R., et al. 2016a, AJ, 152, 213
Schaefer, G. H., Hummel, C. A., Gies, D. R., et al. 2016b, AJ, 152, 213
Shenar, T., Oskinova, L., Hamann, W. R., et al. 2015, ApJ, 809, 135
Shenar, T., Sana, H., Mahy, L., et al. 2022, Nature Astronomy, 6, 1085
Sota, A., Maíz Apellániz, J., Morrell, N. I., et al. 2014, ApJS, 211, 10
Taniguchi, Y., Kajisawa, M., Kobayashi, M. A. R., et al. 2015, Publications of the Astronomical Society of Japan, 67, 104
Thompson, G. B. & Morrison, N. D. 2013, The Astronomical Journal, 145, 95
Tokovinin, A., Fischer, D. A., Bonati, M., et al. 2013, PASP, 125, 1336
van Hamme, W. 1993, AJ, 106, 2096
van Leeuwen, F. 2007, A&A, 474, 653
Wilson, R. E., Van Hamme, W., & Terrell, D. 2010, ApJ, 723, 1469
Wongwathanarat, A., Janka, H. T., & Müller, E. 2013, A&A, 552, A126

Appendix A: Calibrator of ζ Ori: HIP 26108

The most challenging object for the calibration was ζ Ori because the diameter of its calibrator HIP 26108 in the pipeline database (`GRAVI_FAINT_CALIBRATORS.fits`) was clearly wrong, and the squared visibility was greater than one in several wavelength intervals. Therefore, we determined the diameter of the calibrator based on the absolute flux from the photometric catalogues in the VizieR tool (Allen et al. 2014). We used the standard Johnson system photometry (Ducati 2002) and measurements from Hipparcos (Anderson & Francis 2012), Gaia DR3 (Gaia Collaboration 2020), 2MASS (Cutri et al. 2003), WISE (Cutri et al. 2012), MSX (Egan et al. 2003), SkyMapper (Keller et al. 2007), Subaru/Suprime (Taniguchi et al. 2015), Akari (Ishihara et al. 2010), and IRAS (Neugebauer et al. 1984). The data covered the spectral range from 0.42 to 23.88 μm.

For SED modelling, we used the reddening value E_{B-V} = 0.014 mag, i.e. extinction A_V = 0.0434 mag (Green et al. 2019)[6], and the parallax of (6.2 ± 0.1) mas from Gaia, corresponding to d = (161.1 ± 2.5) pc. Based on the spectral type K4III, we used the temperature T = 3 800 K and log g = 2.0. The fit with the lowest χ^2 value (see Fig. A.1) led to the physical radius R = (33.52±0.53) $R_\odot$. We thus recalibrated ζ Ori using the calibrator' angular diameter, $\theta = 2R/d$ = (1.935 ± 0.002) mas.

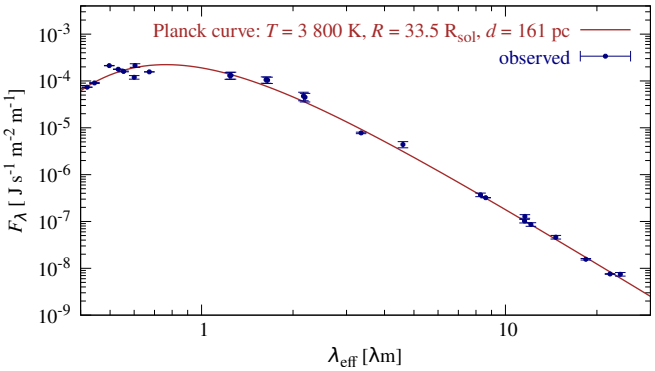

Fig. A.1. SED in terms of the monochromatic flux vs. wavelength for the calibration star HIP 26108, which was used to determine the correct calibrator's radius R = (33.52 ± 0.53) $R_\odot$ and recalibrate the visibilities of ζ Ori.

Appendix B: Radial velocities

Thompson & Morrison (2013) measured RVs of the He I 6678 Å lines on 132 electronic spectra from the Ritter Observatory and found variations ranging from about −10 to +20 km s^{-1}. In an effort to understand the nature of possible RV changes, we measured RVs of various spectral lines available in the high-resolution spectra at our disposal (CFHT, SOPHIE, and CTIO). The RVs were measured in `reSPEFO`, comparing direct and flipped line profiles on the computer screen. The zero point of the velocity scale was checked via measurements of a selection of telluric lines and also interstellar lines. The results of RV measurements are summarised in Table B.1. It is seen that the individual RVs from spectra taken during a particular observing night agree very well, but there are undoubtedly real RV changes from one observing season to another. We note, however, that the RVs of the He II lines of higher ionisation show little evidence of variability. This seems to contradict the presence of orbital motion in a putative binary system. The observed changes can be caused by some velocity fields in the stellar atmosphere and/or envelope. As Fig. B.1 illustrates, H_β line shows variable asymmetry due to partial filling of one or another wing by the emission, which also seems to affect, to some extent, the He I 5876 and 6678 Å lines. A more systematic study of the nature of these changes seems desirable. At present, we conclude that the single-star models are preferable.

[6] http://argonaut.skymaps.info/

Table B.1. Individual radial velocities (in km s^{-1}) measured in the CFHT, SOPHIE, and CTIO electronic spectra.

Line	CFHT	SOPHIE	SOPHIE	CTIO	CTIO
He I 6678 Å	–	26.8	25.7	9.9	10.5
He I 5876 Å	21.6	19.7	19.6	5.4	5.4
He I 5015 Å	22.6	29.6	30.1	17.7	17.5
He I 4922 Å	22.2	27.1	27.2	15.8	15.5
He I 4713 Å	21.8	26.7	25.8	16.0	16.4
Si III 4574 Å	16.6	25.3	23.8	13.9	13.4
Si III 4568 Å	17.9	25.4	26.2	12.6	12.6
Si III 4552 Å	20.5	28.4	27.1	12.4	13.8
He II 5411 Å	29.4	30.7	30.7	26.2	24.1
He II 4686 Å	42.3	44.7	45.4	35.2	37.6
H_β	55.1	50.1	50.5	−22.4	−24.3
H_γ	34.5	35.8	33.6	–	–
H_δ	31.5	33.1	33.4	–	–
H_ε	26.3	28.8	28.9	–	–
H8	25.9	–	–	–	–
H9	24.9	–	–	–	–

Notes. Julian dates (UTC) of the observations were 2454754.1558, 2457015.4119, 2457015.4139, 2460637.7725, 2460637.7732.

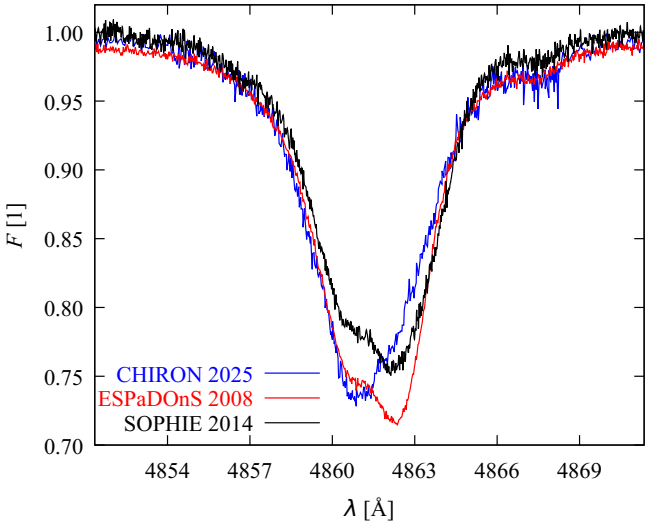

Fig. B.1. The H_β line exhibits variable asymmetry due to partial emission filling in one of the wings.

Appendix C: Supplementary tables

In Tab. C.1, SED of ε Ori is summarised.

Table C.1. Absolute monochromatic fluxes for ε Ori. Dereddening was applied to all measurements, assuming $E(B-V) = 0.050$ mag.

λ [Å]	F_λ [J s^{-1} m^{-2} m^{-1}]	σ [J s^{-1} m^{-2} m^{-1}]	Filter
3531	3.66609 e−02	3.22576 e−03	Johnson:U
3670	3.45552 e−02	7.86573 e−04	Johnson:U, Hvar
4360	1.92305 e−02	5.92874 e−04	Johnson:B, Hvar
4442	1.85143 e−02	1.13899 e−04	Johnson:B
5450	9.07753 e−03	1.49252 e−04	Johnson:V, Hvar
5537	8.64778 e−03	1.36701 e−04	Johnson:V
6730	4.68045 e−03	4.11829 e−04	Gaia:G
6938	4.03631 e−03	3.55151 e−04	Johnson:R
8780	1.64095 e−03	1.44385 e−04	Johnson:I
12 390	4.32121 e−04	9.97331 e−05	2MASS:J
12 500	4.32235 e−04	9.95143 e−05	Johnson:J
16 300	1.32848 e−04	1.91180 e−05	Johnson:H
16 495	1.30820 e−04	1.86919 e−05	2MASS:H
21 638	5.47162 e−05	1.13176 e−05	2MASS:Ks
21 900	5.17698 e−05	1.06892 e−05	Johnson:K

Notes. λ denotes the wavelength; F_λ, the absolute monochromatic flux; and σ, the uncertainty of the absolute flux.

Appendix D: Supplementary figures

We demonstrate the line profiles formation in our model in Figs. D.1 and D.2. Each triangle has a synthetic spectrum, determined by local broadening effects (thermal, pressure, . . .). For example, He I and He II lines form at different locations on a fast or critically rotating star due to strong temperature gradients. He I lines have the lowest intensity on the poles, while He II lines have the highest intensity at the poles. For reference, we show the closure phases for the respective model in Fig. D.4.

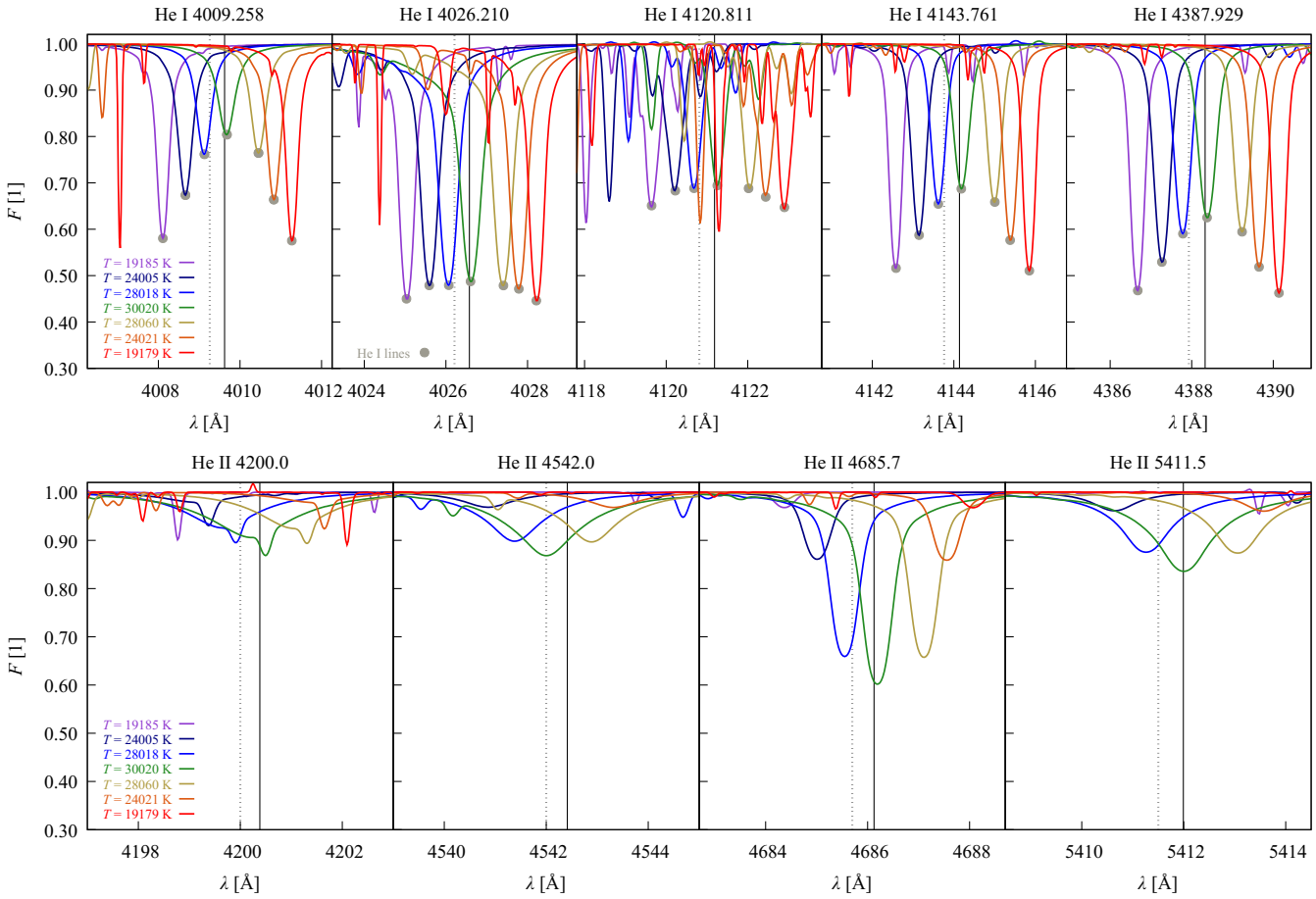

Fig. D.1. Synthetic He I and He II line profiles from our spectroscopic model, corresponding to selected triangles, having a range of temperatures and RVs. For a fast-rotating star, the pole is substantially hotter than the equator. The central line (RV = 0) corresponds to the pole, other lines originate from the equator (RV ≠ 0). He I lines are less intense at the pole, while He II lines are less intense on the equator. The grey points indicate the He I lines for clarity.

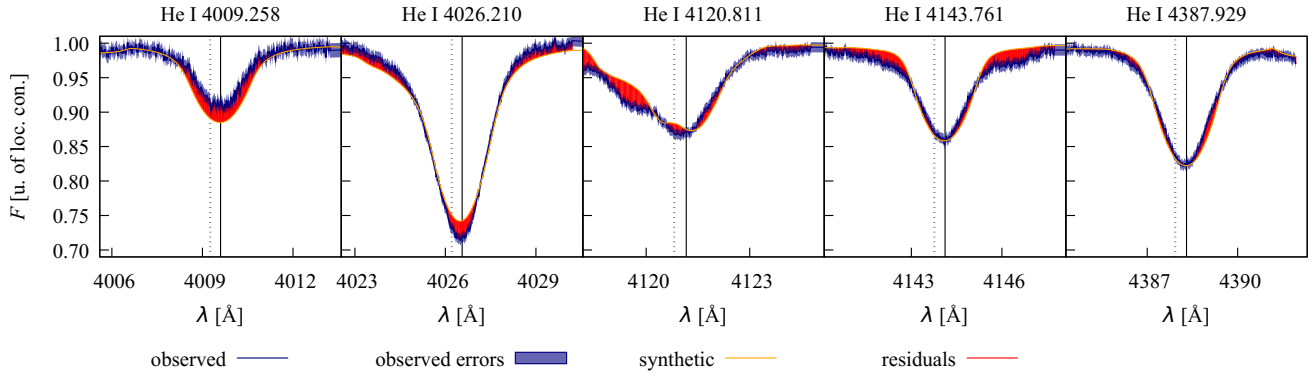

Fig. D.2. Same as Fig. 7 for He I lines. The best-fit spectroscopic model still exhibits systematics (in particular, 4009 and 4026 Å lines). None of these is easy to correct, e.g. by changing T, $\log g$, or metallicity (see also Pablo et al. (2015)).

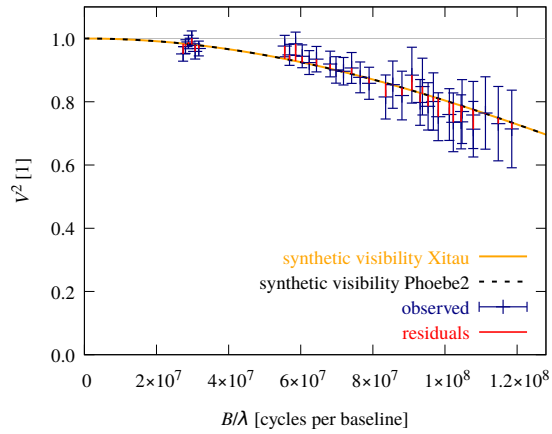

Fig. D.3. Spherical non-rotating model of ε Ori based VLTI/PIONIER observations; the squared visibility vs. the projected baseline B/λ is plotted for two models, Xitau (Brož 2017) and Phoebe (Brož et al. 2025b). The resulting $\chi^2_{\rm VIS} = 12.1$ is the same in both cases. The number of degrees of freedom, $\nu = N - M = 35$. The resulting parameters are $m = 23.52\,{\rm M}_\odot$ (free), $d = 384$ pc (fixed), $T = 27\,000$ K (fixed) (Puebla et al. 2016a), $\log g = 3.0$ (fixed) (Puebla et al. 2016a), $R = 25.40\ {\rm R}_\odot$ (derived), $\theta = 0.615$ mas (derived).

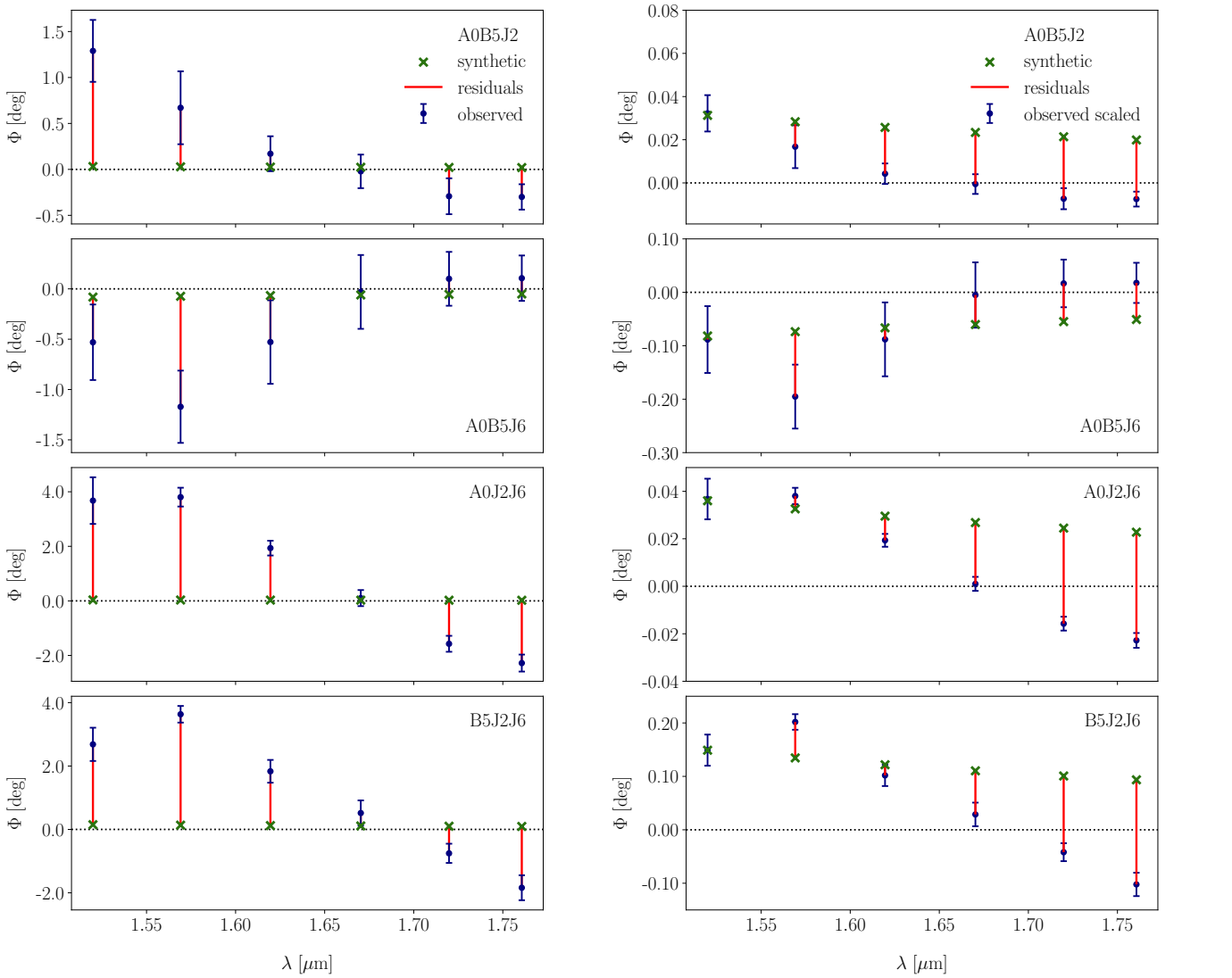

Fig. D.4. Model of ε Ori showing a forward computation of the closure phases with fixed parameters from the visibility model (Fig. 6). The observed closure phases reach up to nearly 4 deg, while the synthetic ones are at most 0.15 deg. If we recalibrate the observed closure phases (left column) by multiplying them by scaling factors 1/40, 1/6, 1/100, and 1/18, respectively for each of the triple baselines (right column), we see similar trends in the observed and synthetic closure phases, $\arg T_3$ vs. B/λ. We used this asymmetry of the flux to set the orientation of the star's equator, as seen by the observer, Ω (favouring 300 deg over 120 deg).

List of publications

[1] **Oplištilová, A.**, Mayer, P., Harmanec, P., Brož, M., Pigulski, A., Božić, H., Zasche, P., Šlechta, M., Pablo, H., Kołaczek-Szymański, P. A., Moffat, A. F. J., Lovekin, C. C., Wade, G. A., Zwintz, K., Popowicz, A., and Weiss, W. W., Spectrum of the secondary component and new orbital elements of the massive triple star δ Ori A. 2023, A&A, 672, A31, DOI: 10.1051/0004-6361/202245272

–**Published.** In Oplištilová et al. (2023), I conducted a comprehensive analysis of the triple star δ Ori A (see Sect. 3), under the guidance of my supervisor. This publication has already been cited 4 times.

[2] Harmanec, P., Božić, H., Koubský, P., Yang, S., Ruždjak, D., Sudar, D., Šlechta, M., Wolf, M., Korčáková, D., Zasche, P., **Oplištilová, A.**, Vršnak, D., Ak, H., Eenens, P., Bakiş, H., Bakiş, V., Otero, S., Chini, R., Demsky, T., Barlow, B. N., Svoboda, P., Jonák, J., Vitovský, K., and Harmanec, A., V1294 Aql = HD 184279: A bad boy among Be stars or an important clue to the Be phenomenon? 2022, A&A, 666, A136, DOI: 10.1051/0004-6361/202244006

–**Published.** For the publication Harmanec et al. (2022), including analysis of Be star V1294 Aql, I contributed photometric observations obtained at the Hvar Observatory using the 0.65m Cassegrain telescope. I collected data over three seasons. This publication has been cited 4 times.

[3] Wolf, M., Harmanec, P., Božić, H., Koubský, P., Yang, S., Ruždjak, D., Šlechta, M., Ak, H., Bakış, H., Bakış, V., **Oplištilová, A.**, and Vitovský, K. Long-term, orbital, and rapid variations of the Be star V923 Aql = HD 183656. 2021, A&A, 647, A97, DOI: 10.1051/0004-6361/202039740

–**Published.** Wolf et al. (2021) is a long-term observational study of V923 Aql. I contributed photometric observations obtained at the Hvar Observatory.

[4] **Oplištilová, A.**, Harmanec, P., Mayer, P., Zasche, P., Šlechta, M., Pablo, H., Pigulski, A., & BRITE Team. Improved Model of Delta Orionis, 2020. Contributions of the Astronomical Observatory Skalnate Pleso
DOI: 10.31577/caosp.2020.50.2.585

–**Published.** The proceedings Oplištilová et al. (2020) include my first analysis that led to the detection of the secondary component of δ Ori. These preliminary results were presented at the 'Universe of Binaries' conference and later included in my first-authored paper (Oplištilová et al. 2023).

[5] **Oplištilová, A.** and Brož, M., Hummel, C. A., Harmanec, P., and Barlow, B. N. VLTI observations of the Orion Belt stars: I. ε Orionis. 2025, A&A, submitted, arXiv:2507.02276, https://arxiv.org/abs/2507.02276, DOI: 10.48550/arXiv.2507.02276

–**Submitted.** In Oplištilová et al. (2025), I modelled the supergiant ε Ori based on VLTI/PIONIER observations from the ESO proposal (ID: 112.25JX, PI A. Oplištilová).

[6] H. Božić, P. Harmanec, J. Horn, K. Juza, P. Koubský, S. Kříž, P. Mayer, P. Hadrava, D. Ruždjak, D. Sudar, S. Štefl, M. Wolf, P. Zasche, M. Brož, J. Havelka, J. Honsa, V. Kocourek, M. Tlamicha, F. Žďárský, A. Harmanec, J. Jonák, **A. Oplištilová**, I. Piantschitsch, I. Skokić, J. Švrcková, K. Vitovský, D. Vršnak, and M. Zummer. Half a century of UBV photometry at Hvar I. Overview and emission-line stars. A&A, submitted in November 2024.

–**Submitted.** Božić et al. summarise and publish 50 years of photometric observations at the Hvar Observatory. I contributed by conducting photometric observations obtained at the Hvar Observatory using the 0.65m Cassegrain telescope. I measured data over three seasons.

[7] Brož, M., Prša, A., Conroy, K. E., **Oplištilová, A.**, and Horvat, M. Physics Of Eclipsing Binaries. VII. Interferometric module. 2025, arXiv e-prints, arXiv:2506.20865

–**To be submitted.** Brož et al. described the implementation of a new interferometric module in PHOEBE 2. I contributed to the testing and debugging of the interferometric module, using VLTI data.

[8] **Oplištilová, A.** , M. Brož, C. A. Hummel, et al. VLTI observations of the Orion Belt stars: II. ζ Orionis.

–**To be submitted.** I am also preparing an analysis of the multiple system ζ Ori, based on VLTI/GRAVITY observations from the ESO proposal (ID: 112.25JX, PI A. Oplištilová) and other available datasets such as spectroscopy, photometry, astrometry, etc. The result will be a complex model of the system with a discussion of possible evolutionary scenarios.

Additional proceedings contributions:

[9] **Oplištilová, A.** 2024, Modelling of Massive Multiple Systems with VLTI Interferometry, BRITE Photometry, and Spectroscopy, in the BRITE Side of Stars. Celebrating the 10th Anniversary of BRITE Constellation, 20, DOI: 10.5281/zenodo.13857790

[10] **Oplištilová, A.** & Brož, M. 2023a, Massive multiple stars in the Orion belt (Delta, Epsilon, Zeta Ori), `https://oh.geof.unizg.hr/images/meetings/HSM-2023/talks/4-Thursday/Oplistilova-stars-orion.pdf`

[11] **Oplištilová, A.** & Brož, M. 2023b, Spectrum of the secondary component and new orbital elements of the massive triple star Delta Ori A, `fys.kuleuven.be/ster/events/conferences/2023/massivebinaries2023/programme.pdf`, p. 15

[12] **Oplištilová, A.**, Brož, M., Harmanec, P., Mayer, P., Pigulski, A., Božić, H., Zasche, P., Šlechta, M., Pablo, H., Kołaczek-Szymański, P. A., Moffat, A. F. J., Lovekin, C. C., Wade, G. A., Zwintz, K., Popowicz, A., Weiss, W. W. 2023c, Constraining orbital parameters of bright multiple systems using Gaia data, in EAS2023, European Astronomical Society Annual Meeting, 1836, `https://ui.adsabs.harvard.edu/abs/2023eas..conf.18360`

In Oplištilová et al. (2023a), I presented the results from my analysis related to Gaia data. Oplištilová et al. (2023b) and Oplištilová et al. (2023c) covered the whole

modelling of δ Ori. The most recent proceedings Oplištilová et al. (2024) presented my initial analysis of VLTI/GRAVITY and VLTI/PIONIER data for Orion's Belt, delivered at the conference The BRITE Side of Stars, Vienna, Austria. The analysis was later included in my first-authored paper (Oplištilová et al. 2025, submit.).